



HAL
open science

Contribution to the understanding of the role of inorganic elements in biomass steam gasification

Tilia Dahou

► **To cite this version:**

Tilia Dahou. Contribution to the understanding of the role of inorganic elements in biomass steam gasification. Chemical and Process Engineering. Université Grenoble Alpes, 2019. English. NNT : 2019GREAI097 . tel-02519820v1

HAL Id: tel-02519820

<https://theses.hal.science/tel-02519820v1>

Submitted on 26 Mar 2020 (v1), last revised 15 May 2020 (v2)

HAL is a multi-disciplinary open access archive for the deposit and dissemination of scientific research documents, whether they are published or not. The documents may come from teaching and research institutions in France or abroad, or from public or private research centers.

L'archive ouverte pluridisciplinaire **HAL**, est destinée au dépôt et à la diffusion de documents scientifiques de niveau recherche, publiés ou non, émanant des établissements d'enseignement et de recherche français ou étrangers, des laboratoires publics ou privés.

THÈSE

Pour obtenir le grade de

DOCTEUR DE LA COMMUNAUTE UNIVERSITE GRENOBLE ALPES

Spécialité : MEP : Mécanique des fluides, Energétique, Procédés

Arrêté ministériel : 25 mai 2016

Présentée par

Tilia DAHOU

Thèse dirigée par **Capucine DUPONT**,
et codirigée par **Mejdi JEGUIRIM** et **Françoise DEFOORT**

préparée au sein du **Laboratoire de Conversion des
Ressources Carbonées par voie Sèche (L2CS)**, **LITEN**, **CEA**
et de l'**Institut de Science des Matériaux de Mulhouse (IS2M)**
dans l'**École Doctorale I-MEP²**

**Contribution à la compréhension du rôle
des éléments inorganiques sur la
cinétique de gazéification sous vapeur
d'eau de la biomasse**

**Contribution to the understanding of the
role of inorganic elements in biomass
steam gasification**

Thèse soutenue publiquement le **13 décembre 2019**,
devant le jury composé de :

Madame Capucine DUPONT

Docteure HDR, IHE Delft Institute for Water Education, Directrice de thèse

Monsieur Kentaro UMEKI

Professeur, Luleå University of Technology, Rapporteur

Monsieur Fabrice PATISSON

Professeur, Université de Lorraine, Rapporteur

Monsieur Gérard MORTHA

Professeur, Grenoble INP, Président

Monsieur Laurent VAN DE STEENE

Docteur, CIRAD, Examineur

Monsieur Mejdi JEGUIRIM

Maître de Conférences HDR, Université de Haute-Alsace, Co-directeur de thèse

Madame Françoise DEFOORT

Docteure, CEA, Co-encadrante de thèse

Monsieur Matthieu CAMPARGUE

Directeur, RAGT Energie, Invité



This research was funded by the Agence de l'Environnement et de la Maîtrise de l'Energie.

Acknowledgements

I would like to acknowledge my supervisors Capucine Dupont, Mejdi Jeguirim and Françoise Defoort for sharing their knowledge with me as well as for their guidance during these three years. I am grateful that they trusted me to work on this project and that they guided me to take ownership of it. It greatly contributed to my development as a researcher and as a person.

I acknowledge Anne-Laure Dubilly from the Agence de l'Environnement et de la Maîtrise de l'Energie who followed the project and brought a broader point of view during our meetings.

I want to thank the jury members, Pr. Umeki, Pr. Patisson, Pr. Mortha, Dr. Van de Steene and M. Campargue, for their constructive remarks in their reports and during the defense. I especially thank Matthieu Campargue from RAGT Energie for supporting this project from the beginning and bringing his industrial point of view.

I extend my acknowledgments to all my colleagues of the CEA biomass team for the enriching discussions during meetings that helped me with my project but also for the more informal moments we spent together at barbecues or Christmas meals. I especially want to thank Sébastien and Maguelone for their help during my experimental work, and Sylvie for exchanging ideas.

I also thank the people I worked with at the IS2M. My stays there were short but I felt welcome and managed to collect a lot of characterization results thanks to their help. I particularly thank Simona Bennici for her help in interpreting the results.

I also want to thank my friends for their support and for the opportunities to have fun and balance the work we did in the lab. First I thank the members of the Colocaloca, my roommates, colleagues and friends, Carolina and Oscar. I appreciate your support and I apologize for all the disco you had to listen to! I also thank the PhD students, Clément, Florent, Morgane, Simon and María at CEA and Melania and Adrian at IS2M, for the good times we had and the friendships we built. Lastly, I want to express my gratitude towards Manon whose friendship means a lot to me.

Finally, I thank my family for being supportive and caring during these years.

Table of contents

Introduction.....	19
Chapter I. Context and state of the art	25
1. Biomass and its composition.....	25
1.1. Biomass definition	25
1.2. Biomass composition.....	25
1.2.1. Organic fraction.....	25
1.2.2. Inorganic fraction	28
1.3. Biomass conversion to energy.....	31
2. The pyrogasification of biomass.....	33
2.1. Gasifier technologies for biomass	33
2.1.1. Fixed bed gasifiers	34
2.1.2. Fluidized bed gasifiers	35
2.1.3. Entrained flow gasifiers	36
2.2. Pyrogasification reactions	37
2.2.1. Pyrolysis reactions	37
2.2.2. Gasification reactions	39
3. The effects of inorganic elements on the steam gasification process	45
3.1. Assessment of the inorganic effects on char gasification	47
3.1.1. Effects of all inorganic compounds	47
3.1.2. The specific effects of K and Si	49
3.2. Proposed mechanisms for the K-catalysis.....	50
3.2.1. Mechanism with intercalation compounds.....	50
3.2.2. Mechanisms with a mechanical action	51
3.2.3. Mechanisms for a carbon atom.....	52
3.2.4. Mechanisms for carbon structures	53
3.2.5. Explanation of the reactivity changes at high conversion.....	54
3.3. Proposed mechanisms for the inhibiting effect of Si	55
3.4. Proposed models.....	56
4. Conclusions and objective of the work	60
Chapter II. Evolution of the char physicochemical properties during gasification	62
1. Materials and experimental installations.....	62
1.1. List of biomass species	62

1.2.	Experimental set-ups.....	64
1.2.1.	Pyrolysis furnace MATISSE	64
1.2.2.	Thermogravimetric analyzer	64
1.2.3.	Gasification devices	66
1.3.	Characterization techniques.....	71
1.3.1.	Raman spectroscopy	71
1.3.2.	N ₂ and CO ₂ adsorption.....	72
1.3.3.	Temperature programmed desorption coupled to mass spectrometry	73
1.3.4.	Inductively coupled plasma with atomic emission spectroscopy	73
1.3.5.	Scanning electron microscopy coupled to energy dispersive X-ray spectroscopy....	74
1.3.6.	Powder X-ray diffraction	74
2.	Choice of the methodology	75
2.1.	Choice of the biomass samples	75
2.2.	Choice of the char production method	77
2.3.	Choice of the gasification device.....	78
2.4.	Thermodynamic equilibrium simulation method	79
3.	Results and discussion.....	82
3.1.	Gasification kinetic profiles	82
3.2.	Results of the characterization of the char carbon matrix.....	85
3.2.1.	Structure of the carbon matrix.....	85
3.2.2.	Porosity of the carbon matrix.....	87
3.2.3.	Surface chemistry of the carbon matrix.....	89
3.2.4.	Conclusions on the carbon matrix properties	93
3.3.	Results of the characterization of the inorganic fraction of the chars.....	94
3.3.1.	Volatilization of the inorganic elements	94
3.3.2.	Determination of the inorganic condensed phases	100
3.3.3.	Conclusions on the inorganic fraction.....	108
4.	Conclusions.....	109
Chapter III.	Experimental study on the influence of K and Si on biomass gasification kinetics.....	111
1.	Materials and methods	111
1.1.	Biomass samples	111
1.2.	Model inorganic compounds.....	113
1.2.1.	Amorphous silica and quartz	113
1.2.2.	Potassium carbonate	113
1.3.	Experimental installation and procedure	113

1.4. Thermodynamic equilibrium simulation method	116
2. Steam gasification of the pure materials	117
2.1. Steam gasification of pure inorganic compounds	117
2.1.1. Amorphous silica and quartz	117
2.1.2. Potassium carbonate	118
2.2. Steam gasification of pure biomass	120
3. Results of the interactions between materials	122
3.1. Influence of K_2CO_3 addition on pyrolysis and steam gasification	122
3.1.1. Influence of K_2CO_3 addition on the pyrolysis reaction	124
3.1.2. Influence of K_2CO_3 addition on the gasification reaction	131
3.1.3. Characterization of the ashes	134
3.1.4. Conclusions on the influence of K_2CO_3 addition	140
3.2. Influence of the addition of SiO_2 on steam gasification	141
3.2.1. Influence of the addition mode	141
3.2.2. Influence of the crystalline form	143
3.2.3. Influence of the concentration	144
1.1.1. Conclusions on the influence of SiO_2 addition	152
4. Conclusions	153
Conclusions and perspectives	155
1. Conclusions	155
2. Perspectives	157
2.1. Towards a full understanding of the K-catalysis mechanisms	157
2.2. Towards a phenomenological modeling of the inorganics influence on biomass gasification kinetics	157
2.3. Towards practical applications to the gasification process	158
References	161
Annex A. Determination of the TGA chemical regime conditions	171
Annex B. Article published in Energies: “The influence of char preparation and biomass type on char steam gasification kinetics”	172
Annex C. Characteristic time analysis of the gasification step	188
Annex D. Pore size distribution of rice husk and sunflower seed shell chars expressed in incremental volume	191
Annex E. Example of detailed results from calculations at thermodynamic equilibrium	192
Annex F. P-XRD analysis of the model inorganic compounds	199

Annex G. Characterization of the residue on the K_2CO_3 from the pyrolysis at 800 °C of rice husks and K_2CO_3 added without contact..... 201

Figures

Figure 0.1 Global estimated renewable share of the total final energy consumption in the world for 2017 (Appavou et al., 2019).	20
Figure 0.2 Renewable share of the total final energy consumption in the European Union for 2017 (Eurostat, 2019).....	20
Figure 0.3 Global estimated shares of bioenergy in the total final energy consumption in the world in 2017 (Appavou et al., 2019).	21
Figure 0.4 Share of available crop residues in final energy consumption in the European Union. Reprinted from (Scarlat et al., 2010) with permission from Elsevier.....	22
Figure I.1 Van Krevelen diagram for various solid fuels. Reprinted from (McKendry, 2002a) with permission from Elsevier.....	26
Figure I.2 Lignocellulosic biomass structure. Reprinted by permission from Springer Nature (Rubin, 2008).....	28
Figure I.3 Thermochemical conversion processes, intermediate products and final energy products. Reprinted from (Patel et al., 2016) with permission from Elsevier.....	32
Figure I.4 Biomass pyrogasification steps. Reprinted from (Baker and Mudge, 1984) with permission from Elsevier.....	33
Figure I.5 Fixed bed gasifiers (Basu, 2010b).	35
Figure I.6 Fluidized bed gasifiers (Dahmen and Sauer, 2015).	36
Figure I.7 Entrained flow gasifier (Dahmen and Sauer, 2015).....	37
Figure I.8 Typical product distribution of the pyrolysis at ~500 °C at several heating rates from data from (Bridgwater, 2015).....	38
Figure I.9 Thermal stability of hemicellulose, lignin and cellulose. Adapted by permission from Springer (Koukios, 1993).	39
Figure I.10 Reactivity versus conversion curves for steam gasification of grapefruit skin char at different partial pressures of steam. Reprinted from (Marquez-Montesinos et al., 2002) with permission from Elsevier.....	41
Figure I.11 Reactivity versus conversion curves for CO ₂ gasification of grapefruit skin char at different temperatures. Reprinted from (Marquez-Montesinos et al., 2002) with permission from Elsevier.	42
Figure I.12 Reactivity between 1 and 80% of conversion of several biomass samples. Reprinted from (Dupont et al., 2016) with permission from Elsevier.	43
Figure I.13 SEM observations of beech chars produced from a. high heating rate pyrolysis (100 °C.s ⁻¹), b. low heating rate pyrolysis (0.05 °C.s ⁻¹). Reprinted from (Septien et al., 2018) with permission from Elsevier.....	44
Figure I.14 Carbon conversion to gas for the catalyzed steam gasification of Douglas fir with dry-mixed (solid line) and solution impregnated (dotted line) (a) K ₂ CO ₃ and (b) Na ₂ CO ₃ . Reprinted from (Elliott et al., 1984) with permission from Elsevier.	48
Figure I.15 Carbon conversion during the CO ₂ gasification of chars from Chinese Guangzhou fir catalyzed with different inorganic elements. Reprinted from (Huang et al., 2009) with permission from Elsevier.....	49
Figure I.16 Li and K intercalation in graphite with the resulting interlayer spacing (Wang et al., 2017) - Published by The Royal Society of Chemistry.	51
Figure I.17 Mechanistic model for the reaction of water with graphite in the presence of KOH. Reprinted from (Delannay et al., 1984) with permission from Elsevier.....	53

Figure I.18 Mechanisms of pre-loaded AAEMs and post-loaded AAEMs on biochar. Reprinted from (Feng et al., 2018b) with permission from Elsevier.....	54
Figure I.19 Reactivity at several conversion values as a function of the K/Si ratio of samples of impregnated beech wood (Bouraoui et al., 2016).	55
Figure I.20 SEM observation of a wheat straw char at 90% gasification conversion, with melted ashes. Reprinted (adapted) with permission from (Strandberg et al., 2017). Copyright (2019) American Chemical Society.	56
Figure II.1 Pyrolysis furnace MATISSE a. scheme and b. picture.	64
Figure II.2 Thermogravimetric analyzer (TGA) a. scheme and b. picture.	65
Figure II.3 TGA procedure for a. raw biomass and b. char.	65
Figure II.4 Macro-thermogravimetric reactor.	67
Figure II.5 The macro-thermogravimetric system at the University of Science & Technology of Hanoi.	68
Figure II.6 Laboratory furnace NEWMANIP a. scheme and b. picture.	69
Figure II.7 Induction furnace PYRATES a. scheme and b. picture. (1) Gas inlet; (2) Inductor; (3) Inconel pipe heated by induction; (4) Sample holder; (5) Metallic sample holder; (6) Quartz pipes; (7) Tar collector; (8) Electrostatic precipitator; (9) Ice trap (0 °C); (10) Isopropanol and dry ice trap (-78 °C); (11) Cartridge filter; (12) Secondary N ₂ (cooling) inlet; (13) Gas outlet towards gas analysis. .	70
Figure II.8 Raman band fitting example (sample RHB_X0).....	72
Figure II.9 TGA of the raw biomass samples presented as the normalized ash free mass as a function of time.	75
Figure II.10 Solid conversion of biomass samples as a function of time during the gasification step.	75
Figure II.11 Gasification average reactivity of seven biomass samples from the database.....	76
Figure II.12 Gasification solid conversion as a function of time, for sunflower seed shells and rice husks, in the case of chars produced directly in the TGA (raw biomass) or in the pyrolysis furnace...	77
Figure II.13 Measured gasification average reactivity of the two biomass samples in four different gasification installations.	78
Figure II.14 Gasification solid conversion of the rice husk and sunflower seed shell chars as a function of time.....	82
Figure II.15 Zoom on the gasification solid conversion of the sunflower seed shell char as a function of time.	82
Figure II.16 Solid conversion rate as a function of the conversion for rice husks and sunflower seed shells in the TGA.....	83
Figure II.17 Evolution of the ash content during pyrolysis and gasification conversion of rice husk and sunflower seed shell chars.	84
Figure II.18 Schematic repartition of ash and carbon matrix at several gasification conversions from calculated values for a. rice husks, b. sunflower seed shells and c. a typical wood (beech from (Dupont et al., 2016)). Numbers correspond to the ash content.	84
Figure II.19 Normalized Raman spectra of rice husk chars at several pyrolysis and gasification conversions.....	85
Figure II.20 Normalized Raman spectra of sunflower seed shell chars at several pyrolysis and gasification conversions.	85
Figure II.21 Evolution of the peak intensity ratios during pyrolysis and gasification conversion of rice husk and sunflower seed shell chars.....	86
Figure II.22 N ₂ adsorption isotherms of rice husk and sunflower seed shell chars at several pyrolysis and gasification conversions.	87

Figure II.23 CO ₂ adsorption isotherms of rice husk and sunflower seed shell chars at several pyrolysis and gasification conversions.	88
Figure II.24 Pore size distribution using DFT model from N ₂ and CO ₂ adsorption isotherms of rice husk and sunflower seed shell chars at several pyrolysis and gasification conversions expressed in terms of incremental area.....	88
Figure II.25 Ultramicropore size distribution using DFT model from CO ₂ adsorption isotherms of rice husk and sunflower seed shell chars at several pyrolysis and gasification conversions expressed in terms of incremental area.....	89
Figure II.26 Cumulative gas desorption between 24 and 800 °C during TPD–MS of rice husk and sunflower seed shell chars at several gasification conversions.	90
Figure II.27 CO ₂ desorption during TPD–MS of rice husk and sunflower seed shell chars at several pyrolysis and gasification conversions.	90
Figure II.28 CO desorption during TPD–MS of rice husk and sunflower seed shell chars at several pyrolysis and gasification conversions.	91
Figure II.29 H ₂ desorption during TPD–MS of rice husk and sunflower seed shell chars at several pyrolysis and gasification conversions.	91
Figure II.30 H ₂ O desorption during TPD–MS of rice husk and sunflower seed shell chars at several pyrolysis and gasification conversions.	91
Figure II.31 CH ₄ desorption during TPD–MS of rice husk and sunflower seed shell chars at several pyrolysis and gasification conversions.	92
Figure II.32 SO ₂ desorption during TPD–MS of rice husk and sunflower seed shell chars at several pyrolysis and gasification conversions.	92
Figure II.33 Carbon surface groups. Reprinted from (Shafeeyan et al., 2010) with permission from Elsevier.	93
Figure II.34 Calculated and measured volatilization of S and Cl in the rice husk samples.	97
Figure II.35 Calculated and measured volatilization of S and Cl in the sunflower seed shell samples.	98
Figure II.36 Calculated and measured volatilization of the three main inorganic elements Si, K and Ca in the rice husk samples.	99
Figure II.37 Calculated and measured volatilization of the three main inorganic elements K, Ca and Mg in the sunflower seed shell samples.	99
Figure II.38 Calculated condensed phases at thermodynamic equilibrium for rice husk samples. .	101
Figure II.39 Calculated condensed phases at thermodynamic equilibrium for sunflower seed shell samples.....	101
Figure II.40 SEM image of a char particle from RHB_X0 with SE detection.	102
Figure II.41 SEM image of a char particle from RHB_X0 with BSE detection.	102
Figure II.42 SEM image of a char particle from SFS_X25 with SE detection.....	103
Figure II.43 SEM image of a char particle from SFS_X25 with BSE detection.	103
Figure II.44 P-XRD diffractograms of rice husk chars at several pyrolysis and gasification conversions.....	104
Figure II.45 P-XRD diffractograms of sunflower seed shell chars at several pyrolysis and gasification conversions.....	105
Figure II.46 Raman spectra showing inorganic compounds of the sample RHB_X100.	107
Figure II.47 Raman spectra showing inorganic compounds of the sample SFS_X75.	108
Figure III.1 Divided crucible (here containing rice husks and K ₂ CO ₃).	114
Figure III.2 TGA procedure for raw biomass.....	114

Figure III.3 Measured mass, equivalent char mass (as used in further interpretations) and corresponding pure K_2CO_3 mass of the experiment on rice husks with K_2CO_3 added without contact.	116
Figure III.4 Mass evolution over time of amorphous silica alone and quartz alone during the pyrolysis and gasification procedure.....	117
Figure III.5 SEM observation of the pure amorphous silica a. before and b. after the gasification procedure.	117
Figure III.6 Mass evolution over time of various initial masses of K_2CO_3 alone during the pyrolysis and gasification procedure.....	118
Figure III.7 Mass evolution over time of various initial masses of K_2CO_3 alone during the gasification procedure and the corresponding models.....	120
Figure III.8 TGA of rice husks, sunflower seed shells and beech wood presented as the normalized mass as a function of time.	120
Figure III.9 TGA of rice husks with and without added K_2CO_3 and of sunflower seed shells presented as the normalized mass as a function of time.....	123
Figure III.10 DTG as a function of time of rice husks with and without added K_2CO_3 and of sunflower seed shells.	123
Figure III.11 DTG as a function of time of rice husks with and without added K_2CO_3 and of sunflower seed shells. Zoom on 1 st peak.....	124
Figure III.12 TGA of rice husks with and without added K_2CO_3 and of sunflower seed shells presented as the normalized mass as a function of time. Zoom on the high temperature pyrolysis.	125
Figure III.13 DTG as a function of time of rice husks with and without added K_2CO_3 and of sunflower seed shells. Zoom on the high temperature pyrolysis.	125
Figure III.14 DTG as a function of temperature during pyrolysis between 450 °C and 800 °C of rice husks alone, K_2CO_3 alone and rice husks with K_2CO_3 added without contact.....	126
Figure III.15 Rice husks with K_2CO_3 added without contact a. before and b. after pyrolysis until 800 °C in the TGA, i.e. procedure stopped before steam injection.	127
Figure III.16 KOH- K_2CO_3 phase diagram.....	128
Figure III.17 TGA of pure K_2CO_3 under N_2 atmosphere and with injection of steam for 21 min during the 450 °C plateau.	129
Figure III.18 Zoom on the 450 to 800 °C section of the DTG curve of pure K_2CO_3 under N_2 atmosphere and with injection of steam for 21 min during the 450 °C hold.	129
Figure III.19 K_2CO_3 after steam injection at 450 °C.....	130
Figure III.20 Gasification solid conversion as a function of time of rice husks with and without added K_2CO_3 and of sunflower seed shells.....	132
Figure III.21 Solid conversion rate as a function of the conversion of rice husks with and without added K_2CO_3 and of sunflower seed shells.....	132
Figure III.22 Gasification solid conversion as a function of time of rice husk char alone produced in presence of K_2CO_3 without contact.	134
Figure III.23 Ashes from pyrolysis and gasification of rice husks.	135
Figure III.24 Ashes from pyrolysis and gasification of rice husks with mixed K_2CO_3 (same aspect without contact).....	135
Figure III.25 SiO_2 - K_2O phase diagram. The dotted line is the 800 °C isotherm with the red portions corresponding to liquid phases.	136
Figure III.26 SEM observation of ashes from pyrolysis and gasification of rice husks.	136
Figure III.27 SEM observation of ashes from pyrolysis and gasification of rice husks with K_2CO_3 without contact (same aspect mixed).....	136

Figure III.28 | TGA of beech wood with and without added K_2CO_3 and of rice husks and sunflower seed shells presented as the normalized mass as a function of time. 137

Figure III.29 | TGA of beech wood with and without added K_2CO_3 and of rice husks and sunflower seed shells presented as the normalized mass as a function of time. Zoom on the high temperature pyrolysis. 138

Figure III.30 | Gasification solid conversion as a function of time of beech wood alone and with added K_2CO_3 , compared to rice husks and sunflower seed shells. 138

Figure III.31 | Mass evolution over time of the silica equivalent (purple curve) and the K_2CO_3 (orange curve) during the pyrolysis and gasification procedure applied to silica with K_2CO_3 added without contact. 139

Figure III.32 | SEM observation of the residue after the TGA of silica with K_2CO_3 added without contact. 139

Figure III.33 | Scheme of the effects of K_2CO_3 on biomass pyrolysis and gasification. 140

Figure III.34 | Solid conversion as a function of time during gasification of rice husks and of sunflower seed shells alone, mixed with 17wt% amorphous silica and with 17wt% amorphous silica without contact. 142

Figure III.35 | Gasification average reactivity between 1% and 80% conversion of rice husks and of sunflower seed shells alone, mixed with 17wt% amorphous silica and with 17wt% amorphous silica without contact. 142

Figure III.36 | Solid conversion as a function of time during gasification of rice husks and of sunflower seed shells alone, mixed with 17wt% amorphous silica and mixed with 17wt% silica quartz. 143

Figure III.37 | Gasification average reactivity between 1% and 80% conversion of rice husks and of sunflower seed shells alone, mixed with 17wt% amorphous silica and mixed with 17wt% silica quartz. 143

Figure III.38 | Solid conversion as a function of time during gasification of rice husks and of sunflower seed shells alone and mixed with 1, 2, 3, 6, 17 and 25wt% amorphous silica. 146

Figure III.39 | Gasification average reactivity between 1% and 80% conversion of rice husks and of sunflower seed shells alone and mixed with 1, 2, 3, 6, 17 and 25wt% amorphous silica. 146

Figure III.40 | Gasification average reactivity between 1% and 80% conversion of mixtures of sunflower seed shells and amorphous silica as a function of the quantity of added silica. 147

Figure III.41 | Optical microscope (left) and SEM (right) observations of residues after gasification of samples of sunflower seed shells a. alone. b. with 1wt% amorphous silica. c. with 2wt% amorphous silica. d. with 3wt% amorphous silica. e. with 6wt% amorphous silica. f. with 17wt% amorphous silica. g. with 25wt% amorphous silica. h. and of amorphous silica alone. 149

Figure III.42 | Gasification solid conversion as a function of time of beech wood and sunflower seed shells both alone and with 17wt% mixed amorphous silica, and of rice husks alone. 151

Figure III.43 | Gasification average reactivity between 1% and 80% conversion of beech wood and sunflower seed shells both alone and with 17wt% mixed amorphous silica, and of rice husks alone. 151

Figure Annex A.1 | Gasification conversion as a function of time for several initial mass of sunflower seed shells chars. 171

Figure Annex C.2 | Characteristic times for the gasification step at bed scale for $H_c = 48\text{mm}$ in PYRATES. 189

Figure Annex C.3 | Characteristic times for the gasification step at bed scale for $T_{\text{gas}} = 800^\circ\text{C}$ 189

Figure Annex C.4 | Characteristic times for the gasification step at bed scale for $H_c = 2\text{mm}$ in the TGA device. 189

Figure Annex C.5 | Characteristic times for the gasification step at particle-scale for $T_{\text{gas}} = 800^\circ\text{C}$ 189

Figure Annex C.6 | Characteristic times for the gasification step at particle-scale for $d_p = 0.2\text{mm}$ 189

Figure Annex C.7 | Characteristic times for the gasification step at particle-scale for $T_{\text{gas}} = 800^\circ\text{C}$ with the uncertainty related to bed porosity and tortuosity values. 190

Figure Annex C.8 | Characteristic times for the gasification step at bed scale for $T_{\text{gas}} = 800^\circ\text{C}$ with the uncertainty related to bed porosity and tortuosity values. 190

Figure Annex D.9 | Pore size distribution using DFT model from N_2 and CO_2 adsorption isotherms of rice husk and sunflower seed shell chars at several pyrolysis and gasification conversions expressed in terms of incremental volume. 191

Figure Annex D.10 | Ultramicropore size distribution using DFT model from CO_2 adsorption isotherms of rice husk and sunflower seed shell chars at several pyrolysis and gasification conversions expressed in terms of incremental volume. 191

Figure Annex F.11 | P-XRD diffractogram of the pure amorphous silica. 199

Figure Annex F.12 | P-XRD diffractogram of the pure quartz. 199

Figure Annex F.13 | P-XRD diffractogram of the pure K_2CO_3 200

Figure Annex G.14 | SEM observation of the residue. 201

Figure Annex G.15 | SEM observation of the residue. Zoom on zone A. 202

Figure Annex G.16 | SEM observation of the residue. Zoom on zone B. 202

Tables

Table I.1 Typical elemental composition in C, O, H, N and S of biomass and coal. From data from (Vassilev et al., 2010).....	26
Table I.2 Main characteristics of the gasifier technologies.	34
Table I.3 Typical gasification reactions and their associated enthalpy at 25 °C (Basu, 2010a).	40
Table I.4 Characteristics of gasifying agents. Reprinted from (Sansaniwal et al., 2017) with permission from Elsevier.....	41
Table I.5 References on the effects of inorganic elements used in this section, organized by gasifying agent, type of feedstock and mode of addition of the inorganic compounds if necessary...	46
Table I.6 Common models for the surface function f(X). Adapted from Romero Millán <i>et al.</i> (Romero Millán et al., 2019).....	57
Table I.7 Gasification kinetic models taking into account the effects of inorganic elements.....	58
Table II.1 Ash content and elemental composition of the preliminary biomass samples (in dry basis).	63
Table II.2 Main characteristics of the gasification devices.	67
Table II.3 Characterization techniques and the properties they measure.....	71
Table II.4 List of samples obtained from pyrolysis and gasification of rice husks and sunflower seed shells.....	79
Table II.5 Initial data for the thermodynamic equilibrium calculations.	80
Table II.6 Initial gas data for the thermodynamic equilibrium calculations of Xn (n= 25 to 75).	80
Table II.7 Inorganic element content and char yield of raw, charM, X0, X25 and X50 rice husk samples (in dry basis).	95
Table II.8 Inorganic element content and char yield of raw, charM, X0, X25 and X50 sunflower seed shell samples (in dry basis).....	96
Table II.9 Volatilization of the inorganic elements measured for raw biomass, charM, X0, X25 and X50 for both species.	97
Table II.10 List of inorganic compounds identified in rice husks biomass and chars.	106
Table II.11 List of inorganic compounds identified in sunflower seed shell biomass and chars.	106
Table III.1 Composition and gasification reactivity properties of rice husks, sunflower seed shells and beech (in dry basis).....	112
Table III.2 Conditions of the TGA experiments.....	115
Table III.3 Initial data for the thermodynamic equilibrium calculations.	116
Table III.4 Fitted coefficient of the polynomial regression of the curves of mass of K ₂ CO ₃ as a function of time for various initial masses.	119
Table III.5 Inorganic composition of the mixture of rice husks and K ₂ CO ₃ (in dry basis).	122
Table III.6 Gasification ash yield measured in TGA and associated theoretical yields.	134
Table III.7 Inorganic composition of the mixtures of sunflower seed shells and amorphous silica (in dry basis).	145
Table III.8 Inorganic composition of the mixture of beech wood and amorphous silica, sunflower seed shells and amorphous silica and of rice husks alone (in dry basis).....	150
Table Annex G.1 Detected elements through ionic chromatography in the residue.....	201
Table Annex G.2 EDX analysis of the residue.	203

Introduction

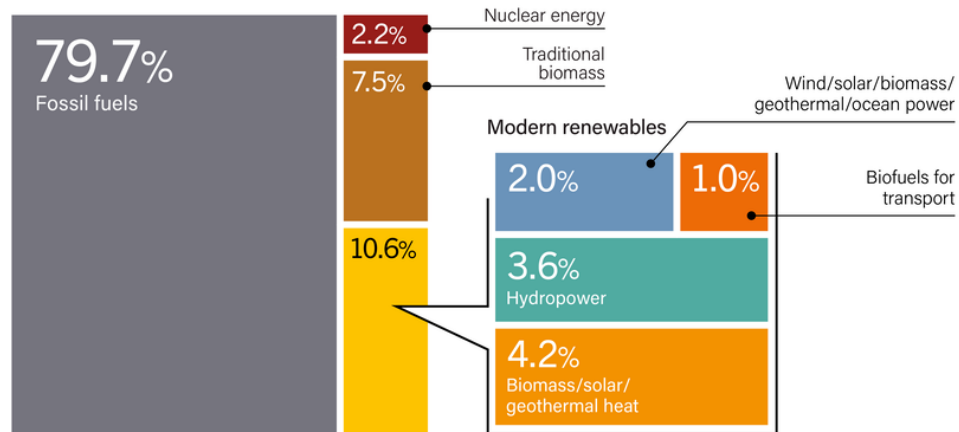
The research presented in the present manuscript started in November 2016. It is a significant date since it coincides with the date of the Paris Agreement entered into force on 4 November 2016 (United Nations Framework Convention on Climate Change, 2019). Within this Agreement, ratified by 185 of 197 Parties to date, the Parties agreed to act towards “holding the increase in the global average temperature to well below 2°C above pre-industrial levels and pursuing efforts to limit the temperature increase to 1.5 °C above pre-industrial levels, recognizing that this would significantly reduce the risks and impacts of climate change” (United Nations Framework Convention on Climate Change, 2015).

The global average surface temperature warmed by 0.85 °C between 1880 and 2012 (Allen et al., 2018). It has already resulted in modifications of human and natural systems causing hazards for populations. In particular, it has induced “increases in droughts, floods, and some other types of extreme weather; sea level rise; and biodiversity loss” (Allen et al., 2018). The human influence on this temperature increase, through greenhouse gases emissions, is today recognized.

According to the International Energy Agency, “energy accounts for two-thirds of total greenhouse gas emissions and 80% of CO₂” (International Energy Agency, 2019a). Therefore, in this global context of climate change mitigation and adaptation, an energy transition must be conducted. In particular, the use of renewable energy sources has become crucial. In the European Union, a target of 20% final energy consumption from renewable sources by 2020 has been set (European Parliament, 2009) and this target will be increased to 32% for 2030 (European Commission, 2018).

Renewable energies include bioenergy (i.e. energy from biomass), wind energy, solar energy, hydropower and geothermal energy. In 2017, they represented 18.1% of the total final energy consumption in the world (Figure 0.1) (Appavou et al., 2019). They represented a share of 17.5% in average for the European Union member states, with large variations from 54.5% for Sweden to 6.4% for Luxembourg (Figure 0.2) (Eurostat, 2019).

Estimated Renewable Share of Total Final Energy Consumption, 2017



Note: Data should not be compared with previous years because of revisions due to improved or adjusted data or methodology. Totals may not add up due to rounding.

Source: Based on OECD/IEA and IEA SHC.

REN21 RENEWABLES 2019 GLOBAL STATUS REPORT

Figure 0.1 | Global estimated renewable share of the total final energy consumption in the world for 2017 (Appavou et al., 2019).

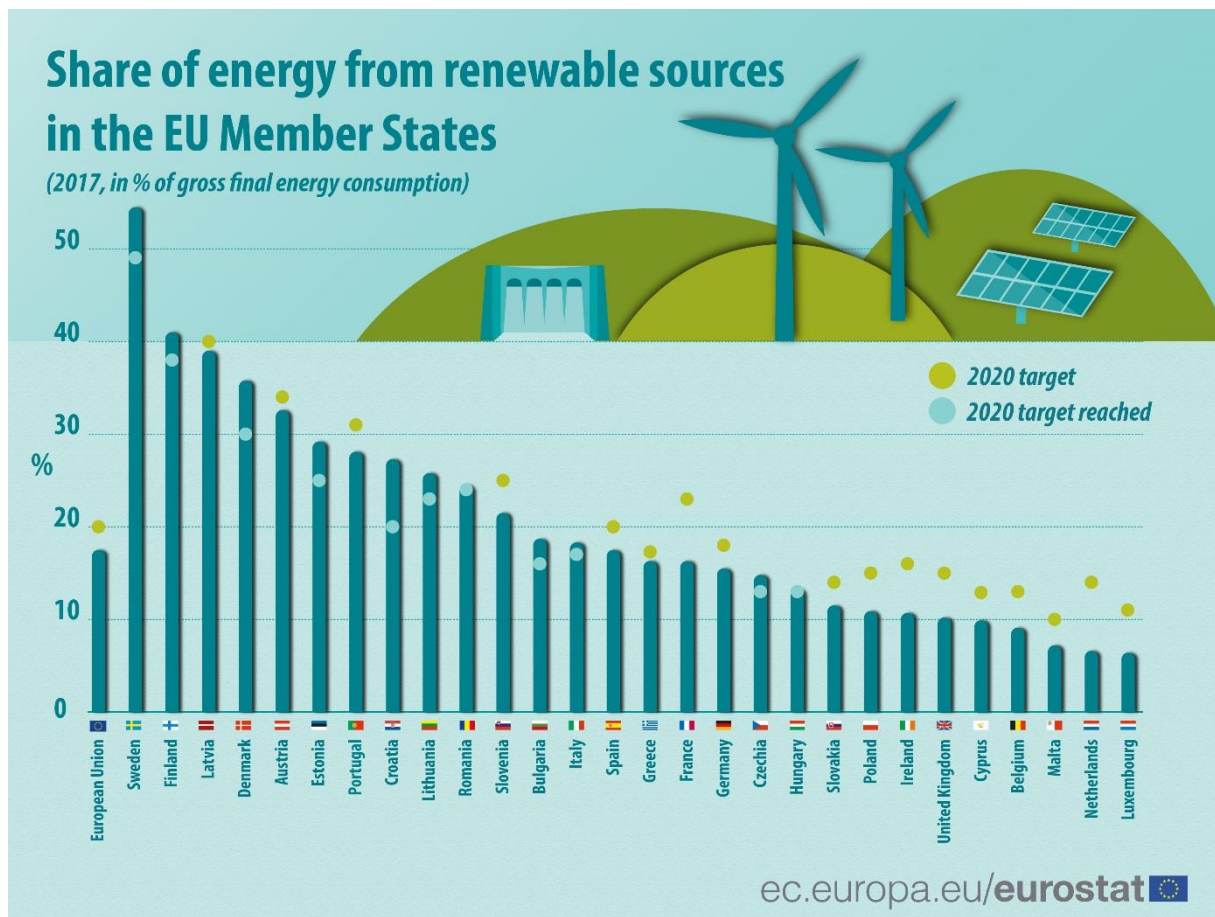
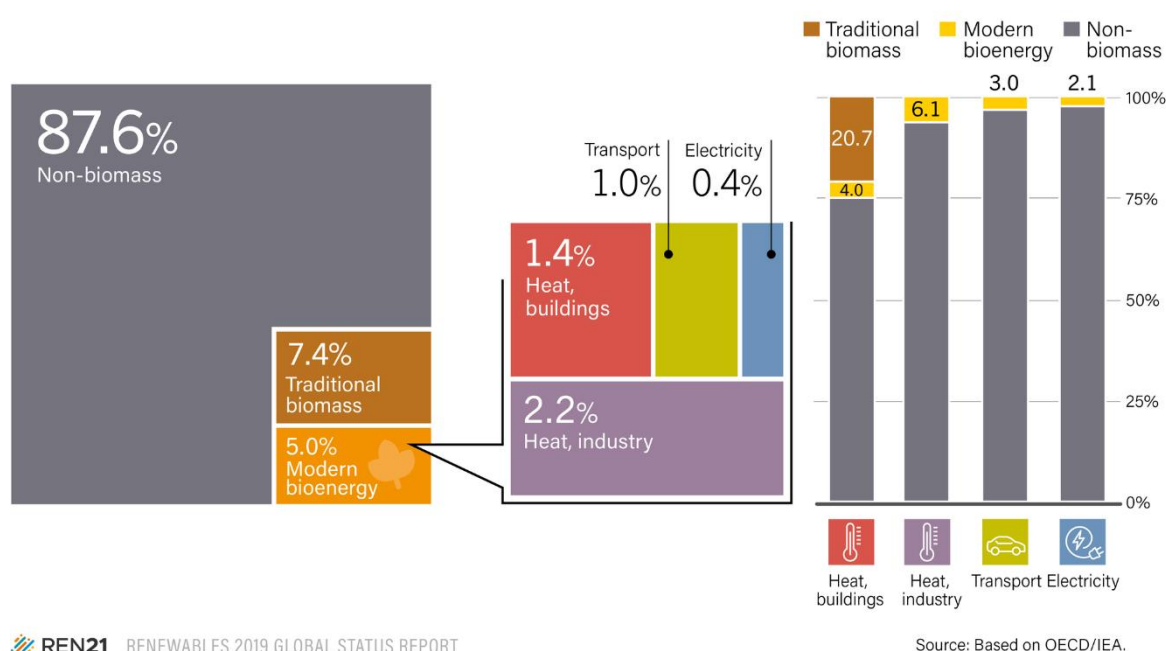


Figure 0.2 | Renewable share of the total final energy consumption in the European Union for 2017 (Eurostat, 2019).

Bioenergy is a valuable mitigation option when it is deployed in a sustainable way, i.e. avoiding pressure on available land and food production; preserving ecosystems and biodiversity; and avoiding potential water and nutrient constraints (de Coninck et al., 2018). It already takes up a large share of the consumed renewable energy, either in traditional forms (i.e. through burning of woody biomass or biomass residues in simple and inefficient devices) or in a more modern way. In 2017, it represented 12.4% of the total final energy consumption worldwide, i.e. more than two-thirds of the renewable share (Figure 0.3) (Appavou et al., 2019).

Estimated Shares of Bioenergy in Total Final Energy Consumption, Overall and by End-Use Sector, 2017



REN21 RENEWABLES 2019 GLOBAL STATUS REPORT

Source: Based on OECD/IEA.

Figure 0.3 | Global estimated shares of bioenergy in the total final energy consumption in the world in 2017 (Appavou et al., 2019).

In the objective of further developing bioenergy production, agricultural residues represent an interesting source as they have an important availability and do not decrease the surface of land available for food production. Scarlat *et al.* assessed the potential of agricultural crop residues for bioenergy production in the European Union (Scarlat et al., 2010). They considered sustainable removal rates of the residues to guarantee soil fertility. They found that agricultural crop residues could account for 2.3 to 4% of the final energy consumption in the European Union. However, this share varied largely according to the country, with values up to 14% in Hungary, 13% in Romania and Bulgaria, 7% in Denmark and 5.7% in France (Figure 0.4).

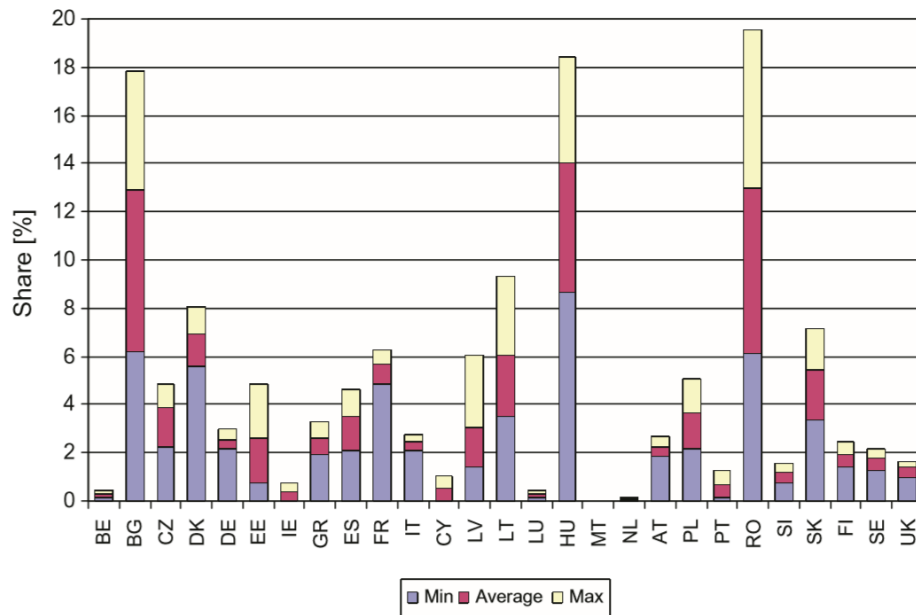


Figure 0.4 | Share of available crop residues in final energy consumption in the European Union. Reprinted from (Scarlat et al., 2010) with permission from Elsevier.

Traditional bioenergy production is for “cooking and heating, using inefficient open fires or simple cookstoves with impacts on health (e.g. due to indoor smoke pollution) and the environment” (International Energy Agency, 2019b). Therefore, a promising non-traditional thermoconversion process for bioenergy production is gasification. It converts lignocellulosic biomass into a syngas, i.e. a mixture of mainly CO and H₂, which can be further processed to obtain heat and power or gaseous and liquid fuels.

However, agricultural residues can be problematic during the gasification process. Indeed, such biomasses can have high inorganic contents compared to traditionally used woods. Such elements can be detrimental to the gasification process by inducing slag formation and/or agglomeration of the gasifier bed (Bartels et al., 2008; Sikarwar et al., 2016). Moreover, different kinetics can be identified among the various biomass species which may influence the gasifiers design. This diversity of reactivity has been empirically correlated to the inorganic content of the agricultural residues—in particular to K, Si and P (Dupont et al., 2016)—but the reactional mechanisms are still not elucidated (Arnold and Hill, 2019; Di Blasi, 2009).

This study aims to contribute to the understanding of the inorganic elements role during biomass steam gasification. In particular, the phenomena involving K and Si during the biomass steam gasification were investigated, especially through the gas phase, and with particular focus on their influence on the reaction kinetics.

To this end, the present manuscript is organized in three chapters and a conclusion and perspective chapter.

Chapter I defines the investigation context of biomass resources and their valorization to energy through the pyrogasification process. It then presents the state of the art on the inorganic elements effects on steam gasification.

Chapter II is an experimental analysis of the relative influence of the inorganic elements compared to the morphology of biomass chars on their gasification kinetics. Various biomass species were characterized, at several gasification conversion values both regarding their morphology and their kinetic behavior.

Chapter III examines the influence of two particular inorganic elements on biomass gasification kinetics: Si and K, which have a high occurrence in biomass and a high activity on gasification kinetics. Thermogravimetric analyses of a Si-rich and a K-rich biomass species were conducted. The influence of a Si-compound and a K-compound was studied using two model compounds. Experiments were particularly designed to investigate the K effect through the gas phase.

The final chapter gathers the conclusions of the present work and suggests perspectives for further investigations.

Chapter I. Context and state of the art

This chapter presents the investigation context as well as the state of the art on the effects of the inorganic elements on steam gasification. In a first section, the biomass definition and composition are given. In a second section, the biomass valorization through the pyrogasification process is presented. It includes a description of the pyrolysis and the gasification processes and an inventory of the available technologies. The third section proposes a literature review on the inorganic element roles during the steam gasification process. It synthesizes the main observed effects, presents the associated mechanisms explaining the phenomena and lists the way this effects have been taken into account in gasification kinetic models. Finally, the last section gives a conclusion and states the objective of the present study.

1. Biomass and its composition

1.1. Biomass definition

The European Parliament directive 2009/28/EC of 23 April 2009 on the promotion of the use of energy from renewable sources defined biomass as “the biodegradable fraction of products, waste and residues from biological origin from agriculture (including vegetal and animal substances), forestry and related industries including fisheries and aquaculture, as well as the biodegradable fraction of industrial and municipal waste” (European Parliament, 2009). Therefore, biomass is a feedstock that includes a variety of different resources. Vassilev et al. classified biomass into six groups: wood and woody biomass, herbaceous and agricultural biomass, aquatic biomass, animal and human biomass wastes, contaminated biomass and industrial biomass wastes (semi-biomass), and biomass mixtures (Vassilev et al., 2010). **In this work, as the focus was on the gasification process, only the first two groups—i.e. dry land-based vegetation—were studied. For simplification purpose, these groups were referred as biomass or lignocellulosic biomass.**

1.2. Biomass composition

Biomass composition is complex and involves several hundreds of compounds, divided between organic and inorganic fractions detailed below. However, some compounds do not perfectly fit with these two fractions. For example, N- and S-compounds can be in both fractions while oxalates are considered as organic minerals (Vassilev et al., 2012).

1.2.1. Organic fraction

1.2.1.1. Organic fraction elements

Biomass is typically composed of organic-forming elements, namely C, O, H, N and S (Vassilev et al., 2010). The proportion of these elements in lignocellulosic biomass expressed in dry ash-free basis is reported in Table I.1. The typical content of coal, the main solid fossil fuel, is also presented. Table I.1 shows a higher ratio of C and S and a lower ratio of O for coal compared to lignocellulosic biomass (Vassilev et al., 2010).

Table I.1 | Typical elemental composition in C, O, H, N and S of biomass and coal. From data from (Vassilev et al., 2010).

	Biomass	Coal
C (%daf*)	40 – 60	60 – 90
O (%daf)	30 – 50	5 – 30
H (%daf)	3 – 10	4 – 6
N (%daf)	0.1 – 5	1 – 3
S (%daf)	0.01 – 1	0.2 – 10

* %daf: percent in dry ash-free basis.

In addition to the composition difference, the biomass energy content is lower than solid fossil fuels. The lower heating value (LHV) of biomass is $15 - 20 \text{ MJ.kg}^{-1}$ whereas for solid fossil fuel it is $20 - 40 \text{ MJ.kg}^{-1}$. Differences between biomass and solid fossil fuels in terms of composition and LHV can be correlated with H/C and O/C ratios, as shown in the Van Krevelen diagram (Figure I.1). Such difference can be explained by the fact that C–H and C–O bonds have a low energy content compared to C–C bonds (McKendry, 2002a).

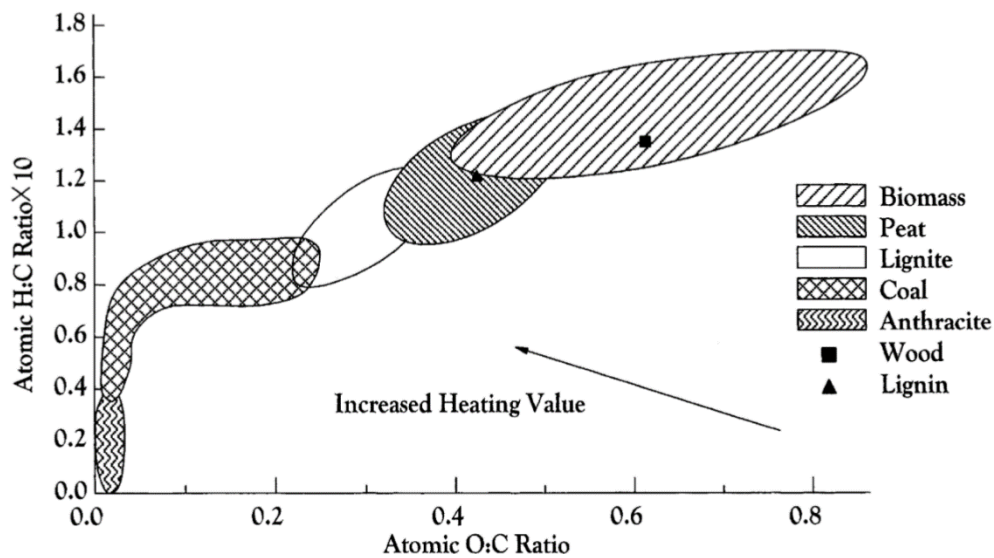


Figure I.1 | Van Krevelen diagram for various solid fuels. Reprinted from (McKendry, 2002a) with permission from Elsevier.

1.2.1.2. Organic fraction macromolecules

The organic fraction of the lignocellulosic biomass is organized in three types of macromolecules: cellulose, hemicellulose and lignin. The lignocellulosic biomass structure is represented in Figure I.2.

Cellulose is a linear and partly crystalline glucose polymer with an average polymerization degree around 10 000 for wood (Bajpai, 2016; Deglise and Donnot, 2017) and an average molecular weight around 100 000 (McKendry, 2002a). It constitutes 40 – 50 % of the biomass by weight (de Lasa et al., 2011; McKendry, 2002a).

Hemicelluloses are polysaccharides whose units are glucose, xylose, galactose, arabinose and mannose. It is a branched macromolecule with a random and amorphous structure and with an average molecular weight lower than 30 000. It represents 20–40 % of the biomass weight (McKendry, 2002a; Vassilev et al., 2012).

Lignin is a highly branched polyaromatic macromolecule. Its building blocks are made up of a three carbon chain attached to an aromatic ring of six carbon atoms, with zero to two methoxyl groups. These building blocks—depicted in Figure I.2—are linked mainly through ether bonds and arranged irregularly forming an amorphous three-dimensional structure that varies among biomass species (McKendry, 2002a; Vassilev et al., 2012).

The exact arrangement of these macromolecules is a subject of ongoing research. The biomass structure seems to be formed of cellulose macromolecules linked by hydrogen and van der Waals bonds in microfibrils, themselves grouped in fibers (Bajpai, 2016). This rigid matrix would then be covered by hemicelluloses and lignin macromolecules.

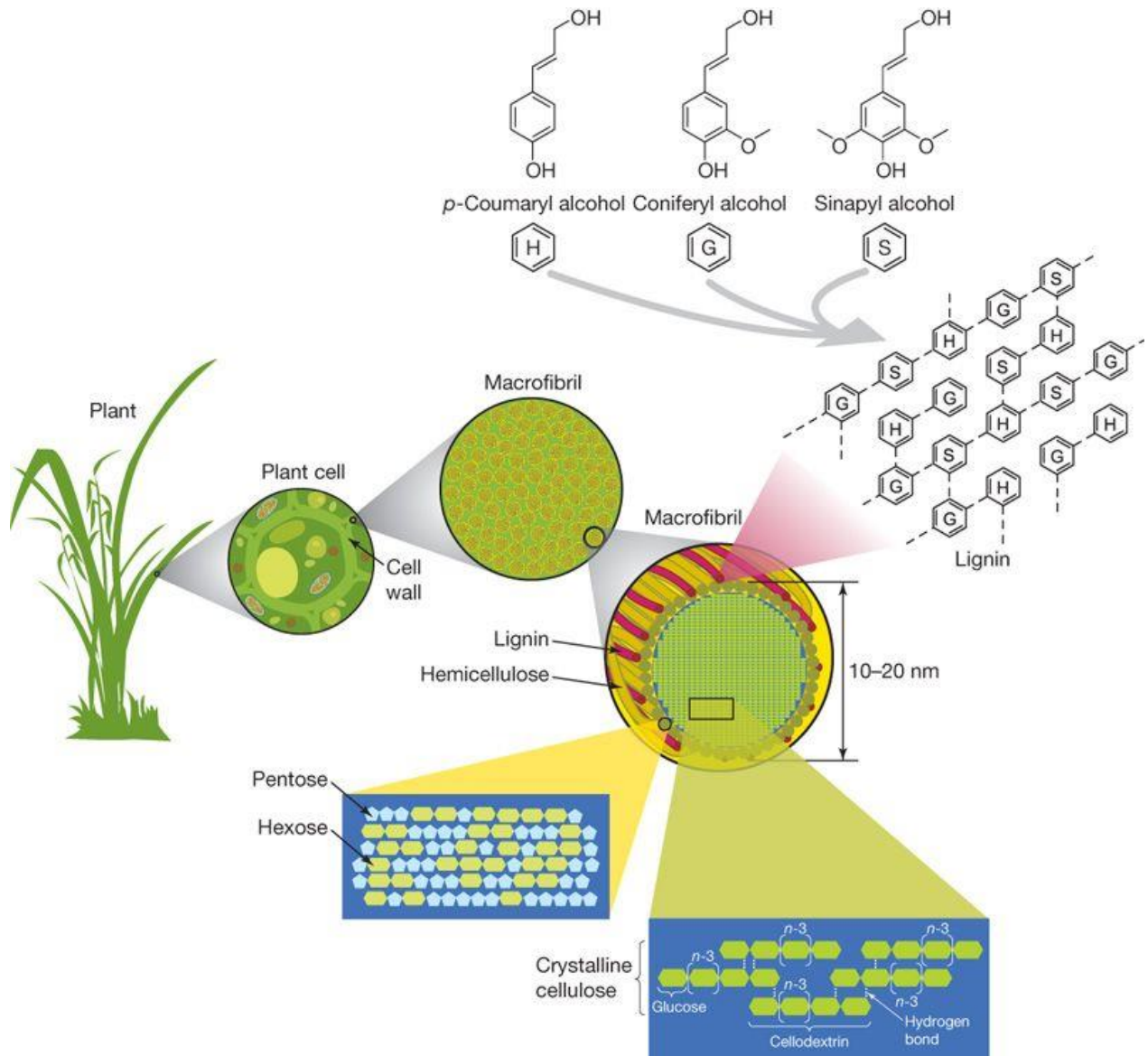


Figure I.2 | Lignocellulosic biomass structure. Reprinted by permission from Springer Nature (Rubin, 2008).

1.2.2. Inorganic fraction

In addition to the organic fraction, biomass contains inorganic elements, namely Cl, Ca, K, Si, Mg, Al, Fe, P and Na. Some other elements can also be found as trace elements (<1 % of the inorganic content), for instance Mn, Ti, B, Be, Rb, Cr, Ni, Cu, Se, Zn (Vassilev *et al.*, 2013).

Few extensive studies are available on the inorganic fraction. This section is mainly based on the work of Vassilev *et al.* who gathered data from literature to publish several reviews on the subject that were complemented by their own experimental work (Vassilev *et al.*, 2010, 2012, 2013).

1.2.2.1. Inorganic elements in biomass

Biomass composition differs from solid fossil fuels. Inorganic elements in biomass are mainly Si, K and Ca, while those in solid fossil fuels are rather Si, Al, Fe and Ca (Vassilev *et al.*, 2010). More specifically, Vassilev *et al.* (Vassilev *et al.*, 2010) identified the main inorganic elements several biomass subgroups:

- Wood and woody biomass: Ca > Si > K > Mg > Al > P
- Herbaceous and agricultural biomass:
 - Grass: Si > K > Ca > P > Mg > Al
 - Straw: Si > K > Ca > Mg > P > Al
 - Other residues such as shells and husks: K > Si > Ca > P > Mg > Al

These rankings are trends from mean values calculated for each subgroup. However, in each subgroup, individual biomass species can have slightly different compositions that modify the order of occurrence of the main inorganic elements.

1.2.2.2. Inorganic compounds in biomass

These inorganic elements are present in the form of various compounds. However, as stated by Vassilev *et al.* (Vassilev et al., 2012), “the direct methods for determination of the structural components [of raw biomass] are very rare”. Nevertheless, they compiled the data of 197 samples from 25 references and of their own characterizations on 8 biomass samples to establish a list of the compounds identified in biomass. Identified inorganic compounds were:

- Silicates such as SiO₂, Ca-silicates or aluminosilicates;
- Oxides and hydroxides such as Mg(OH)₂, Ca(OH)₂ or Fe₂O₃;
- Sulphates, sulphites and sulphides (not typical in lignocellulosic biomass) such as CaSO₄ or K₂SO₄;
- Phosphates such as Ca-phosphates, Ca-Mg-phosphates or K-phosphates;
- Carbonates such as CaCO₃ or CaMg(CO₃)₂;
- Chlorides such as KCl or K-Ca-chloride;
- Nitrates such as KNO₃ or Ca-nitrates;
- Other inorganic matter such as metals or glass (not typical in clean lignocellulosic biomass).

The available data did not allow to link these compounds to particular biomass subgroups. Moreover, there was a high variability due to the inorganic content dependence on several factors such as the biomass genetics, its environment or the biomass part considered (Vassilev et al., 2012).

For example, silicates and in particular SiO_2 are typically found in soil. The presence of these compounds in biomass can be either because they are formed in the biomass (authigenic fraction) or because they are formed outside and then fixated in the biomass (detrital fraction). The detrital fraction of silicates can come from the fixation of fine particles, brought by water or wind from the soil, on the plant surface. These fine particles can also be introduced into the plant by water suspensions. In the particular case of SiO_2 , the authigenic fraction is formed by silicic acid absorption from the soil solutions that precipitates in the biomass structure. SiO_2 gives rigidity to the plant tissues where it is found—husk, straw, bark and other supportive tissues. Other compounds can also have various origins. Other examples of authigenic compounds (i.e. formed in the biomass) are sulphates, nitrates and chlorides that come from the evaporation and precipitation of water in the biomass (Vassilev et al., 2012).

1.2.2.3. Inorganic compounds in biomass ashes

Inorganic elements are often referred to as ash, since the inorganic content of the biomass is usually measured through ash formation by combustion in air at 550 °C (European Standards, 2009). The standards for ash yield measurement are slightly different for biomass and for solid fossil fuels. Ashes are formed at 815 °C for the latter (International Organization for Standardization, 2010). In the case of biomass, such a high temperature can volatilize alkali and alkaline earth compounds, in particular KCl, and induce the release of inorganic carbon as CO_2 from alkali and alkaline earth carbonates, in particular CaCO_3 (Arvelakis et al., 2004; Xiao et al., 2011). The ash content of wood and woody biomass is typically 0.1 – 8 %. It is typically 0.9 – 20 % for herbaceous and agricultural biomass with straws having the highest ash content, grasses the lowest and other residues such as husks and shells ranging in between (Vassilev et al., 2010). In comparison, the ash yield of solid fossil fuels at 815 °C is commonly 4 – 30 %. Solid fossil fuels contain therefore more inorganic elements than wood and woody biomass but can have the same content as some herbaceous and agricultural biomasses.

More data is available regarding the inorganic composition of biomass ashes obtained from combustion rather than that of raw biomass. This is partly due to the higher concentration of inorganic compounds in ashes which makes the characterization easier compared to the case of raw biomass in which detection issues can occur. However, the results obtained on ashes have to be considered carefully as they are obtained after a thermochemical conversion of the biomass. Vassilev *et al.* (Vassilev et al., 2013) stated that the phases identified in biomass ashes were “mostly secondary”, i.e. formed during combustion, and “occasionally primary”, i.e. formed originally in the biomass. Out of 96 identified mineral phases, 52 were dominantly secondary and 26 were dominantly primary.

Vassilev *et al.* reviewed the data from more than 600 references and established a list of 229 species or groups of species identified in the characterization of biomass ashes. They identified 188 species for coal ash by conducting the same work. There were not sufficient quantitative data in literature to determine the proportions of these species in the ashes of each biomass subgroup. Nevertheless, from the characterization of ashes from woody biomass, straw and switchgrass, they established that the mineral species contained in biomass ashes were, in decreasing order of concentration:

- Forming (> 10 % of ashes) such as glass, sylvite KCl, calcite CaCO_3 , leucite KAlSi_2O_6 , anorthite $\text{CaAl}_2\text{Si}_2\text{O}_8$, K–Ca silicate K_2CaSiO_4 or $\text{K}_4\text{CaSi}_3\text{O}_9$ or others, and quartz SiO_2 .

- Major (1–10 %), namely albite $\text{NaAlSi}_3\text{O}_8$, anhydrite CaSO_4 , ankerite $\text{Ca}(\text{Mg,Fe})(\text{CO}_3)_2$, kaolinite $\text{Al}_2\text{Si}_2\text{O}_5(\text{OH})_4$, siderite FeCO_3 , cristobalite SiO_2 , arcanite K_2SO_4 , hematite $\alpha\text{-Fe}_2\text{O}_3$, illite $(\text{KH}_2\text{O})\text{Al}_2(\text{Al,Si})\text{Si}_3\text{O}_{10}(\text{OH})_2$, lime CaO , Na silicate $\text{Na}_2\text{Si}_3\text{O}_7$ or Na_2SiO_3 , fairchildite $\text{K}_2\text{Ca}(\text{CO}_3)_2$, hydroxylapatite $\text{Ca}(\text{PO}_4)_3(\text{OH})$, $\text{Ca}_5(\text{PO}_4)_3(\text{OH})$ or $\text{Ca}_{10}(\text{PO}_4)_6(\text{OH})_2$, merwinite $\text{Ca}_3\text{Mg}(\text{SiO}_4)_2$, periclase MgO , Ca chlorosilicate $\text{Ca}_2\text{SiO}_3\text{Cl}_2$, diopside $\text{CaMgSi}_2\text{O}_6$ or $\text{CaMg}(\text{SiO}_3)_2$, glaserite $\text{K}_3\text{Na}(\text{SO}_4)_2$, K feldspar KAlSi_3O_8 , larnite Ca_2SiO_4 , and portlandite $\text{Ca}(\text{OH})_2$.
- Minor (0.1–1 %) such as K silicate $\text{K}_2\text{Si}_4\text{O}_9$ or others, K phosphate K_3PO_4 , $\text{K}_5\text{P}_3\text{O}_{10}$ or others, and K carbonate K_2CO_3 .
- Some accessory phases (< 0.1 % or only traces) according to the elemental composition of the biomass.

Overall, most of the species identified in biomass ashes were also found in coal ashes. The discrepancies could be explained by the difference in elemental composition. In particular, Ca–K–Mn silicates, Ca–Al–Mn oxides, K–Na–Ca chlorides and K–Ca–Mg–Na carbonates, sulphates and phosphates that were identified in biomass were mostly not found in coal ashes. This result is in accordance with the higher occurrence of Ca, Cl, K, Mg, Mn, Na and P in biomass than in coal. On the opposite, many compounds containing Al, Fe and Ti that are typically found in coal ashes were logically not identified in biomass ashes since the latter contain low amounts of these elements (Vassilev et al., 2013).

Inorganic species such as oxalates, silicates, oxides, hydroxides, sulphates, sulphites, sulphides, phosphates, carbonates, chlorides, nitrates, amorphous inorganic matter and others can be primary phases. Various silicates, oxides, hydroxides, carbonates, sulphates, sulphides, sulphosalts, sulphites, thiosulphates, phosphates, chlorides, chlorites, chlorates, nitrates, oxalates, amorphous inorganic matter and glass can be secondary phases. In particular, glass contained in biomass ashes is the result of the fusion and rapid cooling of inorganic compounds from the biomass during ash formation, i.e. combustion. It mainly contains Si, K, Ca and Na.

1.3. Biomass conversion to energy

Lignocellulosic biomass can be processed to obtain:

- Energy through heat and electricity generation;
- Energy through conversion to liquid or gaseous fuels;
- Chemical feedstock materials.

In the context of the conversion to a fuel, biofuels generations are identified and are related to the biomass nature. First generation biofuels are obtained from edible biomass such as sugar, starch and oil crops. Second generation biofuels rely on non-edible feedstocks such as wood, agricultural residues and forestry waste. They have a lower negative impact on the environment than the first generation as they have a limited influence on the usage of arable land and food crops (Luque et al., 2008; Sikarwar et al., 2017). Third generation biofuels are produced from algae, in particular microalgae. Finally, a fourth generation of biofuels is appearing. It is based on the genetic modification of microorganisms to make them consume higher quantities of CO_2 that what would be released through their use (Alalwan et al., 2019). **Dry lignocellulosic biomass studied in the present work belonged to the second generation.**

Processes for energy production can be grouped in three categories: mechanical extraction, biochemical processes and thermochemical processes (McKendry, 2002b; Sikarwar et al., 2017). However, only thermochemical processes are applied to dry lignocellulosic biomass.

Thermochemical conversion processes include combustion, pyrolysis, gasification and hydrothermal processes. The energy products obtained from each thermochemical process are presented in Figure I.3. Hydrothermal processes, i.e. hydrothermal carbonization and liquefaction, are rather used in the case of wet biomass and not of dry lignocellulosic biomass as in the present work. Combustion produces hot gases at temperatures between 800 and 1000 °C and its energy can be used in the form of heat or can be converted to mechanical power or to electricity (McKendry, 2002b). Pyrolysis and gasification are discussed in detail in the following section.

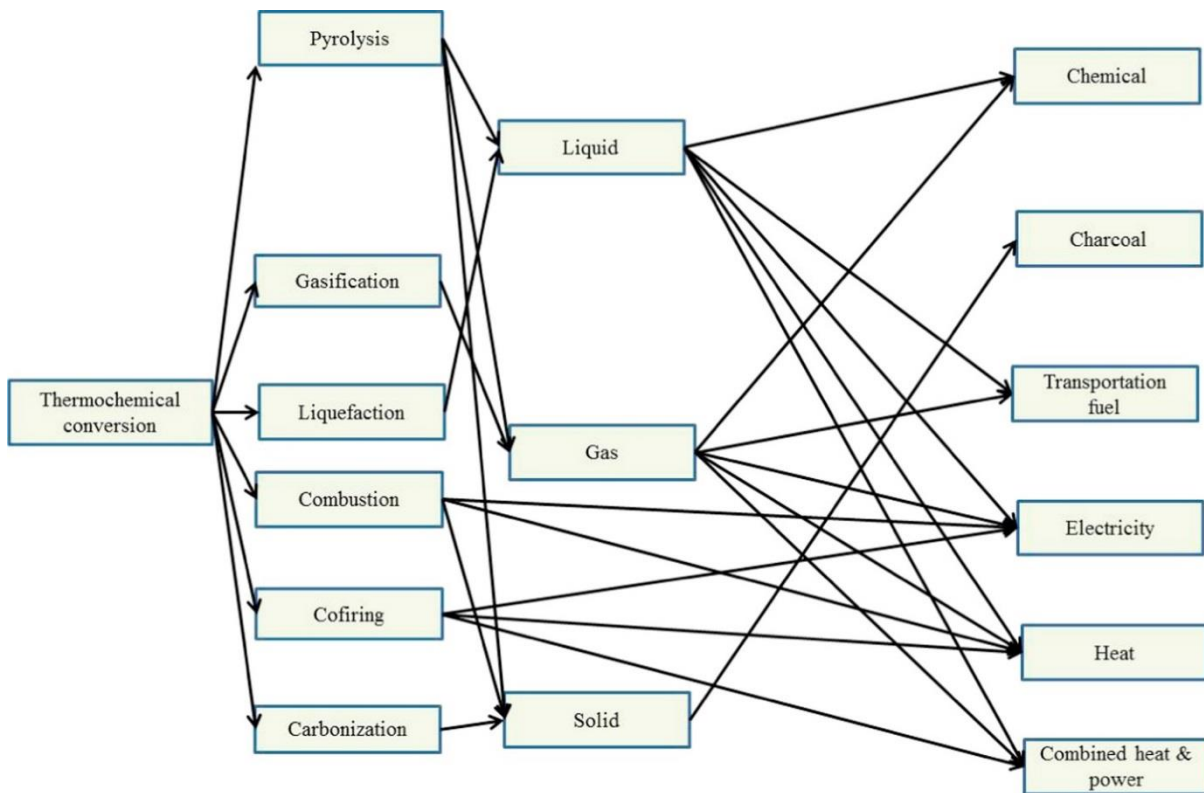


Figure I.3 | Thermochemical conversion processes, intermediate products and final energy products. Reprinted from (Patel et al., 2016) with permission from Elsevier.

The focus of the present work was the biomass gasification thermochemical process.

2. The pyrogasification of biomass

Though it is not widely used in literature, the term of pyrogasification could rather be used to refer to the gasification process. Indeed, it is usually decomposed in three main steps: biomass drying, biomass pyrolysis and residual char gasification (Basu, 2010a; de Lasa et al., 2011; Sikarwar et al., 2017; Van Swaaij, 1981). These steps are overlapping and are themselves groups of various reactions. Figure I.4 shows a more detailed scheme of the pyrogasification steps with the intermediary and final products.

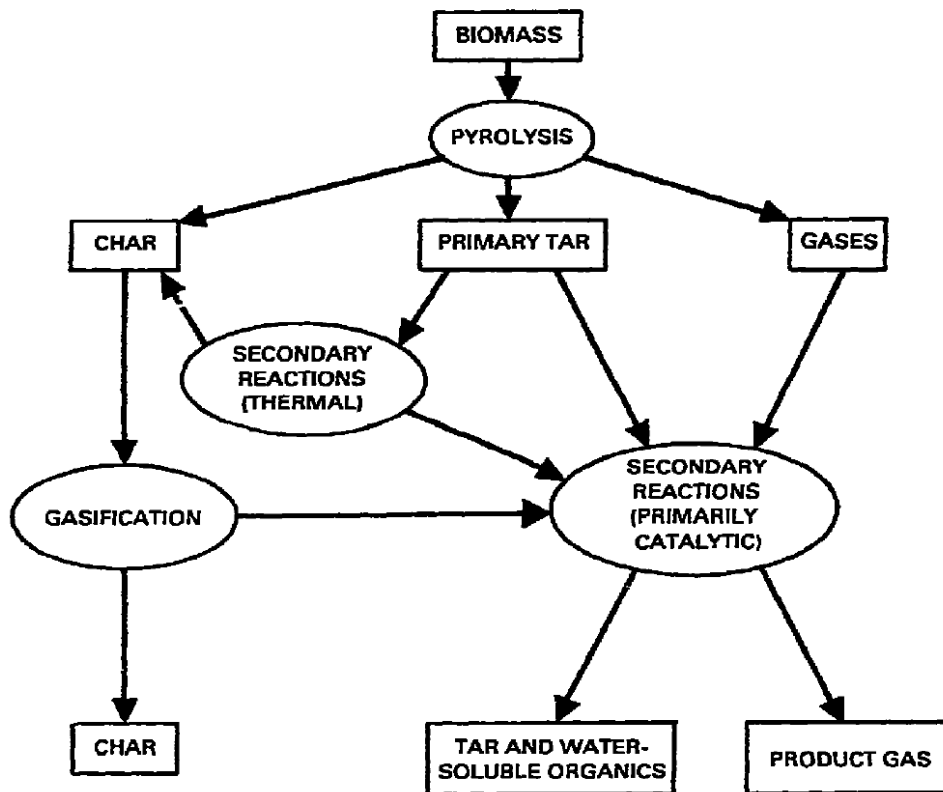


Figure I.4 | Biomass pyrogasification steps. Reprinted from (Baker and Mudge, 1984) with permission from Elsevier.

The following sections present the existing pyrogasification technologies to date and describe the pyrolysis and gasification steps.

2.1. Gasifier technologies for biomass

Three main reactor technologies are in use for biomass pyrogasification: fixed bed gasifiers, fluidized bed gasifiers and entrained flow gasifiers (Basu, 2010a; de Lasa et al., 2011; Sansaniwal et al., 2017; Sikarwar et al., 2017). The gasification requires a heat input. In most gasifiers, this heat is brought by the combustion of a part of the biomass in air or O_2 . Such a configuration is called autothermal, while a configuration where heat is brought from outside the reactor is called allothermal.

The main characteristics of each type of technology are summarized in Table I.2 with their advantages and limitations (Dahmen and Sauer, 2015; de Lasa et al., 2011; McKendry, 2002c; Sikarwar et al., 2017). They are then described in more details in the following subsections.

Table I.2 | Main characteristics of the gasifier technologies.

	Fixed bed	Fluidized bed	Entrained flow
Temperature (°C)	1000	800 – 1000	1400
Pressure (bar)	1 – 40	1 – 40	20 – 70
Particle size (mm)	20 – 80	20 – 80	0.1 – 0.4
Advantages	<ul style="list-style-type: none"> • Simple process • Minimal biomass pretreatment required • <i>Downdraft</i>: low tar content 	<ul style="list-style-type: none"> • Good heat and mass transfers • Low tar content (with catalytic bed material) 	<ul style="list-style-type: none"> • High quality syngas (very low tar content)
Limitations	<ul style="list-style-type: none"> • For small scale • Poor heat and mass transfers • Updraft and cross-draft: high tar content 	<ul style="list-style-type: none"> • For large scale • Bed agglomeration issues (limiting process temperature) • <i>Bubbling</i>: high tar content 	<ul style="list-style-type: none"> • For large scale • Fine biomass grinding required • High pressure

2.1.1. Fixed bed gasifiers

Fixed bed is the historical technology used for the gasification and therefore the most common, especially for small-scale production for local use. Three types of fixed bed gasifiers exist, differing in their airflow direction: updraft, downdraft and cross-draft fixed bed gasifiers. In all types of fixed bed gasifiers, biomass is fed through the top of the reactor and ash removed at the bottom. Biomass particles have a typical size of 20 – 80 mm. The gasification temperature is around 1000 °C (de Lasa et al., 2011; McKendry, 2002c; Sikarwar et al., 2017).

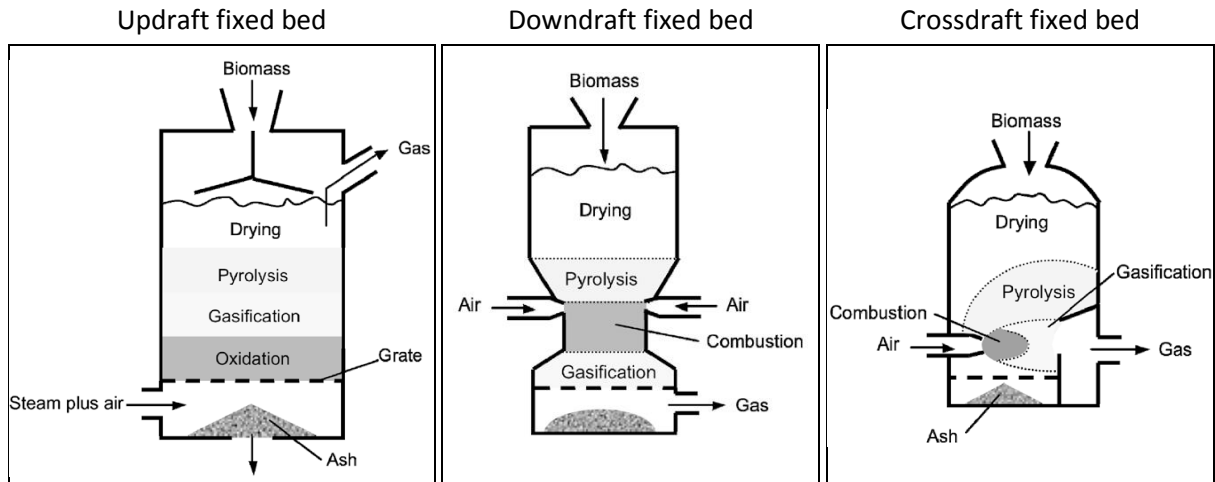


Figure I.5 | Fixed bed gasifiers (Basu, 2010b).

Updraft fixed bed reactors have the gasifying agent, air and/or O_2 entering at the bottom. In this case, gasifying agent first meets the char and combustion occurs. Ash falls at the bottom of the reactor and hot gases at $1000\text{ }^\circ\text{C}$ from combustion flow up and react with unreacted char to produce H_2 and CO cooled around $750\text{ }^\circ\text{C}$. The heat from this gas enables the biomass pyrolysis, which has been dried by the same gas when entering at the top of the gasifier.

Downdraft fixed bed reactors have a restriction part-way down the vessel where the gasifying agent, air and/or O_2 is fed. At this point, temperature is up to $1200 - 1400\text{ }^\circ\text{C}$ and combustion and pyrolysis of biomass occur. Resulting gases flow down through hot char and are gasified to H_2 and CO .

Cross-draft fixed bed reactors are fed in gasifying agent, air and/or O_2 from one side and the gas obtained through gasification is collected on the other side. Combustion followed by gasification occur next to the gas entrance and pyrolysis and drying occur above.

2.1.2. Fluidized bed gasifiers

In fluidized bed gasifiers, a fluidizing agent (gasifying agent, air and/or O_2), goes up through a bed of fine granular particles such as sand in which biomass is injected, also at the bottom of the bed. This technique enhances the homogeneity of heat and mass transfers between bed particles, biomass and gases. There are three types of fluidized bed gasifiers: bubbling, circulating and dual fluidized bed gasifiers. Biomass particles have a typical size of $20 - 80\text{ mm}$. The gasification temperature is around $800 - 1000\text{ }^\circ\text{C}$ (Basu, 2010a; de Lasa et al., 2011; McKendry, 2002c; Sikarwar et al., 2017). The different gasifier schemes are presented in Figure I.6.

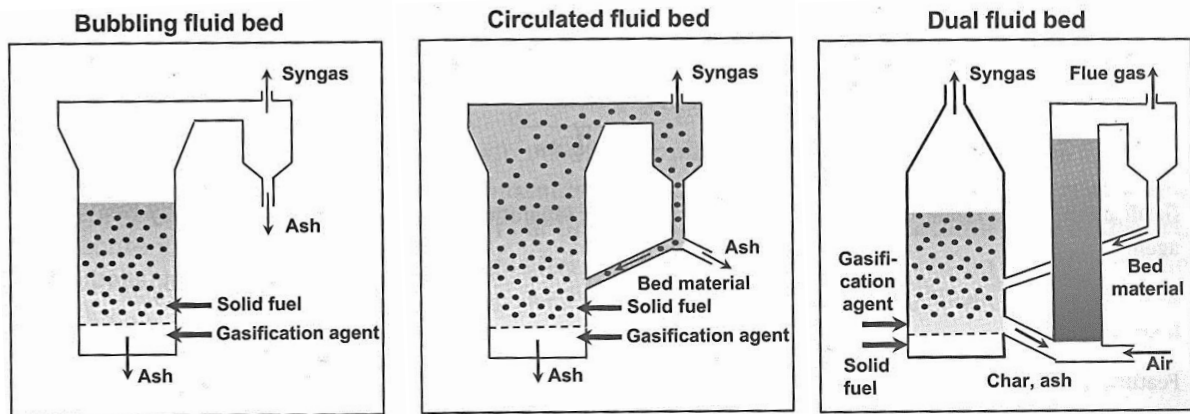


Figure I.6 | Fluidized bed gasifiers (Dahmen and Sauer, 2015).

Bubbling fluidized bed reactors are the simplest design of fluidized bed gasifiers. Pyrolysis and gasification of biomass occur in the hot fluidized bed and ashes are collected at the bottom of the vessel.

In circulating fluidized bed reactors, a cyclone separator is added to the reaction vessel. Gas produced during gasification is separated from the bed material in the cyclone separator and the latter is put back into the vessel, creating a circulation of the bed material between those two parts.

Dual fluidized bed reactors consist in two distinct fluidized beds. In one, the biomass is gasified with the gasifying agent. In the other, the combustion of the residual char from gasification occurs in air or O_2 . Those two parts are joined in a loop, with the bed material circulating between the two reactors. The bed material ensures the heat transfer between the exothermic combustion and the endothermic gasification.

2.1.3. Entrained flow gasifiers

Entrained flow gasifiers are historically used for coal. They request a fine powder fuel but they are also studied for biomass gasification. Biomass and gas (gasifying agent, air and/or O_2) are injected from the same side of the vessel, either at the top or at the bottom. Combustion occurs near the injection point and is followed by gasification. Biomass particles have a typical size inferior to 0.1 – 0.4 mm. The gasification temperature is around 1400 °C and gasifiers are pressurized to 20 to 70 bars (Basu, 2010a; de Lasa et al., 2011). A scheme of the gasifier is presented in Figure I.7.

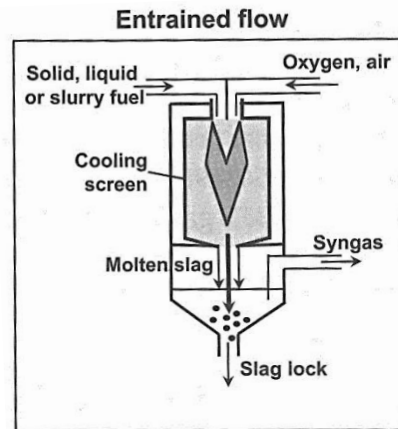


Figure I.7 | Entrained flow gasifier (Dahmen and Sauer, 2015).

Fluidized bed and fixed bed reactors are the most commonly used technologies. They operate at moderate temperatures, i.e. 800 – 1000 °C, contrarily to entrained flow reactors that operate at much higher temperatures. Therefore, this work focused on this temperature range, 800 – 1000 °C.

2.2. Pyrogasification reactions

Dupont *et al.* (Dupont et al., 2007) showed that in typical fluidized bed conditions, i.e. 800 – 1000 °C at atmospheric pressures, and in the case of small particles, i.e. 0.5 mm, the pyrolysis and the steam gasification steps could be considered as successive ones. The steam gasification is slower than the pyrolysis step and is therefore the limiting step in the pyrogasification process. The pyrolysis is controlled by both the chemical reaction and the heat transfer while the steam gasification is only controlled by the chemical reaction and is independent of the mass and heat transfers at the scale of a small particle.

Therefore, the knowledge of the gasification reaction kinetics is essential to the design of the reactors presented above. This can be easily understood in the case of the dual fluidized bed reactor. The gasification kinetics need to be controlled so that enough char goes to the combustion side to produce the heat necessary to the process. This applies to the design of all types of gasifiers: the kinetics of the reactions are controlled as well as the mass and heat transfers.

Therefore, in this study, the focus was on the limiting phenomenon: the gasification reaction kinetics.

2.2.1. Pyrolysis reactions

Pyrolysis is a thermal decomposition in the absence of oxygen. Three fractions are formed: gas, liquid and solid. The liquid is constituted of two phases: organic, i.e. tars, and aqueous. The solid fraction is called the char. Depending on the heating rate and the final temperature, these fractions are formed in various proportions (McKendry, 2002b). Figure I.8 shows typical product distribution for fast, intermediate and slow pyrolysis at around 500 °C (Bridgwater, 2015).

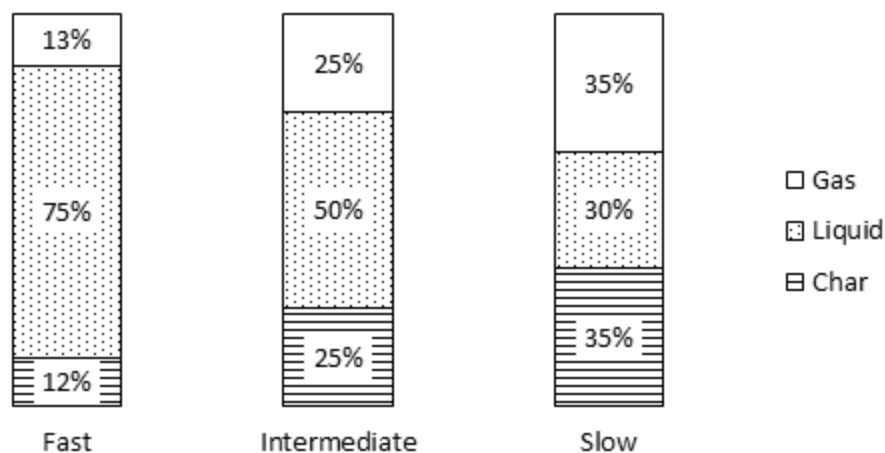


Figure I.8 | Typical product distribution of the pyrolysis at ~ 500 °C at several heating rates from data from (Bridgwater, 2015).

Fast pyrolysis—or high heating rate pyrolysis—corresponds to residence times inferior to 2 seconds or heat flux superior to 10^5 $\text{W}\cdot\text{m}^{-2}$ (Bridgwater, 2015; Deglise and Donnot, 2017). It produces mainly liquid that is called bio-oil. Intermediate pyrolysis corresponds to residence times of around 5 to 30 seconds or heat flux around 10^4 $\text{W}\cdot\text{m}^{-2}$ (Bridgwater, 2015; Deglise and Donnot, 2017). One half of its products is liquid while the other half is divided between gas and char. Slow pyrolysis—or low heating rate pyrolysis, or carbonization—corresponds to residence times of several hours or heat flux inferior to 10^3 $\text{W}\cdot\text{m}^{-2}$ (Bridgwater, 2015; Deglise and Donnot, 2017). It produces char, liquid and gas in approximately the same proportions, with liquid being in a slightly lower quantity. The liquid obtained from slow pyrolysis is constituted of approximately one third (~ 10 % of the total products) of organic fraction and two thirds of aqueous fraction (~ 20 % of the total products).

Moreover, increasing the temperature of the pyrolysis promotes the tar decomposition into gases (Bridgwater, 2015). Therefore, in the pyrogasification conditions the tars represent less than 10 % of the products.

As a first assessment, the kinetics of the pyrolysis of a biomass can be considered as the sum of kinetics of the pyrolysis of its macromolecular constituents, i.e. cellulose, hemicellulose and lignin (Di Blasi, 2008). Research on the pyrolysis kinetics and on the constituent degradation is still ongoing. However, it seems that each constituent degrades over a different temperature range, as represented in Figure I.9. Hemicellulose seems to be the least stable and degrades between 200 and below 300 °C. Then cellulose seems to degrade between 250 and 350 °C. Lignin seems to degrade over the widest range, from 200 to above 500 °C (de Wild, 2011).

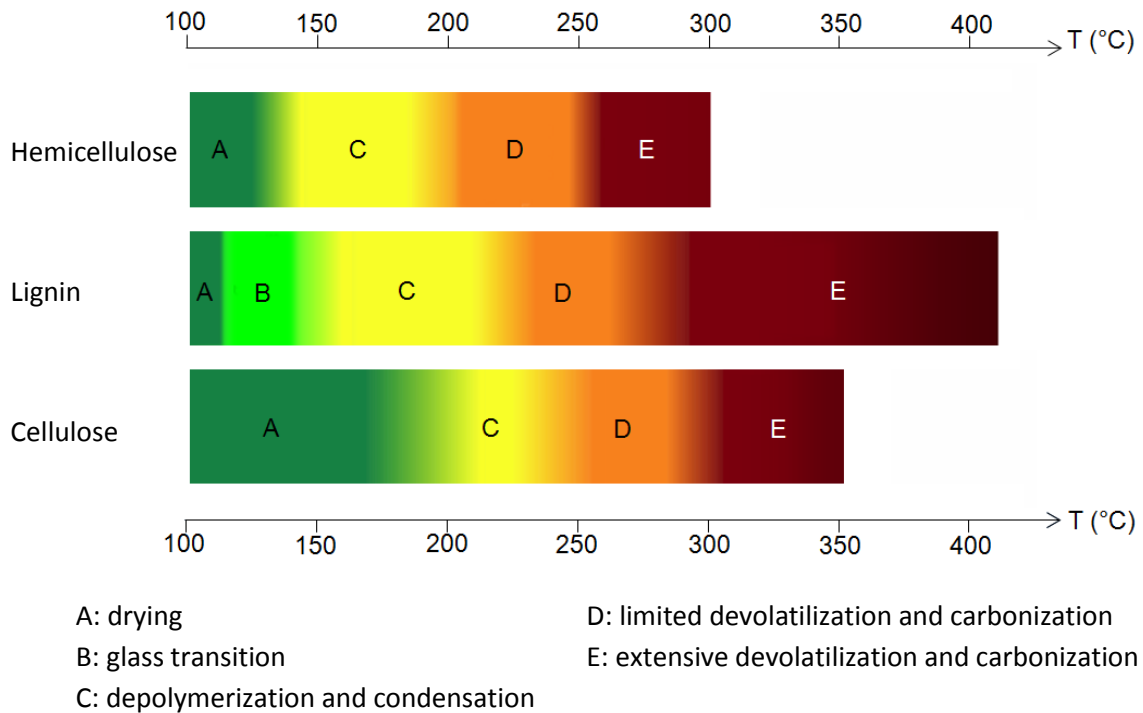


Figure I.9 | Thermal stability of hemicellulose, lignin and cellulose. Adapted by permission from Springer (Koukios, 1993).

These literature observations showed that most of the biomass constituents were degraded below 450 °C, i.e. most of the pyrolysis was completed. Therefore, this temperature was chosen for the experiments of the present work.

2.2.2. Gasification reactions

Gasification is the partial oxidation of the carbonaceous part of biomass that produces syngas, or synthesis gas, which is mainly a mixture of CO and H₂.

2.2.2.1. Reaction equations

The main known reactions as well as their associated enthalpy at 25 °C appear in Table I.3. It includes reactions with carbon, oxidation reactions, water-gas shift reaction, methanation reactions and steam-reforming reactions (Basu, 2010a).

Table I.3 | Typical gasification reactions and their associated enthalpy at 25 °C (Basu, 2010a).

Carbon reactions	
$C + CO_2 \leftrightarrow 2 CO$ (Boudouard)	+ 172 kJ.mol ⁻¹
$C + H_2O \leftrightarrow CO + H_2$ (Water gas or steam)	+ 131 kJ.mol ⁻¹
$C + 2 H_2 \leftrightarrow CH_4$ (Hydrogasification)	- 74.8 kJ.mol ⁻¹
$C + 0.5 O_2 \rightarrow CO$	- 111 kJ.mol ⁻¹
Oxidation reactions	
$C + O_2 \rightarrow CO_2$	- 394 kJ.mol ⁻¹
$CO + 0.5 O_2 \rightarrow CO_2$	- 284 kJ.mol ⁻¹
$CH_4 + 2 O_2 \leftrightarrow CO_2 + 2 H_2O$	- 803 kJ.mol ⁻¹
$H_2 + 0.5 O_2 \rightarrow H_2O$	- 242 kJ.mol ⁻¹
Shift reaction	
$CO + H_2O \leftrightarrow CO_2 + H_2$	- 41.2 kJ.mol ⁻¹
Methanation reactions	
$2 CO + 2 H_2 \rightarrow CH_4 + CO_2$	- 247 kJ.mol ⁻¹
$CO + 3 H_2 \leftrightarrow CH_4 + H_2O$	- 206 kJ.mol ⁻¹
$CO_2 + 4 H_2 \rightarrow CH_4 + 2 H_2O$	- 165 kJ.mol ⁻¹
Steam reforming reactions	
$CH_4 + H_2O \leftrightarrow CO + 3 H_2$	+ 206 kJ.mol ⁻¹
$CH_4 + 0.5 O_2 \rightarrow CO + 2 H_2$	- 36 kJ.mol ⁻¹

There are heterogeneous reactions between the carbon from the biomass and the gas atmosphere as well as homogeneous reactions between the gases. These homogeneous reactions can occur between the reactive gases and the produced gases, or between several produced gases.

It can be noted that the reaction between carbon and the gasifying agent, i.e. CO₂ or H₂O, is endothermic. This explains the energy required for the gasification process described in the section presenting the gasifier technologies.

2.2.2.2. Factors influencing the gasification

Biomass gasification can be carried out using different gasifying environments. Table I.4 lists possible gasifying agents (air, oxygen, steam and carbon dioxide) and the characteristics of each one. Combinations of several gasifying agents can also be used. The gaseous environment during gasification influences the gasification process, in particular the repartition of the products and the energy content of the resulting gas (Sikarwar et al., 2017).

Table I.4 | Characteristics of gasifying agents. Reprinted from (Sansaniwal et al., 2017) with permission from Elsevier.

Gasifying agent	Characteristic
Air	<ul style="list-style-type: none"> ● Partial combustion for heat supply of gasification ● Moderate char and tar content
Oxygen	<ul style="list-style-type: none"> ● Enhanced carbon conversion characteristics ● Enriched H₂, CO and CH₄ in producer gas and reduced tar levels
Steam	<ul style="list-style-type: none"> ● Improved heating value of producer gas (10–15 MJ N/m³) ● Enriched H₂ in producer gas
Carbon dioxide	<ul style="list-style-type: none"> ● High heating value of producer gas ● High concentrations of H₂ and CO in the producer gas and reduced CO₂

In terms of kinetics, at equal oxygen content in the gas flow, steam gasification is faster than CO₂ gasification. For example, in their study on woodchip char at 900 °C, Ahmed *et al.* (Ahmed and Gupta, 2011) observed that the use of steam instead of CO₂ divided the gasification time by almost three and increased the gasification rate by a factor of almost two. **In this work, the focus was made on char steam gasification.**

For both gasifying agents, the reaction rate increases with the steam or CO₂ partial pressure increase. An example from Marquez-Montesinos *et al.* is shown in Figure I.10 for the gasification of grapefruit skin char at different steam partial pressures.

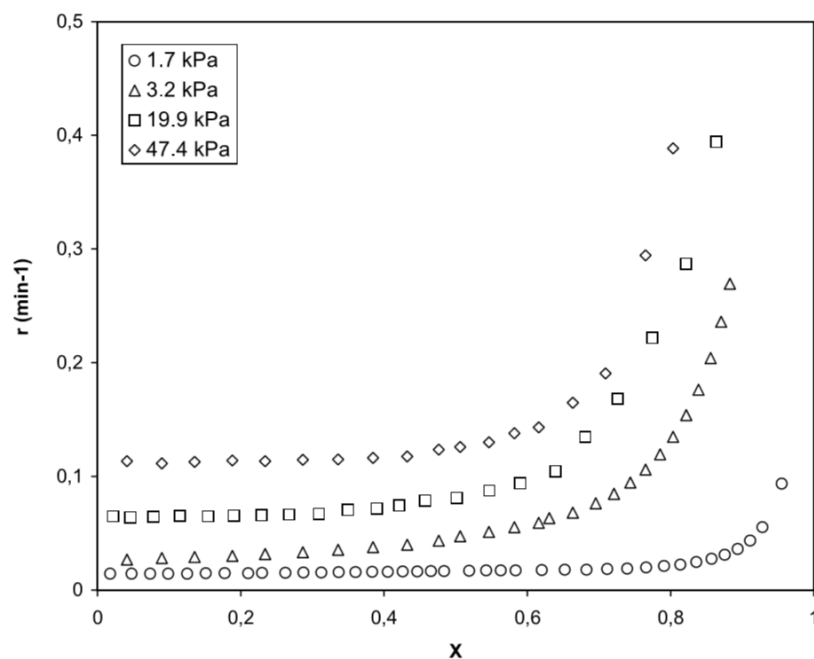


Figure I.10 | Reactivity versus conversion curves for steam gasification of grapefruit skin char at different partial pressures of steam. Reprinted from (Marquez-Montesinos et al., 2002) with permission from Elsevier.

In the same way, the reaction rate increases when the gasification temperature increases. An example is given in Figure I.11 from the same study from Marquez-Montesinos *et al.* under a CO₂ atmosphere.

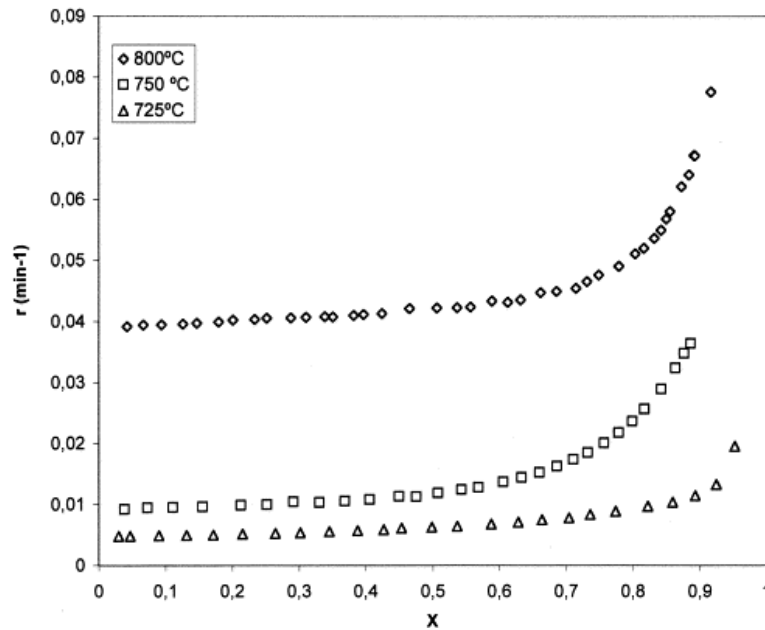


Figure I.11 | Reactivity versus conversion curves for CO₂ gasification of grapefruit skin char at different temperatures. Reprinted from (Marquez-Montesinos et al., 2002) with permission from Elsevier.

In identical operating conditions, biomass samples can have different kinetic behaviors. For example Dupont *et al.* (Dupont et al., 2016) measured the reactivity of 20 biomass species of various types—wood, short rotation coppice and forestry, agricultural residue and microalgae—in steam gasification experiments performed in a thermogravimetric analyzer at 800°C. They found a factor of more than 30 between the reactivities of the fastest and the slowest biomass samples, with gasification times ranging from a few minutes to several hours. The reactivity values are presented in Figure I.12.

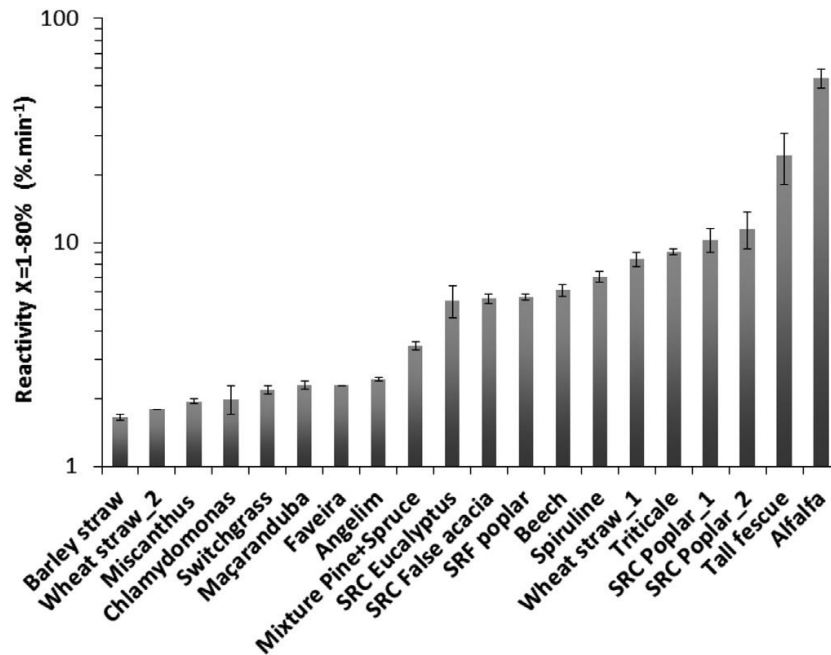


Figure I.12 | Reactivity between 1 and 80% of conversion of several biomass samples. Reprinted from (Dupont et al., 2016) with permission from Elsevier.

Other parameters than CO_2 or H_2O partial pressure and temperature can affect the reactivity of the chars. This can occur including in conditions where only the chemical reaction is limiting, i.e. where heat and mass transfer do not play a role. The two main parameters mentioned in literature are the morphological structure of the char and its composition in inorganic matter (Di Blasi, 2009).

As synthesized in Di Blasi's review (Di Blasi, 2009), the morphological structure is particularly influenced by the release of the volatile species during the pyrolysis which is controlled by the operating conditions of this step. It has been shown that high heating rate pyrolysis produces a char that is more reactive in gasification than low heating rate pyrolysis. Chars from low heating rate pyrolysis keep their natural porosity while chars from high heating rate pyrolysis form larger cavities (Figure I.13) (Di Blasi, 2009; Septien et al., 2018). This larger surface area in the case of high heating rate pyrolysis along with the higher content in O and H results in more available active sites (Guerrero et al., 2008).

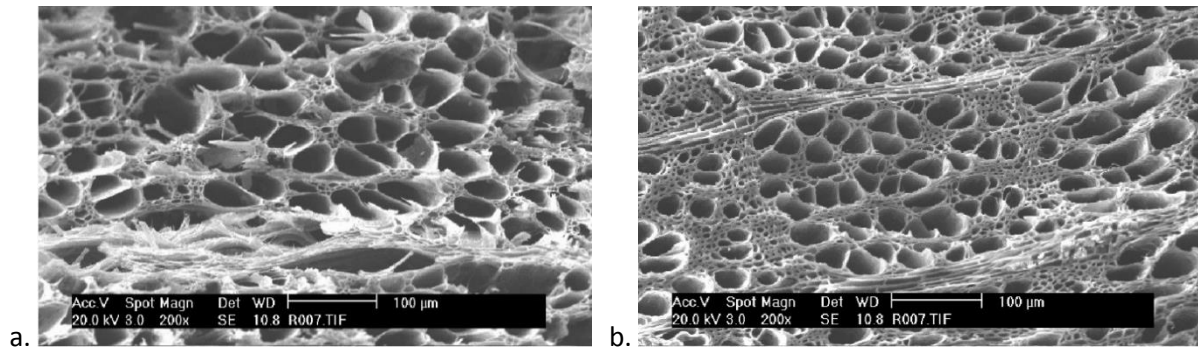


Figure I.13 | SEM observations of beech chars produced from a. high heating rate pyrolysis ($100\text{ }^{\circ}\text{C}\cdot\text{s}^{-1}$), b. low heating rate pyrolysis ($0.05\text{ }^{\circ}\text{C}\cdot\text{s}^{-1}$). Reprinted from (Septien et al., 2018) with permission from Elsevier.

It seems that, for similar conditions for the production of the char, the influence of the morphological structure is weaker than the influence of the inorganic composition, though no clear conclusion is given in literature (Di Blasi, 2009; Gupta et al., 2018). The differences in terms of gasification reactivity of the biomass samples illustrated above in Figure I.12 (Dupont et al., 2016) were attributed to the differences in their inorganic composition. In particular, in that study Dupont *et al.* observed that biomass species that gasified fast were rich in K whereas those that gasified slowly were rich in Si or P.

The present work focused on the effect of the inorganic elements on char steam gasification. These effects are discussed in detail in the following section.

3. The effects of inorganic elements on the steam gasification process

This section reviews the literature on the effects of inorganic compounds on gasification. It has been designed to be as extensive as possible regarding biomass. It also includes references on other feedstocks such as graphite or coal. Indeed, several studies were conducted on these solid fossil fuels and can be relevant in the study of biomass. They are reported here mostly in the form of reviews and more occasionally research articles of particular interest are cited.

The articles cited are reported in Table I.5. They are organized by:

- gasifying agent: H₂O and CO₂;
- type of feedstock: biomass and graphite and/or coal;
- mode of preparation of the feedstock to highlight the effects of the inorganic compounds: raw biomass or char (i.e. inherent inorganic compounds), washed biomass or char (i.e. with removal of the inherent inorganic compounds), sample mixed with an inorganic compound in its solid form and sample impregnated with a solution of the inorganic compound.

Table I.5 | References on the effects of inorganic elements used in this section, organized by gasifying agent, type of feedstock and mode of addition of the inorganic compounds if necessary.

		H ₂ O		CO ₂	
		Biomass	Graphite and/or coal	Biomass	Graphite and/or coal
Experimental works	Raw biomass or char	<ul style="list-style-type: none"> • Dupont, 2011 • Dupont, 2016 • González-Vázquez, 2018 • Hognon, 2014 • López-González, 2014 • Romero Millán, 2019 	—	<ul style="list-style-type: none"> • DeGroot, 1990 • Kannan, 1990 • Link, 2010 • Strandberg, 2017 • Umeki, 2012 	—
	Washed biomass or char	<ul style="list-style-type: none"> • Feng, 2018a • Yip, 2009 	—	<ul style="list-style-type: none"> • DeGroot, 1984 • Jiang, 2017 • Kannan, 1990 • Kramb, 2017 • Zahara, 2018 	—
	Mixed with solid inorganic compound	<ul style="list-style-type: none"> • Elliott, 1984 	<ul style="list-style-type: none"> • Hüttinger, 1986a • Hüttinger, 1986b • Wen, 1980 	<ul style="list-style-type: none"> • Arnold, 2017 • Bach-Oller, 2019 • Jiang, 2017 	<ul style="list-style-type: none"> • Wen, 1980
	Impregnated with inorganic solution	<ul style="list-style-type: none"> • Elliott, 1984 • Lv, 2016 • Zhang, 2008 	<ul style="list-style-type: none"> • Delannay, 1984 • Meijer, 1994 	<ul style="list-style-type: none"> • Bach-Oller, 2019 • Bennici, 2019 • Bouraoui, 2016 • Feng, 2018b • Huang, 2009 • Kirtania, 2017 • Kramb, 2016 • Kramb, 2017 • Lahijani, 2013 • Perander, 2015 	<ul style="list-style-type: none"> • Struis, 2002 • Ding, 2017
Reviews	<ul style="list-style-type: none"> • Baker, 1984 		<ul style="list-style-type: none"> • Moulijn, 1984 		
			<ul style="list-style-type: none"> • Arnold, 2019 • McKee, 1983 • Nzihou, 2013 		

Concerning experimental works on biomass, it can be noted that more studies have been published on CO₂ gasification than on steam gasification. In particular, studies under a CO₂ atmosphere cover a wider range of contact modes between the biomass and the inorganic compounds. This can be explained by the fact that producing a steam atmosphere is more experimentally challenging than working with a CO₂ bottle. Hence, even though this work focused on steam gasification, both gasifying agents are referenced since analogies can be made.

3.1. Assessment of the inorganic effects on char gasification

3.1.1. Effects of all inorganic compounds

3.1.1.1. Methodologies used in literature

It has been shown that, unlike pyrolysis kinetics, gasification kinetics cannot be explained by the macromolecular composition of the biomass (López-González et al., 2014; Romero Millán et al., 2019). On the contrary, some inherent inorganic elements are known to have a significant influence on char gasification kinetics. Several methods to highlight the catalytic and inhibitory effects of inorganic elements were applied in the literature. Studies used raw biomass or biomass char (DeGroot et al., 1990; Dupont et al., 2011, 2016; González-Vázquez et al., 2018; Hognon et al., 2014; Kannan and Richards, 1990; Link et al., 2010; López-González et al., 2014; Romero Millán et al., 2019; Strandberg et al., 2017), biomass or char washed with deionized water and/or with acid to remove the inherent inorganic matter (Feng et al., 2018a; Jiang et al., 2017; Kannan and Richards, 1990; Kramb et al., 2017; Lv et al., 2016; Yip et al., 2009; Zahara et al., 2018), or biomass or char with added inorganic compounds (Arnold et al., 2017; Bach-Oller et al., 2019; Bouraoui et al., 2016; DeGroot and Shafizadeh, 1984; Elliott et al., 1984; Feng et al., 2018b; Jiang et al., 2017; Kannan and Richards, 1990; Kirtania et al., 2017; Kramb et al., 2016, 2017; Lahijani et al., 2013; Lv et al., 2016; Meijer et al., 1994; Mudge et al., 1979; Perander et al., 2015; Zhang et al., 2008). The latter were prepared through solid mixing (Arnold et al., 2017; Bach-Oller et al., 2019; Elliott et al., 1984; Jiang et al., 2017; Mudge et al., 1979) or through impregnation with a solution containing the inorganic compound (Bach-Oller et al., 2019; Bouraoui et al., 2016; DeGroot and Shafizadeh, 1984; Elliott et al., 1984; Feng et al., 2018b; Kirtania et al., 2017; Kramb et al., 2016, 2017; Lahijani et al., 2013; Lv et al., 2016; Meijer et al., 1994; Mudge et al., 1979; Perander et al., 2015; Zhang et al., 2008). In the case of washed samples and impregnated samples a particular attention should be given. In particular, the char textural properties should not be affected in order to not distort the conclusions on inorganic effects. Moreover, inorganic compounds used for impregnation can change form when they crystallize. For example, a K_2CO_3 solution could induce the presence of K bonded to the biomass through ion exchange and $KHCO_3$ crystals as well as K_2CO_3 crystals in the dried sample (Bach-Oller et al., 2019; Kramb et al., 2016). However, impregnation has been the major addition method used in literature since it is simple to carry out and allows a close contact between the inorganics and the biomass.

Few authors compared the effects of various addition methods. Elliott *et al.* (Elliott et al., 1984) and Bach-Oller *et al.* (Bach-Oller et al., 2019) observed a slightly stronger catalytic effect of K_2CO_3 in the case of impregnation compared to dry mixing. However, Elliott *et al.* did not observe this difference in the case of Na_2CO_3 . The curves for both inorganic compounds from Elliott *et al.* are shown in Figure I.14. These results suggest an activity through the gas phase. The slight decrease in activity with dry mixing could be explained by a lower volatilization of the inorganic compound in this case due to mass transfer limitations.

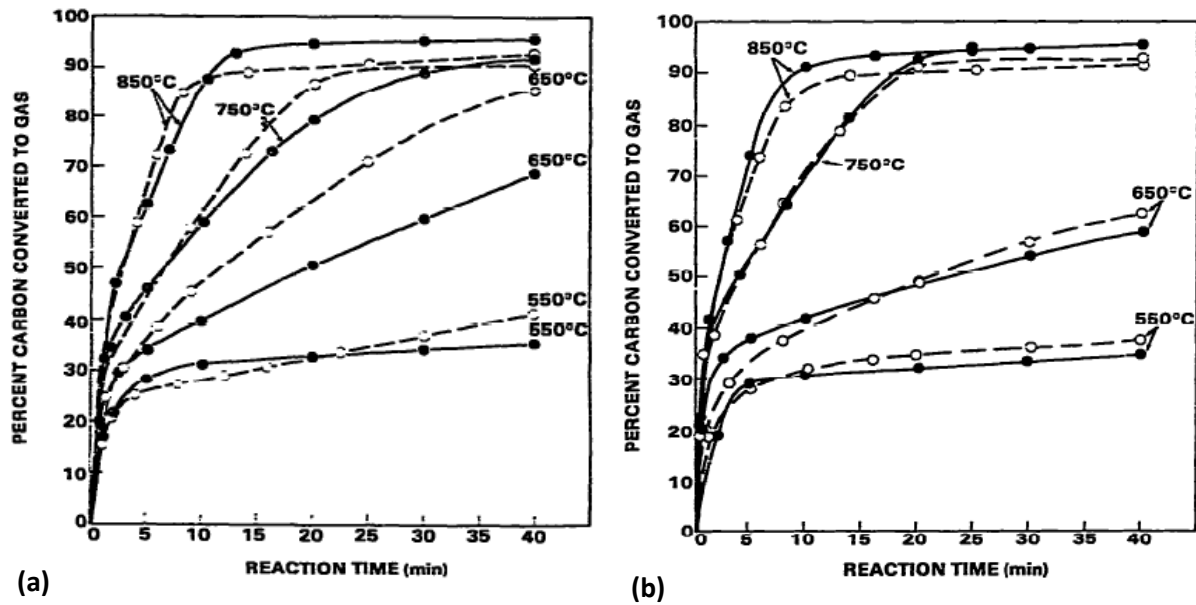


Figure I.14 | Carbon conversion to gas for the catalyzed steam gasification of Douglas fir with dry-mixed (solid line) and solution impregnated (dotted line) (a) K_2CO_3 and (b) Na_2CO_3 . Reprinted from (Elliott et al., 1984) with permission from Elsevier.

3.1.1.2. Catalytic effects

From these studies, it appeared that alkali and alkaline earth metals (AAEMs) tend to have a catalytic effect that enhances biomass gasification kinetics. More specifically, alkali metals, and in particular K which is more present in biomass than Na, are reported to be more active than alkaline earth metals. No significant effect was observed for Mg in the literature (Zahara et al., 2018; Zhang et al., 2008). The catalytic activity of AAEMs was reported to be, in decreasing order, K, Na, Ca and Mg (Huang et al., 2009; Yip et al., 2009; Zhang et al., 2008). An example of the obtained curves of carbon conversion as a function of temperature for several catalysts is given in Figure I.15 (Huang et al., 2009) during the CO_2 gasification of Chinese Guangzhou fir. It can be noted that González-Vázquez *et al.* (González-Vázquez et al., 2018) as well as Bennici *et al.* (Bennici et al., 2019) did not observe a catalytic effect of Ca but a rather negative effect on gasification kinetics under steam and CO_2 atmospheres respectively. However, the conclusion of González-Vázquez *et al.* came from a correlation analysis on several pure biomasses and not from a phenomenological analysis. Observations from Bennici *et al.* came from experiments on impregnated washed biomass but no further explanations were given on the results.

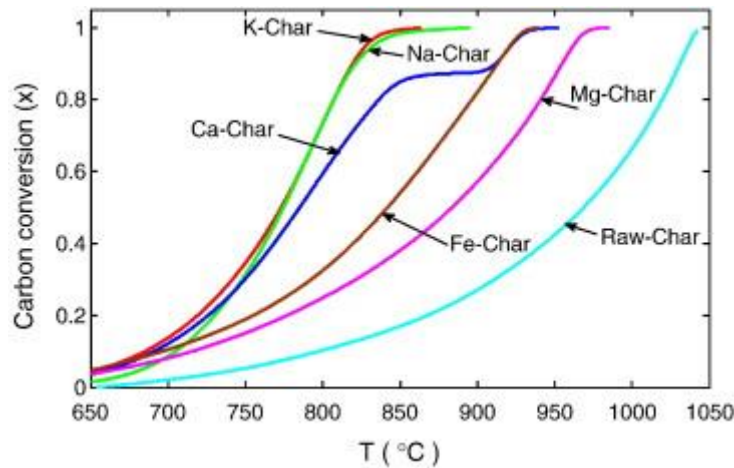


Figure I.15 | Carbon conversion during the CO₂ gasification of chars from Chinese Guangzhou fir catalyzed with different inorganic elements. Reprinted from (Huang et al., 2009) with permission from Elsevier.

Catalytic gasification uses this effect to improve the gasification process. Catalysts usually studied are compounds of AAEMs as well as some heavy metal compounds such as Fe-compounds and Ni-compounds (Arnold and Hill, 2019). Among these elements, those inherent to the biomass are mainly K, Ca and Mg, the others are usually found in low amounts in the biomass. Therefore, biomass species naturally rich in these elements—especially K which has the highest catalytic activity—tend to have the highest gasification reactivity.

3.1.1.3. Inhibitory effects

However, other elements present in the biomass can have the opposite effect and slow the gasification down. In particular, Al, Si and P were reported to inhibit the gasification (Arnold and Hill, 2019; Bouraoui et al., 2016; Dupont et al., 2016; Link et al., 2010; Zhang et al., 2008). In the case of lignocellulosic biomass, Al and P are usually found in low amounts whereas Si can reach high concentrations.

From these general observations of the effects of the inorganic elements on steam gasification, as well as from the knowledge of the typical inorganic composition of lignocellulosic biomass, the importance of K and Si could be highlighted. Understanding the influence of compounds of these two elements is of particular interest. Therefore it was the focus of the present work.

3.1.2. The specific effects of K and Si

Catalysts containing K used in gasification are mostly K₂CO₃ and KOH which are compounds naturally found in biomass (Arnold and Hill, 2019). KNO₃ or KCl were also studied (Bouraoui et al., 2016; Kramb et al., 2017; Lahijani et al., 2013). Kramb *et al.* (Kramb et al., 2016) observed the same effect on CO₂ gasification kinetics with addition of K by KNO₃ as with addition of K₂CO₃. The result for K-compounds was in accordance with the observations of Hüttinger *et al.* (Hüttinger and Minges, 1986a, 1986b) who found the following relative activity : KOH ~ K₂CO₃ ~ KNO₃ > K₂SO₄ > KCl. They also demonstrated that the intermediate species KOH was formed from all salts.

It is important to note that the K catalytic effect can be influenced by the presence of Ca. Indeed, apparent promoting effects can be obtained when combining K and Ca catalysts (Arnold and Hill, 2019; Nzihou et al., 2013). This promoting effect occurs until an optimal concentration of CaCO_3 added with K_2CO_3 to the biomass. After this optimum is reached, further addition of CaCO_3 can be detrimental (Arnold and Hill, 2019).

The inhibiting effect of Si was observed with inherent Si from the biomass (Arnold and Hill, 2019; Bach-Oller et al., 2019; Dupont et al., 2016; Link et al., 2010; Zhang et al., 2008) and with Si from the bed material or added for investigation purpose (Arnold et al., 2017; Bouraoui et al., 2016; Kannan and Richards, 1990).

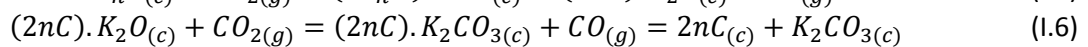
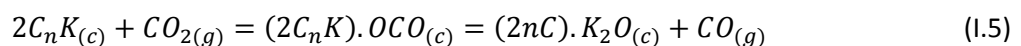
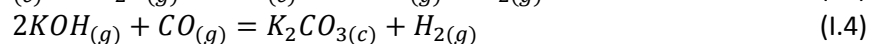
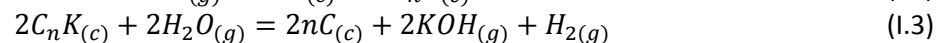
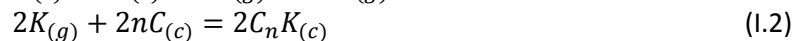
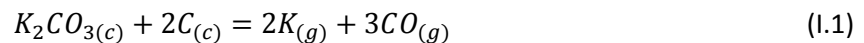
3.2. Proposed mechanisms for the K-catalysis

The catalytic effects of AAEMs, in particular K, and the inhibiting effect of elements such as Si are well described in literature. However, authors have proposed hypotheses but the mechanisms of such effects remain poorly known. This section presents first the inorganic compounds behavior during the char formation through pyrolysis and then the proposed mechanisms of action of these inorganics during gasification.

Several mechanisms have been proposed in the literature to explain the catalysis of steam gasification by K-compounds. Authors agree on the fact that the alkali compounds added as catalysts or inherent to the biomass are not the active compounds. However there is no consensus concerning the active intermediate. The active species mentioned in literature reviews (Arnold and Hill, 2019; Nzihou et al., 2013) are K_xO_y (non-stoichiometric), K_2O , K-O-C, K-C, C_nK .

3.2.1. Mechanism with intercalation compounds

One mechanism suggested in the literature was a mechanism involving intercalation compounds C_nK . Intercalation compounds C_nK are compounds where K is inserted between two graphitic layers. Biomass chars are disorganized carbon structure but contain a fraction of graphitic structures. McKee (McKee, 1983) mentioned the catalytic cycle involving an intercalation compound C_nK , possibly C_{48}K or C_{60}K , suggested by Wen (Wen, 1980). A mechanism was described for CO_2 as a gasifying agent as well as for steam. First, there is a carbothermic reduction of the carbonate to obtain $\text{K}(\text{g})$ and CO (Equation (I.1)). Then, $\text{K}(\text{g})$ reacts with the carbon to form the intercalation compound C_nK (Equation (I.2)). In the case of steam gasification, steam reacts with the intercalation compound C_nK which form $n\text{C}$, $\text{KOH}(\text{g})$ and H_2 (Equation (I.3)). Then the formed $\text{KOH}(\text{g})$ reacts with CO to regenerate the carbonate and produce H_2 (Equation (I.4)). In the case of CO_2 gasification, the compound $(2\text{C}_n\text{K}).\text{OCO}$ is formed and transforms into CO and $(2n\text{C}).\text{K}_2\text{O}$ (Equation (I.5)). The latter reacts with an additional CO_2 molecule to form $(2n\text{C}).\text{K}_2\text{CO}_3$ and to finally regenerate K_2CO_3 (Equation (I.6)).



However, there is no direct evidence of the formation of C_nK during gasification to our knowledge. It has been shown that these compounds can be formed at moderate temperature, i.e. around 250 °C, and can be detected through X-ray diffraction (XRD). However, these compounds are not stable at gasification temperatures, i.e. above 700 °C, and they are hydrolyzed by steam at ambient temperature (McKee, 1983; Tromp and Cordfunke, 1984). Therefore, such mechanism is not likely in the gasification conditions of the present study.

3.2.2. Mechanisms with a mechanical action

Physical effects of the alkali compounds were also discussed in literature. Alternatively to the chemical action of intercalation compounds, they could also have had a mechanical action. It is known that the intercalation of K increases the distance between graphitic planes (Wang et al., 2017), as illustrated in Figure I.16. Therefore, it has been suggested that intercalation of AAEMs in the graphitic layers could open up the structure and make it more easily available for reaction (McKee, 1983). However, as discussed previously, the formation of such compounds in gasification conditions is unlikely.

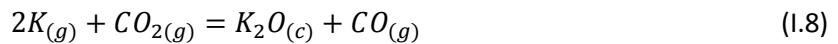
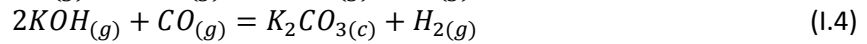
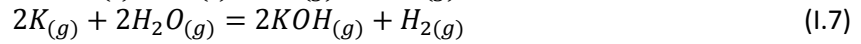
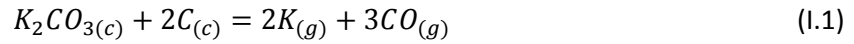


Figure I.16 | Li and K intercalation in graphite with the resulting interlayer spacing (Wang et al., 2017) - Published by The Royal Society of Chemistry.

Another mechanical action could be through swelling. Elliott *et al.* (Elliott et al., 1984) observed that AAEMs can induce swelling during the pyrolysis which could increase the number of active carbon sites available for the gasification reaction. However, gasification of Douglas fir with Na_2CO_3 at two concentrations, $1.5 \cdot 10^{-3}$ and $3.0 \cdot 10^{-3}$ mole Na per g sample, showed similar improved rates while only the higher Na_2CO_3 concentration induced swelling of cellulose samples. Similarly, Na_2CO_3 added to Douglas fir through dry-mixing had a catalytic effect while it did not induce swelling. Therefore, they demonstrated that the swelling phenomenon was not involved in the catalysis of gasification by AAEMs.

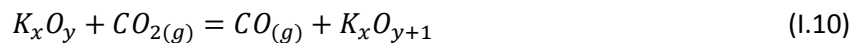
3.2.3. Mechanisms for a carbon atom

McKee (McKee, 1983) proposed a mechanism in three steps from K_2CO_3 . As in the intercalation mechanism, the cycle starts with the carbothermic reduction of the carbonate to obtain $K(g)$ and CO (Equation (I.1)). McKee suggested that it was the limiting step. Then, $K(g)$ reacts with steam which forms $KOH(g)$ and H_2 (Equation (I.7)). Finally, the formed $KOH(g)$ reacts with CO to regenerate the carbonate and produce H_2 , similarly to the intercalation mechanism (Equation (I.4)). A similar reaction pathway was proposed for CO_2 as a gasifying agent (Equation (I.8) and (I.9)) and both could also be applied to Na_2CO_3 .



Equations (I.1) and (I.7) were demonstrated through detection of a larger amount of $K(g)$ that would be expected from dissociation of K_2CO_3 alone, and by the decrease of $K(g)$ and formation of $KOH(g)$ after steam injection. Little information is available on the kinetics of Equations (I.7) and (I.4) but they have strongly negative free energies at gasification temperatures indicating that they are thermodynamically feasible (McKee, 1983).

Moulijn *et al.* (Moulijn *et al.*, 1984) proposed a mechanism from literature review for the case of CO_2 gasification, which could also be applied to gasification in H_2O or O_2 . This mechanism starts with the carbothermic reduction of K_2CO_3 that forms $K(g)$ (Equation (I.1)). The gasification agent then transfers O to K to form K_xO_y . This compound reacts with an additional O that will after react with solid C to form CO as presented in Equations (I.10) and (I.11). However, Moulijn *et al.* stated that “the detailed structure of K_xO_y , and K_xO_{y+1} [was] not clear”.



In conclusion, these mechanisms are a first approach to understand the behavior of alkali carbonates in the catalysis of steam gasification. It highlights that the general role of K is to bring the gasifying agent into contact with the carbon. However, char is not constituted of single carbon atoms. Carbon atoms are linked with each other in structures with various levels of organization, and with other atoms, mainly H and O, especially on char surface. Therefore, some authors proposed more detailed mechanisms mentioning the active sites on char surface, i.e. the functional groups or particular carbon atoms of the structure that are available for reaction.

3.2.4. Mechanisms for carbon structures

The work of Delannay *et al.* (Delannay et al., 1984) on graphite suggests a mechanism following four steps illustrated in Figure I.17. First, water reacts with one carbon from the graphitic layer to form a phenol group. This phenol group then reacts with KOH to form a K-O-C phenolate group. With heat, the latter decomposes to either metallic K and CO or to K₂O, CO and C. Finally, KOH is regenerated from the reaction of K₂O with H₂O. The observation of the produced gases supported this mechanism. Two stages can be identified: the production of hydrogen and hydrocarbons at high rate corresponding to step 1 and then the production of CO and H₂ at a slower rate corresponding to steps 2 to 4 with step 3 being limiting.

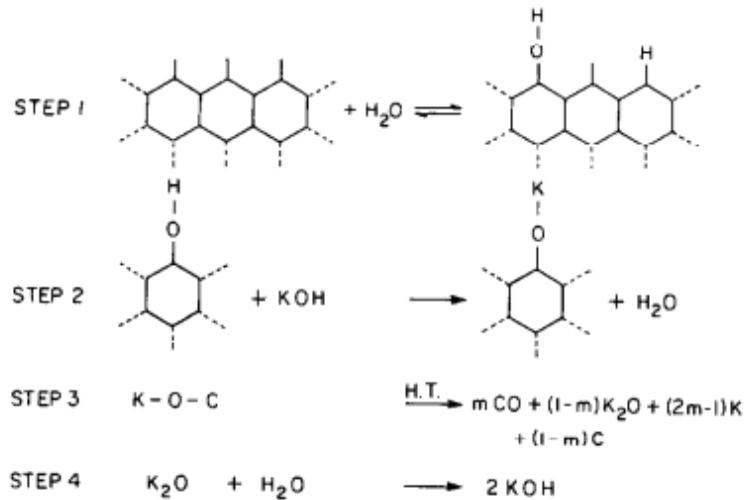


Figure I.17 | Mechanistic model for the reaction of water with graphite in the presence of KOH.
Reprinted from (Delannay et al., 1984) with permission from Elsevier.

Feng et al. (Feng et al., 2018b) also supports the idea of the K-O-C group formation as an active site. They worked with biomass chars impregnated with AAEMs before or after the pyrolysis, i.e. “AAEM pre-loaded biochar” or “AAEM post-loaded biochar” respectively. They proposed mechanisms for each case as illustrated in Figure I.18.

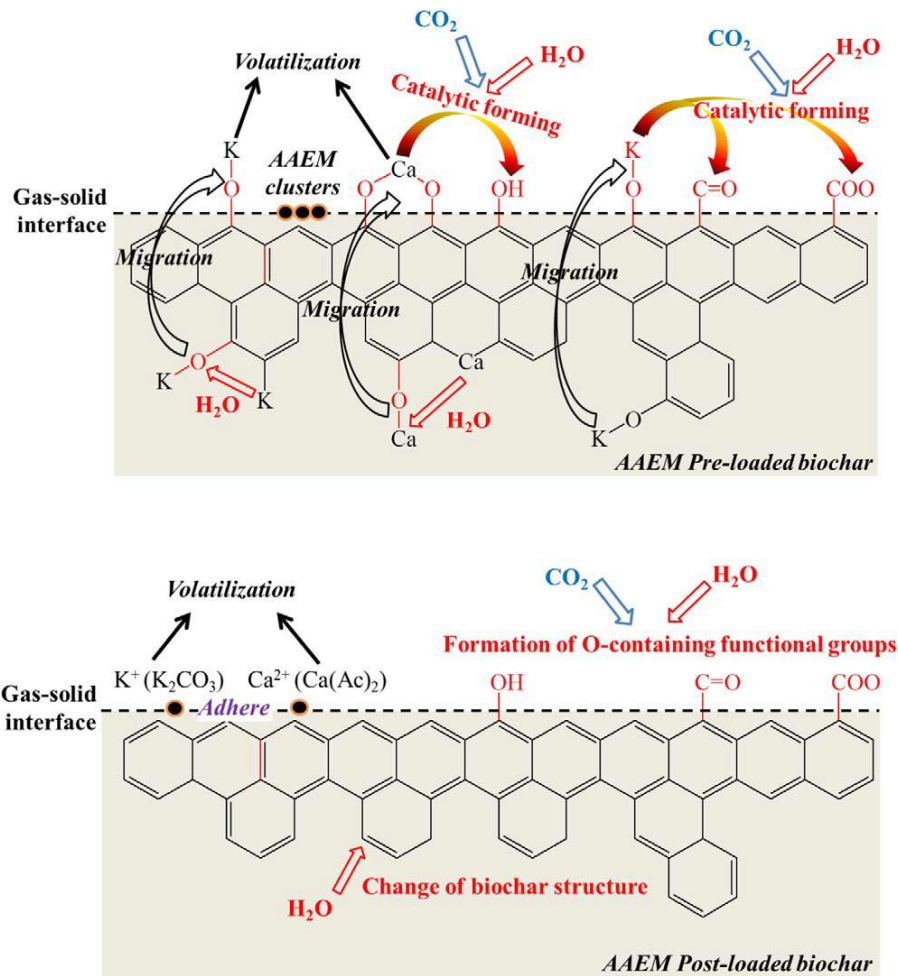


Figure I.18 | Mechanisms of pre-loaded AAEMs and post-loaded AAEMs on biochar. Reprinted from (Feng et al., 2018b) with permission from Elsevier.

In the case of pre-loaded biochar, i.e. char from the pyrolysis of an impregnated biomass, AAEM are linked to the carbon matrix. Unlike in the mechanism of Delannay *et al.* where the gasifying agent reacts on a carbon, here the reaction occurs on those K-matrix sites to form the K-O-C groups inside the carbon matrix. The AAEMs migrate to the gas-solid interface which implies that these groups break and form again, contributing to the condensation of aromatic rings, i.e. the formation of larger rings from small ones. Moreover, due to their valence state, K is bonded to only one carbon site while Ca is bonded to two. Therefore, K is less strongly bonded to the carbon matrix so the bond can easily break to provide active sites for the aromatic condensation which explains the stronger effect of K compared to Ca.

In the case of post-loaded biochar, AAEMs are present only on the surface and not incorporated to the carbon matrix. The bonds are weaker which facilitates the volatilization of the AAEMs and explains the lower reactivity of these chars.

3.2.5. Explanation of the reactivity changes at high conversion

For some biomass species, an acceleration of the gasification is observed at high conversion (Bouraoui et al., 2016; Dupont et al., 2011, 2016; Zhang et al., 2008). For example, results from Bouraoui *et al.* presented in Figure I.19 showed that, for samples of impregnated beech wood, a high K/Si ratio led to an increase in reactivity with conversion.

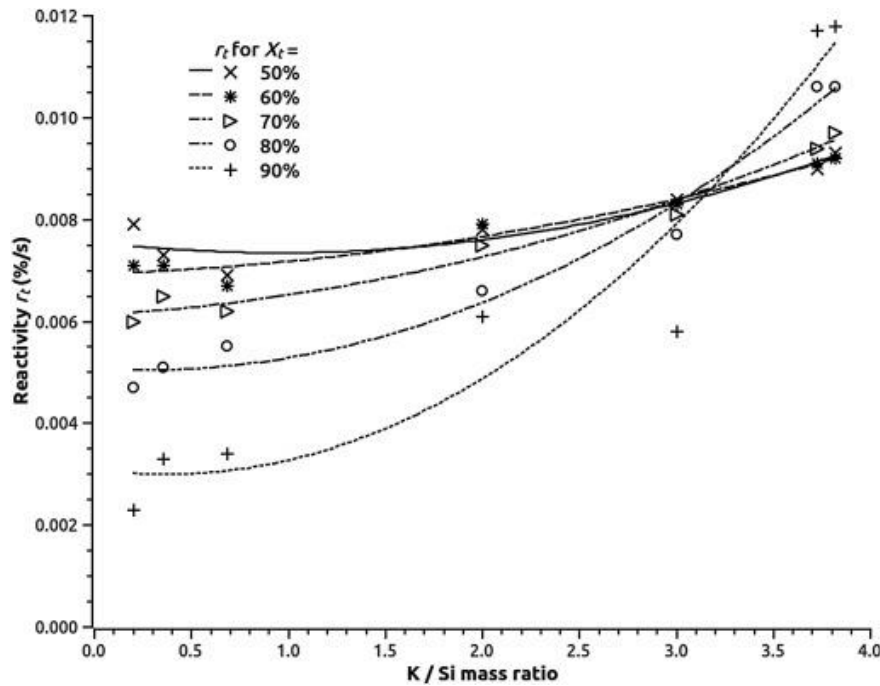


Figure I.19 | Reactivity at several conversion values as a function of the K/Si ratio of samples of impregnated beech wood (Bouraoui et al., 2016).

This gasification acceleration seems to be linked to a significant alkali content and could be explained by several factors. At the end of the gasification, the alkali compounds are more concentrated which could enhance the catalytic effect (Dupont et al., 2011; Zhang et al., 2008). It could also be due to the sudden disintegration of the porous structure of the char, leading to a higher active surface area available to react. Lastly, it could be related to the release of alkali metals previously inactive, such as intercalated alkali (Zhang et al., 2008).

On the opposite, for other biomass species with high alkali content—in particular K—the gasification rate strongly decreases at very high conversion values. This behavior can be observed in the case of K catalysis and can be attributed to the collapse of the numerous pores and channels formed which induces a decrease of the surface available for the reaction (Arnold and Hill, 2019). It could also be explained by interactions between AAEMs and SiO_2 to form silicates either making the AAEM compounds not available for catalysis or forming liquid phases that encapsulate the remaining char (Link et al., 2010; Strandberg et al., 2017).

3.3. Proposed mechanisms for the inhibiting effect of Si

In literature there seems to be an agreement about the fact that the inhibiting effect of Si on gasification is rather due to an inhibition of the catalysis from other elements. It has been shown that Al, Si and P compounds can react with the catalytic AAEM compounds (Arnold and Hill, 2019; Dupont et al., 2016; Zahara et al., 2018; Zhang et al., 2008). They form aluminates, silicates and phosphates with the AAEMs which are stable and non-catalytic compounds. Subsequently, the AAEMs are not available anymore to catalyze the gasification.

Some studies also reported that melted phases containing Si could encapsulate the remaining char. For example, as discussed in the previous section, Strandberg *et al.* (Strandberg et al., 2017) explained the low reactivity at high conversion of a Si- and K-rich wheat straw by the melted ashes that induced a physical inhibition (Figure I.20).

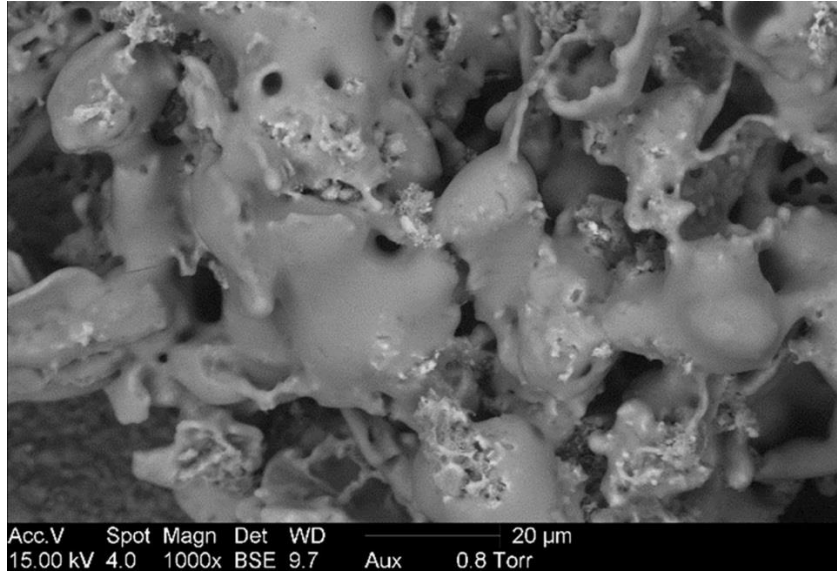


Figure I.20 | SEM observation of a wheat straw char at 90% gasification conversion, with melted ashes. Reprinted (adapted) with permission from (Strandberg et al., 2017). Copyright (2019) American Chemical Society.

However, few studies were conducted to directly investigate the mechanism of action of Si on the gasification kinetics. Published works focused either on the gasification kinetics or on the agglomeration issues related to this element. Therefore, the previous conclusions came from studies highlighting the effects of Si and looking at literature results from agglomeration publication. To our knowledge, there has been no direct study investigating both the gasification kinetics and the residue characterization with Si.

Finally, the apparent promoting effect of Ca on K-catalysis has been attributed to the preferential reaction of this element with SiO_2 to form Ca-silicates (Arnold et al., 2017). There is therefore less SiO_2 available to react with K, which can then keep its catalytic activity.

3.4. Proposed models

To describe the steam gasification of biomass, a first approach can be to simulate the system at its thermodynamic equilibrium. However, this method has been reported to give good results in the case of high temperature entrained flow gasifiers but not in the case of fluidized bed reactors (Sikarwar et al., 2017). In this last case, which is the case related to the present study, the system does not reach its thermodynamic equilibrium. Therefore, kinetic models have to be designed.

Various kinetic models are used in the literature to describe the steam gasification of biomass. Generally, such kinetic models are of the form of Equation (I.12).

$$r = k(T) \times g(P_{\text{H}_2\text{O}}) \times f(X) \quad (\text{I.12})$$

Where $k(T)$ describes the dependence on the reaction temperature T , $f(X)$ is a function of the conversion X that takes into account the change in the char structure during the reaction, and $g(P_{\text{H}_2\text{O}})$ describes the dependence on the partial pressure of the steam which is the gasifying agent.

The temperature dependent factor $k(T)$ follows an Arrhenius law.

$$k(T) = k_0 \exp\left(-\frac{E_a}{RT}\right) \quad (\text{I.13})$$

With k_0 a pre-exponential constant and E_a the activation energy.

The steam partial pressure dependent factor $g(P_{H_2O})$ follows a power law.

$$g(P_{H_2O}) = P_{H_2O}^n \quad (1.14)$$

For the function $f(X)$ there is no consensus in literature about its form. Different models can be used which are dependent on the conditions. Models commonly used for $f(X)$ are listed in Table I.6 which is adapted from Romero Millán *et al.*

Table I.6 | Common models for the surface function $f(X)$. Adapted from Romero Millán *et al.* (Romero Millán *et al.*, 2019).

Model	$f(X)$
0 th order	1
1 st order – Volumetric model	$1 - X$
2 nd order	$(1 - X)^2$
3 rd order	$(1 - X)^3$
n th order	$(1 - X)^n$
One dimensional	$\frac{1}{2X}$
Two dimensional	$\frac{1}{-\ln(1 - X)}$
Three dimensional	$\frac{3}{2} \times \frac{(1 - X)^{\frac{2}{3}}}{1 - (1 - X)^{\frac{1}{3}}}$
Contracting area	$2 \times (1 - X)^{\frac{1}{2}}$
Contracting volume – Shrinking core model – Grain model	$3 \times (1 - X)^{\frac{2}{3}}$
Random pore model	$(1 - X) \times \sqrt{1 - \psi \times \ln(1 - X)}$

Volumetric model, grain model and random pore model, sometimes including modifications, have been the most used models among authors for steam gasification (Dupont *et al.*, 2011; Feroso *et al.*, 2008; González-Vázquez *et al.*, 2018; Hognon *et al.*, 2014; López-González *et al.*, 2014; Romero Millán *et al.*, 2019; Zhang *et al.*, 2008).

However, these models do not achieve a good description of the experimental data for biomass samples showing catalytic effects.

To take these effects into account, authors proposed modifications to the models presented above. Table I.7 summarizes the available kinetic models taking into account the effects of inorganic elements on gasification (Arnold et al., 2017; Ding et al., 2017; Dupont et al., 2011; Hognon et al., 2014; Kramb et al., 2016; López-González et al., 2014; Romero Millán et al., 2019; Struis et al., 2002; Umeki et al., 2012; Zhang et al., 2008).

Table I.7 | Gasification kinetic models taking into account the effects of inorganic elements.

Model	Gasification agent – Feedstock	Ref.
Grain model with additional factor $a_i = 0.1812 \frac{m_K}{m_{Si}} + 0.5877$	Steam – Biomass	Dupont, 2011
If $\frac{K}{Si+P} > 1$, 0 th -order model If $\frac{K}{Si+P} < 1$, 1 st -order/volumetric model	Steam – Biomass	Hognon, 2014
If $\frac{K}{Si+P} > 1$, 0 th -order model $f(X) = 0.15 \times \frac{K}{Si+P} + 0.7$ If $\frac{K}{Si+P} < 1$, 1 st -order/volumetric model $f(X) = (1 - X)^{-1.62 \times \frac{K}{Si+P} + 1.64}$	Steam – Biomass	Romero Millán, 2019
Grain model with additional term $k_a \times X^{n_a}$ with $n_a = 0.254[Ca] + 3.4 \times 10^{-2}$	Steam – Biomass	López-González, 2014
Sum of rates of three regimes: Catalytic with deactivation of catalyst, $f(X) = \exp(-\xi X^2)$ Non-catalytic, 1 st -order/volumetric model Catalytic with no deactivation of catalyst, 0 th -order model	CO ₂ – Biomass	Umeki, 2012
Random pore model with additional factor $1 + (cX)^p$ where c and p are correlated to with K	Steam – Biomass	Zhang, 2008
Random pore model with additional factor $1 + c \times (1 - X)^p$	CO ₂ – Coal	Arnold, 2017
Random pore model with additional factor $1 + (g + 1) \times (bt)^g$	CO ₂ – Coal	Struis, 2002
Sum of rates correlated to [Ca] and to [K], with for each: Random pore model with additional factor $1 + (g + 1) \times (bt)^g$ where ψ , b and g are correlated to the metal concentration	CO ₂ – Biomass	Kramb, 2016
Random pore model where $\psi = f \times \exp(-\phi \times \tau)$, ϕ is a coefficient and τ is a dimensionless time	CO ₂ – Coal	Ding, 2017

These modified models describe well gasification kinetics with catalytic effects due to inorganic elements. However, they are semi-empirical models with no true physical meaning. Therefore, a better understanding of the phenomena involved in catalysis and catalyst inhibition should allow to design a unified phenomenological model. In addition, some models were developed for CO₂ as a gasifying agent but have not been validated to describe steam gasification as the phenomena occurring seem to differ according to the gasifying agent. It is for example the case of the three regime model designed by Umeki *et al.* (Umeki et al., 2012).

4. Conclusions and objective of the work

In the context of the pyrogasification of biomass, authors identified that for identical operating conditions both the char morphology and its inorganic content can influence strongly the gasification kinetics. The inorganic content seems to be the most influential parameter but no clear conclusion is available in literature.

Despite their minor occurrence compared to the organic fraction, inorganic elements can have a major influence on the reaction kinetics. The effects of these elements have been described in details. Alkali and alkaline earth metals (AAEMs) have a catalytic effect on the gasification reaction, with varying degrees, while Al, Si and P have an inhibiting effect. By crossing this information with the typical inorganic composition of biomass species, it appears that the case of K and Si are of particular interest. Indeed, they have a high occurrence in natural lignocellulosic biomass as well as a strong activity.

However, even though the effects have been long known, the mechanisms behind them are still little known. In the case of the K-catalysis, several mechanisms have been proposed with various degrees of detail but none of them makes consensus. Moreover, experimental studies have suggested that K could have an impact through the gas phase but, to our knowledge, no direct demonstration exists. In the case of the inhibition of the gasification by Si, authors tend to agree on the fact that it is rather an inhibition of the AAEM-catalysis. The mechanisms of action of these two elements on gasification are therefore linked.

This low level of knowledge on the mechanisms involving the inorganic compounds during the steam gasification of biomass have impacts at the process design level. It leads to working with kinetic models that can fail to describe the reaction of biomasses when their inorganic content is non-negligible. Some authors have proposed modifications to the models in use to take the catalytic and inhibiting effects into account. Nevertheless, these attempts were semi-empirical and not unified.

In view of this literature review, the objective of this work was to contribute to the understanding of the inorganic elements role during the biomass steam gasification. In particular, it is an investigation of the phenomena involving K and Si during the biomass steam gasification, especially through the gas phase, and with particular attention on their influence on the reaction kinetics. The chosen approach in this study followed five main steps:

- Selecting two biomass samples with opposite kinetic behaviors, one being rich in K and the other one being rich in Si;
- Selecting two model inorganic compounds, one K-based and one Si-based, that also naturally occur in biomass;
- Confirming the strongest effect of inorganic content compared to morphology by characterizing both the morphology and the kinetic behavior of the two selected biomass species during the gasification conversion;
- Demonstrating the effect of K through the gas phase by conducting thermogravimetric analyses with the Si-rich biomass sample and the K-compound;
- Investigating the effect of Si on the gasification kinetics with a direct method by conducting thermogravimetric analyses with the K-rich biomass sample and the Si-compound.

Chapter II. Evolution of the char physicochemical properties during gasification

The objective of this chapter is to analyze the relative influence of the inorganic elements compared to the morphology of biomass chars on their gasification kinetics. Indeed, literature review, as conducted in Chapter I, shows that both parameters can have a significant effect. However, the influence of the inorganic content seems more pronounced but without clear explanations. In order to bring more clarification to the inorganic elements effect, various biomass species were characterized in this present study, at several gasification conversion values both regarding their morphology and their kinetic behavior.

The first part of this chapter lists the materials and methods used. It presents the biomass samples, the experimental set-ups and procedures, the characterization techniques and the method for the calculations at thermodynamic equilibrium. In a second part, the results from the char characterizations at various gasification stages are presented and discussed. They concern both the organic and inorganic fractions of the chars. Experimental results regarding the inorganic fraction are complemented by calculations at thermodynamic equilibrium. Finally, main conclusions are derived.

1. Materials and experimental installations

1.1. List of biomass species

Seven biomass samples covering various compositions were selected for this preliminary study. The selection mainly included agricultural or pruning residues. Samples were ground below 200 μm in a Pulverisette 14 rotor mill (FRITSCH, Idar-Oberstein, Germany). The ash content and inorganic element composition of the samples were measured according to solid fuel standards NF EN 14775 (European Standards, 2009) and NF EN ISO 16967 (International Organization for Standardization, 2015), respectively.

The obtained values for each biomass sample are presented in Table II.1. From these values, the three major inorganic elements in each sample were identified. It is clearly seen that the main inorganic elements contained in all biomass species are Ca and K. The third main element is Si, Mg, or P. Rice husks and wheat straw are Si-rich. Sunflower seed shells and alfalfa are K-rich. The others are rich in Ca.

Table II.1 | Ash content and elemental composition of the preliminary biomass samples (in dry basis).

Biomass sample	Rice husks	Wheat straw	Apple orchard residue	Apricot orchard residue	Vineyard residue	Sunflower seed shells	Alfalfa
Ash at 550 °C (wt%)	14.1	6.8	3.8	3.7	2.6	3.3	7.8
C	41.6	43.1	47.8	48.3	47.2	50.2	44.2
H	5.2	6.2	6.3	6.3	6.4	6.5	5.6
O*	45.1	45.8	43.4	41.8	43.9	40.6	43.2
N	0.5	0.5	0.8	1.3	0.7	0.7	2.3
S	0.1	0.1072	0.0577	0.0819	0.0627	0.1	0.255
Cl	0.1	0.0885	0.0097	0.0326	0.0263	0.1	0.5144
Si	63955	20757	820	990	1012	194	517
K	5822	13063	3771	7254	5045	9729	22545
Ca	1797	5627	9472	10927	7808	4489	12221
Mg	659	693	872	1374	1604	1838	1167
P	981	1373	1325	1161	1011	896	2501
Na	413	164	25	41	37	9	470
Al	228	429	71	104	151	150	66
Fe	192	299	58	88	113	1099	97
Mn	195	50	11	20	42	23	18
SiO ₂	97.2	65.4	4.6	5.7	8.3	1.3	1.4
K ₂ O	5.0	23.2	12.0	23.6	23.4	35.5	34.8
CaO	1.8	11.6	34.9	41.3	42.0	19.0	21.9
MgO	0.8	1.7	3.8	6.2	10.2	9.2	2.5
P ₂ O ₅	1.6	4.6	8.0	7.2	8.9	6.2	7.3
Na ₂ O	0.4	0.3	0.1	0.1	0.2	0.0	0.8
Al ₂ O ₃	0.3	1.2	0.4	0.5	1.1	0.9	0.2
Fe ₂ O ₃	0.2	0.6	0.2	0.3	0.6	4.8	0.2
MnO	0.2	0.1	0.0	0.1	0.2	0.1	0.0
Main Inorganic Elements	Si K Ca	Si K Ca	Ca K P	Ca K Mg	Ca K Mg	K Ca Mg	K Ca P

*Total (i.e. organic and inorganic) oxygen calculated by difference with all other elements.

1.2. Experimental set-ups

1.2.1. Pyrolysis furnace MATISSE

Chars were produced in large quantities, i.e. several grams, in the pyrolysis installation MATISSE illustrated in Figure II.1.

It consists of a stainless steel sample holder of 40 mm height and 70 mm diameter swept by $1 \text{ L}\cdot\text{min}^{-1} \text{ N}_2$ and placed in a furnace.

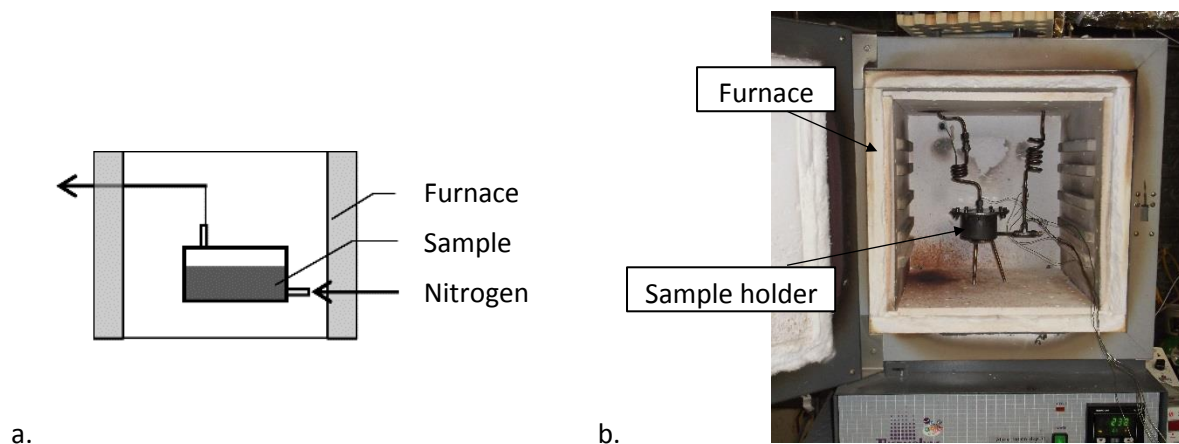


Figure II.1 | Pyrolysis furnace MATISSE a. scheme and b. picture.

Low heating rate (LHR) pyrolysis of the biomass samples was carried out. The sample holder was filled in with 30 to 50 g of ground sample depending on the biomass. Biomass samples were then heated to $450 \text{ }^\circ\text{C}$ at a heating rate of $10 \text{ }^\circ\text{C}\cdot\text{min}^{-1}$ and kept at this temperature for 60 min.

The mass of sample was weighted before and after pyrolysis to determine the char yield.

1.2.2. Thermogravimetric analyzer

Thermogravimetric analysis (TGA) was used to determine the intrinsic kinetic behavior of the samples—raw biomass or char. Experiments were carried out at atmospheric pressure using a Setsys thermobalance (SETARAM, Caluire, France) coupled with a Wetsys steam generator.

The thermobalance is illustrated in Figure II.2. It consists of a crucible placed in a furnace and hung to an electronic weighing scale. The furnace was swept by the selected gas from below. A cylindrical platinum crucible of 2.5 mm height and 7 mm diameter was used.

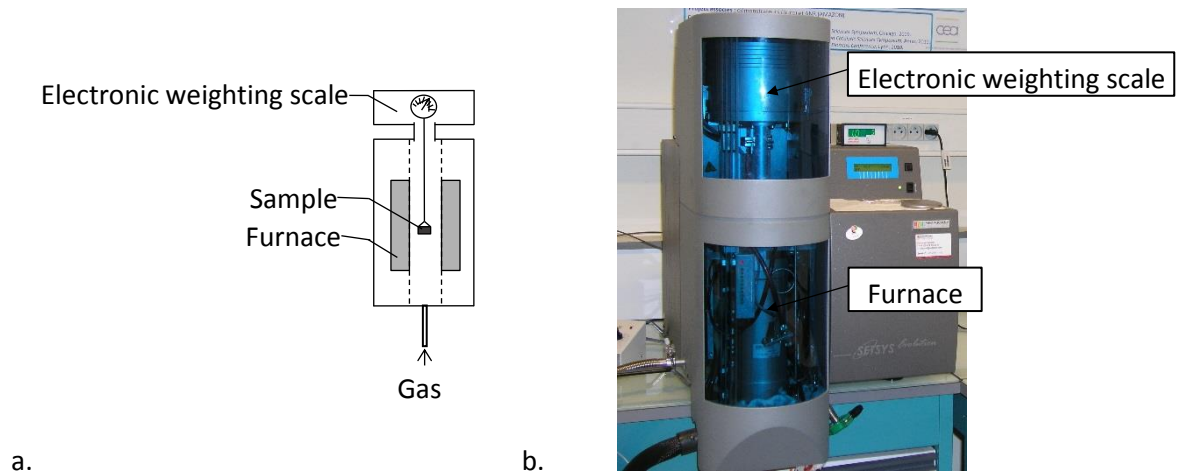


Figure II.2 | Thermogravimetric analyzer (TGA) a. scheme and b. picture.

The experimental procedure was slightly different for raw biomass and for char, so that in both cases the pyrolysis and gasification steps were separated (Figure II.3).

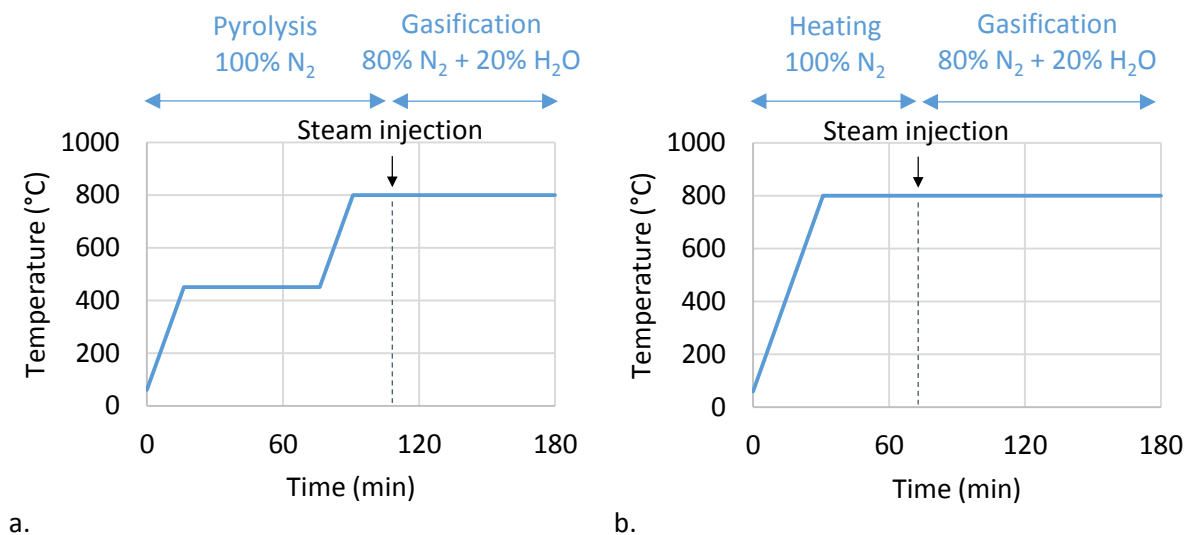


Figure II.3 | TGA procedure for a. raw biomass and b. char.

In the case of raw biomass (Figure II.3a), the procedure described by Hognon *et al.* (Hognon *et al.*, 2014) was applied. A mass of approximately 15 mg was used to be in chemical regime (Annex A). Samples were heated at $24\text{ }^{\circ}\text{C}\cdot\text{min}^{-1}$ until $450\text{ }^{\circ}\text{C}$ under $0.05\text{ L}\cdot\text{min}^{-1}\text{ N}_2$ and kept for 60 min at this temperature. They were then heated at $24\text{ }^{\circ}\text{C}\cdot\text{min}^{-1}$ until $800\text{ }^{\circ}\text{C}$ and kept at this temperature until the end of the experiment. Samples were swept by N_2 after the final temperature was reached to ensure pyrolysis completion and mass stability (12 min). Gas was then switched to a mixture of 20 vol% H_2O in N_2 . This marked the beginning of the gasification step. The experiment was ended when the mass was stabilized, i.e. when the gasification was finished and only ashes remained.

In the case of char (Figure II.3b), the holding time at $450\text{ }^{\circ}\text{C}$ was not necessary as pyrolysis had already been conducted. A mass of approximately 4 mg was used to be in chemical regime (Annex A). Samples were heated at $24\text{ }^{\circ}\text{C}\cdot\text{min}^{-1}$ directly until $800\text{ }^{\circ}\text{C}$ under $0.05\text{ L}\cdot\text{min}^{-1}\text{ N}_2$. Samples were swept by N_2 after the final temperature was reached to ensure pyrolysis completion and mass stability (45 min). Gas was then switched to a mixture of 20 vol % H_2O in N_2 to start the gasification step. The experiment was ended when the mass is stabilized.

All experiments were conducted at least in duplicates. In the case where results were plotted as curves, only one of the repetitions was selected. In the case where results were plotted in bar graphs, the average value was plotted and variations between the repetitions were shown with error bars representing the minimum and maximum measured values.

Results can be plotted as the normalized mass or the normalized ash free mass:

$$\text{Normalized mass:} \quad \frac{m(t)}{m_i}, \quad (\text{II.15})$$

$$\text{Normalized ash free mass:} \quad \frac{m(t) - m_f}{m_i - m_f}, \quad (\text{II.16})$$

where m_i , $m(t)$, and m_f are the mass of initial raw biomass, the mass measured at the time t and the mass measured at the end of gasification (remaining ash), respectively.

Gasification solid conversion was defined from the mass loss measured as a function of time during TGA by using the following expression:

$$X(t) = \frac{m_{i\text{char}} - m(t)}{m_{i\text{char}} - m_f}, \quad (\text{II.17})$$

where $m_{i\text{char}}$ is the mass of char before gasification (at the time of steam injection).

The gasification rate was then defined as the variation of conversion versus time:

$$r(t) = \frac{dX}{dt}. \quad (\text{II.18})$$

An average reactivity between two values of conversion X_1 and X_2 was also defined:

$$r_{X_1-X_2} = \frac{\int_{t_{X_1}}^{t_{X_2}} \frac{r(t) dt}{1 - X(t)}}{t_{X_2} - t_{X_1}}. \quad (\text{II.19})$$

There is no standardized definition for the reactivity (Barrio et al., 2001). In this study, the average reactivity was calculated between 1 and 80% conversion as in several investigations in literature (Barrio et al., 2001; Dupont et al., 2011; Hognon et al., 2014). This choice allowed to obtain a trend that was not affected by the particular phenomena that can occur at high conversion values.

1.2.3. Gasification devices

Three set-ups were used to carry out gasification on larger char samples than with the TGA: a macro-thermogravimetric reactor (macroTG), a laboratory furnace (NEWMANIP) and an induction furnace (PYRATES). Their main characteristics are summarized in Table II.2 and detailed in the following sub-sections.

Table II.2 | Main characteristics of the gasification devices.

	MacroTG	Laboratory furnace NEWMANIP	Induction furnace PYRATES
Initial mass of char	0.15 g	0.2 g	5-8 g
Crucible Material	Refractory steel	Pt – 5% Au	Stainless steel
Crucible Diameter	∅ 46 mm	∅ 15.7 mm	∅ 30 mm
Crucible Height	h = 5 mm	h = 2 mm	h = 45 mm
Gas flow rate	0.67 NL.min ⁻¹	0.33 NL.min ⁻¹	1 NL.min ⁻¹

1.2.3.1. Macro-thermogravimetric reactor

The macro-thermogravimetric reactor (macroTG) is located at the University of Science & Technology of Hanoi. It is illustrated in Figure II.4 and Figure II.5. It consists of a ceramic tube (1) of 111 cm in length, with an internal diameter of 7.5 cm. The ceramic tube is placed in an electric furnace of Carbolite Gero brand (2), with single ramp to set-point and process timer. Electrical heating is ensured by three independently controlled heating zones (T₁, T₂ and T₃). This helps to create a uniform temperature throughout the reactor. The reaction atmosphere is generated by a mixture of N₂ and a reactive gas in selected proportions. Each gas is controlled by a flowmeter (M₁, M₂, and M₃). The gas mixture is preheated in a 2-m-long-coiled tube (3) located inside at the upper heated part of the reactor. This ensures the uniformity of the gas mixture and allows to reach the desired temperature of the gas flow before reacting with the sample. The gas flow is then sucked by an extractor (6) and flown outside. The sample is placed on a refractory-steel crucible of 46 mm diameter and 5 mm height, on the top of the sample holder (4). The latter is connected with the weighting scale (5) at the bottom of the equipment using a stick in ceramic. The weighting scale (Precisa Gravimetrics AG ES320A) is accurate to 0.1 mg. All of the sample and the holder are weighted and registered continuously in the computer with the help of a monitoring software.

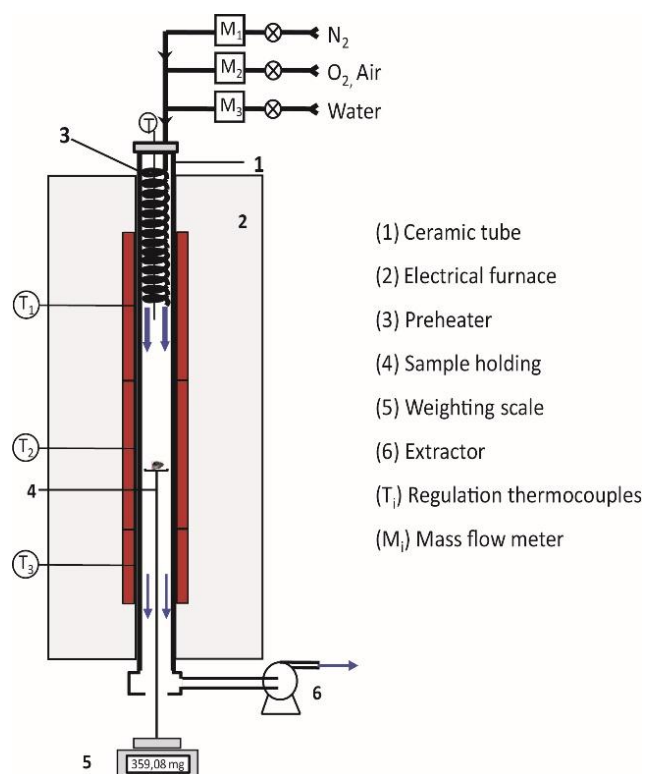


Figure II.4 | Macro-thermogravimetric reactor.

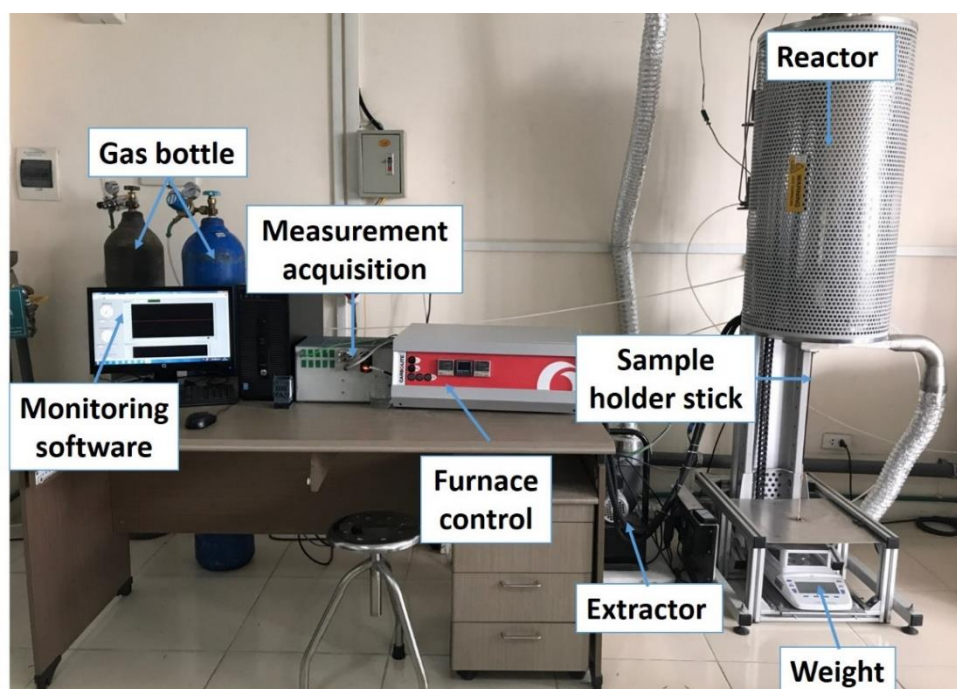


Figure II.5 | The macro-thermogravimetric system at the University of Science & Technology of Hanoi.

Steam gasification experiments were carried out under fixed operating conditions. For each experiment, the reactor was first heated to 800°C. When the desired temperature was reached, approximately 150 mg of char sample was lifted to the desired position inside the reactor. It was initially placed under inert atmosphere, i.e. nitrogen, at a gas flow of 0.67 NL.min⁻¹ to remove all residual volatiles and moisture adsorbed during storage.

When a constant mass was reached, gas was switched to a mixture of 20 vol% H₂O in N₂. As gasification took place, the char mass decreased progressively until a constant mass was reached, which corresponds to the ash content and marked the end of a test.

The gasification solid conversion, the gasification rate and the average reactivity were defined from Equations (II.17), (II.18) and (II.19) similarly to the case of TGA.

1.2.3.2. Laboratory furnace NEWMANIP

A laboratory furnace called NEWMANIP was also used in the present study. It includes three main parts: a sample holder, a controlled atmosphere chamber and a vertical tubular furnace. The sample holder is a structure sustained with two aluminum oxide rods. It supports the platinum crucible of 15.7 mm diameter and 2 mm height on which the sample is deposited. The temperature is monitored by three thermocouples fixed to this structure. It is placed inside the controlled atmosphere chamber. The latter is made up of an Inconel 600 tube with a 25 mm diameter. The gas input tube is welded around to preheat the gas. The top of the chamber is closed by a plug with the gas outlet and an air-tight passage for the thermocouples. The chamber is placed inside the tubular furnace—Al₂O₃ (C 530), Nabertherm RT 50-250/13—which is closed by two Macor plugs to avoid heat loss during the experiments. A simplified scheme of the device is shown in Figure II.6.

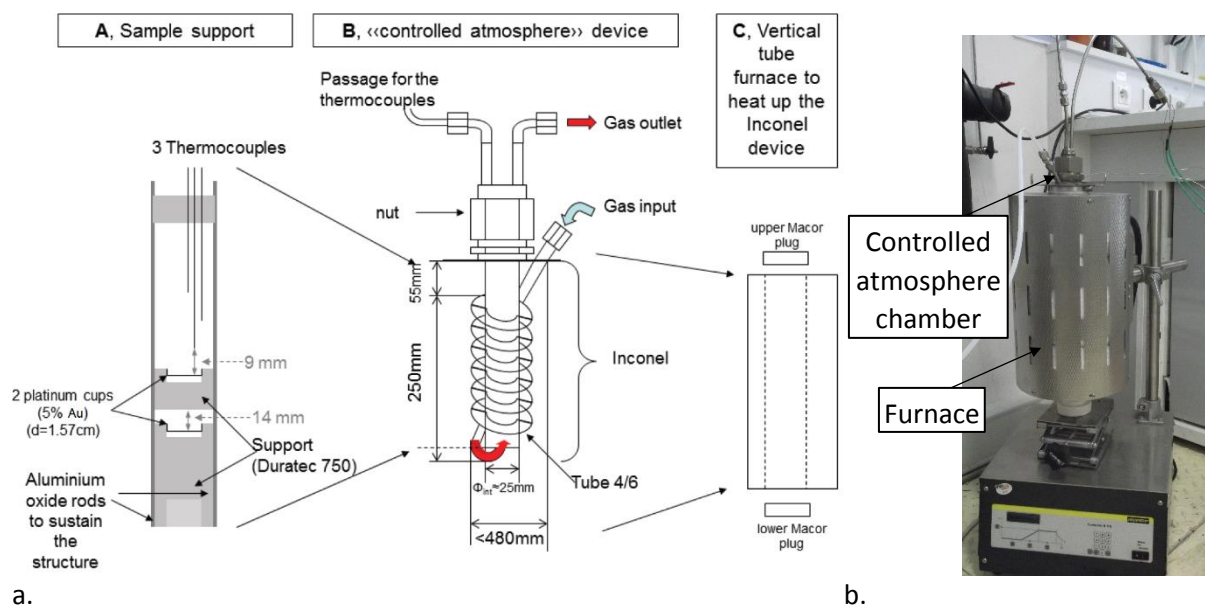


Figure II.6 | Laboratory furnace NEWMANIP a. scheme and b. picture.

The produced gases went through an electrostatic precipitator, two cold traps at $0\text{ }^{\circ}\text{C}$ and a cartridge filter in order to collect the condensable species. Incondensable gases are analyzed online (see 1.2.3.4).

During gasification tests, 200 mg of char were loaded into the device. This sample was heated at $24\text{ }^{\circ}\text{C}\cdot\text{min}^{-1}$ until $800\text{ }^{\circ}\text{C}$ under $0.33\text{ L}\cdot\text{min}^{-1}\text{ N}_2$. It was swept by N_2 for 30 min after the final temperature to ensure pyrolysis completion. Then, gas was switched to a mixture of 20 vol % H_2O in N_2 to start the gasification step. At the end of the experiment, the gas was switched back to pure N_2 and the sample was quenched by removing the controlled atmosphere chamber from the furnace and letting it cool down at room temperature.

1.2.3.3. Induction furnace PYRATES

The induction furnace PYRATES had initially been developed for high heating rate pyrolysis (Gauthier et al., 2013). It was used here to gasify char samples of a few grams. It consists of a mesh basket sample holder placed in a tube swept by the selected gas from below and heated by induction. A simplified scheme is presented in Figure II.7.

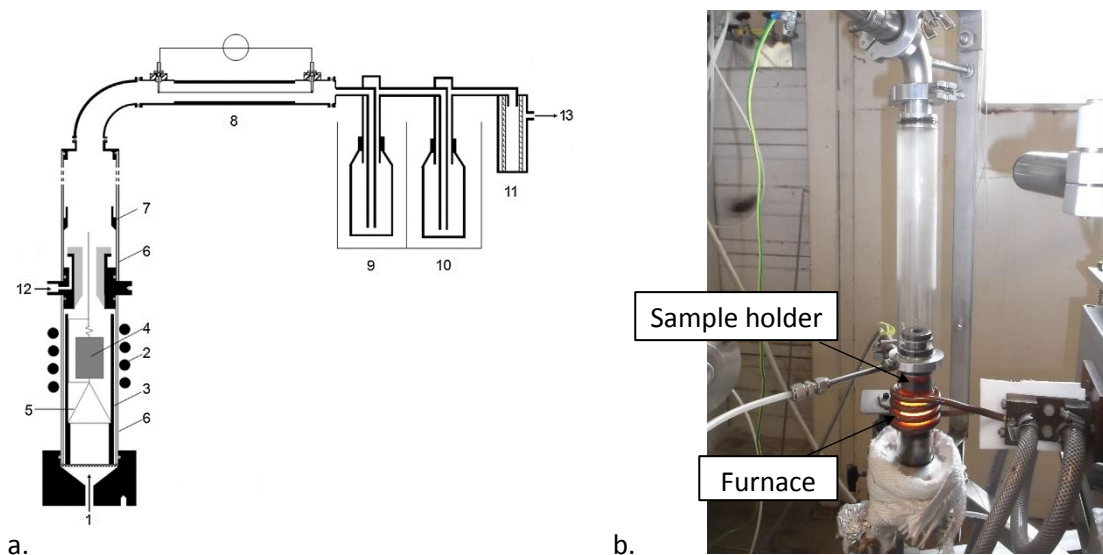


Figure II.7 | Induction furnace PYRATES a. scheme and b. picture. (1) Gas inlet; (2) Inductor; (3) Inconel pipe heated by induction; (4) Sample holder; (5) Metallic sample holder; (6) Quartz pipes; (7) Tar collector; (8) Electrostatic precipitator; (9) Ice trap (0 °C); (10) Isopropanol and dry ice trap (-78 °C); (11) Cartridge filter; (12) Secondary N₂ (cooling) inlet; (13) Gas outlet towards gas analysis.

To collect the condensable species, the produced gases go through an electrostatic precipitator, two cold traps at 0 °C and -78 °C respectively and a cartridge filter. The incondensable gases are analyzed online (see 1.2.3.4).

For the gasification experiments, a mass of 5 to 8 g was loaded into the sample holder. It was heated at 24 °C.min⁻¹ until 800 °C under 1 L.min⁻¹ N₂. It was swept by N₂ for 30 min after the final temperature was reached to ensure pyrolysis completion. Gas was then switched to a mixture of 20 vol % H₂O in N₂ to start the gasification step. The experiment ended when no more produced gas was detected.

1.2.3.4. Incondensable gas analysis and data treatment

For the laboratory furnace NEWMANIP and the induction furnace PYRATES, the reaction kinetics were measured through the incondensable gas analysis, contrarily to the TGA and macroTG where they were measured through the mass measurement.

Incondensable gases were analyzed continuously with two techniques: a Nicolet IR 550 FTIR analyzer and an Agilent 3000A micro-Gas Chromatograph (μGC) equipped with four columns (two 5 Å molecular sieves, one Poraplot U column and one CP wax column). An additional cold trap at 0 °C was placed before the μGC to protect it from humidity. The μGC took measurements every 220 seconds. The species quantified by both techniques were: CO, CO₂, CH₄, C₂H₂, C₂H₄ and CH₃OH. Additionally, H₂, C₂H₆, C₃H₈, C₆H₆, C₇H₈ and CH₃CH₂OH were quantified by μGC only and H₂O was quantified by FTIR only.

During gasification, the mass of tars was considered as negligible and the significant carbonaceous gases produced were CO, CO₂ and CH₄. Therefore, the carbon conversion was defined as:

$$X_C(t) = \frac{m_{CO}(t) + m_{CO_2}(t) + m_{CH_4}(t)}{m_{Ci}} \quad (\text{II.20})$$

where $m_{CO}(t)$, $m_{CO_2}(t)$ and $m_{CH_4}(t)$ are the masses at the time t of CO, CO₂ and CH₄ respectively and m_{Ci} is the initial mass of carbon.

The gasification rate and the average reactivity were calculated from Equations (II.18) and (II.19) similarly to the case of a solid conversion X .

1.3. Characterization techniques

Six different techniques were used to characterize the physical and chemical properties of the char samples: Raman spectroscopy, N_2 and CO_2 adsorption, temperature programmed desorption coupled to mass spectrometry (TPD–MS), inductively coupled plasma with atomic emission spectroscopy (ICP–AES), scanning electron microscopy coupled to energy dispersive X-ray spectroscopy (SEM–EDX) and powder X-ray diffraction (P-XRD). These techniques were combined to investigate the structure, porosity and surface chemistry of the carbon matrix of the chars as well as the content, structure and repartition of the inorganic compounds present in the chars. The techniques and the corresponding evaluated properties are listed in Table II.3 and described in details in the following subsections.

Table II.3 | Characterization techniques and the properties they measure.

Characterization technique	Measured property
Raman spectroscopy	Structure of the carbon matrix
N_2 and CO_2 adsorption	Porosity of the carbon matrix
TPD–MS	Surface chemistry of the carbon matrix
ICP–AES	Inorganic elemental composition
SEM–EDX	Morphology of the chars and surface elemental composition
P-XRD	Crystalline phases

1.3.1. Raman spectroscopy

Raman spectroscopy was used to study the structure of the char carbon matrix. Acquisition of the Raman spectra was performed with a BX40 LabRam, Jobin Yvon Horiba spectrometer in a backscattered configuration with a laser at 532 nm. For each sample a layer of the material was placed on a glass slide and Raman spectra was recorded at 9 locations.

The Raman spectra were analyzed as a combination of five bands corresponding to five carbonaceous structures (Chabalala et al., 2011; Guizani et al., 2016; Liu et al., 2015; Sadezky et al., 2005; Sheng, 2007):

- The G band at 1590 cm^{-1} is the only existing band for perfect graphite. It corresponds to the stretching vibration mode with E_{2g} symmetry in the aromatic layers of the graphite crystallite.
- The D1 band at 1350 cm^{-1} is related to graphene layers edges. It corresponds to graphitic lattice vibration mode with A_{1g} symmetry and in-plane imperfections such as defects and hetero-atoms.
- The D2 band at 1620 cm^{-1} is related to surface graphene layers. It corresponds to the stretching vibration mode with E_{2g} symmetry in the graphene layers which are not directly sandwiched between two other graphene layers.

- The D3 band at 1500 cm^{-1} is found in poorly organized materials. It corresponds to sp^2 carbons in amorphous structures (organic molecules, fragments, functional groups). It is suggested as being related to reactive sites.
- The D4 band at 1200 cm^{-1} is found in very poorly organized materials. It corresponds to sp^2 - sp^3 sites at the periphery of crystallites and to C-C and C=C stretching vibrations of polyene-like structures. It is suggested as being related to reactive sites.

Band fitting was carried out with the Origin software from OriginLab. An example of fitting is given for sample RHB_X0 in Figure II.8. Band intensity ratios were calculated with the intensity of each taken as the fitted area of the peak. Ratios of ID1/IG, ID2/IG, ID3/IG, ID4/IG, IG/IALL and ID3/IALL were calculated with ID1, ID2, ID3, ID4, IG and IALL the intensity of the bands D1, D2, D3, D4, G and the sum of the intensities of all bands respectively.

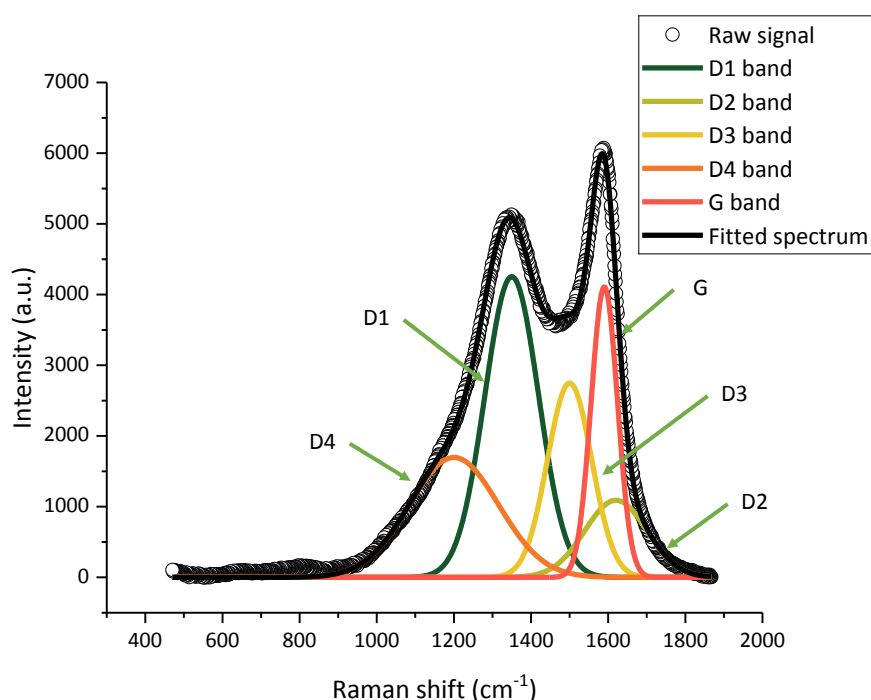


Figure II.8 | Raman band fitting example (sample RHB_X0).

In the Raman shift range of the spectra acquisition, peaks corresponding to some inorganic compounds could be recorded in addition to the carbon matrix bands. These peaks were identified by comparison to spectra from the Handbook of Minerals Raman Spectra (ENS Lyon, 2019).

1.3.2. N₂ and CO₂ adsorption

N₂ adsorption and CO₂ adsorption were used to characterize the porosity of the carbon matrix of the chars. The samples were outgassed overnight at 300 °C before the analyses. N₂ adsorption was conducted with a Micrometrics ASAP 2024 instrument at 77 K. CO₂ adsorption was conducted with a Micrometrics ASAP 2020 instrument at 273 K. For both adsorbable molecules, pore size distribution was determined with the density functional theory (DFT) model for slit pores with a finite depth. The porosity of the inorganic fraction of the chars was neglected. The results were then expressed in dry ash-free basis.

1.3.3. Temperature programmed desorption coupled to mass spectrometry

Temperature programmed desorption coupled to mass spectrometry (TPD–MS) was used to analyze the surface chemistry of the char carbon matrix. Approximately 10 mg of sample were placed in a quartz crucible. This crucible was introduced in a heated quartz tubular reactor connected to a vacuum pump and a mass spectrometer. The analysis consisted in two steps. First, the sample was outgassed by creating vacuum at ambient temperature. Then, the sample was heated to 800 °C at a rate of 5 °C/min and kept at this temperature for 30 min. The emitted gas CO₂, CO, H₂, H₂O, CH₄ and SO₂ were continuously quantified by mass spectrometry. The total pressure was also measured with a Bayard Alpert gauge. Mass balance was checked from these two measurements. For each gas, desorption was calculated by integrating the TPD–MS curves. The results were expressed in dry ash-free basis.

1.3.4. Inductively coupled plasma with atomic emission spectroscopy

Inductively coupled plasma with atomic emission spectroscopy (ICP–AES) was used to measure the inorganic elemental composition of the chars. The analysis was conducted after mineralization of the samples for all inorganic species, except for Si which underwent an alkaline melting. The measured elements were: Si, K, Ca, Mg, P, Na, Al and Fe. Measures could not be conducted on samples SFS_X50, both X75 and both X100 because of low quantities obtained after gasification tests. For samples X25 and X50, Na, Al and Fe were not measured.

Results are given as mass fractions C_i^{raw} or C_i^{char} for raw biomass or char, respectively. It corresponds to the mass of element in the sample divided by the mass of sample—the sample being either raw biomass or char.

These mass fractions were used to calculate the volatilization yield V_i^{char} of each element i by comparison with the raw biomass content. It was defined as follows:

$$V_i^{char} = \frac{C_i^{raw} - C_i^{char} \times \text{char yield}}{C_i^{raw}} \quad (\text{II.21})$$

These expressions rely on the char yields of each char samples. In the case of charM, the yield was directly measured during char production. In the case of X0 and Xn ($n = 25$ or 50) it was obtained from the following equations:

$$\text{X0} \quad \text{Char X0 yield} = \text{CharM yield} \times \text{Char X0 from charM yield} \quad (\text{II.22})$$

$$\text{Xn (n = 25 or 50)} \quad \text{Char Xn yield} = \text{Char X0 yield} \times \left(1 - \frac{n}{100}\right) \quad (\text{II.23})$$

where *Char X0 from charM yield* is the char yield between charM and X0 and is measured from TGA results.

The deviation of the mass fraction was calculated as $\pm 20\%$ from the repetition of the analysis on three samples of rice husks and sunflower seed shells. This is due to the combination of the measure uncertainty and of the biomass variability. The uncertainty on the char yield was obtained from the weighing precision and was of approximately 5%. From these values, the relative uncertainty $u(V_i^{char})$ of the measured volatilization was calculated:

$$\frac{u(V_i^{char})}{V_i^{char}} = \frac{u(C_i^{char})}{C_i^{char}} + \frac{u(\text{char yield})}{\text{char yield}} + \frac{u(C_i^{raw})}{C_i^{raw}} = 45\% \quad (\text{II.24})$$

1.3.5. Scanning electron microscopy coupled to energy dispersive X-ray spectroscopy

Scanning electron microscopy coupled to energy dispersive X-ray spectroscopy (SEM–EDX) was used to study the morphology of the chars and their surface elemental composition. A Philips XL30 microscope was used with a 15 kV electron beam. Secondary electrons (SE) as well as back-scattered electrons (BSE) detection were used. SE detection creates a contrast related to topology while BSE detection creates a contrast related to atomic number. Samples were placed on graphite tape and graphitized before analysis.

1.3.6. Powder X-ray diffraction

Powder X-ray diffraction (P-XRD) was used to identify the crystalline phases in the samples. It was carried out on a Panalytical X'Pert powder diffractometer equipped with a copper anode ($\lambda K\alpha_1=1.5406$ Å, $\lambda K\alpha_2=1.5444$ Å) and an X'Celerator 1D detector. It was configured in Bragg–Brentano geometry, with a variable divergence slit on the primary beam path and a set of anti-scattering slits positioned before and after the sample. Axial divergence was limited by 0.02 rad Soller slits. Samples were placed on zero background holders made from monocrystalline Si. Phase identification was done using the International Centre for Diffraction Data (ICDD) database on the Panalytical Highscore software.

2. Choice of the methodology

2.1. Choice of the biomass samples

The gasification kinetics of the seven raw biomass samples presented in Table II.1 were investigated through TGA in order to select two biomass species to examine deeply the inorganic elements effects. The evolution of the normalized ash free mass of the samples as a function of time is presented in Figure II.9 for both pyrolysis and gasification steps.

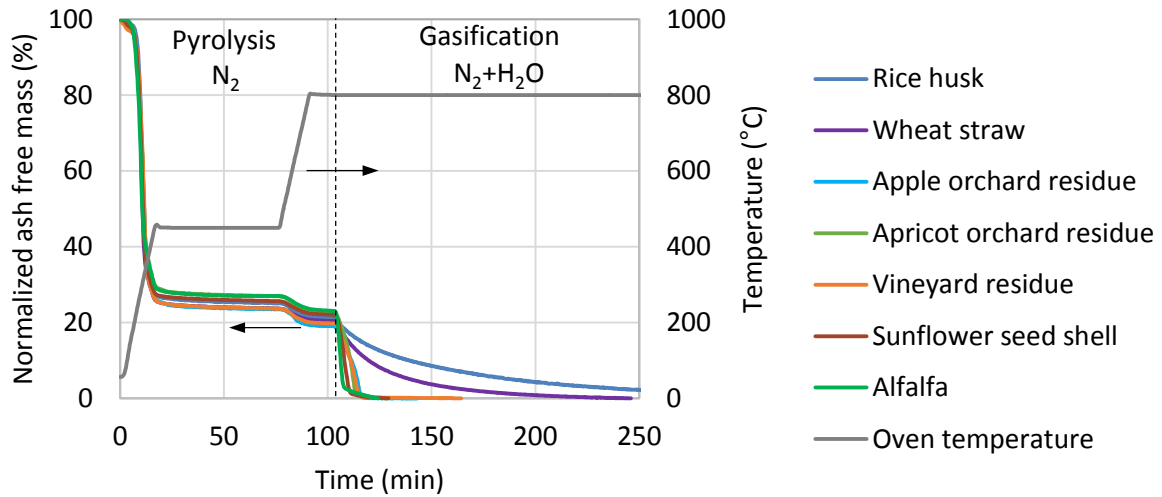


Figure II.9 | TGA of the raw biomass samples presented as the normalized ash free mass as a function of time.

The mass profiles obtained during the pyrolysis of biomass samples were very similar. The highest mass loss was observed for temperatures below 450 °C with approximately 75% of the mass volatilized. Subsequently, around 5% of the mass was lost between 450 °C and 800 °C. These yields are in agreement with literature (Anca-Couce, 2016).

The results of these experiments are presented during the gasification step and expressed as solid conversion in Figure II.10.

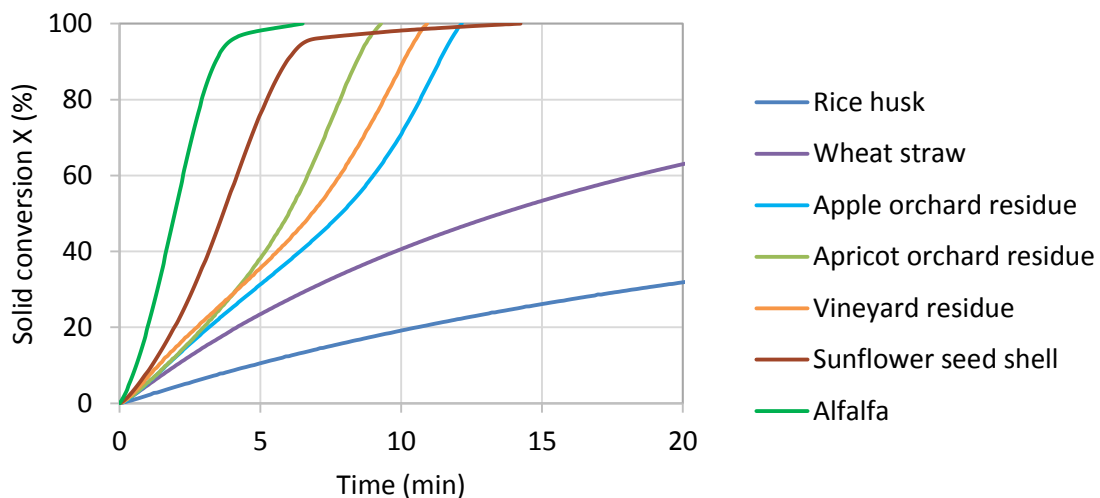


Figure II.10 | Solid conversion of biomass samples as a function of time during the gasification step.

Three families of behavior could be recognized, as identified in literature (Dupont et al., 2016):

- Family 1 had the highest conversion rate which was constant and then increased. It included apple orchard residue, apricot orchard residue and vineyard residue. These three biomass species were Ca-rich (Table II.1).
- Family 2 had the slowest conversion rate which was continuously decreasing. It included rice husks and wheat straw. These two biomass species were Si-rich (Table II.1).
- Family 3 had an intermediate conversion rate which was constant and then decreased. It included sunflower seed shells and alfalfa. These two biomass species were K-rich (Table II.1).

The average gasification reactivity was calculated for each species to quantify these differences in terms of gasification rate. The results are plotted in Figure II.11.

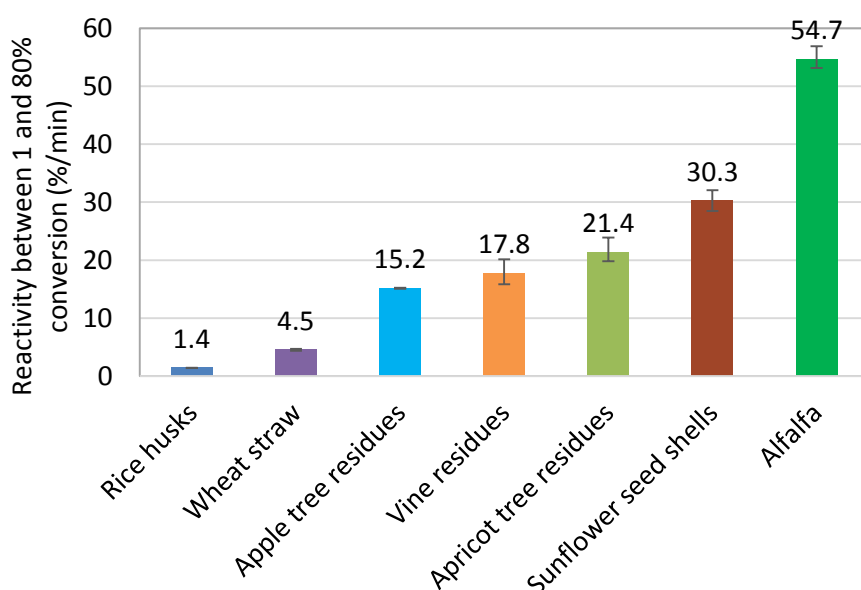


Figure II.11 | Gasification average reactivity of seven biomass samples from the database.

Substantial variations were found between the gasification reactivity of the samples with a factor of almost 50 between the average reactivities of rice husk—slowest sample to be gasified at $1.4 \text{ \%}\cdot\text{min}^{-1}$ —and alfalfa—fastest sample to be gasified at $54.7 \text{ \%}\cdot\text{min}^{-1}$. The corresponding gasification times were ranging from around five minutes for alfalfa to around five hours for rice husks. These results are in agreement with literature (Dupont et al., 2016; Hognon et al., 2014; Link et al., 2010; Romero Millán et al., 2019).

From these results, two biomass species were kept for further investigations:

- rice husk: family 2, slow gasification, Si-rich;
- sunflower seed shells: family 3, fast gasification, K-rich.

They were selected because they were:

- agricultural residues;
- different in terms of inorganic composition;
- significantly different in terms of gasification kinetics, i.e. gasification families.

2.2. Choice of the char production method

This section aims to verify if the char preparation method has an influence on the kinetics of the subsequent gasification and to decide how char will be produced in the rest of the work. This investigation has already been published (Dahou et al., 2018) and is reproduced in Annex B. The article provides data on two additional pyrolysis procedures. In addition to the present experimental results, it comprises an analysis of the characteristic times of the phenomena involved in the process. The characteristic time calculations showed that, for the pyrolysis step, the chemical regime was not reached. This could result in chars with different properties at the beginning of the gasification step and therefore different gasification kinetic behaviors. It was then necessary to check experimentally if the gasification kinetics of the chars produced in the pyrolysis furnace MATISSE were similar to those of the raw biomass samples presented in the previous section.

The results are presented in Figure II.12 as the solid conversion versus time for rice husks and sunflower seed shells.

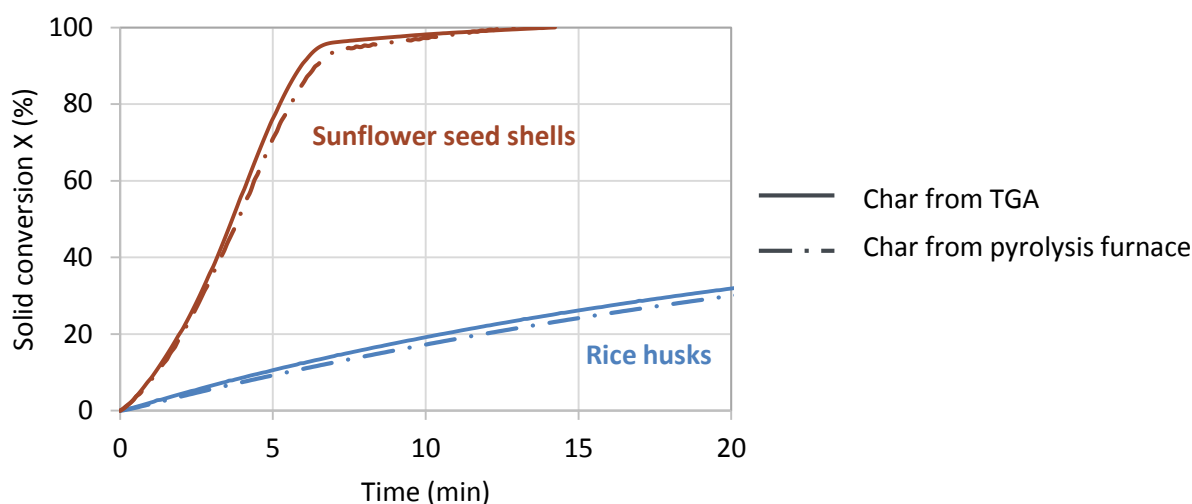


Figure II.12 | Gasification solid conversion as a function of time, for sunflower seed shells and rice husks, in the case of chars produced directly in the TGA (raw biomass) or in the pyrolysis furnace.

For each biomass, the char produced in the separate pyrolysis furnace had the same gasification kinetics as the char produced directly in the TGA from raw biomass.

This result confirms that producing the chars in a separate pyrolysis furnace to obtain large quantities does not affect the biomass species behavior during gasification. Therefore this procedure can be employed without compromising the results of the kinetic study.

Char samples obtained from pyrolysis of large quantities of biomass at 450 °C in the pyrolysis furnace are referred to as RHB_charM and SFS_charM for rice husks and sunflower seed shells, respectively.

2.3. Choice of the gasification device

As previously demonstrated, the chemical regime is reached in TGA. Therefore, TGA is the reference installation to measure the gasification kinetics of the chars. Nevertheless, TGA has the disadvantage of admitting less than 4 mg at once, which corresponds to even lower amounts of material after partial or complete gasification. Yet, to conduct characterizations on the residues, higher amounts were needed. The characteristic time analysis (Annex C) of the gasification step in the conditions of the TGA (4 mg) and of the induction furnace PYRATES (5 g) showed that the chemical regime was reached whatever the set-up. In this context, the present section aims to verify experimentally if the gasification conducted in devices at larger scale still respects the chemical regime established in TGA. To this end, the gasification average reactivities of rice husks and sunflower seed shells were measured in TGA, macroTG, laboratory furnace NEWMANIP (only for sunflower seed shells) and induction furnace PYRATES. Results are plotted in Figure II.13.

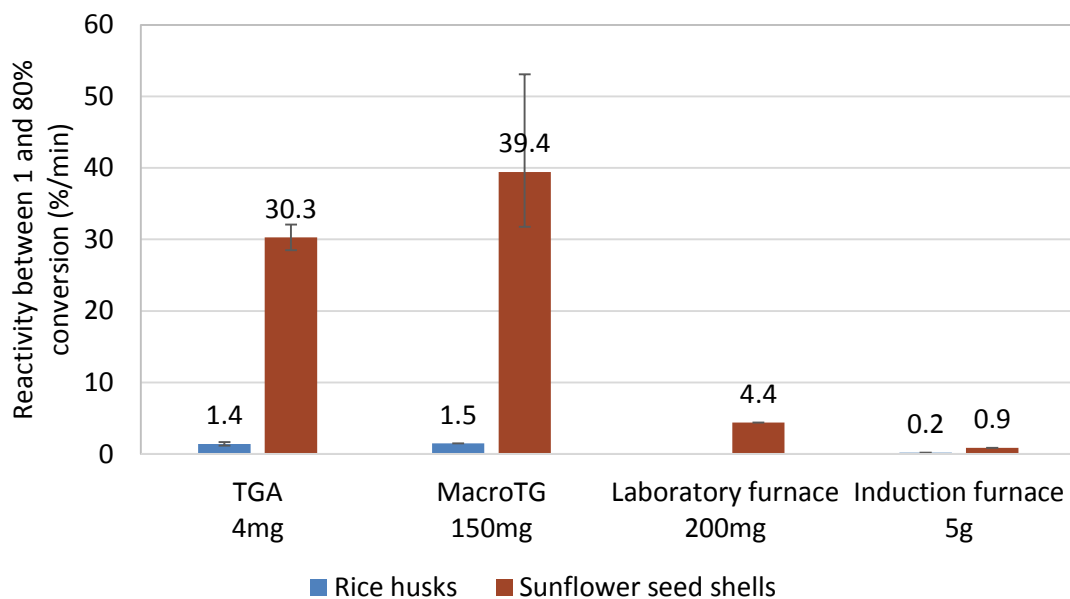


Figure II.13 | Measured gasification average reactivity of the two biomass samples in four different gasification installations.

First, it is important to note that the average reactivities presented here were calculated from conversion values obtained with different data depending on the gasification device. As shown previously, TGA and macroTG gave mass profiles and allowed to calculate solid conversions. The laboratory and induction furnaces did not allow to measure the total mass but a carbon conversion could be calculated from the analysis of the produced gases. However, most of the mass was converted to carbonaceous gases, therefore it was supposed that the reactivities obtained by the two methods were comparable.

Figure II.13 shows that only the macroTG gave results similar to TGA. The reactivities measured in the case of the laboratory and induction furnaces were substantially inferior. The decrease of the apparent reactivity was attributed to heat and mass transfer limitations, though no further investigation was conducted to verify this hypothesis. These results in disagreement with the characteristic time analysis showed the limit of such analysis that relies on parameters known with limited accuracy, such as the mass transfer coefficients.

The macroTG was therefore selected for char steam gasification in larger quantities than in the TGA. It allowed to gasify around 150 mg of char instead of only 4 mg while still operating in the chemical regime. This is of importance as it allowed to characterize the residues obtained in the same conditions as in the TGA.

Resulting samples are referred to as RHB_X100 and SFS_X100 for rice husks and sunflower seed shells, respectively. Samples stopped before steam injection—i.e. after only heating until 800 °C in N₂—are referred to as RHB_X0 and SFS_X0 for rice husks and sunflower seed shells, respectively.

From these experiments, the gasification time required to reach conversion values of X = 25%, 50% and 75% was determined for each biomass. Gasification of charM was then carried out until these conversion values. Resulting samples are referred to as RHB_X25, RHB_X50 and RHB_X75 for rice husks gasification until 25%, 50% and 75% conversion respectively, and SFS_X25, SFS_X50 and SFS_X75 for sunflower seed shells gasification until 25%, 50% and 75% conversion respectively.

The list of samples is summarized in Table II.4.

Table II.4 | List of samples obtained from pyrolysis and gasification of rice husks and sunflower seed shells

Sample production conditions	Rice husks	Sunflower seed shells
Char from pyrolysis at 450 °C	RHB_charM	SFS_charM
Char from pyrolysis at 800 °C, i.e. X = 0%	RHB_X0	SFS_X0
Char from gasification at 800 °C stopped at X = 25%	RHB_X25	SFS_X25
Char from gasification at 800 °C stopped at X = 50%	RHB_X50	SFS_X50
Char from gasification at 800 °C stopped at X = 75%	RHB_X75	SFS_X75
Ashes from gasification at 800 °C, i.e. X = 100%	RHB_X100	SFS_X100

2.4. Thermodynamic equilibrium simulation method

Thermodynamic equilibrium calculations were performed to simulate pyrolysis and gasification in the macroTG. It is well known that biomass gasification at temperatures below 1000 °C is kinetically limited regarding the formation of the gaseous species—CO, CO₂, CH₄, H₂ (Kersten et al., 2002). However, for inorganic species in the gas phase, no kinetic limitation has been reported so far except for NH₃ (Kilpinen et al., 1991). The calculations aim to estimate the behavior of the inorganic species, i.e. their volatilization and the fate of the gaseous and condensed phases.

The calculations were performed by minimization of the Gibbs free energy of the total system with the FactSage 7.2 software and the databases GTOX 5.0, FTSalt and FactPS (Bale et al., 2002; Hack et al., 2012). The initial composition of the system was taken as the mass of each element in the sample and the total mass of gas used in the experiment. The temperature was the same as the experimental conditions. All initial data are summarized in Table II.5. Data for X_n (n = 25, 50, 75 or 100) initial gas are detailed in Table II.6: the total gas was the sum of the pyrolysis gas (N₂) and of the gasification gas (mixture of 20vol% H₂O in N₂) for each species.

Table II.5 | Initial data for the thermodynamic equilibrium calculations.

Simulated sample	Temperature	Initial solid	Initial gas
CharM	450 °C	55 g raw rice husks or 40 g raw sunflower seed shells: composition in Table II.1	75 g N ₂ (1 L.min ⁻¹ , 60 min)
X0	800 °C	150 mg charM: composition in Table II.7 and Table II.8	25 g N ₂ (0.67 L.min ⁻¹ , 30 min)
Xn (n = 25, 50, 75 or 100)	800 °C	150 mg charM: composition in Table II.7 and Table II.8	See Table II.6

Table II.6 | Initial gas data for the thermodynamic equilibrium calculations of Xn (n= 25 to 75).

Conversion	Pyrolysis (all biomass species)	Rice husks gasification	Sunflower seed shells gasification
X25	25 g N ₂ (0.67 L.min ⁻¹ , 30 min)	10 g N ₂ + 1.6 g H ₂ O (0.67 L.min ⁻¹ , 15 min)	1 g N ₂ + 0.2 g H ₂ O (0.67 L.min ⁻¹ , 1.5 min)
X50		28 g N ₂ + 4.5 g H ₂ O (0.67 L.min ⁻¹ , 42 min)	2 g N ₂ + 0.3 g H ₂ O (0.67 L.min ⁻¹ , 2.9 min)
X75		62 g N ₂ + 10 g H ₂ O (0.67 L.min ⁻¹ , 93 min)	3 g N ₂ + 0.5 g H ₂ O (0.67 L.min ⁻¹ , 4.5 min)
X100		150 g N ₂ + 24 g H ₂ O (0.67 L.min ⁻¹ , 224 min)	6 g N ₂ + 1 g H ₂ O (0.67 L.min ⁻¹ , 8.8 min)

The simulation gave results in terms of phases and their composition. The calculated volatilization of each element could be obtained from the elemental composition of the gas phase calculated at equilibrium. The calculated volatilization for charM $V_{i\text{calc}}^{\text{charM}}$ was obtained directly (Equation (II.25)). The calculated volatilization $V_{i\text{calc}}^{\text{X0}}$ for X0 and $V_{i\text{calc}}^{\text{Xn}}$ for Xn (n = 25, 50, 75 or 100) depended on the measured volatilization for charM V_i^{charM} (Equation (II.26) and Equation (II.27) respectively). In the case where V_i^{charM} was negative, due to uncertainty, its value in the calculation was taken as 0.

$$\text{CharM} \quad V_{i \text{ calc}}^{\text{charM}} = \frac{m_{i \text{ calc}}^{\text{charM gas}}}{m_i^{\text{raw}}} \quad (\text{II.25})$$

$$\text{X0} \quad V_{i \text{ calc}}^{\text{X0}} = V_i^{\text{charM}} + (1 - V_i^{\text{charM}}) \times \frac{m_{i \text{ calc}}^{\text{X0 gas}}}{m_i^{\text{charM}}} \quad (\text{II.26})$$

$$\text{Xn (n = 25, 50, 75 or 100)} \quad V_{i \text{ calc}}^{\text{Xn}} = V_i^{\text{charM}} + (1 - V_i^{\text{charM}}) \times \frac{m_{i \text{ calc}}^{\text{Xn gas}}}{m_i^{\text{charM}}} \quad (\text{II.27})$$

with:

$m_{i \text{ calc}}^{\text{charM gas}}$ the calculated mass of element i in the gas phase for charM;

$m_{i \text{ calc}}^{\text{X0 gas}}$ the calculated mass of element i in the gas phase for X0;

$m_{i \text{ calc}}^{\text{Xn gas}}$ the calculated mass of element i in the gas phase for Xn (n = 25, 50, 75 or 100);

m_i^{raw} the measured mass of element i in the raw biomass;

m_i^{charM} the measured mass of element i in charM;

V_i^{charM} the measured volatilization of element i during charM production (0 if negative).

3. Results and discussion

The objective is to determine which parameter has the most influence on char steam gasification kinetics between the inorganic elements and the char morphology. To this end, this section presents the results of the char gasification and characterizations, as well as the corresponding thermodynamic equilibrium calculations. Both organic and inorganic fractions were investigated.

3.1. Gasification kinetic profiles

Gasification solid conversions of the chars produced from rice husks and sunflower seed shells in the macroTG are plotted versus time in Figure II.14 and Figure II.15. The profiles obtained through TGA are also plotted for comparison. Results are also plotted as the solid conversion rate versus the conversion in Figure II.16.

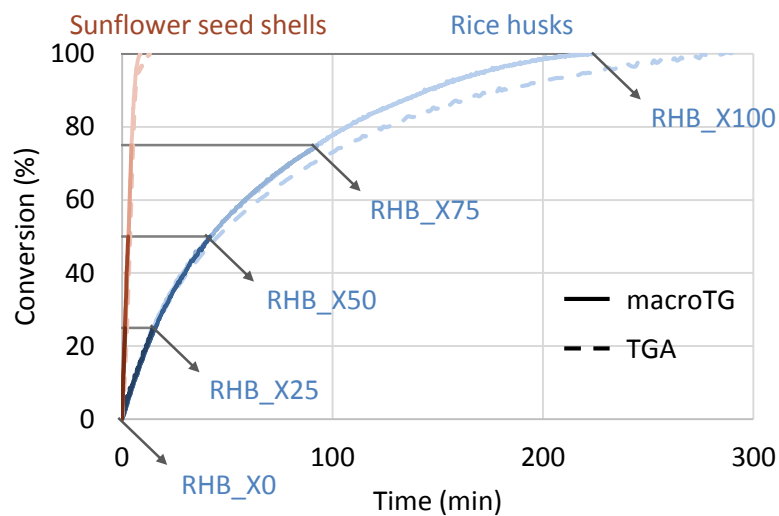


Figure II.14 | Gasification solid conversion of the rice husk and sunflower seed shell chars as a function of time.

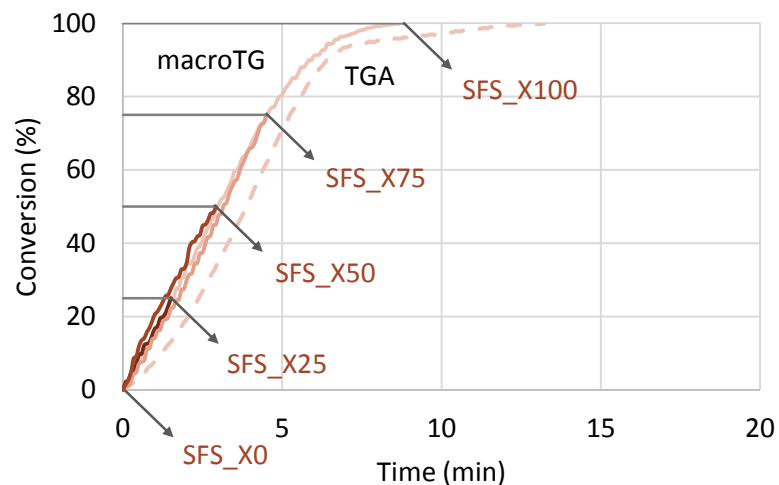


Figure II.15 | Zoom on the gasification solid conversion of the sunflower seed shell char as a function of time.

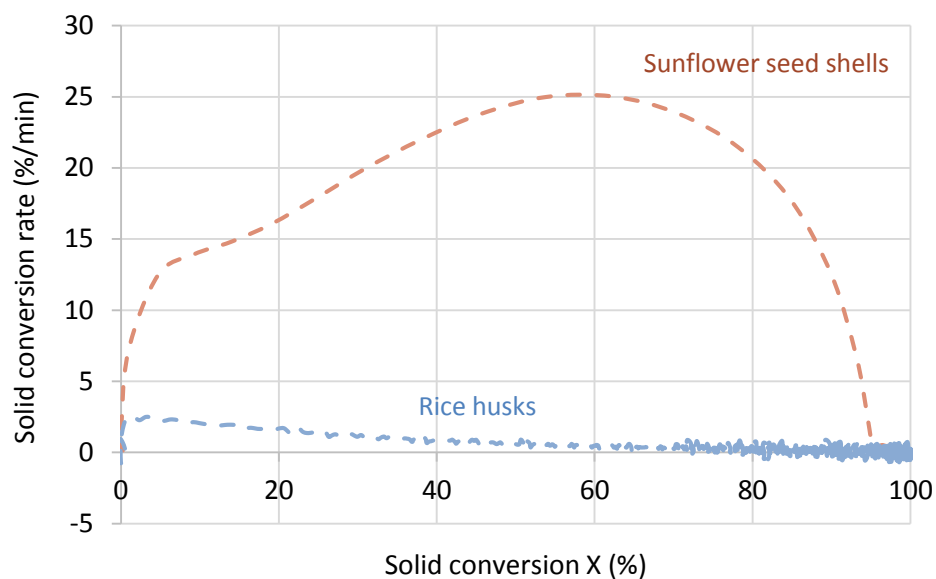


Figure II.16 | Solid conversion rate as a function of the conversion for rice husks and sunflower seed shells in the TGA.

For both biomass samples, their kinetic behavior in macroTG was similar to their behavior in TGA. Rice husks gasified slowly— $1.4 \text{ \%}\cdot\text{min}^{-1}$ (Figure II.11)—and had a decreasing gasification rate along conversion (Figure II.16). Sunflower seed shells gasified fast— $30.3 \text{ \%}\cdot\text{min}^{-1}$ (Figure II.11)—and had a gasification rate that decreased at high conversion values (Figure II.16).

Moreover, good repeatability was observed for each biomass in the macroTG. However, fast cooling could not be carried out which resulted in an additional mass loss under inert atmosphere. This additional mass loss was measured as 10-15% of the initial ash-free mass of rice husks and 20-25% of sunflower seed shells. This observation must be kept in mind when discussing the results of the sample characterizations.

For each biomass species, the ash content of the chars was calculated from raw biomass ash content and char yield. Results are presented at several steps of the pyrolysis and gasification process for rice husks and sunflower seed shells in Figure II.17. A schematic representation is also given in Figure II.18 for both biomass species and for a typical wood for comparison. The wood ash content and char yield come from Dupont *et al.* (Dupont et al., 2016).

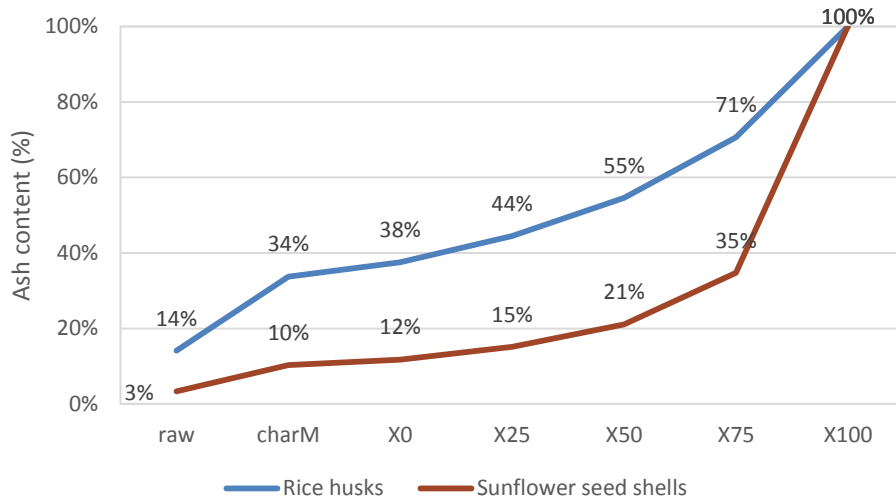


Figure II.17 | Evolution of the ash content during pyrolysis and gasification conversion of rice husk and sunflower seed shell chars.

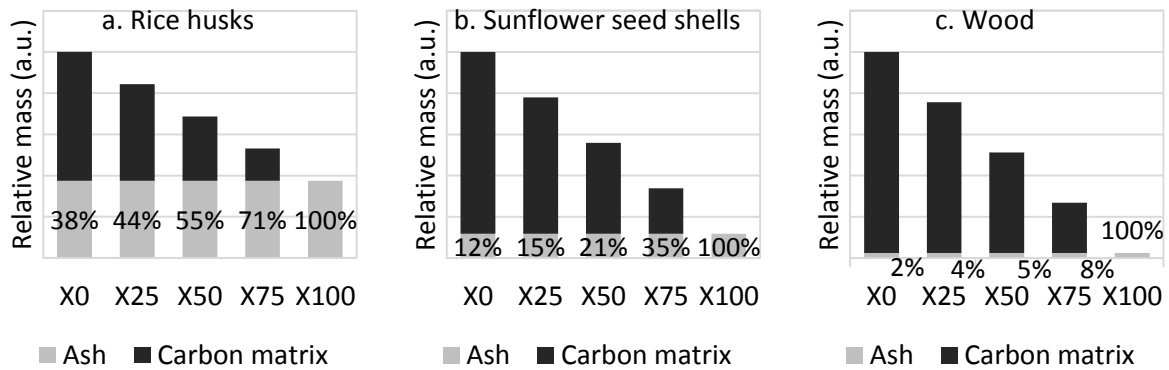


Figure II.18 | Schematic repartition of ash and carbon matrix at several gasification conversions from calculated values for a. rice husks, b. sunflower seed shells and c. a typical wood (beech from (Dupont et al., 2016)). Numbers correspond to the ash content.

From these results, it is easily seen that the inorganic fraction of the chars was non-negligible. In the case of rice husks it even quickly represented the majority of the sample mass. Some characterization techniques, such as N₂ and CO₂ adsorption and TPD–MS, only investigate the carbon matrix. In literature, these techniques are usually applied to samples with a low ash content and the results are expressed in dry char basis, which includes the negligible ashes. However, in the present work, it is not relevant to apply these techniques to the whole char. Therefore, the N₂ and CO₂ adsorption and TPD–MS results were expressed in dry ash-free basis.

3.2. Results of the characterization of the char carbon matrix

The aim of this section is to investigate if the properties of the carbon matrix of the chars can explain the difference in terms of reactivity observed between the two biomass species. It presents the results of the analysis of three physical properties of the carbon matrix: its structure, its porosity and its surface chemistry.

3.2.1. Structure of the carbon matrix

The structure of the char carbon matrix was investigated through Raman spectroscopy. Typical Raman spectra obtained for rice husk and sunflower seed shell chars are presented in Figure II.19 and Figure II.20, respectively. To allow comparison, intensities were normalized by setting the maximum intensity—at the Raman shift of the center of the G band—to 1.

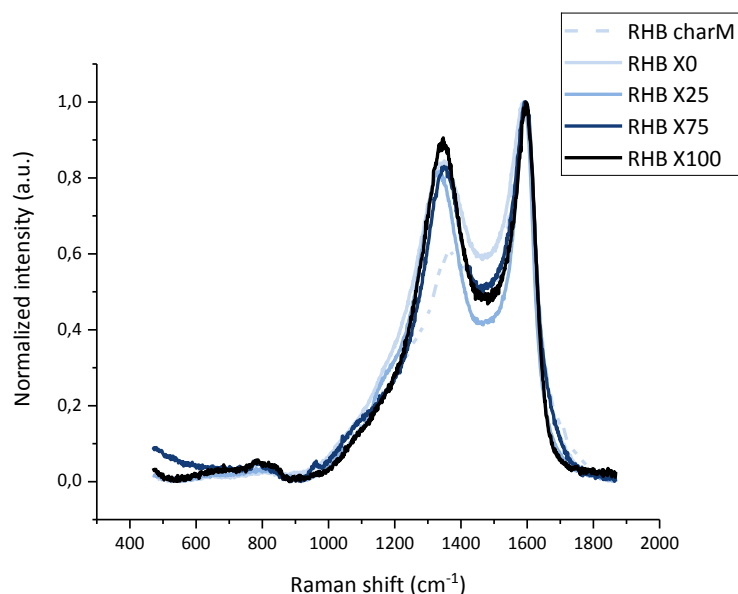


Figure II.19 | Normalized Raman spectra of rice husk chars at several pyrolysis and gasification conversions.

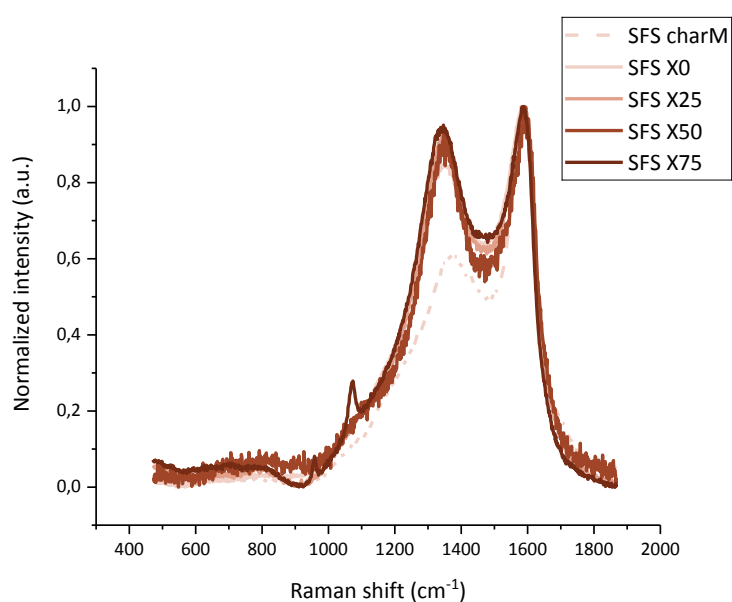


Figure II.20 | Normalized Raman spectra of sunflower seed shell chars at several pyrolysis and gasification conversions.

Carbon could still be detected in sample RHB_X100 which indicates that gasification was not completely carried out until completion.

The Raman spectra analysis was supplemented by the calculation of peak intensity ratios. The evolution of the peak intensity ratios during conversion is shown in Figure II.21.

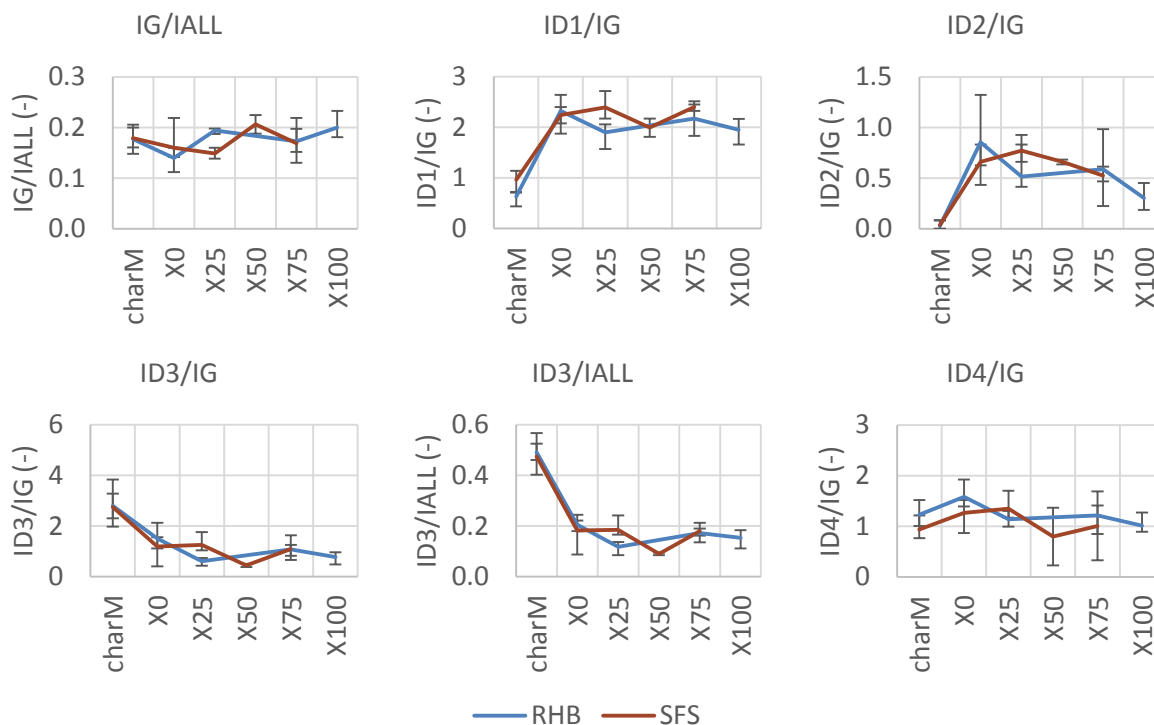


Figure II.21 | Evolution of the peak intensity ratios during pyrolysis and gasification conversion of rice husk and sunflower seed shell chars.

For both biomass samples, the only noticeable changes occurred when the pyrolysis temperature increased from 450 °C (charM) to 800 °C (X0). When the pyrolysis temperature increased there was an increase of the D1 and D2 band intensities and a decrease of the D3 band intensity. This suggests that the amorphous carbon structures became more organized and formed graphene layers. The latter seemed to be independent and not to stack on top of each other. This is in accordance with literature observations for biomass and coal chars (Guizani et al., 2017; Wang et al., 2016; Zhao et al., 2016). For instance, Guizani *et al.* (Guizani et al., 2017) acquired the Raman spectra of chars from beech wood produced by pyrolysis at temperatures ranging from 500 to 1400 °C. They concluded that the chars became more ordered—with a condensation of the aromatic ring structures—when the preparation temperature increased.

No significant difference could be observed between the spectra acquired at various gasification conversion rates. Variations were in the range of the measurement uncertainty and were significantly inferior to the variations between the two pyrolysis temperatures. Some authors observed that steam injection could induce the condensation of aromatic ring structures that were merged into larger ones (Guizani et al., 2016; Lv et al., 2018). Such a conclusion could not be drawn from the results of the present work.

More importantly, when comparing the two biomass samples at each conversion value, no significant difference could be observed either. **This result shows that the structural properties of the carbon matrix of the chars do not explain the difference in gasification reactivity that exists between the two types of biomass.**

3.2.2. Porosity of the carbon matrix

The porosity of the carbon matrix was first investigated through N_2 adsorption. N_2 adsorption isotherms of rice husk and sunflower seed shell chars during pyrolysis and gasification conversion are presented in Figure II.22.

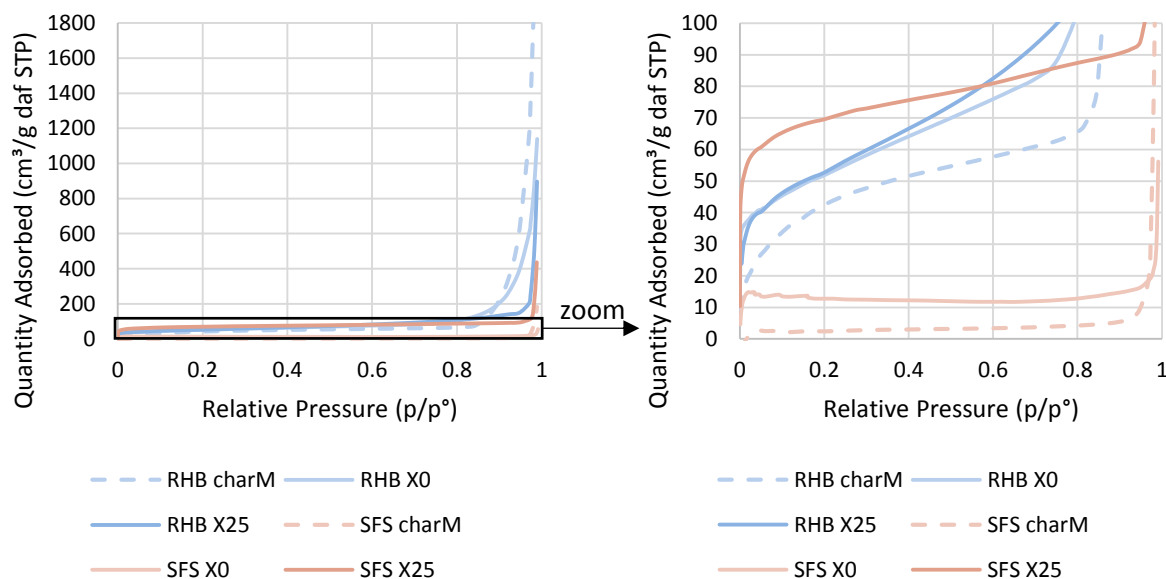


Figure II.22 | N_2 adsorption isotherms of rice husk and sunflower seed shell chars at several pyrolysis and gasification conversions.

N_2 adsorption isotherms could not be obtained for chars from gasification at 50% conversion and above for either biomass indicating no or small porosity. Isotherms obtained from N_2 adsorption on chars from pyrolysis and gasification at 25% conversion were IUPAC type I (Thommes et al., 2015) indicating that the char samples were mainly microporous for both biomass types.

N_2 adsorption can only measure large micropores (1-2 nm), mesopores (2-50 nm) and macropores (>50 nm). Therefore a more narrow porosity, i.e. ultramicroporosity (<1 nm), was evaluated through CO_2 adsorption as the CO_2 molecule (0.33 nm) is smaller than the N_2 molecule (0.36 nm) (Tascón, 2012). Results for both biomass types are presented in Figure II.23.

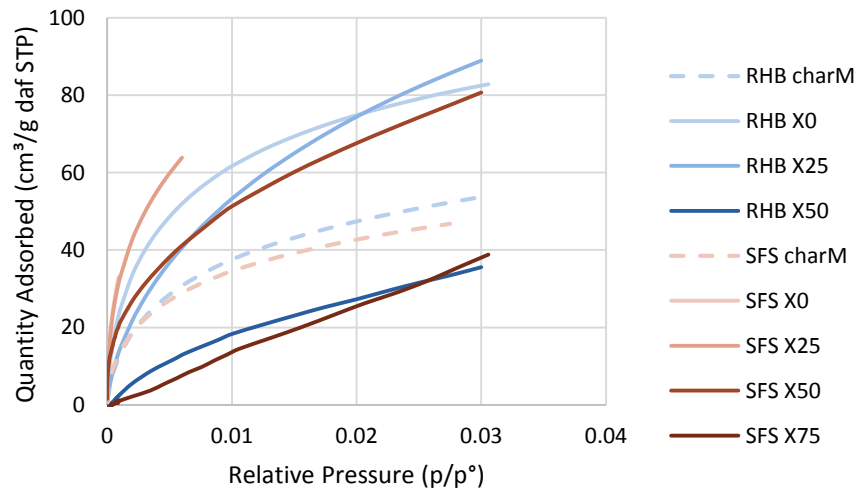


Figure II.23 | CO₂ adsorption isotherms of rice husk and sunflower seed shell chars at several pyrolysis and gasification conversions.

Resulting N₂ and CO₂ adsorption isotherms were analyzed using the DFT model to obtain a pore size distribution for each sample. It is presented in Figure II.24 expressed in terms of incremental area, with a focus on narrow pores measured from CO₂ adsorption in Figure II.25. The results expressed in terms of incremental volume are presented in Annex D.

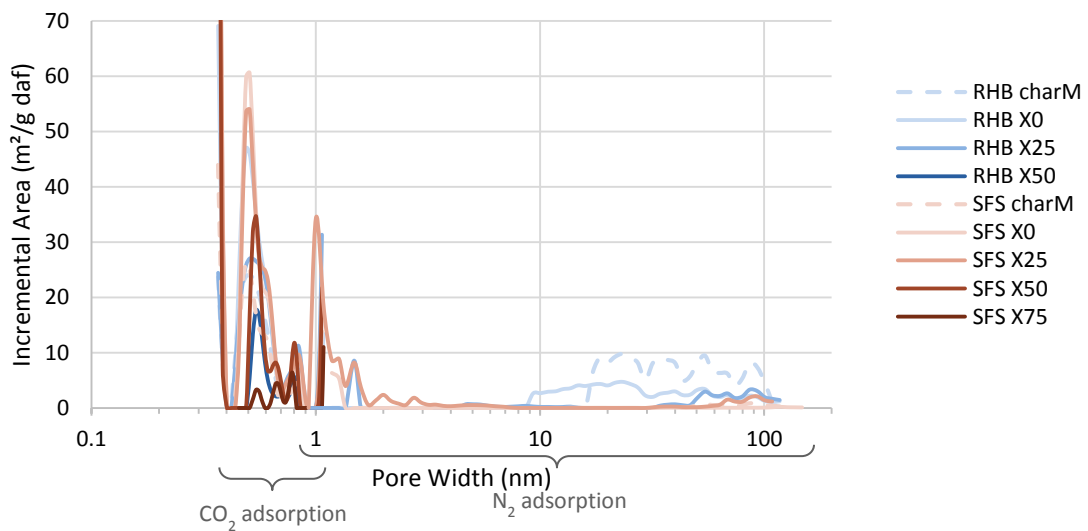


Figure II.24 | Pore size distribution using DFT model from N₂ and CO₂ adsorption isotherms of rice husk and sunflower seed shell chars at several pyrolysis and gasification conversions expressed in terms of incremental area.

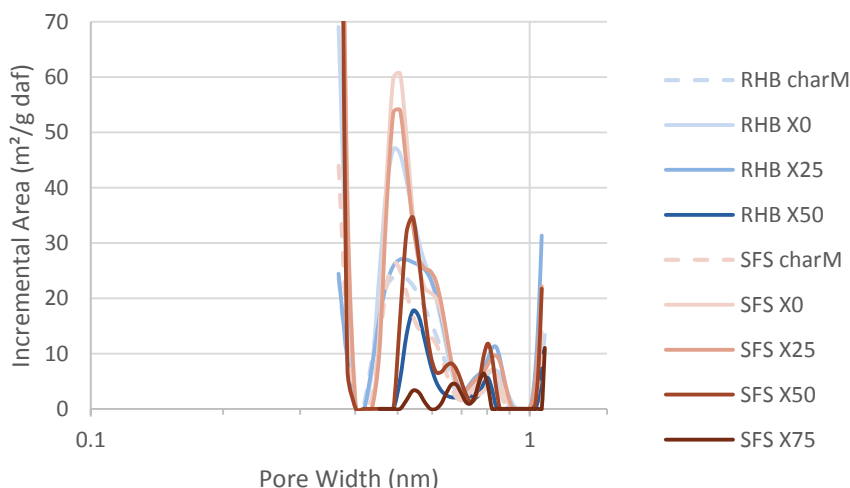


Figure II.25 | Ultramicropore size distribution using DFT model from CO₂ adsorption isotherms of rice husk and sunflower seed shell chars at several pyrolysis and gasification conversions expressed in terms of incremental area.

For both biomass types, when the pyrolysis temperature increased from 450 °C (charM) to 800 °C (X0), the ultramicroporosity (< 1 nm) area increased and there was no or low wider porosity. This corresponds to the opening of new ultramicropores during the devolatilization. During gasification, the ultramicroporosity area decreased in favor of wider microporosity (around 1 nm), while mesoporosity and macroporosity remained low. This behavior suggests a coalescence of the ultramicropores into wider micropores during the char interaction with the gasifying agent. To our knowledge, there is no study available on the evolution during gasification of the ultramicroporosity measured by CO₂ adsorption in the gasification literature. However, this technique is in use in the field of activated carbons. The physical activation process is equivalent to a gasification. The results obtained in the present study are in accordance with the observations reported in the activated carbon literature (Rodríguez-Reinoso et al., 1995). In particular, Rodríguez-Reinoso *et al.* concluded that “water vapor widens the microporosity from the early stages of the [physical activation] process”.

When comparing biomass types, for the chars from pyrolysis charM and X0, sunflower seed shells and rice husks had similar micro- and ultramicroporosity areas. Rice husks had a higher macroporosity area, though it remained low (Figure II.24). For the chars from gasification, the ultramicroporosity area of rice husks (slow gasifying biomass) was lower than sunflower seed shells (fast gasifying biomass)—almost half. Their wider porosity was similar. This difference in terms of ultramicroporosity could be linked to the difference in terms of gasification reactivity. Indeed, a lower ultramicroporosity area in the case of rice husks could be related to their slower gasification due to a reduced reacting surface. However, the ultramicroporosity of both biomass chars at steam injection—i.e. X0 samples—were similar and the differences only occurred during gasification (Figure II.25). **This indicates that the porosity properties are not the cause of the differences between the gasification reactivities of the biomass samples but rather a consequence of another mechanism.**

3.2.3. Surface chemistry of the carbon matrix

The surface chemistry of the carbon matrix was characterized through TPD–MS. Cumulative gas desorption between 24 and 800 °C during TPD–MS of rice husk and sunflower seed shell chars at several pyrolysis and gasification conversions is presented in Figure II.26. Samples SFS_X50 and SFS_X75 could not be analyzed due to low char amounts.

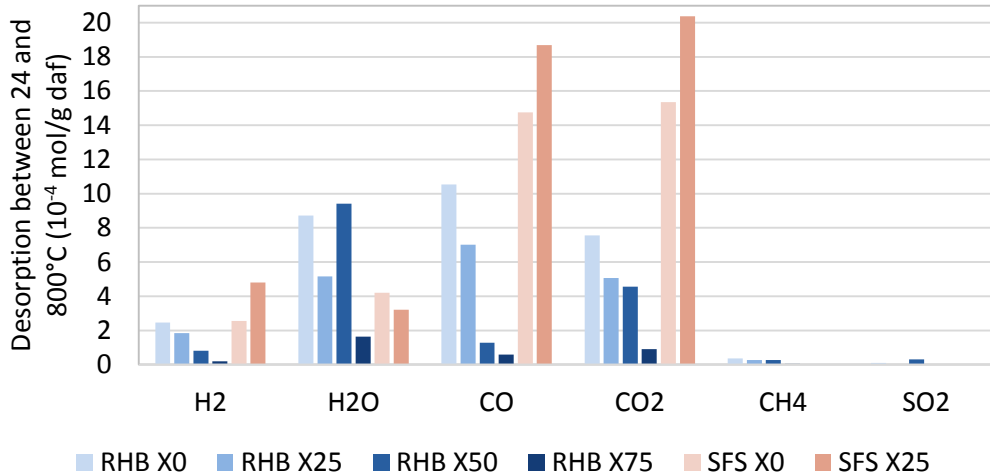


Figure II.26 | Cumulative gas desorption between 24 and 800 °C during TPD–MS of rice husk and sunflower seed shell chars at several gasification conversions.

Sunflower seed shell chars released much more CO and CO₂ than rice husk chars. Another noticeable difference between the two biomass types was the gas desorption evolution during gasification conversion. For rice husk chars gas desorption decreased during conversion, except H₂O, while for sunflower seed shell chars it seemed to increase, except for H₂O. In addition, a slight desorption of CH₄ and SO₂ was observed for rice husks but not for sunflower seed shells. Both biomass species had the same S content (Table II.1). Therefore, this TPD-MS result indicate that this element occurred in a different form in both biomass species and behaved differently.

The detail of the desorption of each released gas as a function of temperature is presented in Figure II.27 to Figure II.32 at several pyrolysis and gasification conversions for the two biomass types. It is to be noted that the scale of desorption rate is different for each desorbed gas.

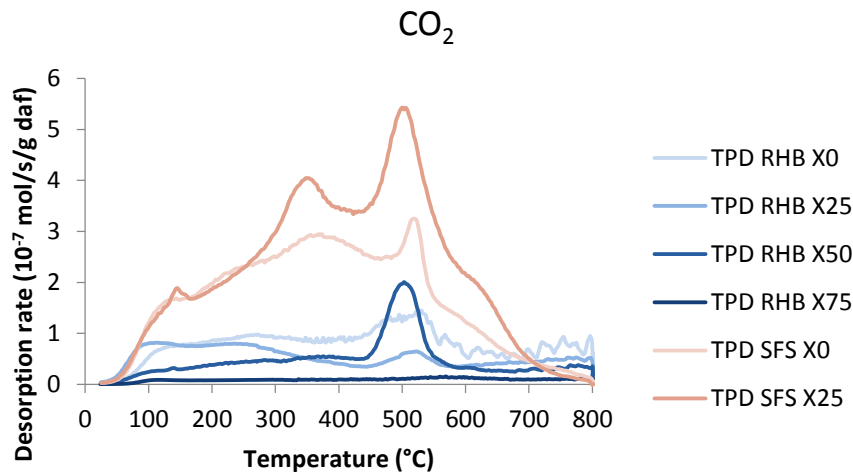


Figure II.27 | CO₂ desorption during TPD–MS of rice husk and sunflower seed shell chars at several pyrolysis and gasification conversions.

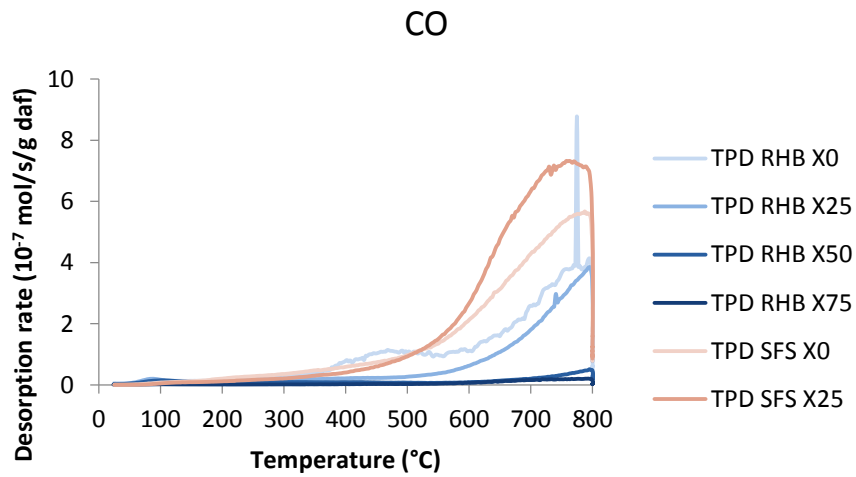


Figure II.28 | CO desorption during TPD–MS of rice husk and sunflower seed shell chars at several pyrolysis and gasification conversions.

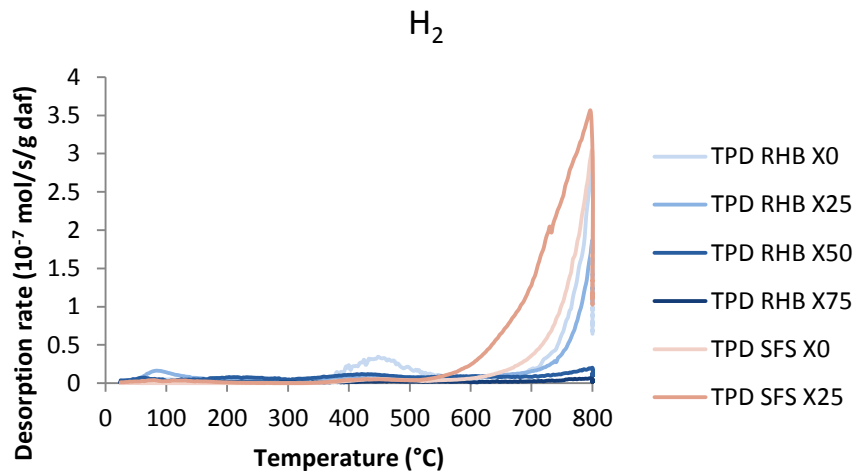


Figure II.29 | H₂ desorption during TPD–MS of rice husk and sunflower seed shell chars at several pyrolysis and gasification conversions.

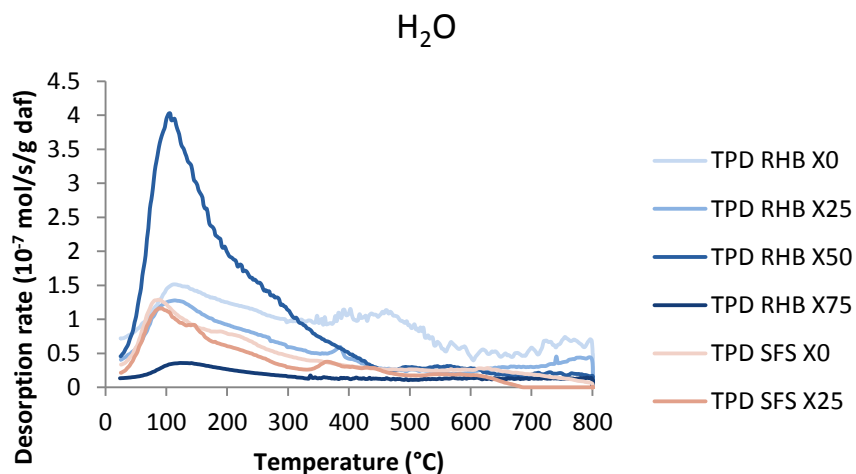


Figure II.30 | H₂O desorption during TPD–MS of rice husk and sunflower seed shell chars at several pyrolysis and gasification conversions.

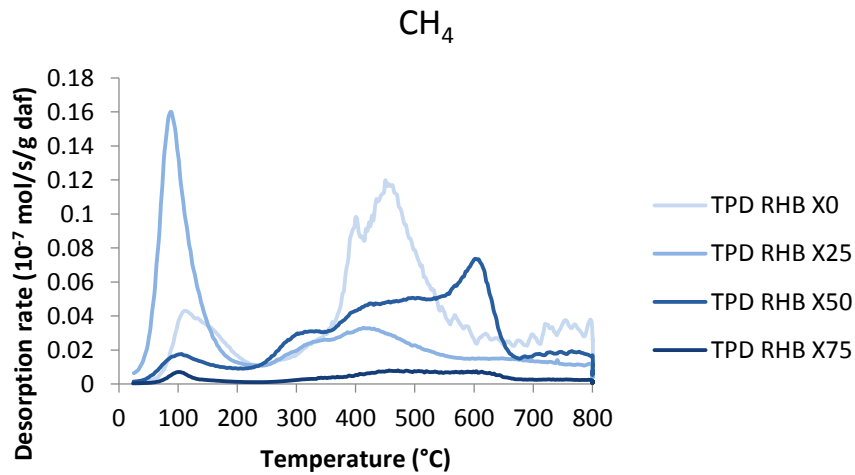


Figure II.31 | CH_4 desorption during TPD–MS of rice husk and sunflower seed shell chars at several pyrolysis and gasification conversions.

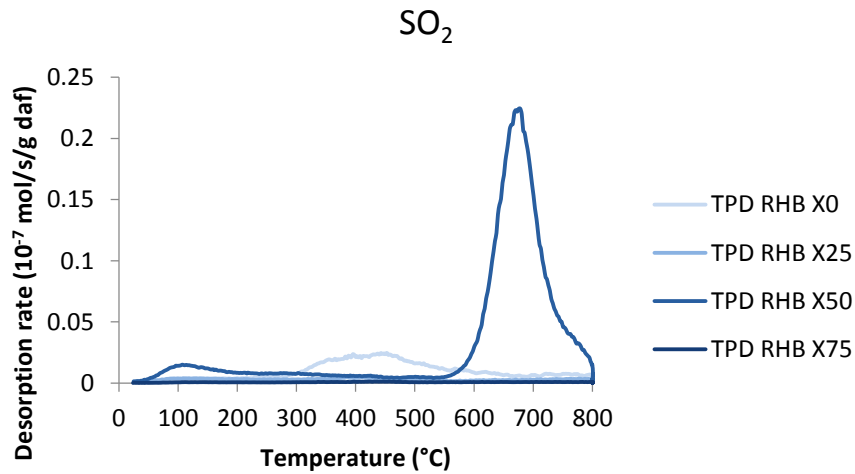


Figure II.32 | SO_2 desorption during TPD–MS of rice husk and sunflower seed shell chars at several pyrolysis and gasification conversions.

Desorption was of the same order of magnitude and occurred around the same temperatures as what has been observed in literature for gasification chars (Guizani et al., 2016).

Desorption peaks and bands of sunflower seed shell chars were higher than rice husk chars ones as seen with cumulative gas desorption results (Figure II.26). The gases desorption is due to the decomposition of the carbon surface groups (Figure II.33) that occur on specific temperature ranges. Desorption occurred at the same temperatures for both biomass types. Therefore the functional groups in chars from both biomass types were similar. Functional groups also remained similar along gasification conversion.

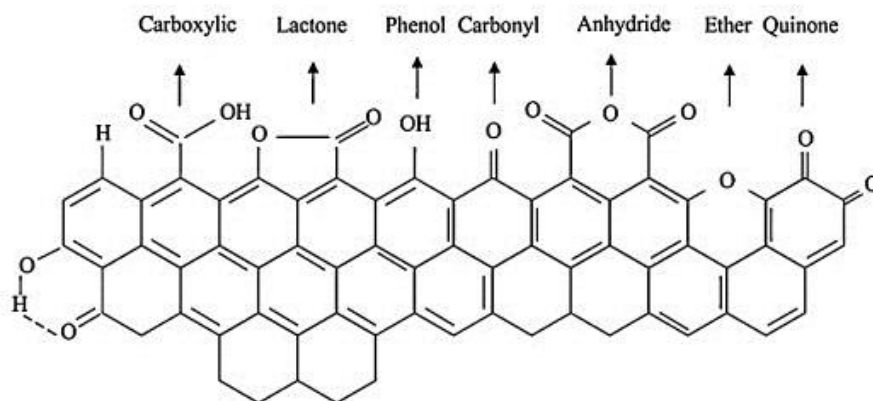


Figure II.33 | Carbon surface groups. Reprinted from (Shafeeyan et al., 2010) with permission from Elsevier.

At low temperature—i.e. below 400 °C, CO₂ and H₂O were released (Figure II.27 and Figure II.30). It corresponds to the decomposition of carboxyles. They either directly decomposed to CO₂ or dehydrated to form lactones and anhydrides (Figueiredo et al., 1999; Guizani et al., 2016). These groups then decomposed to CO₂, as well as CO for anhydrides, until around 600 °C (Figure II.27 and Figure II.28). Then CO was produced at higher temperatures (Figure II.28). It resulted from the decomposition of ethers, phenol, carbonyls and quinones (Figueiredo et al., 1999; Guizani et al., 2016). H₂ was also observed at high temperatures—i.e. above 700 °C (Figure II.29). It originated in the thermal decomposition of C – H bonds (Guizani et al., 2016).

In conclusion, the only difference between the two biomass types was the concentration—and not the nature—of surface functions, with a higher concentration in the case of sunflower seed shell chars. This evolution of this property follows the evolution of the microporosity: sunflower seed shells also have a higher microporosity. The similar evolution of the microporosity and of the surface functions concentration has also been observed in literature. For example, Arriagada *et al.* conducted the steam gasification of peach stones and observed the increase of its microporosity as well as the increase of the number of oxygen surface groups along conversion (Arriagada et al., 1997).

3.2.4. Conclusions on the carbon matrix properties

The characterization of the physical properties of the carbon matrix of chars produced at several gasification conversion values did not provide direct explanations regarding the difference between the gasification reactivities of the two studied biomass species.

The carbon structure measured with Raman spectroscopy was similar for the two biomass species. The microporosity of the two pyrolysis chars just before steam injection was also similar for the two biomass species. Therefore, these properties do not justify the observed reactivity difference.

However, during steam gasification the microporosity and the quantity of surface functions became higher in the case of sunflower seed shell chars, which was the fast gasifying biomass. This suggests that the evolution of these properties was not the cause of the higher reactivity but rather a consequence of another catalytic mechanism.

3.3. Results of the characterization of the inorganic fraction of the chars

The aim of this section is to determine not only the elements that form the inorganic fraction but how they are organized in compounds. It presents the results of the characterizations conducted on the inorganic fraction of the chars. They were supported by calculations to simulate the samples behavior at thermodynamic equilibrium. First, the volatilization of the inorganic elements was investigated. Then, the inorganic fraction was characterized by SEM-EDX, P-XRD and Raman at several gasification conversion values and the results were compared to calculations at thermodynamic equilibrium.

3.3.1. Volatilization of the inorganic elements

The volatilization of the inorganic elements contained in the biomass and chars during thermochemical treatment was investigated. First, the samples were simulated at thermodynamic equilibrium. Then, these calculated results were compared to measured values. Due to low amounts of material, measured values were not available at high conversion values.

The inorganic elemental composition of the charM, X0, X25 and X50 samples was analyzed by ICP–AES. Results are presented in Table II.7 and Table II.8 for rice husks and sunflower seed shells respectively, and compared to raw biomass values. From these measurements, the measured volatilization of the three main inorganic elements of each biomass species during pyrolysis was obtained (Equation (II.21)). Values are given in Table II.9.

Table II.7 | Inorganic element content and char yield of raw, charM, X0, X25 and X50 rice husk samples (in dry basis).

Sample	Raw RHB	RHB charM	RHB X0	RHB X25	RHB X50	
Char yield (%)	100	42	38**	28***	14***	
C	} (wt%)	41.6	57.1	—	—	
H		5.2	3.3	—	—	
O*		45.1	23	—	—	
N		0.5	0.8	—	—	
S	} (mg.kg ⁻¹)	1000	1840	—	—	
Cl		1016	325	—	—	
Si		63955	130000	141000	199000	411000
K		5822	15000	17000	23000	48000
Ca		1797	4000	4000	7000	12000
Mg		659	1000	2000	2000	4000
P		981	2000	2000	2000	5000
Na		413	<1000	<1000	—	—
Al	228	<1000	<1000	—	—	
Fe	192	1000	<1000	—	—	
Main inorganic elements	Si – K – Ca	—	—	—	—	

*Total (i.e. organic and inorganic) oxygen calculated by difference with all other elements.

**Calculated from Equation (II.22) with *Char X0 from charM yield = 90%* measured from TGA results.

***Calculated from Equation (II.23).

Table II.8 | Inorganic element content and char yield of raw, charM, X0, X25 and X50 sunflower seed shell samples (in dry basis).

Sample	Raw SFS	SFS charM	SFS X0	SFS X25	SFS X50	
Char yield (%)	100	32	28**	21***	11***	
C	} (wt%)	50.2	76.6	—	—	
H		6.5	3.8	—	—	
O*		40.6	12.4	—	—	
N		0.7	1.2	—	—	
S	} (mg.kg ⁻¹)	1000	1180	—	—	
Cl		1000	959	—	—	
Si		194	<1000	19000	<1000	10000
K		9729	27000	29000	15000	20000
Ca		4489	13000	14000	15000	<1000
Mg		1838	6000	6000	6000	28000
P		896	3000	2000	2000	6000
Na		9	<1000	2000	—	—
Al		150	<1000	2000	—	—
Fe		1099	5000	5000	—	—
Main inorganic elements	K – Ca – Mg	—	—	—	—	

*Total (i.e. organic and inorganic) oxygen calculated by difference with all other elements.

**Calculated from Equation (II.22) with *Char X0 from charM yield* = 88% measured from TGA results.

***Calculated from Equation (II.23).

Table II.9 | Volatilization of the inorganic elements measured for raw biomass, charM, X0, X25 and X50 for both species.

Volatilization	RHB				SFS			
	charM	X0	X25	X50	charM	X0	X25	X50
S	23%	—	—	—	62%	—	—	—
Cl	87%	—	—	—	69%	—	—	—
Si	15%	17%	12%	9%	—	—	—	—
K	-8%	-10%	-11%	-16%	11%	16%	68%	78%
Ca	7%	16%	-10%	6%	7%	12%	30%	98%
Mg	—	—	—	—	-4%	8%	31%	-60%

These experimental results are discussed in the following subsections. They are complemented with results from calculations at thermodynamic equilibrium. An example of the detailed results from calculations is given in Annex E for each biomass species.

3.3.1.1. Volatilization of S and Cl

The S and Cl volatilization results, both calculated and measured, are presented in Figure II.34 and Figure II.35 for rice husks and sunflower seed shells, respectively.

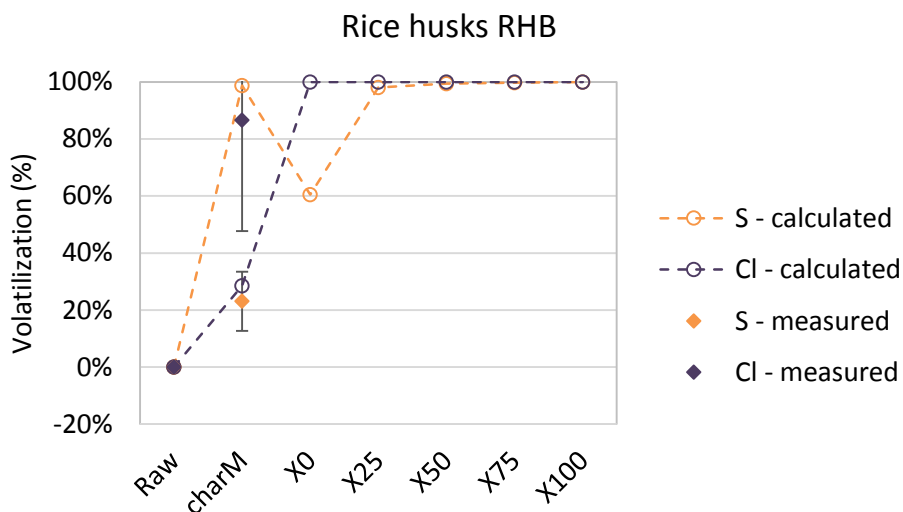


Figure II.34 | Calculated and measured volatilization of S and Cl in the rice husk samples.

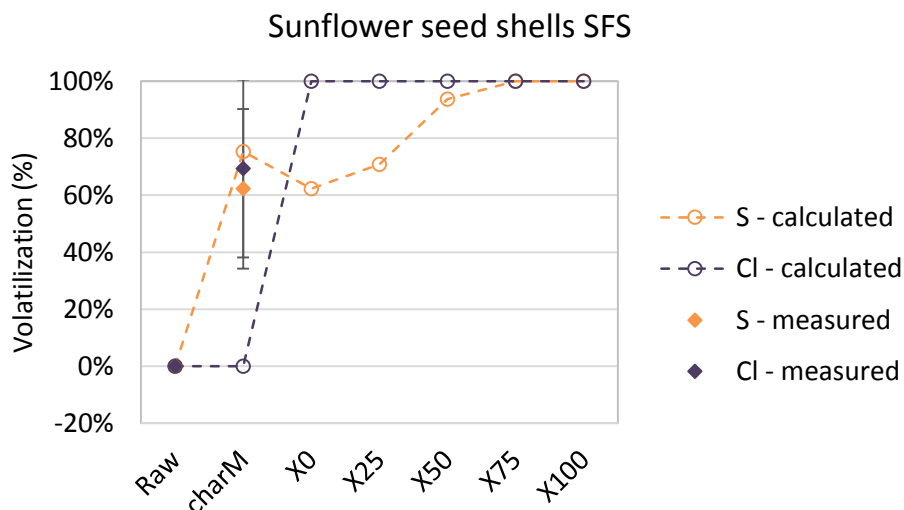


Figure II.35 | Calculated and measured volatilization of S and Cl in the sunflower seed shell samples.

It must be noted that the apparent decrease observed for some points in calculated volatilization is only explained by the fact that calculations at each conversion step were based on the previous experimental—and not calculated—volatilization value, which could be lower than the calculated one.

The calculated S and Cl volatilization during pyrolysis (charM and X0) varied with the biomass species. For rice husks, all the S was completely volatilized from pyrolysis at 450 °C (charM), mainly as H₂S(g). Only 30% of Cl was volatilized at this temperature, mainly as HCl(g), and the complete volatilization occurred at 800 °C (X0), mainly as KCl(g).

For sunflower seed shells, there was a stabilization of the S calculated volatilization, mainly as H₂S(g). This was due to the simulated formation of condensed CaS, that did not occur for rice husks. The formation of this phase can be explained by its lower O content compared to rice husks (Table II.7 and Table II.8) (Petit et al., 2009). Moreover, sunflower seed shells had more Ca and less Si and P. It can have resulted in less Ca immobilized in silicates and phosphates (Arnold et al., 2017; Porbatzki et al., 2011) and therefore more Ca available to form CaS. Cl only volatilized at 800 °C (X0), mainly as KCl(g).

Then, during gasification, both S and Cl from rice husks were completely volatilized in calculations. For sunflower seed shells, the S calculated volatilization progressively increased to be complete at 75% conversion. The Cl calculated volatilization was 100% from X0.

The measured volatilizations of S and Cl were only available for charM, i.e. after pyrolysis at 450 °C.

In the case of rice husks, the measured S volatilization was significantly lower than the predicted complete volatilization. It was in accordance with the TPD-MS results that showed some remaining S in the chars from gasification, desorbed as SO₂(g) (Figure II.32). On the opposite, a low Cl volatilization was predicted but experimental data showed an almost complete volatilization.

In the case of sunflower seed shells, the measured S volatilization was similar to the predicted one, i.e. around 70%. From the TPD-MS results (Figure II.32), no S was detected in the chars from gasification, which suggests a complete volatilization. A high volatilization of Cl was measured while no volatilization was calculated at this temperature.

In conclusion, these experimental results showed a partial volatilization of S and Cl during the pyrolysis at 450 °C in agreement with literature (Björkman and Strömberg, 1997; Knudsen et al., 2004) and with calculations for S in sunflower seed shells. This low temperature and the important mass (30-50 g) of pyrolyzed biomass inducing mass transfer limitations (see 2.2) are detrimental to reach equilibrium. Experimental results at higher temperatures would have been of better interest, but not enough material was available for S and Cl characterization for these samples. Nevertheless, calculations allowed to give the speciation of the gas phase for S and Cl which was in agreement with literature (Bläsing et al., 2013).

3.3.1.2. Volatilization of the main inorganic elements Si, K, Ca and Mg

The volatilization of the main inorganic elements Si, K, Ca and Mg are shown in Figure II.36 and Figure II.37 for rice husks and sunflower seed shells, respectively.

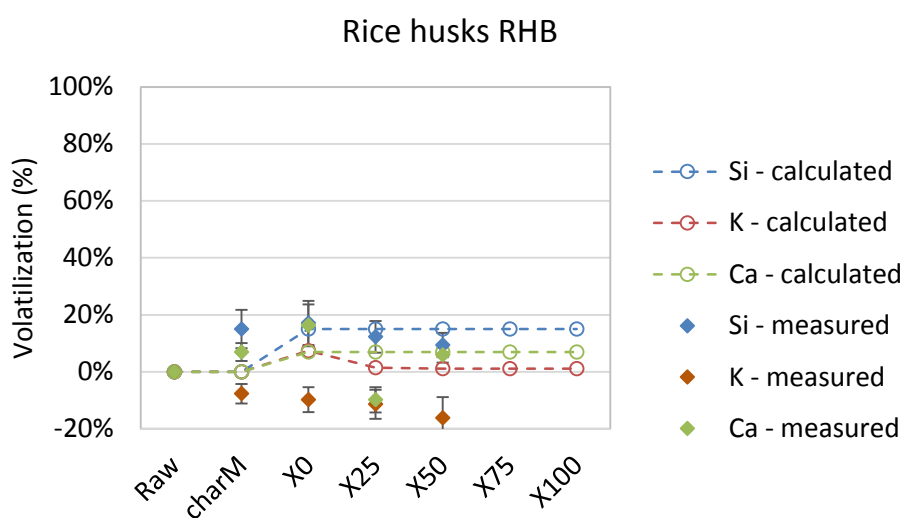


Figure II.36 | Calculated and measured volatilization of the three main inorganic elements Si, K and Ca in the rice husk samples.

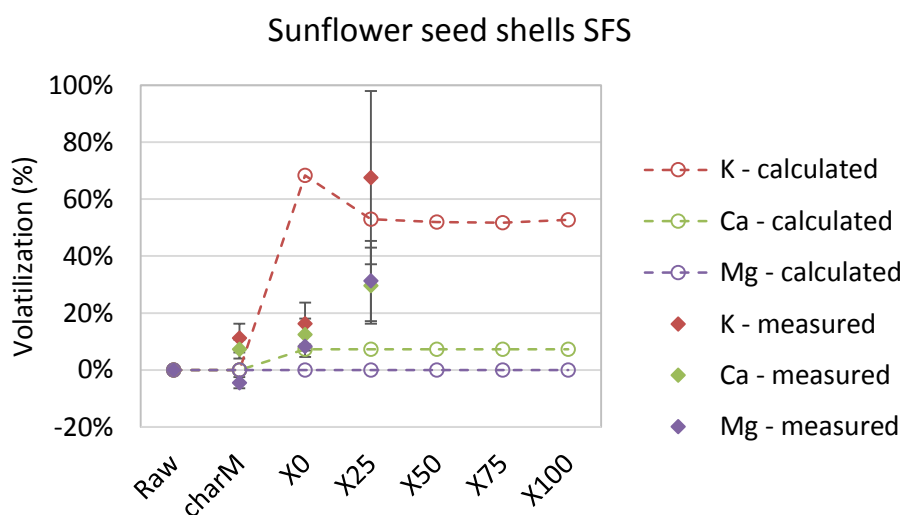


Figure II.37 | Calculated and measured volatilization of the three main inorganic elements K, Ca and Mg in the sunflower seed shell samples.

For both biomass species, **calculations** predicted that no volatilization would occur in the case of charM at 450 °C. Then for X0 samples pyrolyzed at 800 °C and for all gasified samples, the volatilization remained non-existent or low (< 20%) except for K in sunflower seed shells. In this last case, the calculated volatilization was above 50%. From the calculated volatilization of Cl, it probably formed KCl(g). However, it could not form only KCl(g) since in sunflower seed shells the molar ratio K/Cl was of 8.8 (calculated from data in Table II.8) and was superior to the molar ratio of 1 from KCl(g). Calculations showed that K was released in the form of KOH(g), K(g) and KCl(g).

From the measures on rice husks samples, no significant volatilization of the main inorganic elements was detected during both the pyrolysis and the gasification steps. This is in accordance with the calculation at thermodynamic equilibrium. Authors in literature also observed the lack of or low volatilization during pyrolysis (Dirbeba et al., 2016; Lane et al., 2015).

In the case of sunflower seed shells, no significant volatilization of the main inorganic elements was detected during the pyrolysis step—i.e. for SFS_charM and SFS_X0. This is in accordance with calculated volatilizations during pyrolysis. Then, during gasification, K was volatilized as predicted by calculations at thermodynamic equilibrium while Ca and Mg remained in the condensed phases.

In conclusion, when looking at the main inorganic elements Si, K, Ca and Mg alone and not the compounds they form, the chars at the end of pyrolysis were not different from the initial raw biomass. Then, during gasification, only K from sunflower seed shells was volatilized. Mg as well as the main elements of rice husks Si, K and Ca remain in condensed phases.

3.3.2. Determination of the inorganic condensed phases

The elements forming the inorganic fraction are an important data. However, it is essential to also characterize the condensed phases they form in order to understand the role of the inorganic fraction in the gasification mechanisms. Indeed, as presented in the state of the art, the same element can be active or not depending on the condensed phase it forms. For example, K has a catalytic activity on gasification in KOH or K₂CO₃ but not when it forms K-silicates.

In this section, results on the condensed phases from calculations at thermodynamic equilibrium are presented. They were used as a tool to predict the condensed phases forming the inorganic fraction of the char samples. Then, SEM–EDX, P-XRD and Raman spectroscopy results were combined in order to determine the experimental condensed phases.

3.3.2.1. Calculated phases

Results from calculations at thermodynamic equilibrium are plotted in Figure II.38 and Figure II.39 for rice husks and sunflower seed shells, respectively. For both biomass species, condensed C, i.e. carbon matrix of the char, was calculated before steam injection but not in presence of steam. It confirmed the kinetic limitations on the carbon species. Therefore, results are presented normalized to 100% without C(s), i.e. with only the inorganic phases.

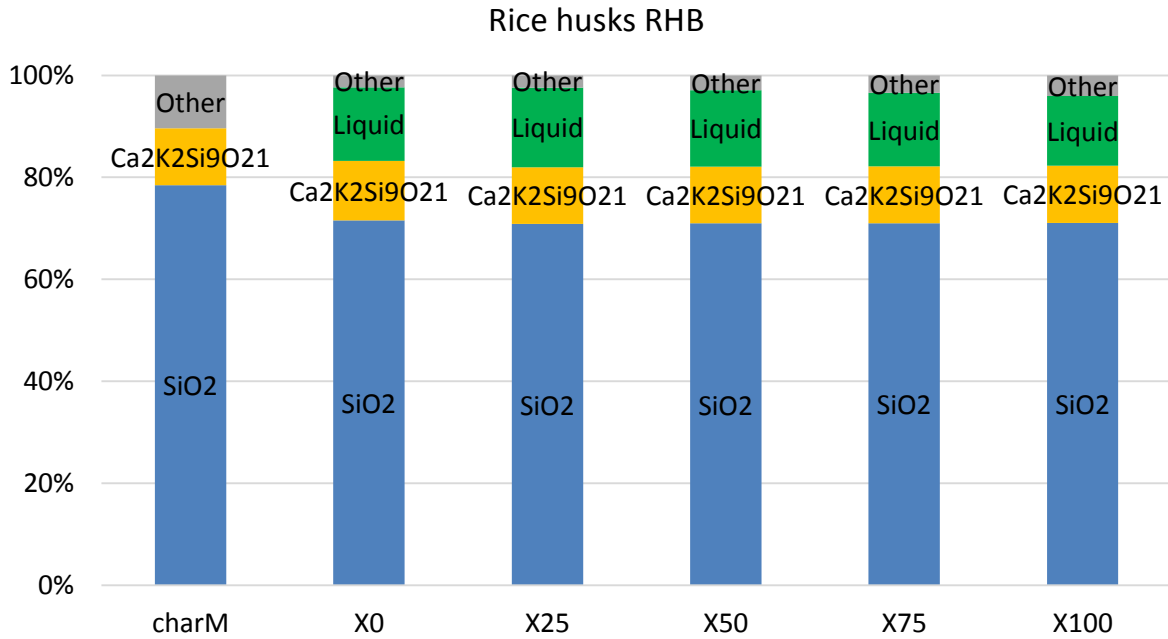


Figure II.38 | Calculated condensed phases at thermodynamic equilibrium for rice husk samples.

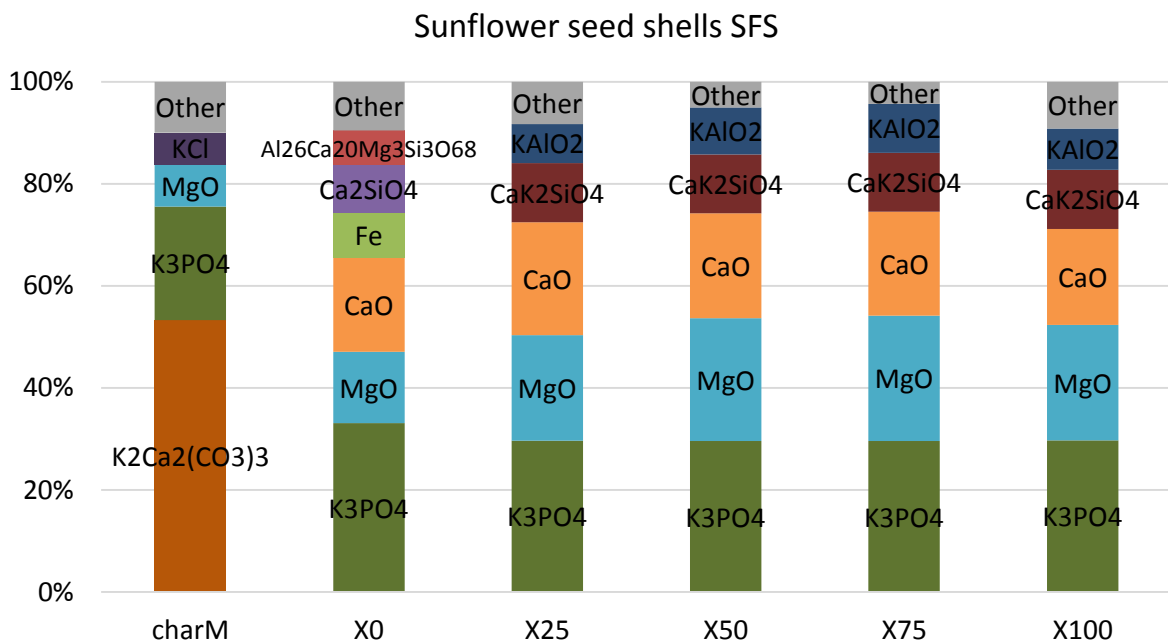


Figure II.39 | Calculated condensed phases at thermodynamic equilibrium for sunflower seed shell samples.

Calculated condensed phases for rice husk chars were mainly SiO₂ and Ca₂K₂Si₉O₂₁ for all samples. At 800 °C, both with and without H₂O—i.e. samples RHB_X0 to RHB_X100, a liquid phase was present. This liquid phase contained mainly Si, O and K.

In the case of sunflower seed shell chars, more condensed phases appeared in calculations. The phases MgO and K_3PO_4 were found in all samples. In the case of SFS_charM, the main phase was $K_2Ca_2(CO_3)_3$ and some KCl was also calculated. The KCl was not present in the subsequent sample, in accordance with the calculated Cl volatilization presented in the previous section. From SFS_X0, a CaO phase appeared. In this sample, Ca was also present as the silicate Ca_2SiO_4 . In the presence of H_2O —i.e. in SFS_X25 to SFS_X100, K was incorporated to this silicate to form CaK_2SiO_4 . It must be noted that sunflower seed shells were K and Ca-rich which corresponds to a poorly known part of the thermodynamic database (Lindberg et al., 2013). The calculations must therefore be considered with caution.

3.3.2.2. Measured phases

SEM–EDX analysis showed that for each biomass type the chars consisted of various phases. It is a semi-quantitative method that only allows local observations. For each sample, several particles were observed and EDX was conducted on several points of each particle. It can be noted that, with a BSE detection, phases containing mainly carbon (i.e. the carbon matrix) appeared clearly as dark phases while inorganic phases appeared lighter due to the atomic number contrast.

In the case of rice husks, char samples comprised a carbonaceous matrix without any inorganic element whose quantity seemed to decrease during conversion as expected. The second main phase in rice husk chars was SiO_2 that appeared in the form of grains, often with a characteristic bumpy shape as described in literature for ash and raw biomass (Ganesh et al., 1992; Krishnarao et al., 2001; Park et al., 2003; Ryu et al., 1997). Other phases that did not appear as proper grains could be observed. They were constituted of K, Si and O, and were therefore probably K-silicates. These phases sometimes also contained Ca. However, Ca was observed in few samples even though it was the third main element contained in rice husks after Si and K. This can be explained by the fact that SEM–EDX is a technique that analyses the chars locally. Therefore, dispersed compounds, which can be the case of Ca-compounds, can be difficult to locate. In addition, silicates were found in smooth phases which indicates that it was liquid at the process temperature. These results were in agreement with the calculation at thermodynamic equilibrium even if the composition of the K-Ca-silicate was not experimentally determined. An example of SEM images is given in Figure II.40 and Figure II.41 for RHB_X0 with SE (topology contrast) and BSE (atomic number contrast) detection respectively.

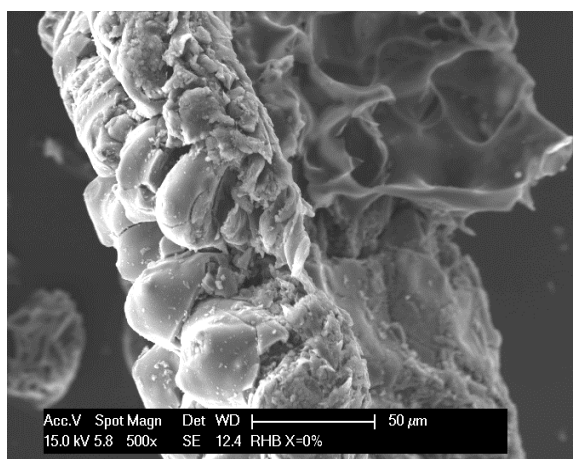


Figure II.40 | SEM image of a char particle from RHB_X0 with SE detection.

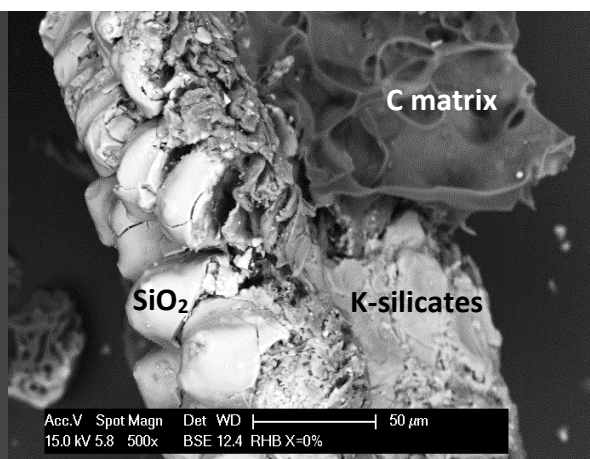


Figure II.41 | SEM image of a char particle from RHB_X0 with BSE detection.

In the case of sunflower seed shell chars, the carbonaceous matrix often contained some K and sometimes also some Ca. Smooth phases were observed that contain K, Ca and/or Mg with O and maybe C which could not be seen because of the sample graphitization. They were probably carbonate phases. Phases containing K, S and O could also be found. KCl was also present at the surface of the chars in the form of flakes or grains distinct from the matrix. In addition, grains containing Fe, Cr and Ni could be observed which most likely indicates a pollution by stainless steel. It might have originated from shell grinding or pelletization. An example of SEM image is given in Figure II.42 and Figure II.43 for SFS_X25 with SE and BSE detection respectively.

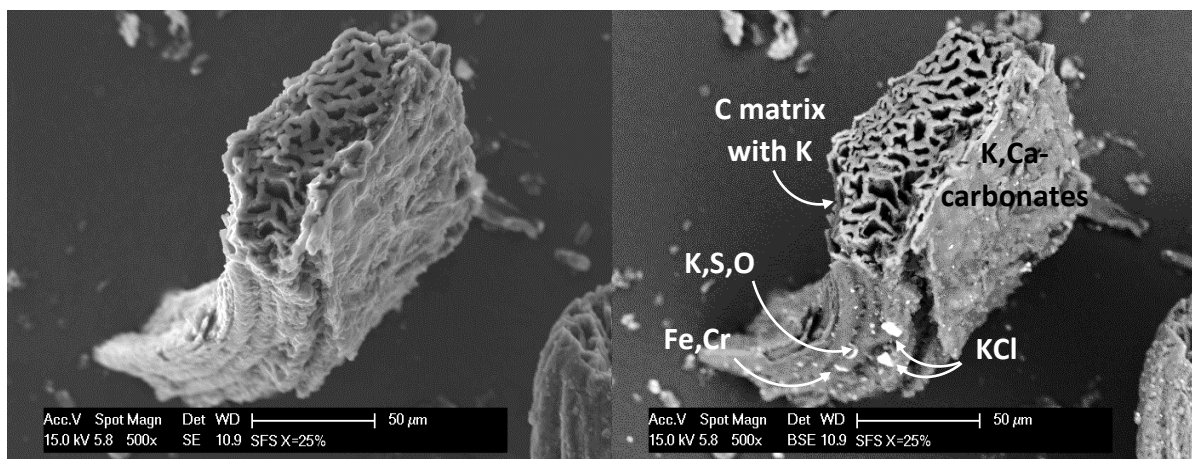


Figure II.42 | SEM image of a char particle from SFS_X25 with SE detection.

Figure II.43 | SEM image of a char particle from SFS_X25 with BSE detection.

SEM–EDX analysis was completed with P-XRD analysis to investigate the crystalline inorganic compounds.

The evolution of the P-XRD diffractograms at several pyrolysis and gasification conversions is presented in Figure II.44 for rice husks and in Figure II.45 for sunflower seed shells. The identified phases are summarized in Table II.10 and Table II.11.

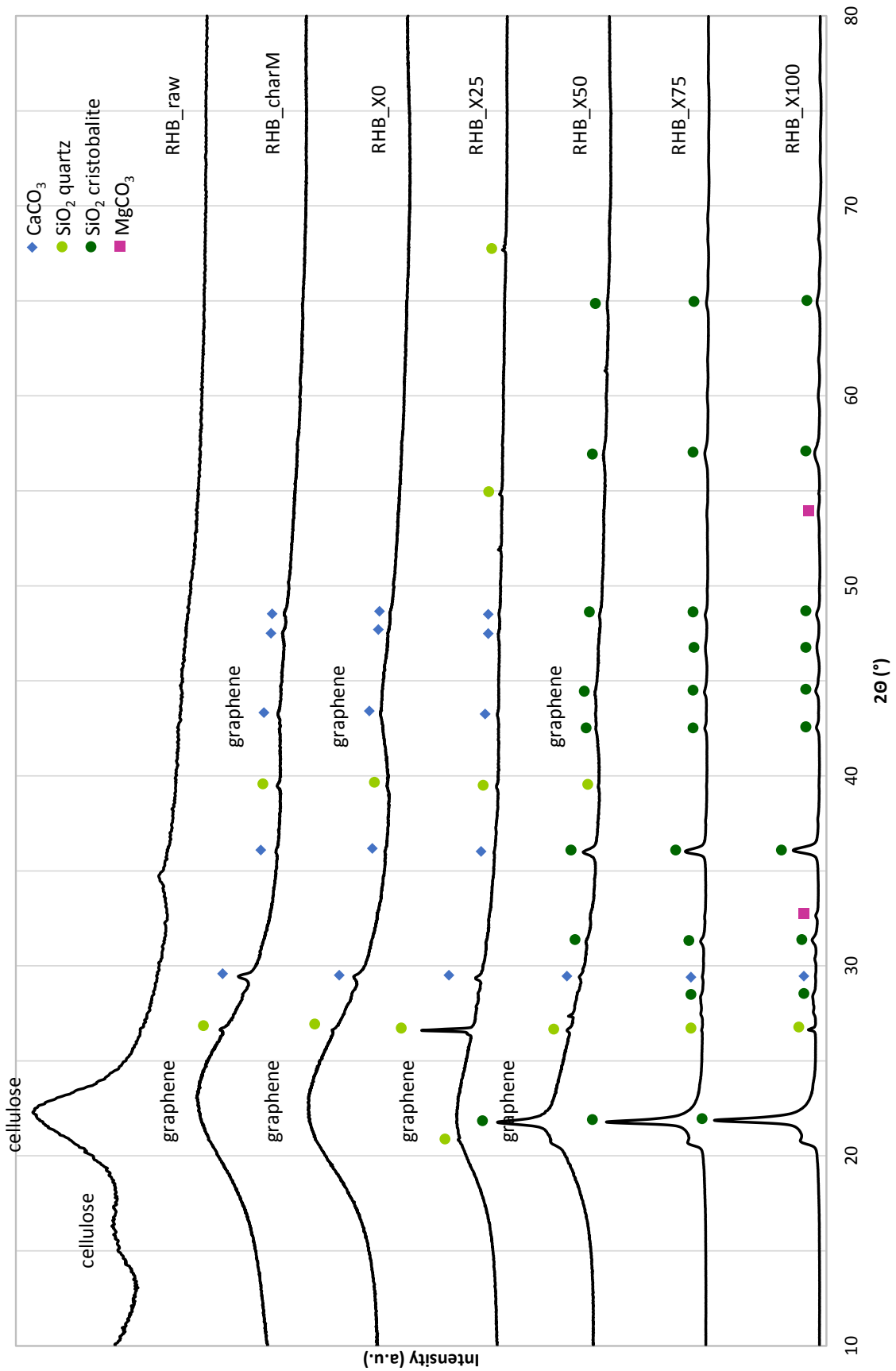


Figure II.44 | P-XRD diffractograms of rice husk chars at several pyrolysis and gasification conversions.

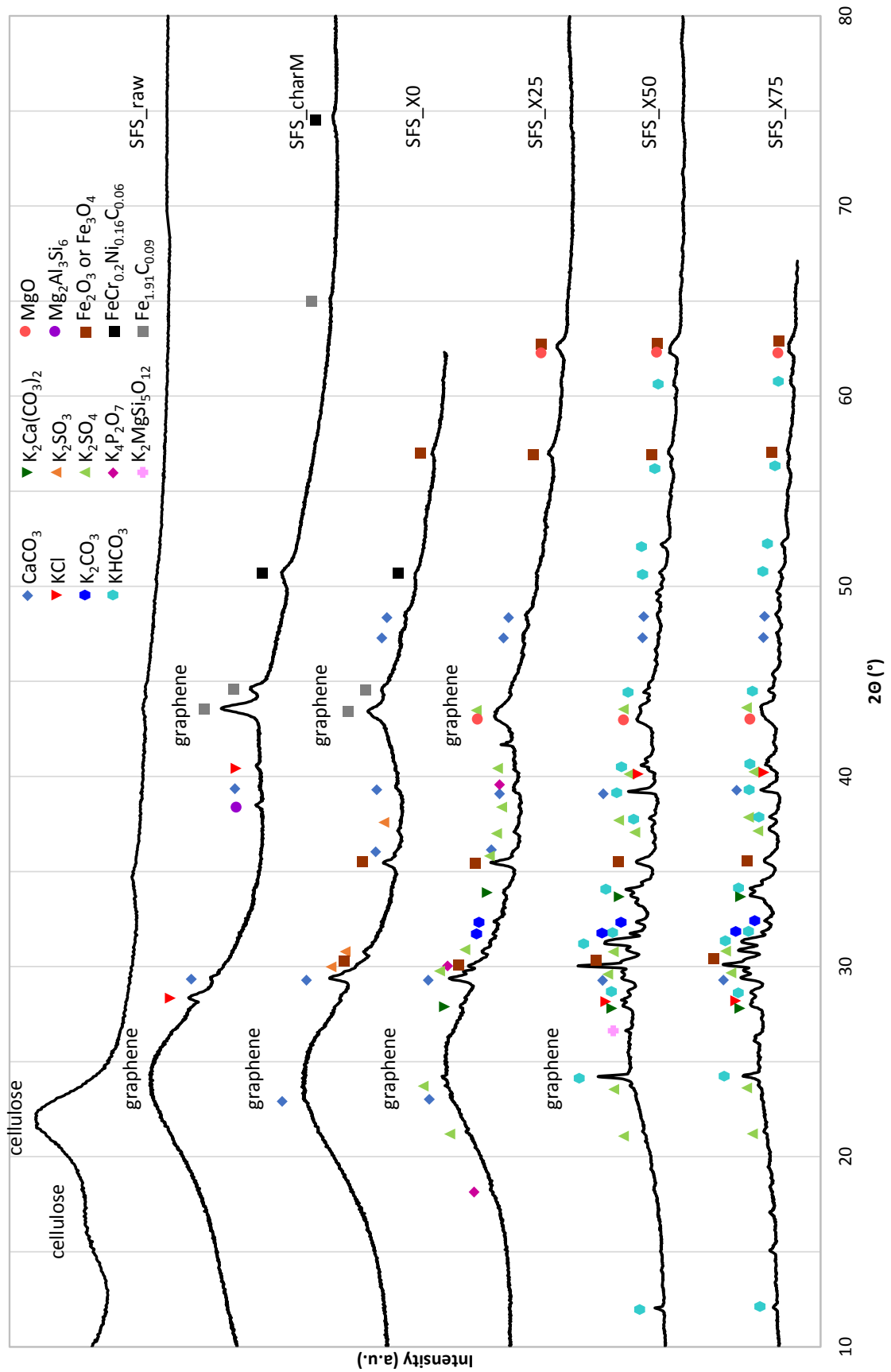


Figure II.45 | P-XRD diffractograms of sunflower seed shell chars at several pyrolysis and gasification conversions.

Table II.10 | List of inorganic compounds identified in rice husks biomass and chars.

	Rice husks Si – K – Ca						
	Raw	CharM	X0	X25	X50	X75	X100
Cellulose	x						
Graphene		x	x	x	x		
Liquid v			o	o	o	o	o
SiO ₂ quartz v	o	x	x	x	x	x	x
SiO ₂ opal or cristobalite+tridymite					x	x	x
K silicates	o	o	o	o	o	o	o
Ca-K silicates v		o		o			o
Ca silicates	o						
CaCO ₃		x	x	x	x	x	x
MgCO ₃							x

x Characterized by P-XRD.

o Local elemental observations only, i.e. characterized through SEM–EDX.

v Predicted by calculations at thermodynamic equilibrium.

Table II.11 | List of inorganic compounds identified in sunflower seed shell biomass and chars.

	Sunflower seed shells K – Ca – Mg						
	Raw	CharM	X0	X25	X50	X75	X100*
Cellulose	x						
Graphene		x	x	x	x	x	
CaCO ₃ v	o	x	x	x	x	x	
K ₂ Ca(CO ₃) ₂ v	o	o	o	x	x	x	
Ca-K-Mg carbonates		o	o		o	o	o
K ₂ CO ₃				x	x	x	
KHCO ₃					x	x	
KCl v		x			x	x	
K ₂ SO ₃	o		x				
K ₂ SO ₄				x	x	x	
K ₄ P ₂ O ₇ v				x			
K ₂ MgSi ₅ O ₁₂					x		
MgO v				x	x	x	
Mg ₂ Al ₃ Si ₆		x					
Fe _{1.91} C _{0.09}	o	x	x				
FeCr _{0.2} Ni _{0.16} C _{0.06}	o	x	x				
Fe ₃ O ₄			x	x	x	x	o

x Characterized by P-XRD.

o Local elemental observations only, i.e. characterized through SEM–EDX.

v Predicted by calculations at thermodynamic equilibrium. (K₄P₂O₇ predicted as K₃PO₄; K₂Ca(CO₃)₂ predicted as K₂Ca₂(CO₃)₃; CaCO₃ predicted as CaO)

The broad peaks observed for both raw biomass samples correspond to partially ordered cellulose and are typical of raw biomass P-XRD diffractograms (Vassilev et al., 2012). The two broad peaks around 2 θ = 23° and 44° in char diffractograms correspond to graphene layers (Saavedra Rios et al., 2018).

P-XRD analysis of rice husk chars confirmed the presence of Si in the SiO_2 form. SiO_2 was found as quartz in all samples. From 50% conversion another form of SiO_2 appeared. However, the data did not allow to conclude on the exact form. The new SiO_2 phase could have been opal which is poorly referenced in the diffractograms database and is not a pure structure but a combination of cristobalite, tridymite and hydrated amorphous SiO_2 . It could also have been cristobalite, which was properly identified, and tridymite, for which a peak at $2\theta = 23^\circ$ did not appear here. CaCO_3 as well as MgCO_3 for RHB_X100 were also present in the chars but were not observed with SEM–EDX. This can be explained by the fact that SEM–EDX is a technique that analyses the chars locally and CaCO_3 was a minor compound. No K-compound was identified through this technique while K was the second main inorganic element contained in rice husks. This can be explained by the fact that P-XRD only detects crystalline phases so K-compounds might have been present in non-crystalline forms.

P-XRD analysis of sunflower seed shell chars also confirmed some phases observed during SEM–EDX analysis: KCl; carbonates identified as CaCO_3 , K_2CO_3 , KHCO_3 and $\text{K}_2\text{Ca}(\text{CO}_3)_2$; K-, S- and O-containing phases identified as K_2SO_3 and K_2SO_4 ; Mg-containing phases mainly identified as MgO ; steel in the form of $\text{FeCr}_{0.2}\text{Ni}_{0.16}\text{C}$ and $\text{Fe}_{1.91}\text{C}_{0.09}$ that seemed to be oxidized to Fe_2O_3 or Fe_3O_4 at the end of the gasification reaction.

Raman spectra at high conversion also confirmed some of the compounds identified through SEM–EDX and P-XRD analyses. In some repetitions of the spectra, peaks appeared that were not related to carbon structure and therefore correspond to inorganic compounds. A spectrum with such peaks is shown in Figure II.46 for rice husk char sample RHB_X100 and in Figure II.47 for sunflower seed shell char sample SFS_X75.

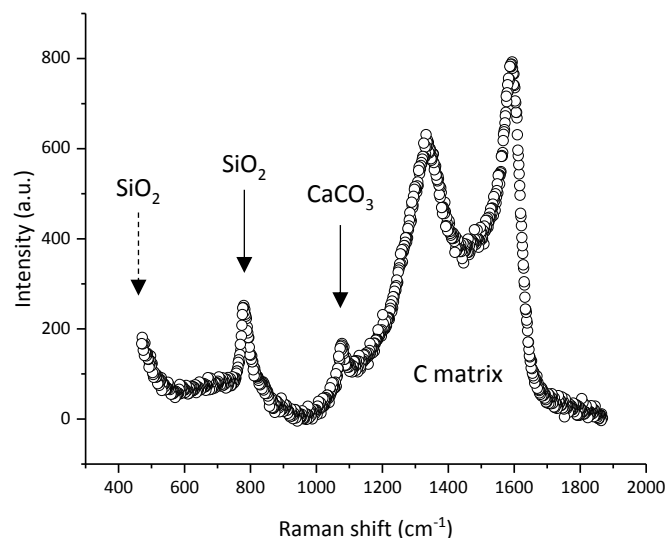


Figure II.46 | Raman spectra showing inorganic compounds of the sample RHB_X100.

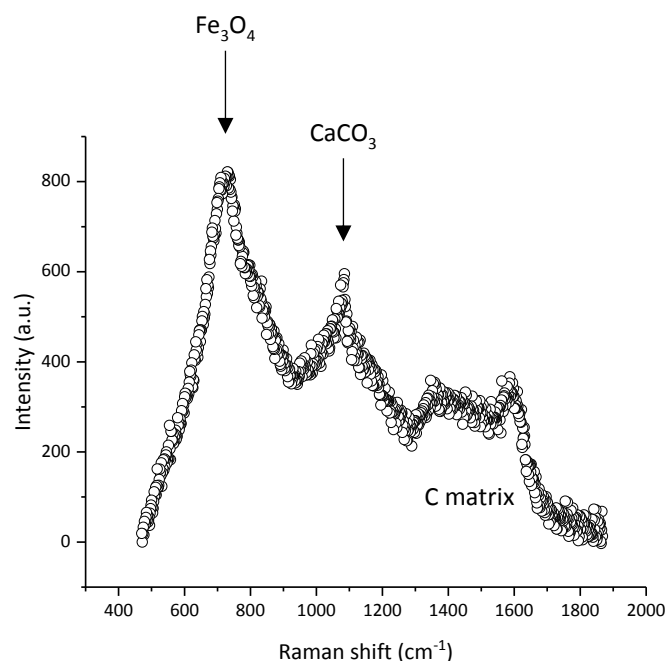


Figure II.47 | Raman spectra showing inorganic compounds of the sample SFS_X75.

For both biomass species, CaCO_3 was clearly identified. Raman data also permitted to identify the iron oxide present in sunflower seed shell char samples as Fe_3O_4 and not Fe_2O_3 . Lastly, the peak at 800 cm^{-1} in spectra from rice husk chars can correspond to a weak peak of SiO_2 cristobalite or tridymite, that have similar patterns, but their main peak is around $420\text{--}430\text{ cm}^{-1}$ which is out of the recorded Raman shift range.

3.3.3. Conclusions on the inorganic fraction

The differences in the elemental composition of the raw biomass samples (Table II.1) were also found in the chars at several pyrolysis and gasification conversions, rice husks being rich in Si and sunflower seed shells being rich in K. In addition to these elemental differences, the forms of the inorganic elements varied between the species.

The techniques used for the characterizations could only account for the crystallized compounds—through P-XRD—and the amorphous compounds that were not too dispersed—through SEM–EDX whose observations were elemental and local.

Rice husk char carbonaceous matrix did not contain dispersed inorganics whereas sunflower seed shell char carbonaceous matrix contained dispersed K and sometimes Ca. The techniques used could not determine if they were finely dispersed inorganic compounds or if the elements were directly bonded with the C-matrix. In addition to these dispersed inorganic elements, compounds such as KCl or K_2SO_4 formed crystallites clearly distinct from the carbonaceous matrix. In both biomass types, carbonates and silicates were present as separate phases from the carbonaceous matrix but had a smooth aspect that suggested liquid formation at the process temperature as predicted by calculations at thermodynamic equilibrium.

4. Conclusions

This chapter investigated the relative influence of the inorganic content compared to the physical properties of biomass chars on the gasification kinetics. To this end, both organic and inorganic fractions of the chars from pyrolysis and during gasification were characterized in depth.

The chosen approach combined several characterization techniques usually used for chars. These techniques mainly focused on the carbonaceous matrix which generally represents 99% of the char mass in the case of woods. However, agricultural residues have a higher ash content—up to 14.6 wt% in the present study—which then could not be neglected. Therefore, these characterizations were enriched with an investigation of the inorganic compounds contained in the chars. In particular, Raman spectroscopy, which is traditionally used to characterize carbon structure, was also used here to identify mineral phases in the chars.

The analyses were conducted on two biomass species with significantly different gasification reactivities: rice husks that gasify slowly and sunflower seed shells that gasify faster. The aim was to determine the main parameter explaining this difference in terms of reactivity.

Both biomass species had similar porosity and carbon structure before steam injection. Therefore, these properties do not justify the reactivity difference between them. Nevertheless, there was a higher microporosity and quantity of surface functions during steam gasification for the fast gasifying biomass—sunflower seed shells. This does not directly explain the gasification reactivity difference between both species but it suggests that the evolution of these properties was a consequence of another catalytic mechanism.

Characterization of the inorganic compounds present in the chars revealed that, in addition to the difference of elemental composition, there was a difference in the volatility of K that was released for sunflower seed shells but not for rice husks. Other differences concerned their form and location in the chars. Sunflower seed shell chars—that gasify faster—contained K and sometimes Ca directly into its carbonaceous matrix which was not the case for rice husk chars. In addition, some compounds such as KCl were present as small crystallites at the surface of the matrix for sunflower seed shell chars.

When working with thermodynamic equilibrium calculations, there can be limitations related to the database and to the fact that the system can be in a non-equilibrium state. However, even with these limitations in mind, calculation results gave reasonable trends in terms of volatilization and of condensed phase composition. The results helped assessing the inorganics behavior when experimental data were difficult to obtain.

In conclusion, these results showed that the physical properties of the carbon matrix do not have a major influence on the gasification reactivity. On the opposite, the inorganic composition is the main parameter that seems to explain the differences between the gasification kinetic behaviors of the two studied biomass species. Moreover, it also seemed to affect the physical properties of the chars, namely their microporosity and their amount of surface functions.

Based on this conclusion, the next chapter focuses on the influence of two major inorganic elements: Si and K. They were specifically chosen because, out of the main inorganic elements in biomass, they are said to have the most inhibitory and catalytic influence on gasification, respectively (Link et al., 2010; Yip et al., 2009; Zhang et al., 2008).

Chapter III. Experimental study on the influence of K and Si on biomass gasification kinetics

This chapter investigates the influence of two particular inorganic elements on biomass gasification kinetics: Si and K. Indeed, we have demonstrated in the previous chapter that the inorganic composition of biomass has a major role compared to the char physical properties. In addition, from literature review, Si and K have been identified as the two most interesting elements to consider due to their high occurrence in biomass species and their high activity on the gasification kinetics. The present investigation used thermogravimetric analysis of a Si-rich and a K-rich biomass species: rice husks and sunflower seed shells respectively, along with beech wood which has a very low inorganic content as a reference. The influence of a Si-compound and a K-compound was studied using two model compounds: SiO_2 and K_2CO_3 . They were added to the biomass species either through direct solid mixing or without contact in a crucible with two separated compartments. Experiments were particularly designed to investigate the K effect through the gas phase. The first part of the chapter describes the materials and methods. The second part gives and discusses the results of the steam gasification of the pure materials—inorganic compounds and biomass species. The results of the interactions between the materials are given and discussed in a third part. Finally a conclusion is given.

1. Materials and methods

1.1. Biomass samples

The two biomass species selected previously in Chapter II were kept for this study:

- Rice husks (RHB) that are Si-rich and gasify slowly;
- Sunflower seed shells (SFS) that are K-rich and gasify fast.

Another biomass, beech wood, was chosen due to its very low inorganic content and in particular the very low Si content.

The samples were ground below 200 μm . Their properties are summarized in Table III.1.

Table III.1 | Composition and gasification reactivity properties of rice husks, sunflower seed shells and beech (in dry basis).

Biomass sample	Rice husks	Sunflower seed shells	Beech
Ash at 550 °C	14.6	3.3	0.6
Ash at 815 °C	14.4	2.8	—
C	41.6	50.2	45.9
H	5.2	6.5	6.2
O*	45.1	40.6	47.1
N	0.5	0.7	0.3
S	0.1	0.1	0.058
Cl	0.1	0.1	0.005
Si	63955	194	115
K	5822	9729	910
Ca	1797	4489	2516
Mg	659	1838	475
P	981	896	75
Na	413	9	3.6
Al	228	150	12
Fe	192	1099	34
SiO ₂	97.2	1.3	4.1
K ₂ O	5.0	35.5	18.3
CaO	1.8	19.0	58.7
MgO	0.8	9.2	13.1
P ₂ O ₅	1.6	6.2	2.9
Na ₂ O	0.4	0.0	0.1
Al ₂ O ₃	0.3	0.9	0.4
Fe ₂ O ₃	0.2	4.8	0.8
Main inorganic elements	Si – K – Ca	K – Ca – Mg	Ca – K – Mg
Gasification average reactivity between 1 and 80% conversion (%.min ⁻¹)	1.4	30.3	4.9

*Total oxygen calculated by difference with all other elements.

1.2. Model inorganic compounds

Two model inorganic compounds were selected for the study:

- Si-compound: silica (SiO_2)
- K-compound: potassium carbonate (K_2CO_3)

These compounds were selected since they can be found naturally in biomass as observed in Chapter II as well as in literature (Vassilev et al., 2012).

1.2.1. Amorphous silica and quartz

Two forms of SiO_2 were compared:

- Amorphous which is representative of a solidified liquid rich in SiO_2 ;
- Quartz which is the low temperature crystalline form of SiO_2 .

The amorphous silica used as a model compound was Rhodia Tixosil® 331. It was amorphous hydrated silica with a median diameter of 3.5 μm usually used for toothpaste thickening. Supplier documentation stated that it contained 2.5 % soluble salts. Internal analysis revealed 3 % soluble salts, mainly constituted of Na_2SO_4 which is commonly used in the production of glass in particular because of its anti-foaming properties (Min'ko and Binaliev, 2013). Its P-XRD diffractogram (Annex F) showed only a broad band in the 2θ range of 15-30° which is characteristic of amorphous SiO_2 (Biswas et al., 2018). Na_2SO_4 peaks were not observed probably because its amount was too low to be observed by this technique.

The quartz used was Fisher Chemical Ottawa sand, general purpose grade. Supplier documentation stated that its particle size is 20-30 mesh, i.e. 590-840 μm . Its particle size distribution obtained with a Retsch Camsizer XT showed a $d_{50} = 740 \mu\text{m}$, which was in accordance with supplier documentation. For the experiments, the sand was ground in a planetary ball mill to a $d_{50} = 8 \mu\text{m}$ in order to be close to the particle size of amorphous silica. Its P-XRD diffractogram (Annex F) confirmed that the material was pure SiO_2 quartz.

1.2.2. Potassium carbonate

Merck potassium carbonate EMSURE® ACS, ISO, Reag. Ph Eur, $\geq 99.0\%$ was used. Its P-XRD diffractogram (Annex F) showed that it had few impurities in the form of $\text{K}_2\text{CO}_3 \cdot 1.5\text{H}_2\text{O}$. The K_2CO_3 powder was ground from around 500 μm to $<100 \mu\text{m}$ with a mortar and pestle, in a N_2 atmosphere to prevent its hydration. It was then kept in a vacuum desiccator.

1.3. Experimental installation and procedure

Steam gasification behavior of the samples was investigated through thermogravimetric analysis (TGA). Experiments were carried out at an atmospheric pressure using the SETARAM Setsys thermobalance coupled with the Wetsys steam generator previously described in Chapter II.

A home-made crucible was used for the present investigation. It is a divided crucible which consists of a cylindrical platinum crucible of 2 mm height and 10 mm diameter with a partition of the same height along its diameter made up of platinum with 5% gold (Figure III.1).

Figure III.1 | Divided crucible (here containing rice husks and K_2CO_3).

Experiments were conducted in three different configurations: biomass or inorganic compound alone; mixtures of biomass and inorganic powders; biomass and inorganic compound without contact in the crucible.

Inorganic fractions were expressed as a percentage of the total sample:

$$\%Inorganic = \frac{m_{Inorganic}}{m_{Inorganic} + m_{Biomass}} \quad (III.28)$$

with $m_{Inorganic}$ the mass of inorganic added and $m_{Biomass}$ the mass of biomass.

Mixtures of biomass and inorganic powders were prepared with approximately 140 mg of biomass and the necessary mass of inorganic compound to obtain the desired concentration. The two powders were added to a plastic flask with a few glass beads of 3 mm diameter. Homogeneous mixing was obtained by shaking the flask by hand for around one minute.

The procedure was similar to the one previously described for raw biomass in Chapter II. It is illustrated in Figure III.2 and the conditions are summarized in Table III.2.

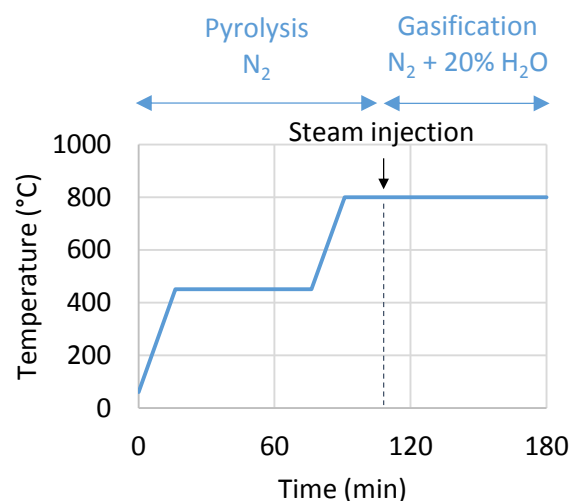


Figure III.2 | TGA procedure for raw biomass.

Table III.2 | Conditions of the TGA experiments.

Sample initial mass	Biomass 14 mg K ₂ CO ₃ 1-3 mg SiO ₂ 3 mg Mixture 15 mg
Total gas flow	0.05 L·min ⁻¹
Pyrolysis gas atmosphere	N ₂
Gasification gas atmosphere	20 vol% H ₂ O in N ₂
Heating rate	24 °C·min ⁻¹
Pyrolysis holding time at 450 °C	60 min
Steam injection time	After mass stabilization (12 min after reaching 800 °C)

Experiments were conducted at least in duplicates.

From the mass evolution measurements, several values previously described were obtained: the gasification solid conversion X , the gasification rate r and the gasification average reactivity between 1 and 80% conversion $r_{1-80\%}$. Additionally, the derivative thermogravimetric (DTG) curve was obtained with the following equation:

$$DTG(t_n) = -\frac{m_{n+1} - m_{n-1}}{t_{n+1} - t_{n-1}}. \quad (\text{III.29})$$

To allow comparison between the different samples, results from pyrolysis and gasification of samples with added inorganic compounds (mixtures and without contact) were corrected by subtracting the equivalent mass profiles of pure inorganic compound to the measured mass profiles. An example is given in Figure III.3 for the case of the experiment on rice husks with K₂CO₃ added without contact. The black curve is the mass as directly measured in TGA. The orange curve is the pure K₂CO₃ profile that is subtracted. Finally, the blue curve is the equivalent char mass with the K₂CO₃ subtracted. It is this last mass that is used in further data treatments and interpretations.

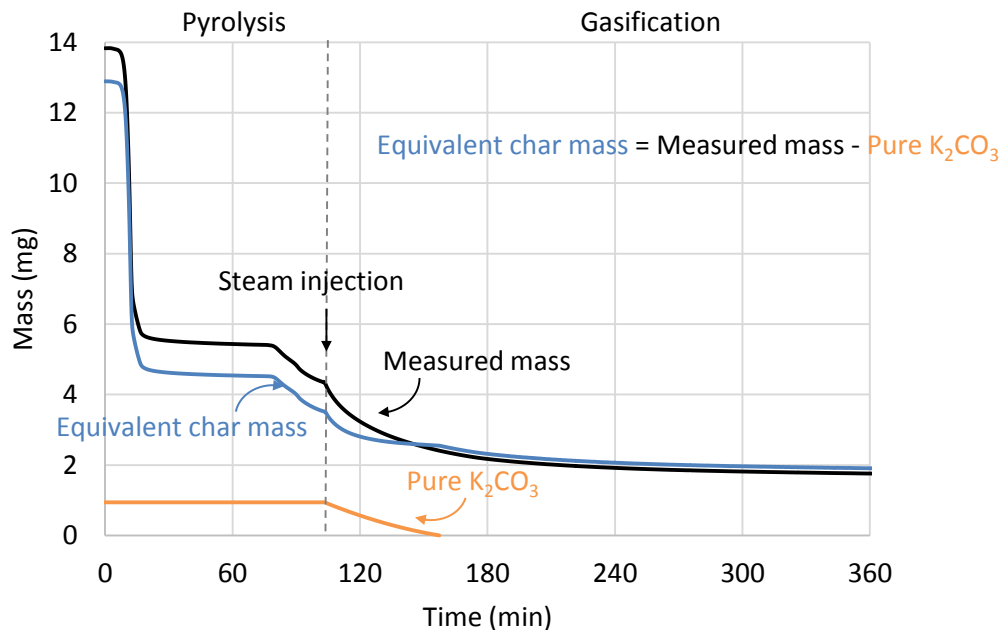


Figure III.3 | Measured mass, equivalent char mass (as used in further interpretations) and corresponding pure K_2CO_3 mass of the experiment on rice husks with K_2CO_3 added without contact.

1.4. Thermodynamic equilibrium simulation method

Calculations at thermodynamic equilibrium were performed to simulate the behavior of K_2CO_3 under steam.

They were performed by minimization of the Gibbs free energy of the total system with the FactSage 7.2 software and the databases FTsalt and FactPS (Bale et al., 2002; Hack et al., 2012).

The steam gasification procedure applied to pure K_2CO_3 was simulated at thermodynamic equilibrium. The initial data are listed in Table III.3. K_2CO_3 initial mass was slightly different from the experimental initial mass put in the TGA since calculations only concerned the gasification step and there was a slight mass loss before gasification (Figure III.6).

Table III.3 | Initial data for the thermodynamic equilibrium calculations.

Temperature	800 °C
Initial solid	K_2CO_3 0.54 mg 0.70 mg 1.23 mg 1.73 mg 2.99 mg
Initial gas	0 to 1.5 g N_2 + 0 to 0.241 g H_2O (0.5 L.min ⁻¹ , 0 to 30 min)

2. Steam gasification of the pure materials

This section presents the steam gasification results for the pure materials. It gives a reference for the next section that focuses on the interactions between the biomass and inorganic compounds.

2.1. Steam gasification of pure inorganic compounds

2.1.1. Amorphous silica and quartz

The pyrolysis and gasification procedure was applied to amorphous silica alone and quartz alone. Results are plotted in Figure III.4.

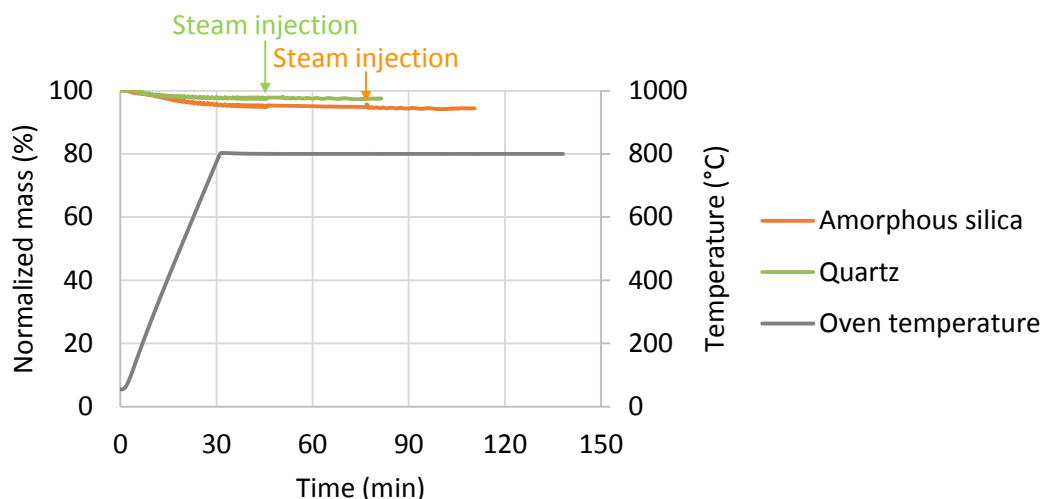


Figure III.4 | Mass evolution over time of amorphous silica alone and quartz alone during the pyrolysis and gasification procedure.

For both materials, i.e. amorphous silica and quartz, almost no volatilization was observed during the process, in accordance with the literature (Arvelakis et al., 2004). Therefore, the contribution from SiO_2 was neglected in the samples mass evolution where it was added.

Moreover, visual and SEM observations of the samples at the end of the process confirmed that they did not melt. Such result was in agreement with the melting temperature of SiO_2 of 1713 °C (Lide, 1996). The SEM observation of the amorphous silica before and after TGA is shown in Figure III.5.

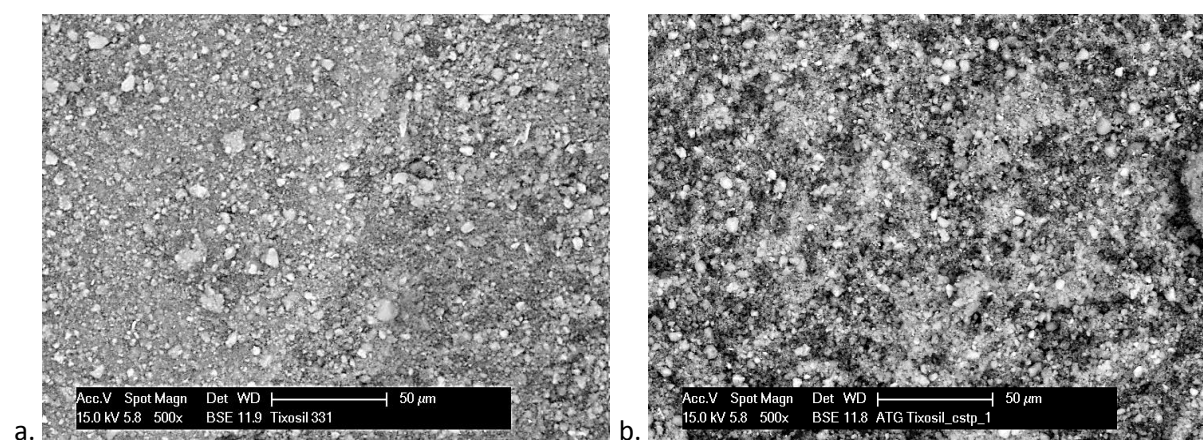


Figure III.5 | SEM observation of the pure amorphous silica a. before and b. after the gasification procedure.

2.1.2. Potassium carbonate

The pyrolysis and gasification procedure was applied to samples of K_2CO_3 of various masses. Figure III.6 shows the evolution of the mass of the samples as a function of time.

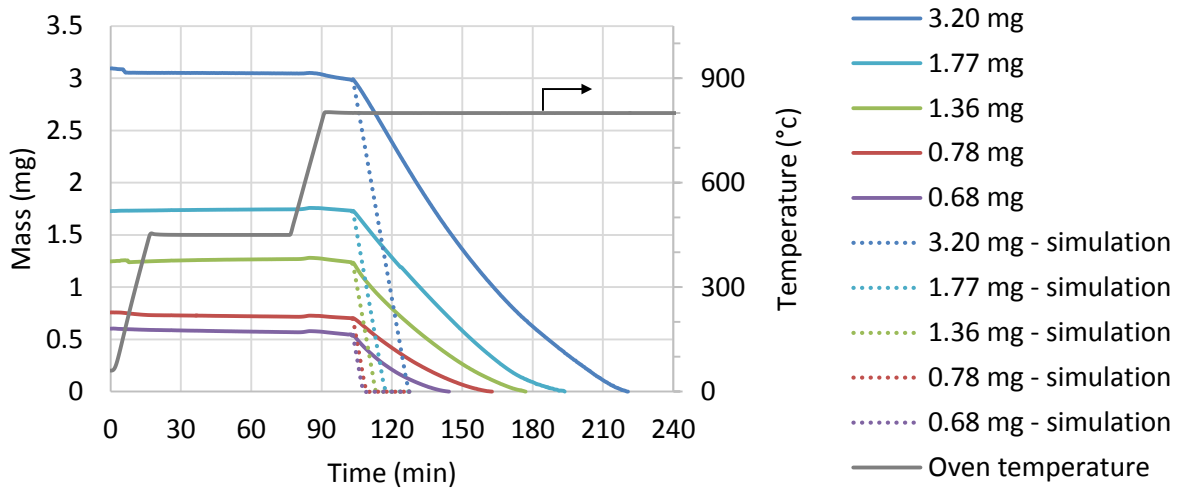
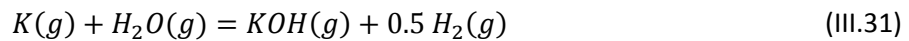


Figure III.6 | Mass evolution over time of various initial masses of K_2CO_3 alone during the pyrolysis and gasification procedure.

A very low volatilization of K_2CO_3 was observed during the pyrolysis step. On the contrary, the whole mass was volatilized when steam was injected. This behavior is in accordance with literature (Arvelakis et al., 2004; Knudsen et al., 2004; Zhao et al., 2018). The volatilization time depends on the initial mass. For the masses in this study—0.68 to 3.20 mg—it varied from 40 min to 2h.

To explain these results, a thermodynamic equilibrium simulation of the process with pure K_2CO_3 was conducted. In thermodynamic equilibrium conditions, K_2CO_3 was slightly volatilized as $K(g)$ and $CO_2(g)$ in an inert atmosphere and largely volatilized as $KOH(g)$ in a steam atmosphere. These volatilized species can be explained by the following reactions in accordance with literature (Sergeev et al., 2019; Wood and Sancier, 1984):



The simulated mass evolution of K_2CO_3 during the gasification step is plotted in dotted lines in Figure III.6. The simulation predicted that the whole amount of K_2CO_3 would volatilize in 2 to 20 minutes in thermodynamic equilibrium conditions. It showed that either the reaction was kinetically limited, or there remained mass transfer limitations during K_2CO_3 volatilization. The latter could be due to the configuration of the crucible in the carrier gas and/or to the K_2CO_3 particle size.

The mass evolution of K_2CO_3 as a function of time and initial mass was modeled to generalize the experimental results. It has not been attempted in the present work to give a signification to these coefficients like it has sometimes been done in literature (Knudsen et al., 2004). For example, Knudsen *et al.* modelled the evaporation of pure K-compounds based on mass transfer for a carrier gas sweeping the crucible parallel to its surface, on the contrary to the TGA configuration where the gas is perpendicular. They assumed it was controlled by diffusion through an external gas film and used mass transfer correlations to obtain the coefficients. Here, the objective was only to model experimental results in the TGA configuration to be able to extrapolate the results to other initial masses in the studied range. The mass loss during pyrolysis was neglected. For the gasification step, each curve was estimated by a second-degree polynomial of general equation:

$$m = at^2 + bt + c \quad (\text{III.32})$$

where m is the mass of K_2CO_3 during the gasification step in milligrams, t is the gasification time in seconds and a , b and c are the coefficients of the polynomial.

The fitted coefficients are presented in Table III.4.

Table III.4 | Fitted coefficient of the polynomial regression of the curves of mass of K_2CO_3 as a function of time for various initial masses.

Initial mass (mg)	a ($mg.s^{-2}$)	b ($mg.s^{-1}$)	c (mg)	R^2
2.99	3.8×10^{-8}	-7.0×10^{-4}	3.04	0.9999
1.73	3.4×10^{-8}	-3.4×10^{-4}	1.77	0.9987
1.23	3.9×10^{-8}	-4.5×10^{-4}	1.21	0.9997
0.70	3.7×10^{-8}	-4.0×10^{-4}	0.72	0.9999
0.54	7.4×10^{-8}	-5.2×10^{-4}	0.54	0.9995

Coefficient a was considered to be constant and its value was taken as the mean of the experimental values, with the value from 0.54 mg K_2CO_3 considered an outlier and excluded from the mean:

$$a = 3.7 \times 10^{-8} \text{ mg} \cdot \text{s}^{-2}. \quad (\text{III.33})$$

Coefficient b was modeled as a linear function of the initial mass of K_2CO_3 m_0 :

$$b = -1.4 \times 10^{-4} \times m_0 - 2.8 \times 10^{-4}. \quad (\text{III.34})$$

Coefficient c value was taken as the initial mass of K_2CO_3 :

$$c = m_0. \quad (\text{III.35})$$

The mass profiles of the various samples were recalculated from the resulting model. The experimental profiles as well as the corresponding models are presented in Figure III.7.

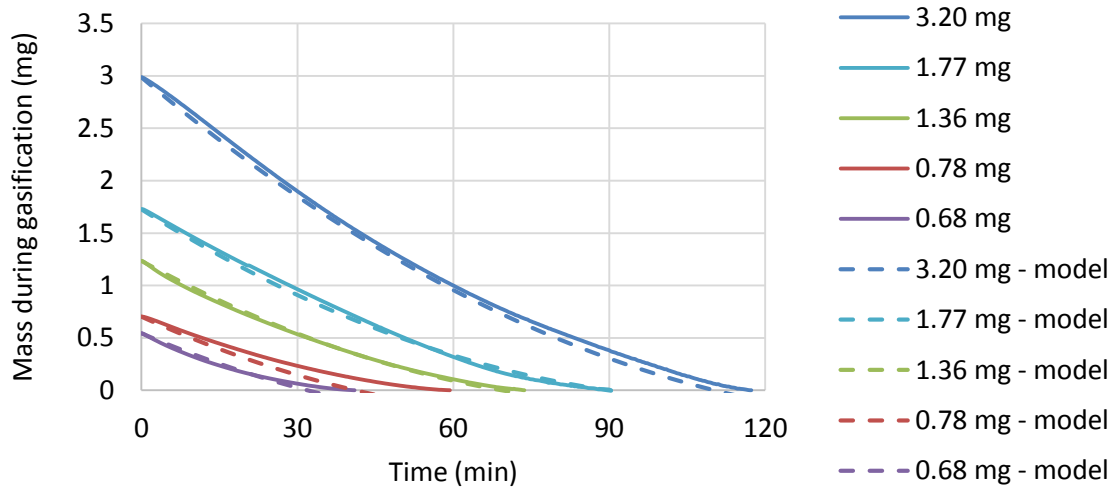


Figure III.7 | Mass evolution over time of various initial masses of K_2CO_3 alone during the gasification procedure and the corresponding models.

The model could be used to predict the volatilization profile of any mass of K_2CO_3 within the studied range during the gasification step. The modeled mass could be subtracted to results obtained from TGA of samples with added K_2CO_3 (mixtures and without contact).

2.2. Steam gasification of pure biomass

The steam gasification kinetic behavior of rice husks and sunflower seed shells has been presented in detail in Chapter II. The main results are reminded here along with the results for beech wood.

The normalized mass of the three biomass samples is plotted against time in Figure III.8.

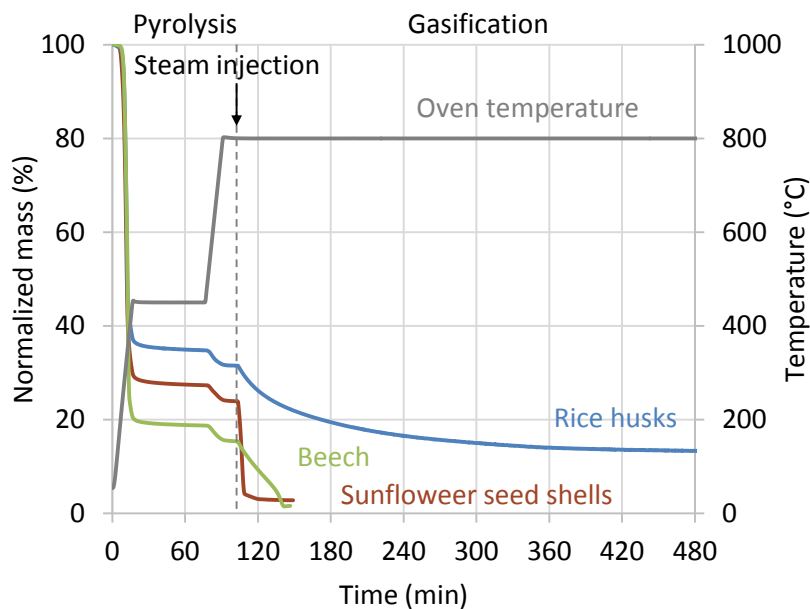


Figure III.8 | TGA of rice husks, sunflower seed shells and beech wood presented as the normalized mass as a function of time.

The three biomass species showed similar behaviors during pyrolysis where most of the mass was lost below 450 °C. Then significantly different behaviors were observed during gasification. Gasification of rice husks needed more than six hours to be completed while gasification of sunflower seed shells required less than 20 minutes. Rice husks had a gasification rate that was continuously decreasing whereas sunflower seed shells had a constant and then decreasing conversion rate. Beech wood had an intermediate behavior with a gasification time of around 40 minutes and a gasification rate that was constant and then increased.

3. Results of the interactions between materials

3.1. Influence of K_2CO_3 addition on pyrolysis and steam gasification

Pyrolysis and gasification of rice husks—slow-gasifying biomass—were carried out with K_2CO_3 added in two configurations: mixed and without contact in a divided crucible. Both configurations had approximately the same proportion of added K_2CO_3 , i.e. 7 wt%. This proportion corresponds to 4 wt% of K in the initial mixture (Table III.5). Such a high content (see natural contents < 1 wt% of K in raw biomass, in Table III.1) was selected to clearly observe the phenomena. Results were compared to rice husks and sunflower seed shells alone. The evolution with time of the normalized mass of the samples—including ashes—is presented in Figure III.9. As stated in the Materials and Methods section (section 1.3), the measured mass profiles were corrected by subtracting the equivalent mass profiles of pure inorganic compound.

Table III.5 | Inorganic composition of the mixture of rice husks and K_2CO_3 (in dry basis).

Biomass sample	Rice husks	Rice husks + 7wt% K_2CO_3	Sunflower seed shells
Ash at 550 °C (wt%)	14.6	20.3*	3.3
Si	63955	59518	194
K	5822	44632	9729
Ca	1797	1672	4489
Mg	659	613	1838
P	981	913	896
Na	413	384	9
Al	228	212	150
Fe	192	179	1099
SiO_2	97.2	62.8	1.3
K_2O	5.0	26.5	35.5
CaO	1.8	1.2	19.0
MgO	0.8	0.5	9.2
P_2O_5	1.6	1.0	6.2
Na_2O	0.4	0.3	0.0
Al_2O_3	0.3	0.2	0.9
Fe_2O_3	0.2	0.1	4.8
Main inorganic elements	Si – K – Ca	Si – K – Ca	K – Ca – Mg

*Theoretical, calculated as: $\%K_2CO_3 + (100 - \%K_2CO_3) \times \text{Ash of rice husks}$

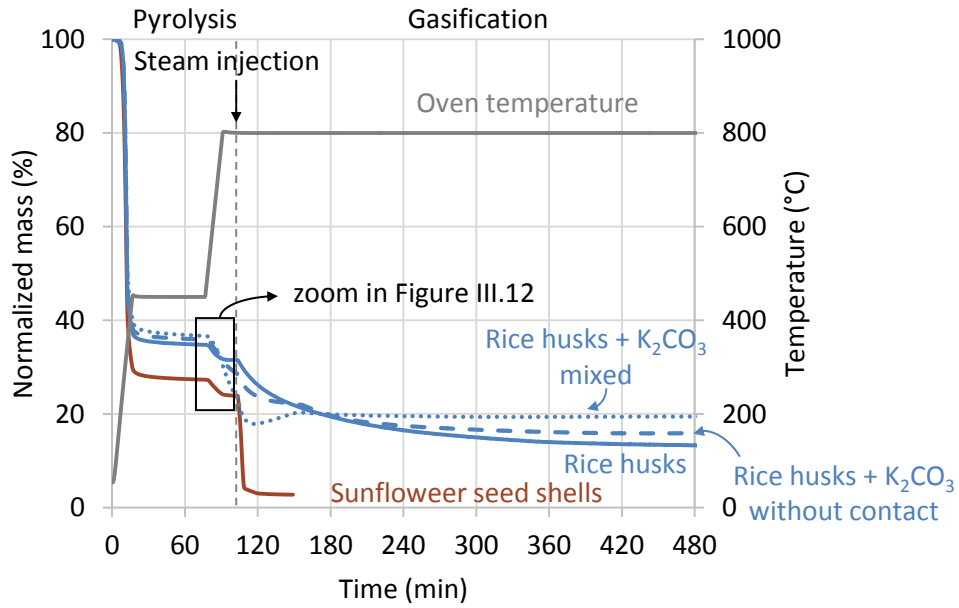


Figure III.9 | TGA of rice husks with and without added K_2CO_3 and of sunflower seed shells presented as the normalized mass as a function of time.

The results are also represented with the DTG curves in Figure III.10 and Figure III.11 (zoom).

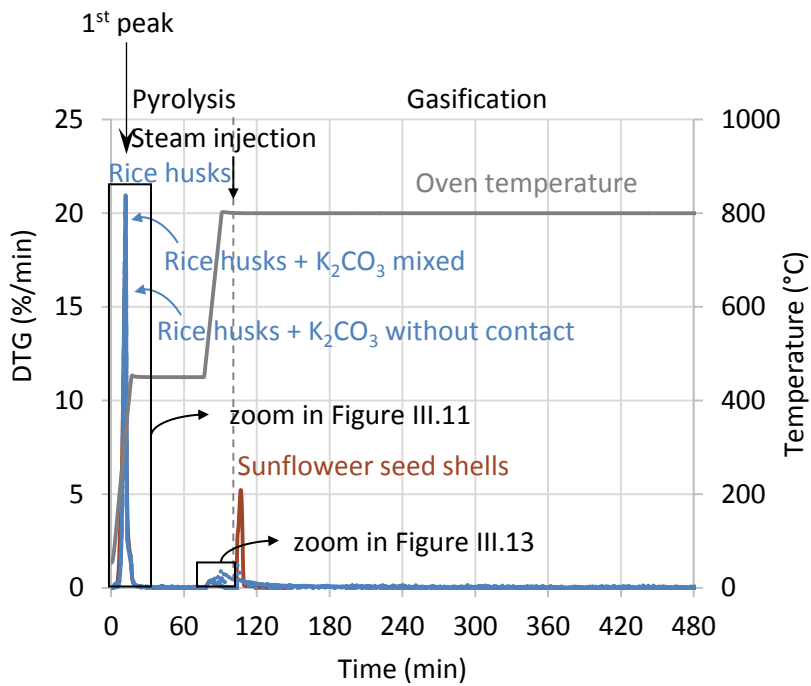


Figure III.10 | DTG as a function of time of rice husks with and without added K_2CO_3 and of sunflower seed shells.

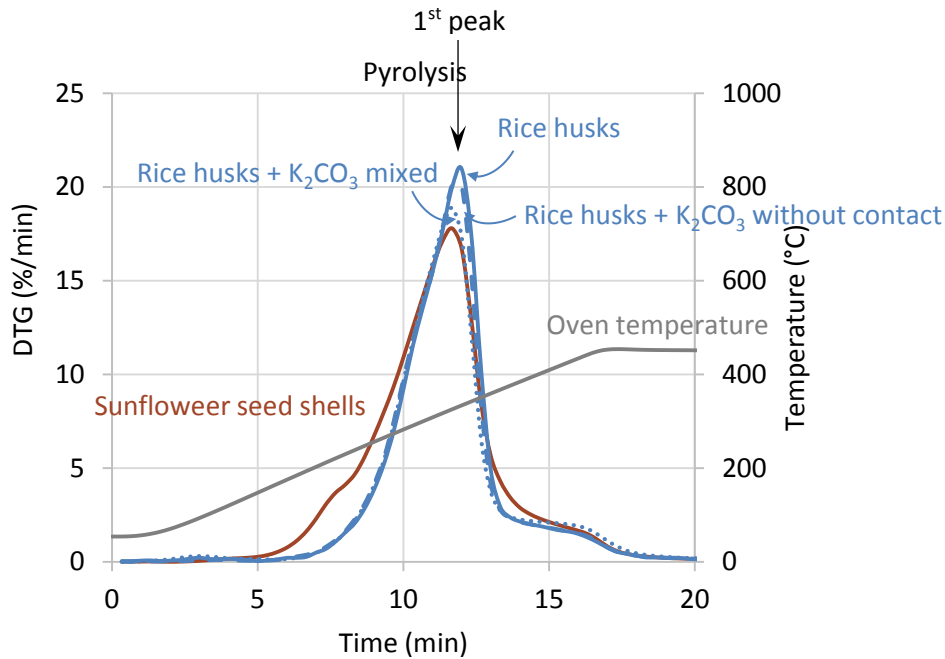


Figure III.11 | DTG as a function of time of rice husks with and without added K_2CO_3 and of sunflower seed shells. Zoom on 1st peak.

The apparent difference between the two biomass species during low temperature pyrolysis was due to the difference of ash content. When looking at the DTG curves it can be seen that all samples with and without K_2CO_3 had the same behavior during low temperature pyrolysis, i.e. **a first very high peak below 450 °C** (Figure III.11). It corresponds to the degradation of the biomass macromolecular constituents (de Wild, 2011).

Above 450 °C, the curves indicate that K_2CO_3 addition had an effect on both pyrolysis and gasification steps. For each step, the results are discussed in detail in the following sections. First, the behavior during high temperature pyrolysis is analyzed, i.e. above 450 °C. Then, the focus is put on the behavior during gasification. In a third section, the residues are characterized. Finally conclusions are given on the influence of K_2CO_3 addition.

3.1.1. Influence of K_2CO_3 addition on the pyrolysis reaction

Though the present study focuses on the gasification reaction, an effect of the K addition already appeared during the pyrolysis step at high temperature, before steam injection. Since the char formed during pyrolysis is the starting material of the gasification reaction, it is important to also investigate these phenomena.

3.1.1.1. First observations

Figure III.12 and Figure III.13 are zooms on the high temperature pyrolysis from Figure III.9 and Figure III.10 respectively. They show the evolution of the normalized mass and DTG of the samples during the thirty minutes preceding steam injection, i.e. during the heating from 450 to 800 °C.

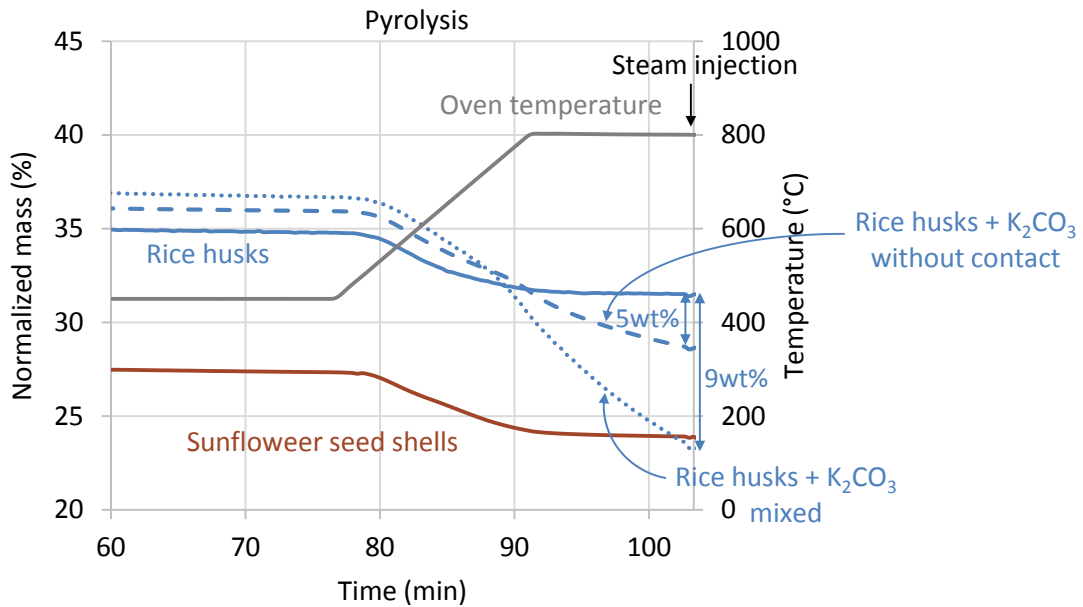


Figure III.12 | TGA of rice husks with and without added K_2CO_3 and of sunflower seed shells presented as the normalized mass as a function of time. Zoom on the high temperature pyrolysis.

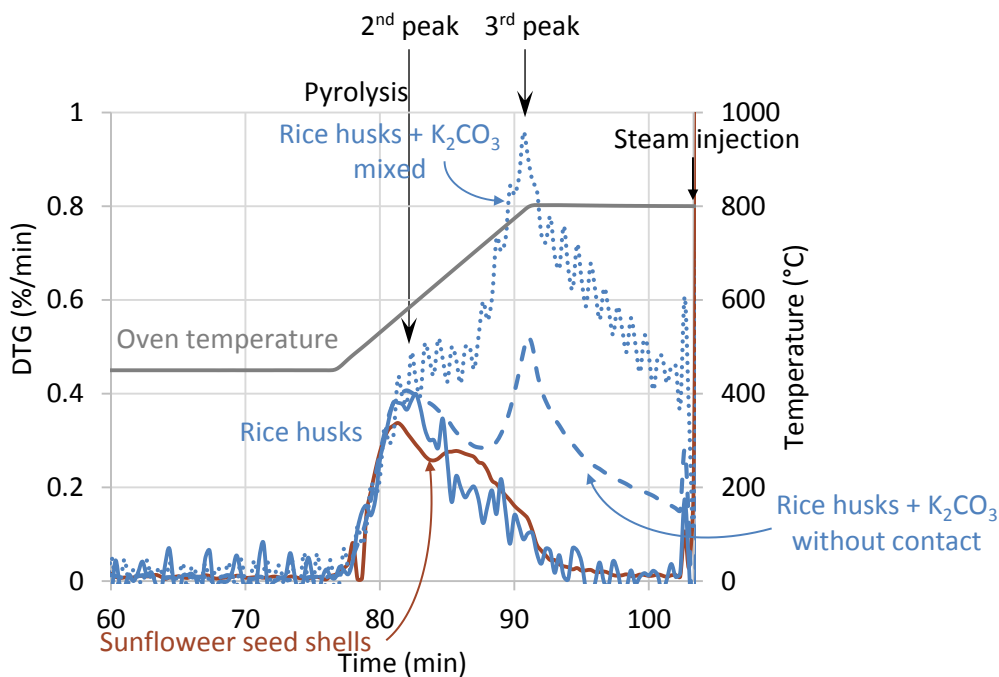


Figure III.13 | DTG as a function of time of rice husks with and without added K_2CO_3 and of sunflower seed shells. Zoom on the high temperature pyrolysis.

The oscillations observed for some of the curves were due to the experimental set-up and were considered as not significant.

Above 450 °C, a second DTG peak was observed around 82 min and 500 °C for all samples with and without added K_2CO_3 . It corresponds to the **typical mass loss observed when heating up the samples between 450 and 800 °C**, as seen with pure biomass, and is due to a residual devolatilization of the char.

However, **when K_2CO_3 was added to rice husks (mixed and without contact), a third DTG peak was observed** close to the beginning of the 800 °C holding time. The effect was stronger when K_2CO_3 was mixed with rice husks. Nevertheless, it appeared even if rice husks were not in contact with the added K_2CO_3 which means it was related to the gas phase and probably to K volatilization. The stronger effect in the case of the mixture can then be explained by a higher concentration of K-compound in the gas layer around the biomass in this case.

3.1.1.2. Additional experiments

Three additional experiments were conducted in order to determine the origin of this third DTG peak.

In the additional set of experiments n°1, the same experiments as previously were conducted but samples were heated up to 1000 °C instead of 800 °C. It aimed to determine the temperature of the third DTG peak maximum. The same procedure was applied to K_2CO_3 alone. Results are presented in Figure III.14 as DTG as a function of temperature between 450 °C and 1000 °C for rice husks alone, K_2CO_3 alone and the two added without contact.

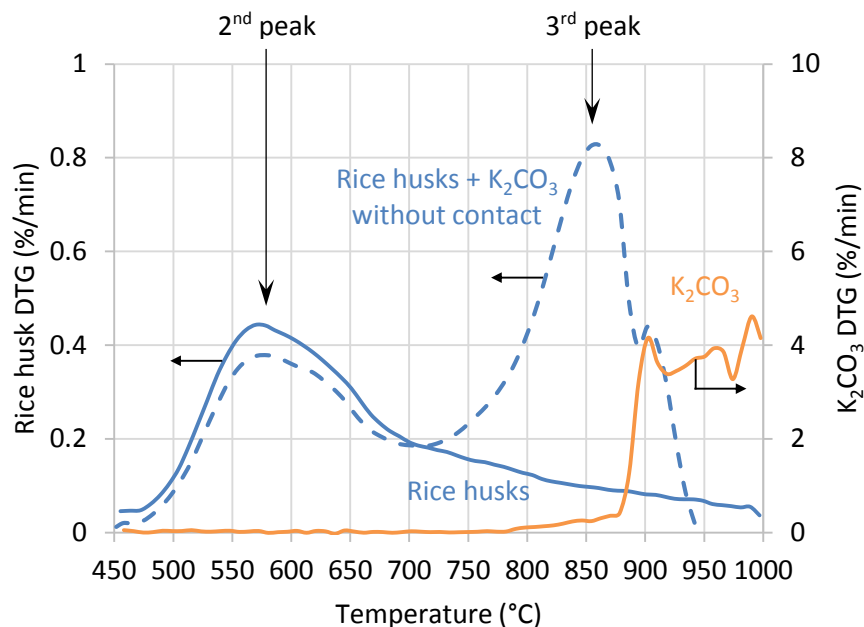


Figure III.14 | DTG as a function of temperature during pyrolysis between 450 °C and 800 °C of rice husks alone, K_2CO_3 alone and rice husks with K_2CO_3 added without contact.

Results confirmed that the third DTG peak had in reality its maximum at a temperature around 860 °C after starting around 700 °C. It occurred just before the high mass loss observed from around 900 °C for K_2CO_3 alone, corresponding to its melting at 901 °C (Bale et al., 2002). A slight mass loss of pure K_2CO_3 started from around 750-800 °C.

In the additional experiment n°2, the same procedure was conducted on rice husks with K_2CO_3 added without contact but it was stopped after the pyrolysis step at 800 °C, i.e. before steam injection. Optical microscope observation of the crucible before and after the experiment are presented in Figure III.15.

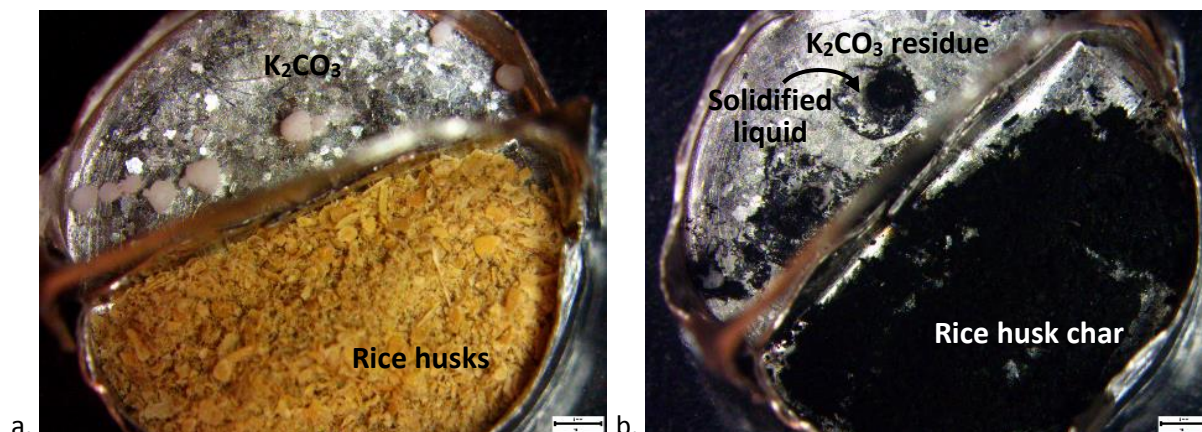


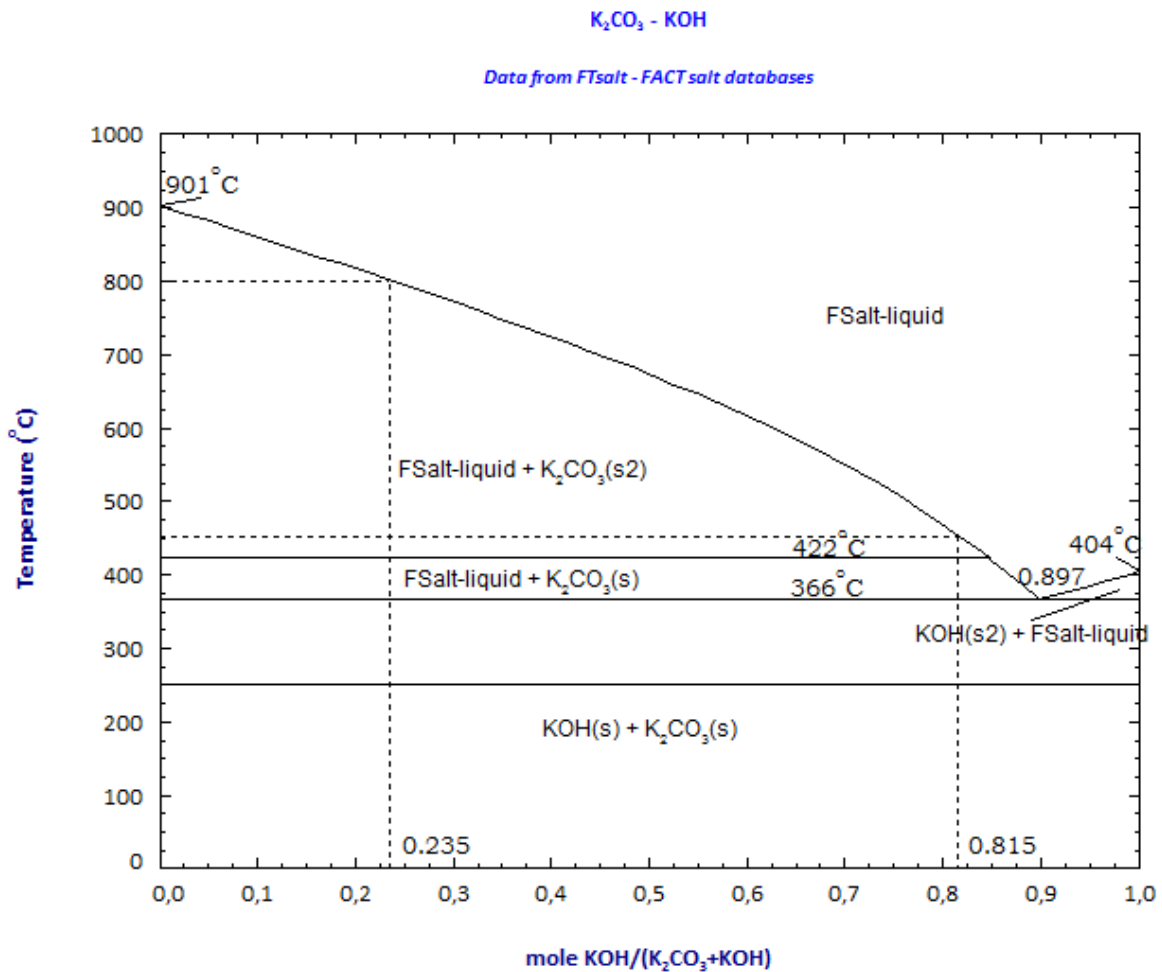
Figure III.15 | Rice husks with K_2CO_3 added without contact a. before and b. after pyrolysis until 800 °C in the TGA, i.e. procedure stopped before steam injection.

Rice husk chars did not show any visual particularity at this scale. On the K_2CO_3 side, grains which were initially white were covered with a black layer after pyrolysis until 800 °C and material under each grain suggested a partial fusion. The black layer most likely was carbon deposited on top of the inorganic residue. It is in agreement with literature observations, where authors observed higher char yields with K impregnation due to condensation of tars (Di Blasi et al., 2009; Zaror et al., 1985; Zhao et al., 2013). However, they observed a competition between this char formation and tar cracking (Zaror et al., 1985). Regarding the residue under the black layer, it could not have been pure K_2CO_3 (whose melting point is 901 °C (Bale et al., 2002), i.e. above the pyrolysis temperature) but a material with a lower melting point. Since liquid formation is associated to a higher volatilization, it is in agreement with the fact that the third DTG peak also occurred before the pure K_2CO_3 melting point. These results indicate that a reaction occurs on the K_2CO_3 side when it is in presence of biomass, even without contact.

It is known that pyrolysis gases (CO_2 , H_2O , CO , H_2) and inorganic gases (H_2S , NH_3 , HCl , KCl , etc.) are released during biomass devolatilization (Björkman and Strömberg, 1997; Bridgwater, 2015). Therefore, the liquid observed at 800 °C could have been from the reaction of K_2CO_3 with one of these gases.

The residue at 800 °C on the K_2CO_3 side was analyzed by non-quantitative ionic chromatography (Annex G). Only K^+ and CO_3^- were found. This was confirmed by SEM-EDX analysis where only K, C and O were detected (Annex G). H cannot be detected by either of these two methods.

Therefore K_2CO_3 most likely reacted with $H_2O(g)$ originating from biomass devolatilization. The residue was then a mixture of K_2CO_3 and KOH where a core of K_2CO_3 was at equilibrium with a liquid phase (solidified at ambient temperature). The phase diagram of K_2CO_3 and KOH from the FTsalt – FACT salt database (Bale et al., 2002) is presented in Figure III.16.

Figure III.16 | KOH-K₂CO₃ phase diagram.

The phase diagram predicts that, at 800 °C, solid K₂CO₃ is in equilibrium with a liquid for compositions up to 23.5mol% KOH. This is a reasonable composition that could have been obtained from the reaction with H₂O(g) from the biomass devolatilization. It also predicts that a liquid phase can appear at 450 °C, the temperature of the first plateau of the TGA procedure.

Additional experiment n°3 was conducted to simulate this H₂O(g) release from the devolatilization of biomass and its influence on pure K₂CO₃. The same pyrolysis procedure was applied to K₂CO₃ alone but steam was injected for 21 min during the 450 °C plateau. Results are shown in Figure III.17 and Figure III.18 and compared to the normalized mass profile of K₂CO₃ when the gas atmosphere is only N₂.

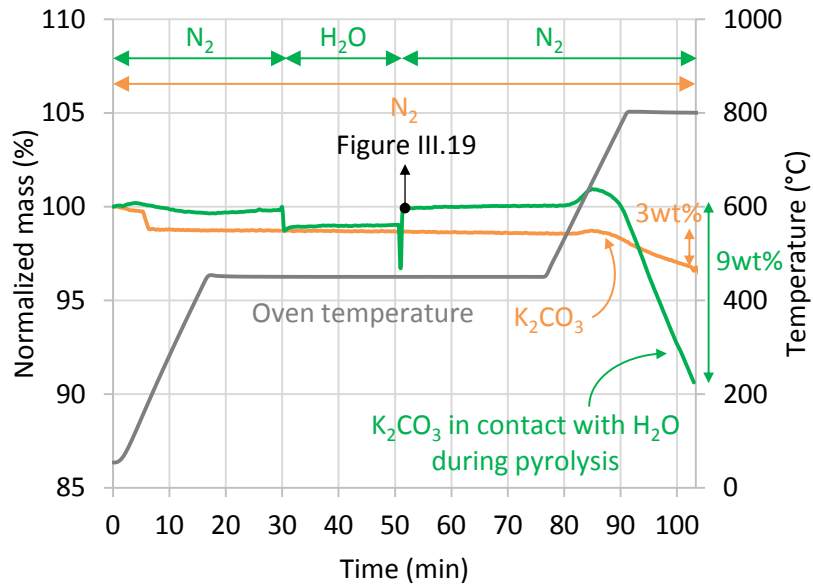


Figure III.17 | TGA of pure K_2CO_3 under N_2 atmosphere and with injection of steam for 21 min during the 450 °C plateau.

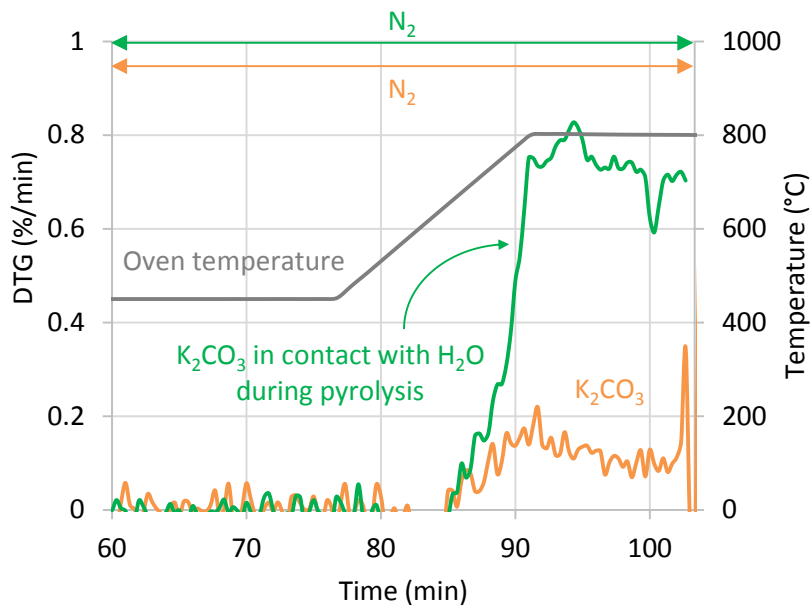


Figure III.18 | Zoom on the 450 to 800 °C section of the DTG curve of pure K_2CO_3 under N_2 atmosphere and with injection of steam for 21 min during the 450 °C hold.

It must be noted that the apparent slightly lower mass observed during H_2O injection in Figure III.17 was only due to a shift in the baseline because of the different gas atmosphere. It had therefore no physical meaning.

When steam was injected at 450 °C to K_2CO_3 alone, no significant change in mass was observed (Figure III.17). A repetition of the experiment was stopped after steam injection at 450 °C. Liquid was observed (Figure III.19) which confirms the K_2CO_3 -liquid equilibrium at this temperature that was predicted at thermodynamic equilibrium (Figure III.16).

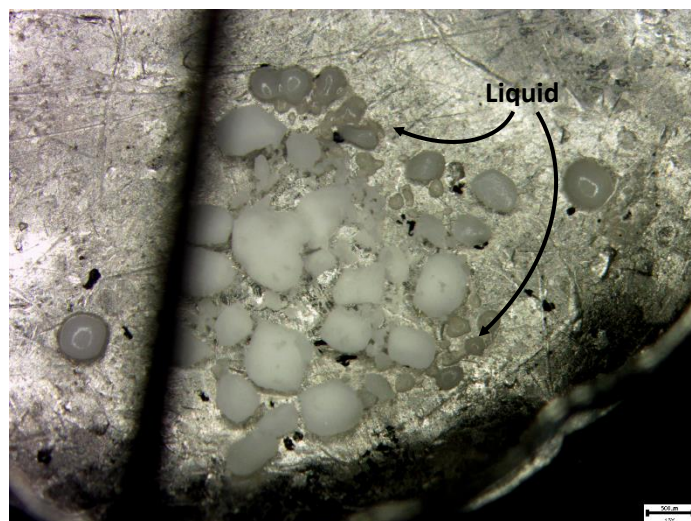


Figure III.19 | K_2CO_3 after steam injection at 450 °C.

However, a difference between the mass profiles of the two experiments occurred when the sample was further heated up to 800 °C. Indeed, as previously observed, the mass loss of pure K_2CO_3 under N_2 atmosphere was very low, i.e. around 3wt% (Figure III.17). On the opposite, **after K_2CO_3 was put in a steam atmosphere for 21 min at 450 °C, a higher mass loss occurs at high temperatures, i.e. around 9wt% (Figure III.17).** This mass loss started close to the beginning of the 800 °C holding time, from around 650-700 °C (Figure III.18). **The temperature of this mass loss corresponded to the temperature where the third DTG peak at the beginning of the 800 °C holding time was observed when K_2CO_3 was added to rice husks (Figure III.13).**

3.1.1.3. Pyrolysis results summary and comparison to literature

These observations confirm that $H_2O(g)$ reacted with pure K_2CO_3 to form a mixture of K_2CO_3 and KOH where a core of K_2CO_3 was at equilibrium with a liquid phase (solidified at ambient temperature). This material had similar properties at moderate temperatures but a higher volatilization above around 700 °C. Therefore, the third DTG peak was related to the volatilization of this mixture.

However, the whole mass loss corresponding to this third DTG peak of rice husks with added K_2CO_3 could not only be explained by an earlier volatilization of K_2CO_3 . Indeed, compared to rice husks alone, the third DTG peak corresponded to an additional mass loss of approximately 5wt% in the case where K_2CO_3 was added without contact and 9wt% when it was mixed (Figure III.12) while only 0.6wt% of this mass loss could be attributed to a loss of K_2CO_3 from the previous results (with 20vol% steam for 21 minutes), i.e. 9wt% (Figure III.17) of the 7wt% added K_2CO_3 . The steam concentration and duration could have been different but most likely remained in this order of magnitude. **This indicates that the third DTG peak had an additional contribution than only the K_2CO_3 –KOH volatilization. It was then attributed to the devolatilization of the carbon matrix catalyzed by a K-compound released to the gas phase.**

In literature, authors do not usually conduct pyrolysis at such high temperatures. Indeed, as previously stated, the main mass loss occurs below 450 °C so studies are focused on that temperature range. However, other fields can shed light on the present results, in particular the literature regarding carbon activation. Carbons can be activated, i.e. the porosity of carbon materials can be increased, through two types of processes: physical or chemical. Physical activation, also called thermal activation, consists of gasification under CO₂, H₂O or their mixture. Chemical activation consists of carbonization, i.e. pyrolysis, of the carbonaceous feedstock with a chemical compound (Marsh and Rodríguez-Reinoso, 2006a). The most commonly used chemicals are phosphoric acid (H₃PO₄), zinc chloride (ZnCl₂), potassium hydroxide (KOH) and potassium carbonate (K₂CO₃) (Marsh and Rodríguez-Reinoso, 2006b). In the case of a biomass or char sample impregnated with a K-compound, it has been shown that pyrolysis at 700 °C or below induces a low porosity while at 850 °C or above it produces activated carbons with a high porosity. Moreover, at these high temperatures, the char yield is lower (Marsh and Rodríguez-Reinoso, 2006b). These observations are in accordance with the results from the present work where pyrolysis at high temperature in the presence of a K-compound induced an additional mass loss, i.e. third DTG peak. However, in the case of activated carbons the K-compound is added through impregnation of an aqueous solution, or occasionally through dry mixing (Amoco process) (Marsh and Rodríguez-Reinoso, 2006b), whereas in the present study the effects have been observed including when K₂CO₃ was not in contact with the biomass.

For the first time it is here demonstrated that the effect occurs through the gas phase. The main explanation regarding the mechanism of action involves the intercalation of K followed by its explosive removal to form the pores (Marsh and Rodríguez-Reinoso, 2006b). As stated in Chapter I, the intercalation mechanism is not likely in the case of steam gasification (McKee, 1983; Tromp and Cordfunke, 1984). However, in the case of high temperature pyrolysis, the instability of the intercalated compounds can explain the observed phenomenon (Marsh and Rodríguez-Reinoso, 2006b).

3.1.2. Influence of K₂CO₃ addition on the gasification reaction

3.1.2.1. First observations

After pyrolysis, K₂CO₃ had an effect on the gasification step. Figure III.20 and Figure III.21 show the gasification solid conversion, and conversion rate respectively, of rice husks with and without added K₂CO₃ compared to that of sunflower seed shells.

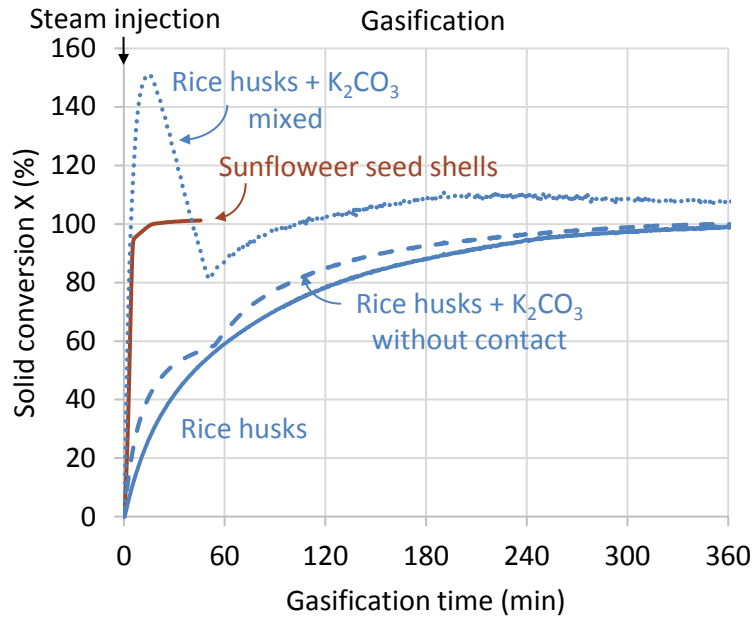


Figure III.20 | Gasification solid conversion as a function of time of rice husks with and without added K₂CO₃ and of sunflower seed shells.

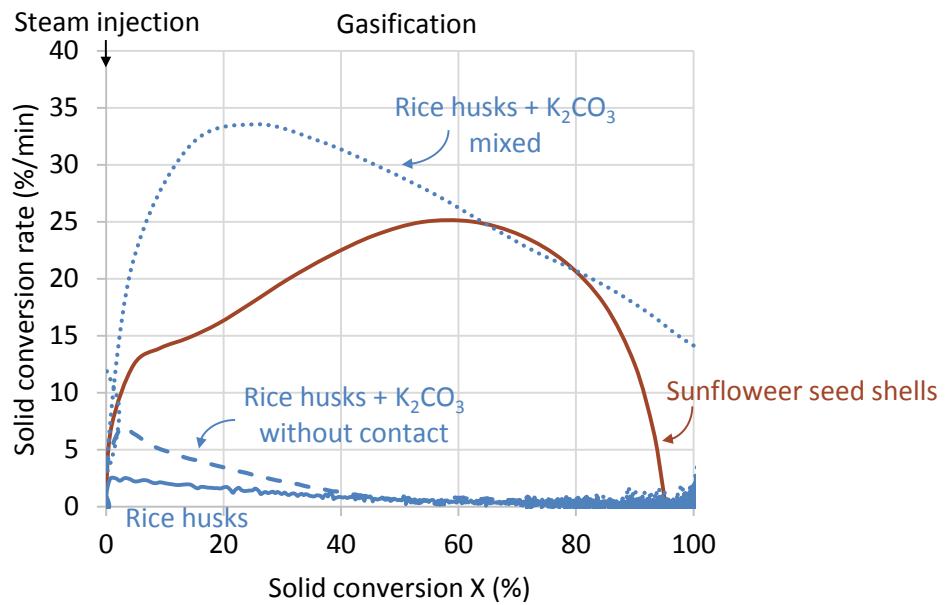


Figure III.21 | Solid conversion rate as a function of the conversion of rice husks with and without added K₂CO₃ and of sunflower seed shells.

It must be noted that the reaction continued after 360 min and all samples stabilized at 100% conversion as fixed by the solid conversion X calculation (Chapter II).

As stated in the Materials and Methods section (see 1.3), the results were corrected by subtracting the equivalent mass profiles of pure K_2CO_3 to the measured mass profiles of the total sample. Therefore, if the rice husks and K_2CO_3 behaviors were independent, their mass profiles would have been additive and the presented equivalent mass profile of rice husks would have been similar to rice husks alone. Yet, the conversion profile of the sample of rice husks and K_2CO_3 mixed went above 100%. In additions, both samples with added K_2CO_3 , mixed and without contact, had a sudden slope change approximately 50 min after steam injection, which corresponds to the completion of the pure K_2CO_3 volatilization that was subtracted to the results. Moreover, both curves were above the curve of rice husks alone. These observations show that there was an interaction between the biomass and the inorganic sample both when K_2CO_3 was mixed and without contact. The behaviors of the samples could not be assessed through the simple addition of the behaviors of the pure rice husks and K_2CO_3 . This means that the equivalent rice husks profiles presented do not represent the real mass loss on the rice husks side. Therefore, quantitative conclusions could not be drawn from these data but trends still could be analyzed.

When comparing the addition mode of K_2CO_3 , it can be seen that mixing induced a stronger catalytic effect during gasification. However, even if it was weak, the effect of K_2CO_3 without contact with rice husks was present. This demonstrates that it acted, at least partially, through the gas phase. The stronger effect in the case of the mixture can then be explained by a higher concentration of K-compound in the gas layer around the biomass in this case.

1.1.1.1. Additional experiment

An additional experiment was designed to investigate if a reaction during pyrolysis influenced the behavior during gasification. Pyrolysis of rice husks with added K_2CO_3 without contact was carried out and the resulting char was gasified alone, after the residue on the K_2CO_3 side was removed. Results are shown in Figure III.22.

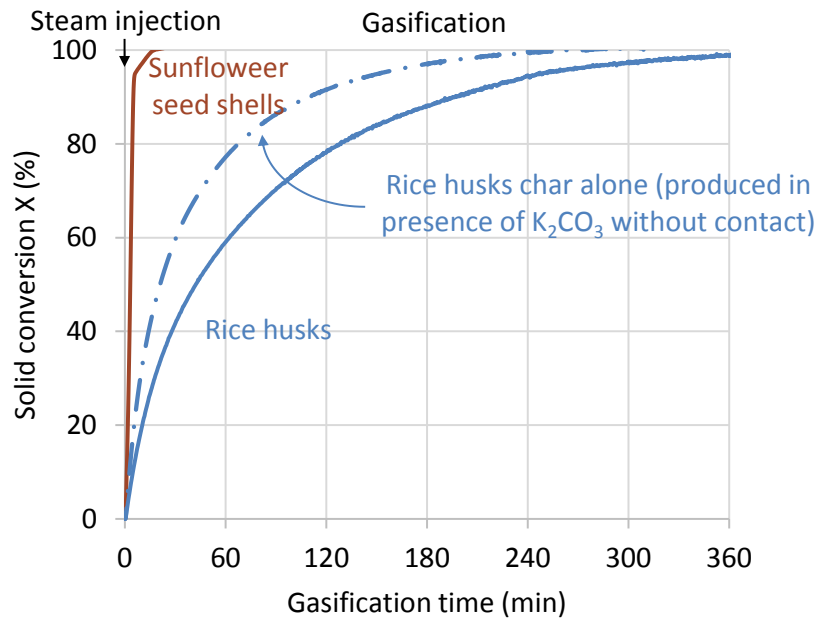


Figure III.22 | Gasification solid conversion as a function of time of rice husk char alone produced in presence of K_2CO_3 without contact.

In this experiment, only char was gasified, therefore no subtraction of a K_2CO_3 profile needed to be done. This explains that the curve does not have the sudden slope change like the previous ones. It is seen directly that the gasification rate of rice husks increased while K_2CO_3 was not present anymore during gasification. Its average reactivity between 1 and 80% conversion increased from 1.4 to $2.2 \text{ \%} \cdot \text{min}^{-1}$. **This is an important new result that demonstrates that the interaction between K_2CO_3 and char during the pyrolysis step catalyzes a subsequent gasification. Moreover, this effect occurs without contact between the biomass and the inorganic compound, so through the gas phase during pyrolysis.**

3.1.3. Characterization of the ashes

3.1.3.1. First observations

From the normalized mass profiles presented in Figure III.9, it is observed that when K_2CO_3 was added to rice husks, mixed or without contact, the mass stabilized at a higher ash yield (19.7 and 15.2wt\% respectively) than rice husks alone (13.6wt\%) (Table III.6).

Table III.6 | Gasification ash yield measured in TGA and associated theoretical yields.

	Rice husks	Rice husks + K_2CO_3 without contact	Rice husks + K_2CO_3 mixed
Added K_2CO_3 (wt%)	—	7.0 ± 0.3	
Experimental (wt%)	13.6 ± 0.5	15.2 ± 0.7	19.7 ± 1.3
Theoretical if all K_2O remains* (wt%)	—	17.4 ± 0.8	
Theoretical if all K_2CO_3 remains** (wt%)	—	19.6 ± 0.8	

$$* \text{Ash}_{with K_2O} = \%K_2CO_3 \times \frac{M_{K_2O}}{M_{K_2CO_3}} + (100 - \%K_2CO_3) \times \text{Ash}_{rice \text{ husks}}$$

$$** \text{Ash}_{with K_2CO_3} = \%K_2CO_3 + (100 - \%K_2CO_3) \times \text{Ash}_{rice \text{ husks}}$$

This higher ash yield suggests that at least a part of the added K_2CO_3 was incorporated to the biomass ashes. The increase was observed including in the case of addition without contact. Therefore, the K_2CO_3 was incorporated after its volatilization. As a result, the K-species in the ashes could have been another form than directly K_2CO_3 , such as K_2O . The higher ash yield value corresponds to the theoretical ash yield calculated if all the added K_2CO_3 was incorporated to the ashes, either directly as K_2CO_3 (19.6wt%) or as K_2O (17.4wt%).

To investigate this supposed reaction of a K-species with the rice husk ashes, the ashes from the previous experiments were characterized through optical microscope and SEM-EDX.

Pictures from microscope observation of ashes from rice husks alone and mixed with K_2CO_3 are presented in Figure III.23 and Figure III.24 respectively.



Figure III.23 | Ashes from pyrolysis and gasification of rice husks.



Figure III.24 | Ashes from pyrolysis and gasification of rice husks with mixed K_2CO_3 (same aspect without contact).

Ashes in the presence of K_2CO_3 showed some black glassy agglomerates on top of the white ashes (Figure III.24) that were absent from rice husks alone (Figure III.23). It suggests the formation of liquid at the process temperature that solidified at ambient temperature. The phase diagram of SiO_2 and K_2O from the FToxid – FACT oxide database (Bale et al., 2002) presented in Figure III.25 confirms that liquid can be present at the process temperature of 800 °C. The $SiO_2/(K_2O+SiO_2)$ ratio for a mixture of rice husks and 7wt% of K_2CO_3 is of 0.79 (from rice husks composition in Table III.1). However, concentrations could have varied largely locally to reach lower or higher ratios. The change in appearance in the presence of K_2CO_3 —including without contact—confirmed a reaction occurred between the added K_2CO_3 or one of its decomposition products and the inorganic compounds naturally contained in the biomass—most likely SiO_2 which represents 94 wt% of the inorganic content of rice husks.

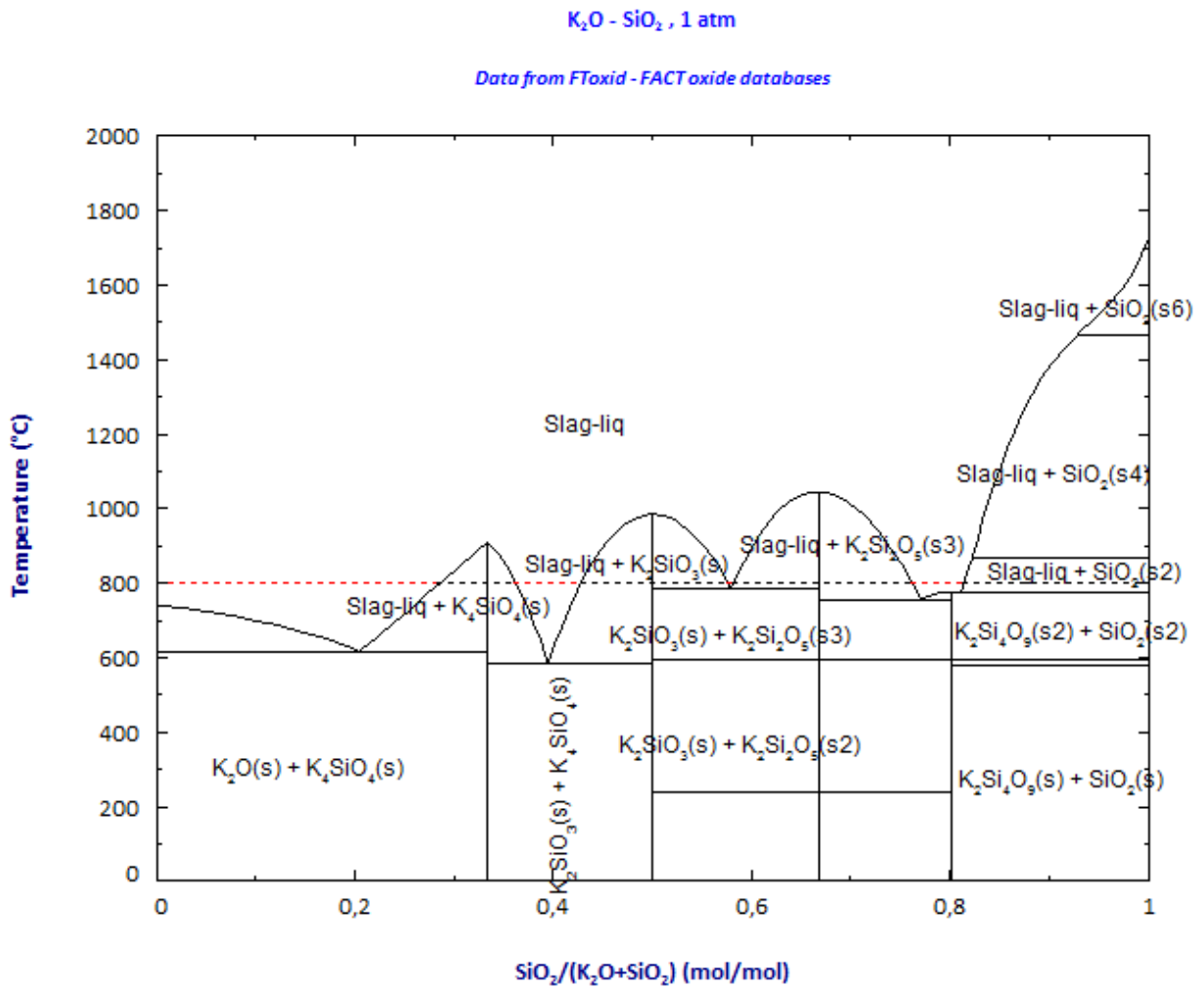


Figure III.25 | SiO₂-K₂O phase diagram. The dotted line is the 800 °C isotherm with the red portions corresponding to liquid phases.

The same ashes were characterized through SEM-EDX, as presented in Figure III.26 and Figure III.27 for rice husks alone and with K₂CO₃ without contact.

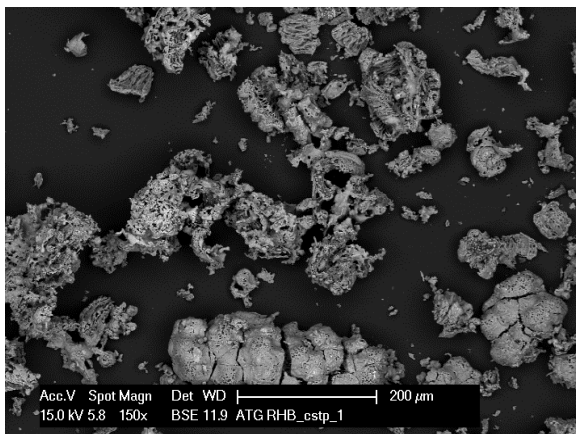


Figure III.26 | SEM observation of ashes from pyrolysis and gasification of rice husks.

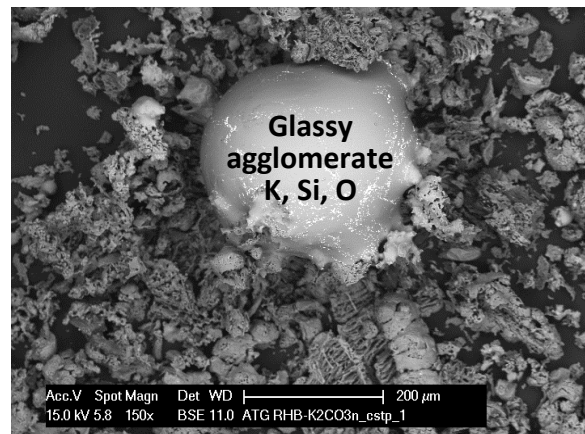


Figure III.27 | SEM observation of ashes from pyrolysis and gasification of rice husks with K₂CO₃ without contact (same aspect mixed).

Again with SEM, the typical rice husk ashes and the glassy agglomerates could be distinguished. The EDX analysis confirmed that the typical rice husk ashes contained mainly SiO_2 . In the glassy agglomerates, the detected elements were K, Si and O. This supports the idea of K-silicates formation.

This demonstrates that, in addition to influencing the pyrolysis and gasification of the carbonaceous matrix, the added K_2CO_3 also reacts with the inorganic elements inherent to the rice husks. This is supported by literature observations of the reaction between K-compounds and SiO_2 to form K-silicates, as described in Chapter I (Gupta et al., 2018; Kannan and Richards, 1990; Link et al., 2010). However, our study suggests that the reaction involves the gas phase, which is not mentioned in literature.

It results in a limitation of the catalysis of the gasification by K_2CO_3 due to its reaction on the SiO_2 inherent to the rice husks.

3.1.3.2. Additional experiments

To demonstrate these competing interactions, two experiments were conducted: one on beech wood and the other on pure silica, both with K_2CO_3 added without contact. In both cases the same pyrolysis and gasification TGA procedure was applied. In the first experiment, beech wood had a very low SiO_2 content so the K_2CO_3 should have induced a stronger catalysis than for rice husks. The second experiment, on pure silica, aimed to check how K_2CO_3 would react with SiO_2 through the gas phase during the pyrolysis and gasification procedure.

For the first experiment, on beech wood, the normalized mass evolution is shown in Figure III.28 for beech wood alone and with K_2CO_3 without contact during pyrolysis and gasification, with a zoom on the high temperature pyrolysis in Figure III.29. The gasification conversion profiles are shown in Figure III.30.

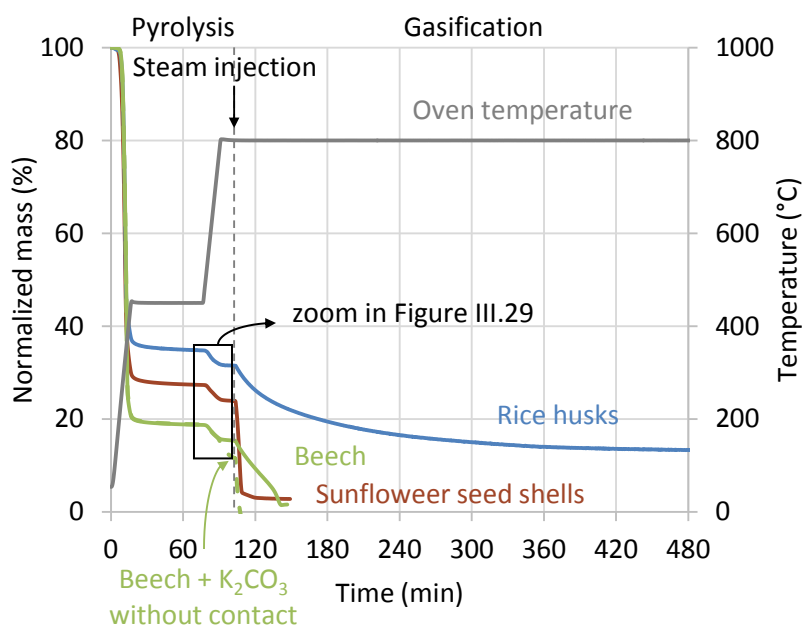


Figure III.28 | TGA of beech wood with and without added K_2CO_3 and of rice husks and sunflower seed shells presented as the normalized mass as a function of time.

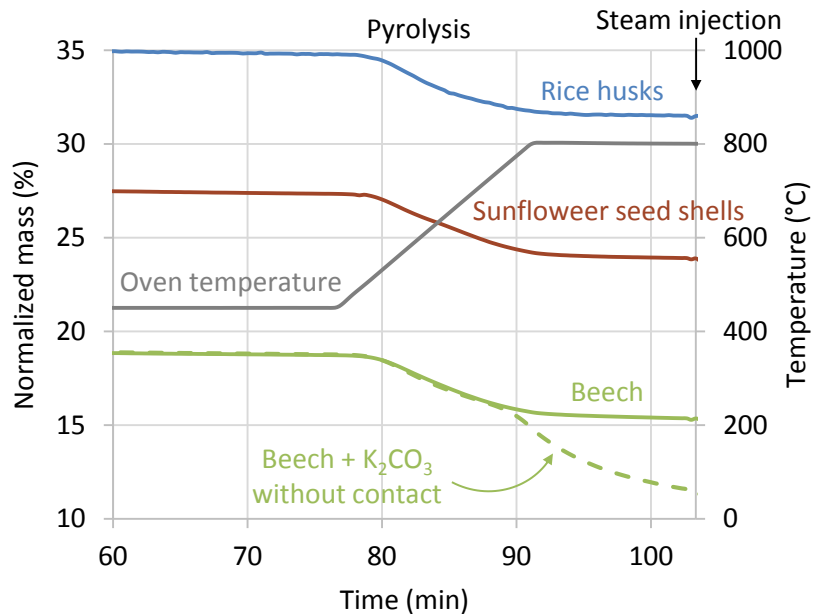


Figure III.29 | TGA of beech wood with and without added K_2CO_3 and of rice husks and sunflower seed shells presented as the normalized mass as a function of time. Zoom on the high temperature pyrolysis.

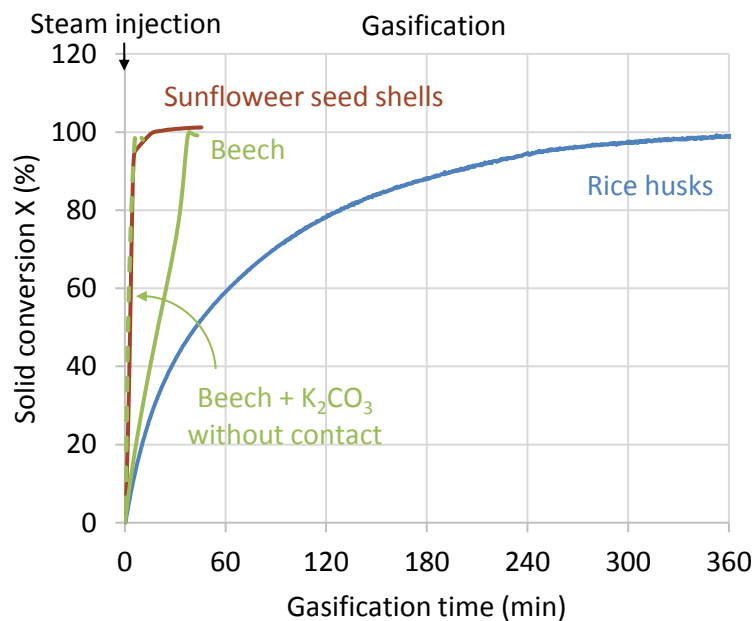


Figure III.30 | Gasification solid conversion as a function of time of beech wood alone and with added K_2CO_3 , compared to rice husks and sunflower seed shells.

The additional mass loss during high temperature pyrolysis (Figure III.29) occurred for beech in the same way as for rice husks (third DTG peak).

Regarding gasification (Figure III.30), when K_2CO_3 was added without contact, beech wood reactivity greatly increased (average reactivity increasing from $r_{1-80\%} = 4.9$ to $42.4\% \cdot \text{min}^{-1}$). It reached sunflower seed shells level ($r_{1-80\%} = 30.3\% \cdot \text{min}^{-1}$). The catalysis was very high compared to what was observed in the case of rice husks (average reactivity increasing from $r_{1-80\%} = 1.4$ to $2.2\% \cdot \text{min}^{-1}$). As stated previously, beech had a very low ash, and Si, content. **Therefore it confirmed that the competing reaction of K_2CO_3 decomposition product on the inherent SiO_2 prevented it to catalyze the gasification.**

For the second experiment, on pure silica, results were expressed as a silica equivalent mass by subtracting the mass profile of pure K_2CO_3 and are shown in Figure III.31.

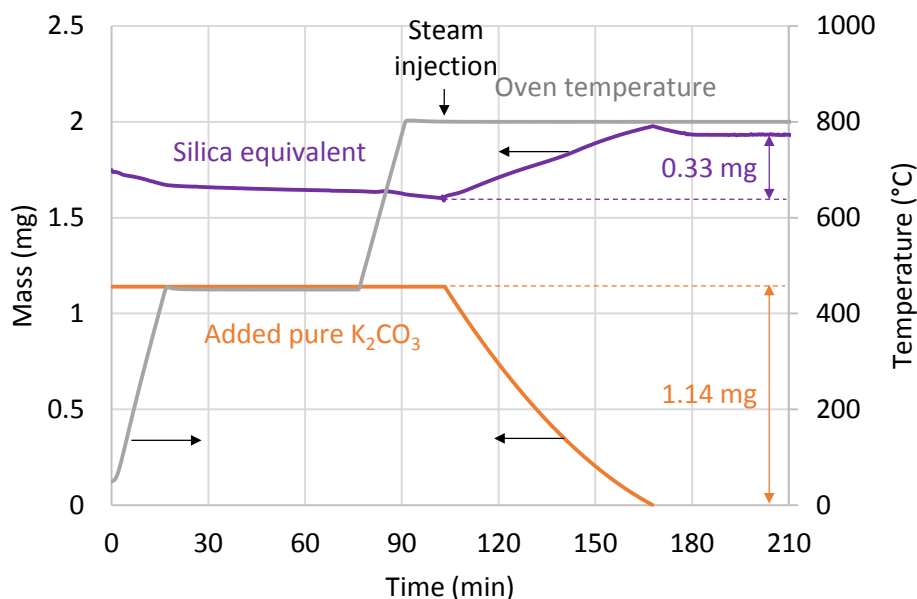


Figure III.31 | Mass evolution over time of the silica equivalent (purple curve) and the K_2CO_3 (orange curve) during the pyrolysis and gasification procedure applied to silica with K_2CO_3 added without contact.

There was an increase of mass of the silica after steam injection and K_2CO_3 volatilization (purple curve in Figure III.31). At the end of the experiment, the whole mass of K_2CO_3 was volatilized. This suggests that at least a part of the volatilized K_2CO_3 reacted with SiO_2 . If the mass gain corresponded directly to K_2CO_3 , it means that 29wt% ($= 0.33 \text{ mg} / 1.14 \text{ mg}$, Figure III.31) of the initial mass reacted. If the mass gain rather corresponded to K_2O from the decomposition of K_2CO_3 , the mass gain corresponded to 42wt% ($= 0.33 \text{ mg} / (1.14 \text{ mg} \times M_{K_2O} / M_{K_2CO_3})$, Figure III.31) of the theoretical initial K_2O . In both cases, that indicates that a reaction occurred and that a fraction of the K_2CO_3 volatilization products was bonded to the silica.

The residue was characterized by SEM-EDX as presented in Figure III.32.

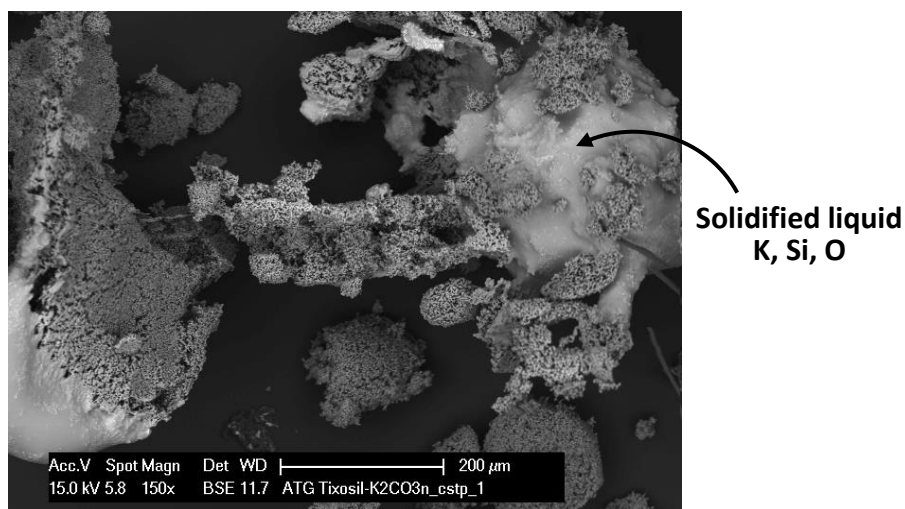


Figure III.32 | SEM observation of the residue after the TGA of silica with K_2CO_3 added without contact.

Even though K_2CO_3 was added without contact, phases containing K, Si and O were found on residue on the silica side of the crucible. This confirms that a reaction occurred through the gas phase. Authors in literature already observed a reaction between K_2CO_3 and SiO_2 , either under a steam or a CO_2 atmosphere (Anicic et al., 2018; Zhao et al., 2018). However, they only worked in the case of mixtures. The present work demonstrates for the first time in a direct manner that the gas phase is involved.

These TGA and SEM-EDX characterizations on silica with K_2CO_3 added without contact confirmed the results of the experiments on rice husks with K_2CO_3 added without contact presented above. The volatile decomposition products of K_2CO_3 react with SiO_2 through the gas phase.

3.1.4. Conclusions on the influence of K_2CO_3 addition

The addition of K during the pyrolysis and gasification of rice husks had effects at several levels. It influenced the kinetics of both pyrolysis and gasification steps and it interacted with the inorganic compounds inherent to the biomass.

It is important to note that all these effects occurred whether K_2CO_3 was in contact or not with the biomass. This highlights the fact that K_2CO_3 mechanisms of action are through the gas phase, with the formation of $KOH(g)$. Effects observed in the case of mixtures were stronger than without contact which can be explained by a higher concentration of K-compound in the gas layer around the biomass in this case.

The effects of K_2CO_3 on biomass pyrolysis and gasification demonstrated in the present study are summarized in Figure III.33.

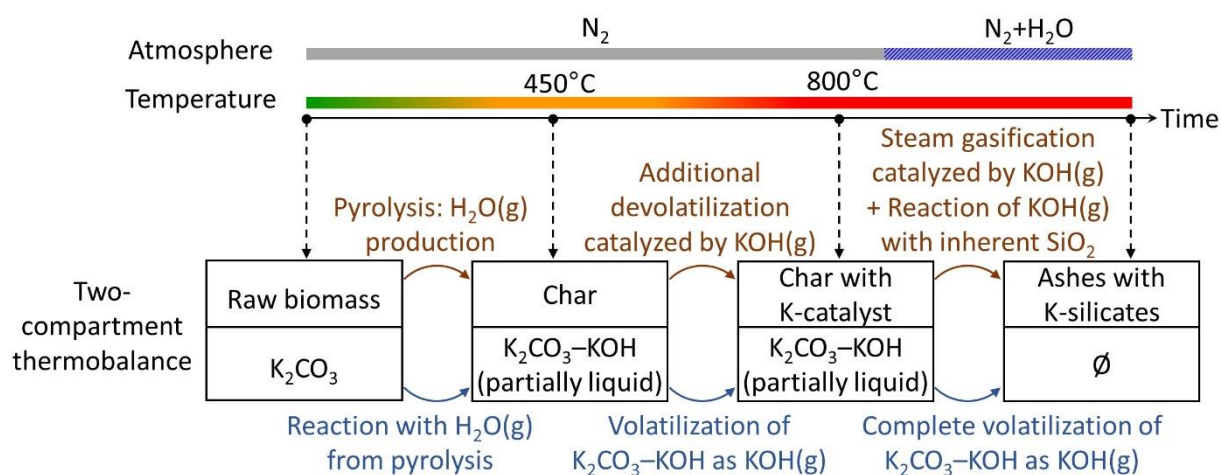


Figure III.33 | Scheme of the effects of K_2CO_3 on biomass pyrolysis and gasification.

It was demonstrated that the interaction of K_2CO_3 with the biomass during the pyrolysis was decisive for the ulterior gasification. Indeed, catalysis was observed including when the two materials were in presence only during pyrolysis and not during gasification.

However, the catalytic effect remained weaker than what has been observed in literature in the case of impregnation or occasionally mixing, as described in Chapter I (Feng et al., 2018b; Mudge et al., 1979; Sueyasu et al., 2012). This is attributed to the fact that the present work intended to catalyze rice husks that have a high content in Si, while most literature studies work with materials with a low ash content (Bourraoui et al., 2016; Huang et al., 2009; Kirtania et al., 2017; Kramb et al., 2016, 2017; Lahijani et al., 2013; Meijer et al., 1994; Perander et al., 2015; Zhang et al., 2008). Hence, we have confirmed this fact by experiments on beech wood that has a very low Si content. Along with the characterization of the ashes from the TGA experiments, these results **highlighted a competition between on the one hand the influence of K_2CO_3 on the biomass pyrolysis and char gasification kinetics and on the other hand its interaction with the SiO_2 inherent to the rice husks.**

As stated in Chapter I, Si is known to react with K and inhibit its catalytic effect (Dupont et al., 2016; Kannan and Richards, 1990; Link et al., 2010). However, this has not been demonstrated directly in literature. Indeed, works investigating the influence of SiO_2 on kinetics are usually based on correlations and not on experimental additions of SiO_2 (Bach-Oller et al., 2019; Dupont et al., 2016; Link et al., 2010; Zahara et al., 2018; Zhang et al., 2008). As a result, the following section focuses on the particular influence of SiO_2 on sunflower seed shells that gasify fast.

3.2. Influence of the addition of SiO_2 on steam gasification

Gasification of sunflower seed shells—fast-reacting biomass species—was carried out with addition of silica in various conditions. The latter were chosen to characterize the influence of three parameters: the mode of addition of silica (mixture or without contact), its crystalline form (amorphous or quartz) and its concentration. Results were compared to sunflower seed shells alone and to rice husks that naturally contain approximately 14 wt% SiO_2 .

3.2.1. Influence of the addition mode

The gasification behaviors of i) sunflower seed shells, ii) a mixture of amorphous silica and sunflower seed shells and iii) the two materials in the same proportions but without contact were compared.

Solid conversion profiles of the three samples and rice husks alone are presented in Figure III.34. The corresponding average reactivities calculated between 1 and 80% conversion are plotted in Figure III.35.

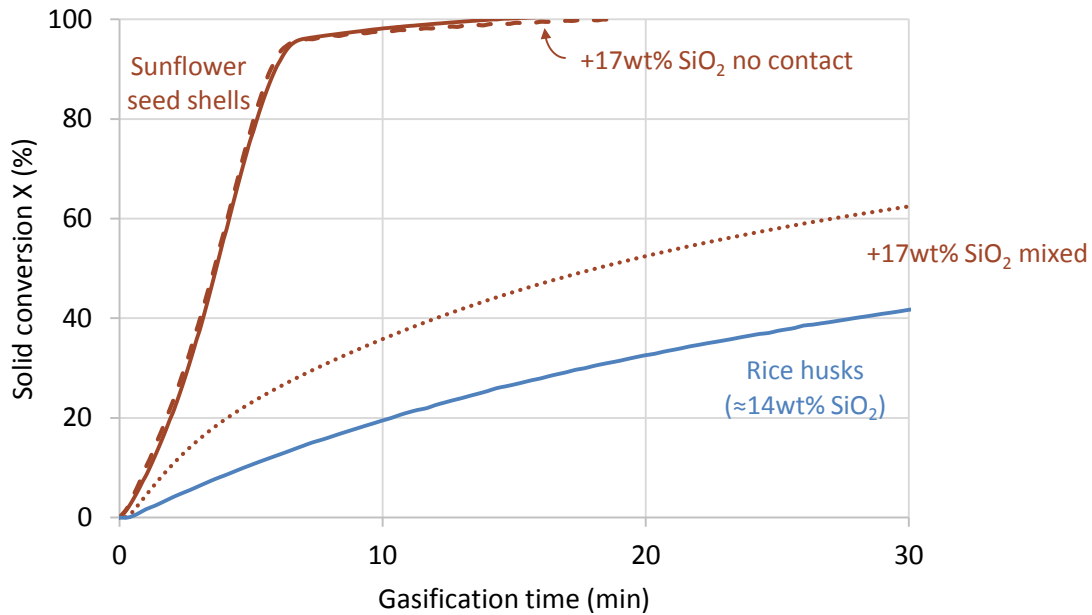


Figure III.34 | Solid conversion as a function of time during gasification of rice husks and of sunflower seed shells alone, mixed with 17wt% amorphous silica and with 17wt% amorphous silica without contact.

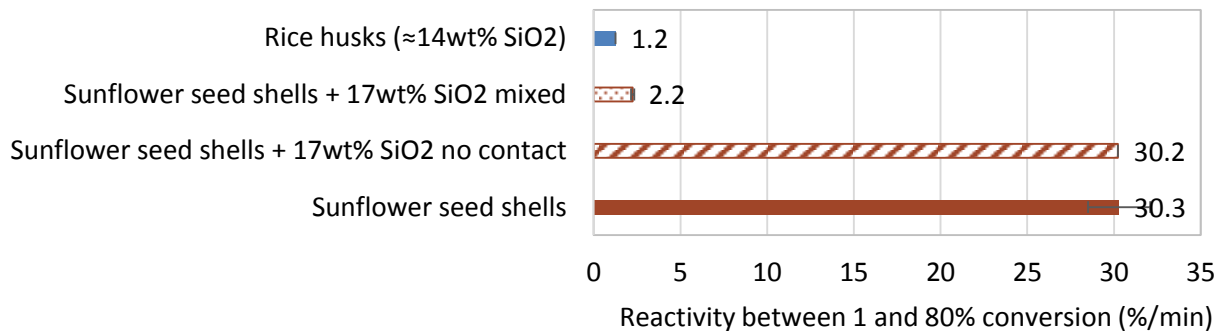


Figure III.35 | Gasification average reactivity between 1% and 80% conversion of rice husks and of sunflower seed shells alone, mixed with 17wt% amorphous silica and with 17wt% amorphous silica without contact.

The conversion profile of sunflower seed shells with addition of silica without contact overlaps the profile of sunflower seed shells alone. This means that **there was no TGA detectable interaction between the biomass and amorphous silica when there was no contact between them**. However, it has been shown in Chapter II that there was a volatilization of K from sunflower seed shells as KOH(g) during the gasification. Thus an interaction between KOH(g) and SiO₂ was expected as shown previously (Figure III.31) but was not detectable here. This might be explained by the fact that, in the present case, the volatile K-species were inherent to the sunflower seed shell char and farther from SiO₂. Therefore they might have catalyzed the gasification before having reached SiO₂.

On the contrary, **with mixed amorphous silica, the conversion of sunflower seed shells was significantly slower**. Its average reactivity between 1 and 80% was divided by a factor 15, going from 35%.min⁻¹ to 2%.min⁻¹. Moreover, **the shape of the curve changed to become similar to the one of rice husks alone**. The effect of SiO₂ in this case might be explained by the fact that, in the mixture, all species—char, K-species, SiO₂—were in close presence.

3.2.2. Influence of the crystalline form

Gasification of a mixture of sunflower seed shells and SiO_2 crystallized as quartz was conducted and compared to the previous results to evaluate the influence of the crystalline form of SiO_2 . Conversion profiles against time are presented in Figure III.36 and reactivities between 1% and 80% conversion are plotted in Figure III.37.

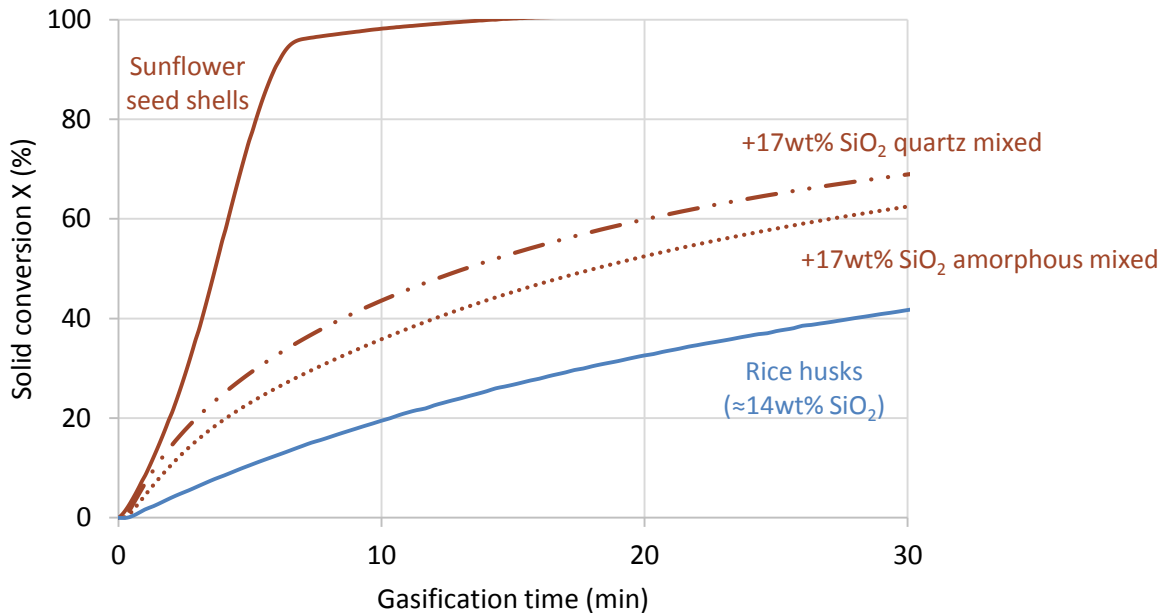


Figure III.36 | Solid conversion as a function of time during gasification of rice husks and of sunflower seed shells alone, mixed with 17wt% amorphous silica and mixed with 17wt% silica quartz.

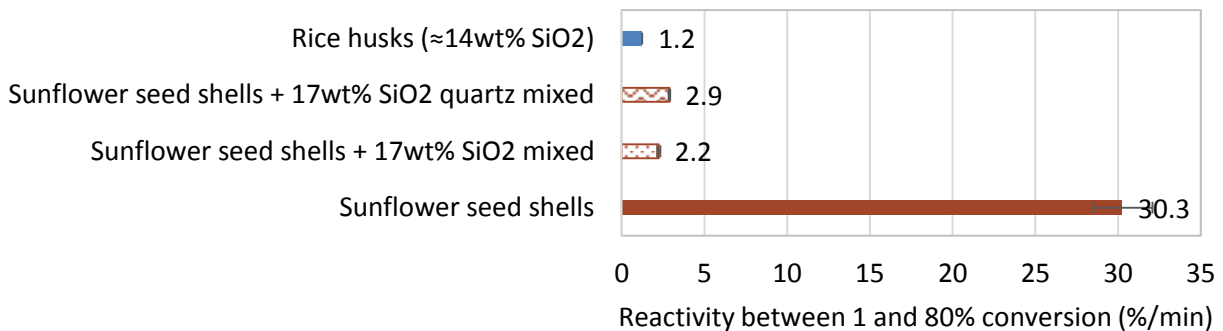


Figure III.37 | Gasification average reactivity between 1% and 80% conversion of rice husks and of sunflower seed shells alone, mixed with 17wt% amorphous silica and mixed with 17wt% silica quartz.

As in the case of amorphous silica, the conversion of sunflower seed shells was significantly slower when mixed with quartz. Its average reactivity between 1 and 80% decreased from $35\%.\text{min}^{-1}$ to $3\%.\text{min}^{-1}$ and the shape of the curve changed to become similar to the one of rice husks alone. **Therefore, the effect of SiO_2 on gasification kinetics does not depend on its crystalline form. It is the first time several forms of SiO_2 were compared and this result was demonstrated.**

3.2.3. Influence of the concentration

The influence of the SiO_2 concentration on gasification kinetics was investigated by gasifying mixtures of sunflower seed shells and 1, 2, 3, 6, 17 and 25wt% amorphous silica. The inorganic compositions of the initial mixtures are presented in Table III.7. The resulting solid conversion curves are presented in Figure III.38 and the corresponding reactivities between 1% and 80% conversion are plotted in Figure III.39.

Table III.7 | Inorganic composition of the mixtures of sunflower seed shells and amorphous silica (in dry basis).

Sample	Sunflower seed shells	+1wt% SiO ₂	+2wt% SiO ₂	+3wt% SiO ₂	+6wt% SiO ₂	+17wt% SiO ₂	+25wt% SiO ₂
Ash at 550 °C (wt%)	3.3	4.6*	5.3*	5.8*	9.6*	19.8*	27.2*
Si	194	6653	9769	12502	30448	80302	116718
K	9729	9594	9529	9472	9098	8058	7299
Ca	4489	4427	4397	4371	4198	3718	3368
Mg	1838	1813	1800	1790	1719	1522	1379
P	896	884	878	872	838	742	672
Na	9	9	9	9	8	7	7
Al	150	148	147	146	140	124	113
Fe	1099	1084	1076	1070	1028	910	824
SiO ₂	1.3	31.0	39.5	46.2	68.0	86.9	92.0
K ₂ O	35.5	25.1	21.7	19.7	11.4	4.9	3.2
CaO	19.0	13.5	11.6	10.6	6.1	2.6	1.7
MgO	9.2	6.5	5.6	5.1	3.0	1.3	0.8
P ₂ O ₅	6.2	4.4	3.8	3.4	2.0	0.9	0.6
Na ₂ O	0.0	0.0	0.0	0.0	0.0	0.0	0.0
Al ₂ O ₃	0.9	0.6	0.5	0.5	0.3	0.1	0.1
Fe ₂ O ₃	4.8	3.4	2.9	2.6	1.5	0.7	0.4
Main inorganic elements	K Ca Mg	K Si Ca	Si K Ca	Si K Ca	Si K Ca	Si K Ca	Si K Ca

*Theoretical, calculated as: %SiO₂ + (100 - %SiO₂) × Ash Sunflower seed shells

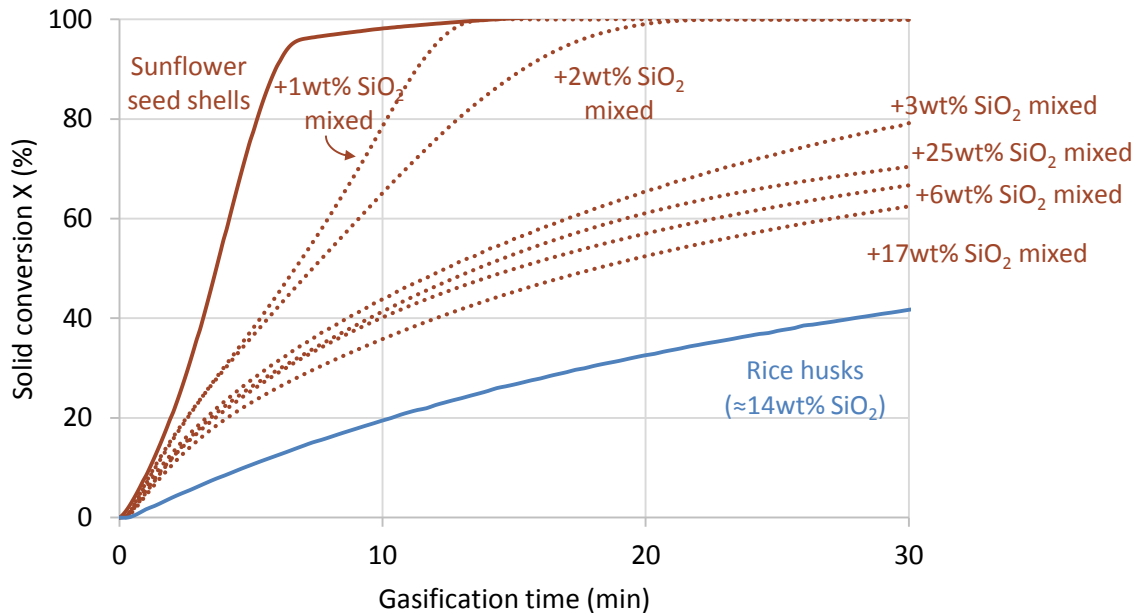


Figure III.38 | Solid conversion as a function of time during gasification of rice husks and of sunflower seed shells alone and mixed with 1, 2, 3, 6, 17 and 25wt% amorphous silica.

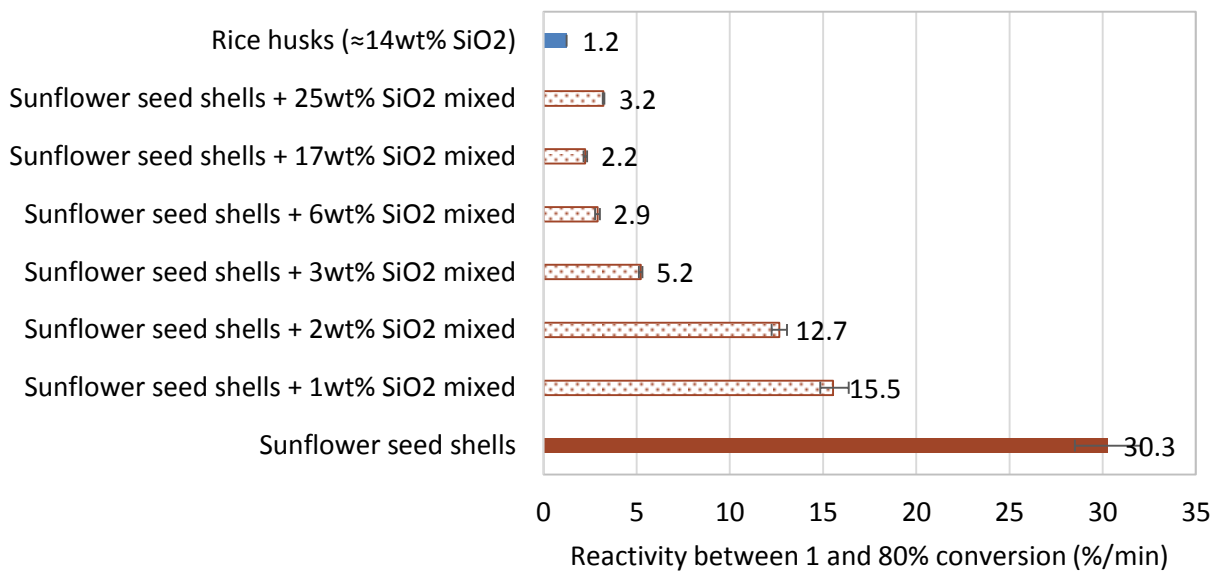


Figure III.39 | Gasification average reactivity between 1% and 80% conversion of rice husks and of sunflower seed shells alone and mixed with 1, 2, 3, 6, 17 and 25wt% amorphous silica.

When silica was added to sunflower seed shells, the shape of its gasification profile progressively changed to get the shape observed for rice husks. Samples with 1 and 2wt% had an intermediary shape with an acceleration of the gasification at high conversion values.

The gasification reactivity became lower when more silica was added until stabilization from 6wt% added amorphous silica, i.e. from 30000 mg.kg⁻¹ Si in the biomass. Figure III.40 represents the reactivity as a function of the quantity of added silica.

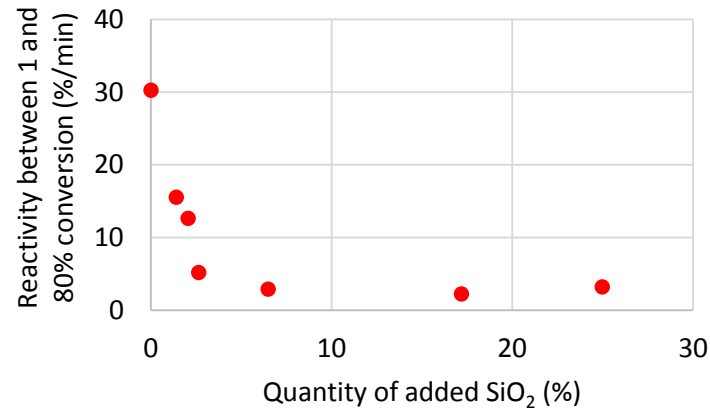
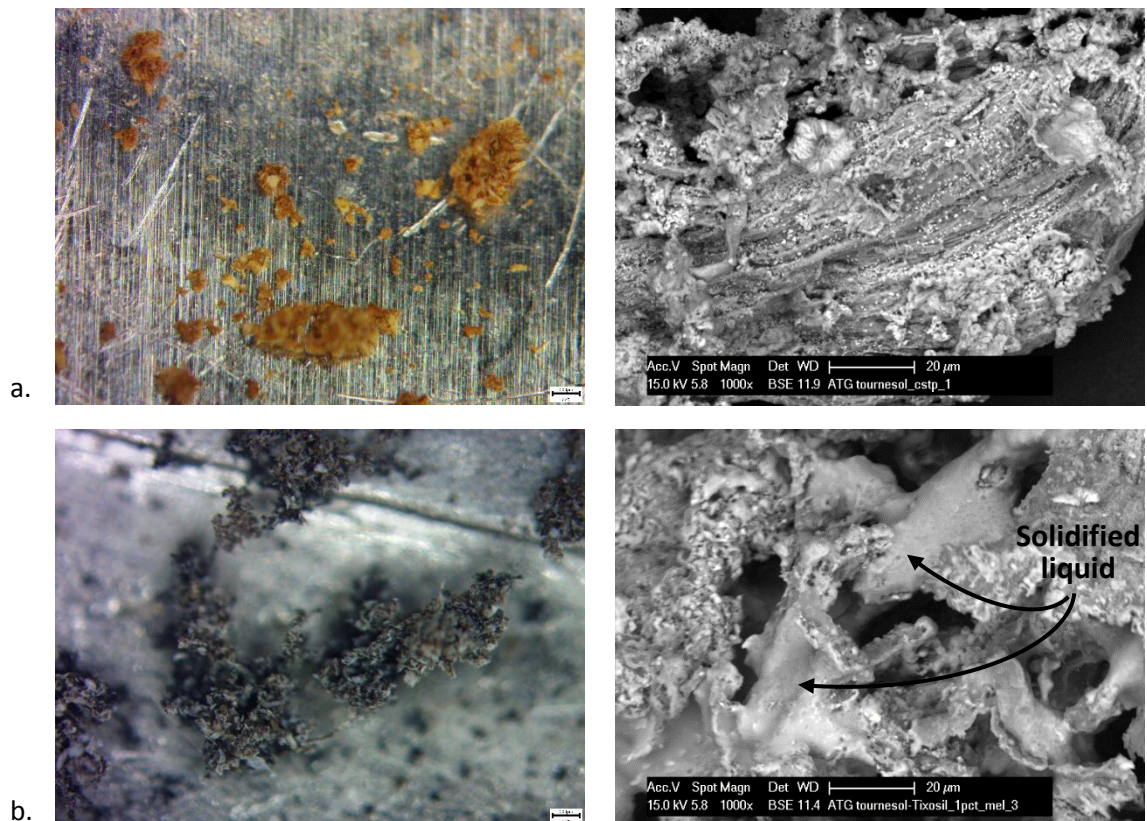
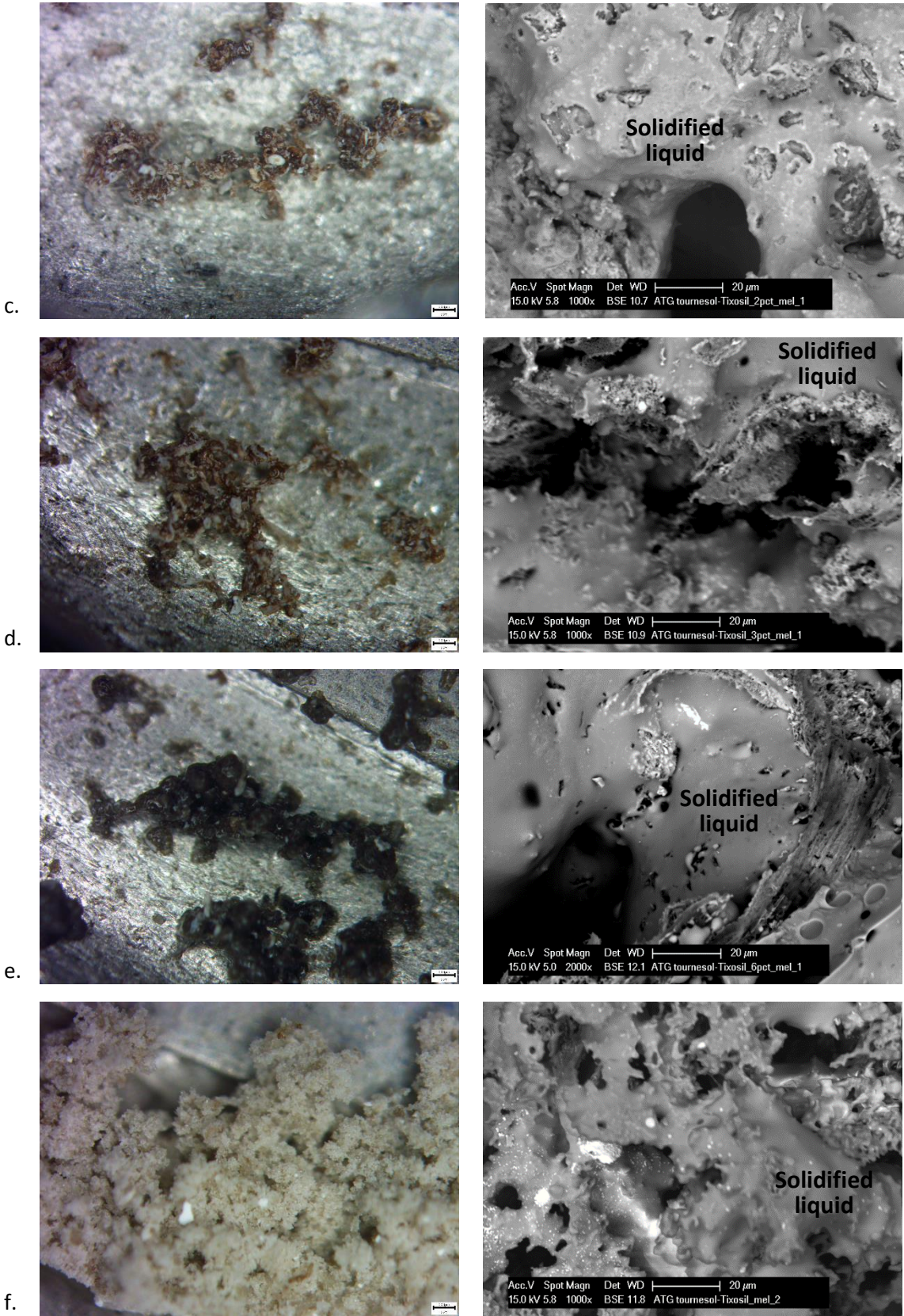


Figure III.40 | Gasification average reactivity between 1% and 80% conversion of mixtures of sunflower seed shells and amorphous silica as a function of the quantity of added silica.

There was not a linear relation between the reactivity and the quantity of added silica. The effect of SiO₂ was not proportional to its concentration in the sunflower seed shells and there seemed to be a saturation effect.

To try and explain this behavior, the ashes of the experiments at various concentrations were characterized through optical microscope observation and scanning electron microscope (SEM) observation. Pictures are presented in Figure III.41.





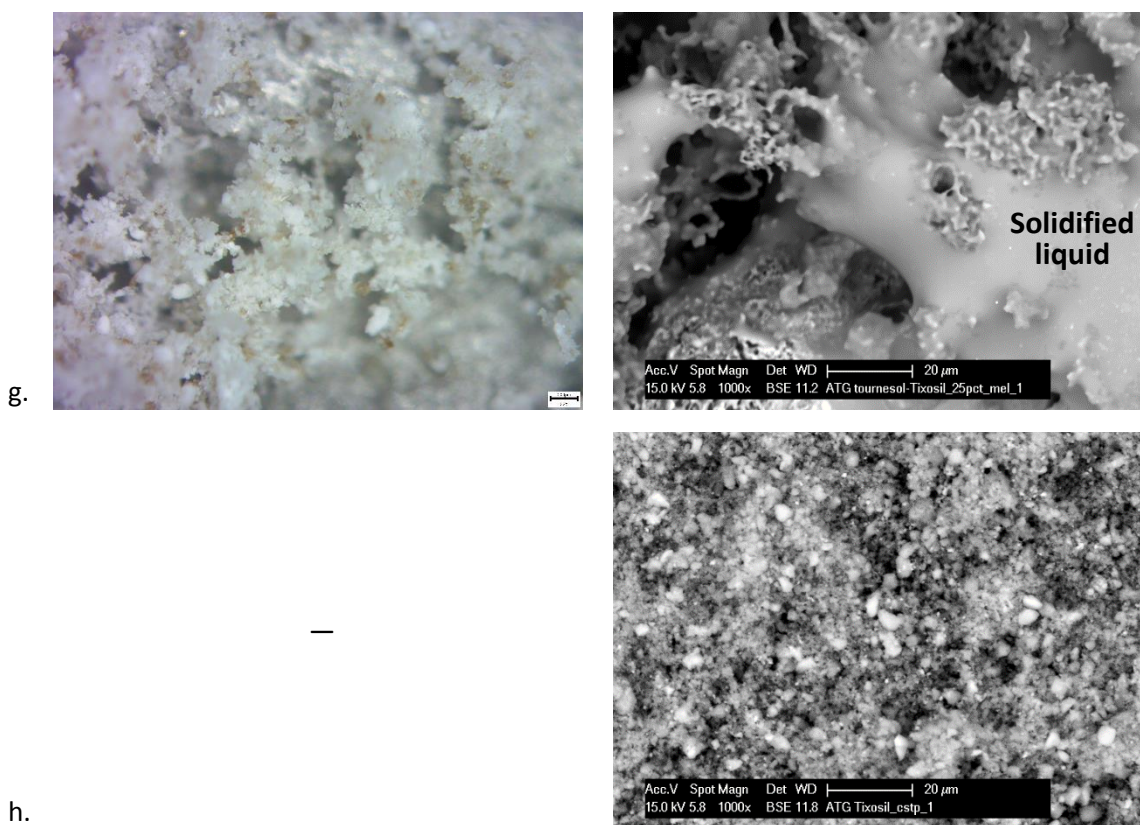


Figure III.41 | Optical microscope (left) and SEM (right) observations of residues after gasification of samples of sunflower seed shells a. alone. b. with 1wt% amorphous silica. c. with 2wt% amorphous silica. d. with 3wt% amorphous silica. e. with 6wt% amorphous silica. f. with 17wt% amorphous silica. g. with 25wt% amorphous silica. h. and of amorphous silica alone.

These observations showed that sunflower seed shells alone and amorphous silica alone remained solid after the gasification procedure while residues of the mixtures contained solidified liquid phases from the first percent of added silica. SEM analysis was complemented by EDX analysis to identify the elements in the phases. It must be noted that samples were coated with graphite for the analysis so the presence of C in the residues could not be detected. Solidified liquid phases mainly contained Si, K and O, sometimes Ca, with a lower K content when more silica was added. Solid phases contained a mixture of Si, K, Ca, Mg and O when small amounts of silica were added, and they contained mainly SiO_2 when higher amounts of silica were added.

These results confirmed that SiO_2 reacts with inorganic compounds naturally present in the biomass/char, namely K-compounds. It complements Anicic *et al.* (Anicic *et al.*, 2018) study on the reaction between SiO_2 sand and K_2CO_3 . When low amounts of SiO_2 are present ($< 10000 \text{ mg.kg}^{-1}$ Si in the biomass), K-compounds are still available to catalyze the gasification reaction which is then fast ($> 10\%.\text{min}^{-1}$). On the contrary, when high amounts of SiO_2 are present ($> 10000 \text{ mg.kg}^{-1}$ Si in the biomass), these catalytic compounds completely react with the SiO_2 and are not available to enhance the gasification reaction.

This explains the slow and decreasing reactivity of rice husks in gasification, since the same K-Si-O liquid phases were found in the ashes (Chapter II).

As a validation, gasification of beech wood with 17wt% added silica was conducted. The inorganic composition of the initial mixture is given in Table III.8 and its gasification rate is presented in Figure III.42. The corresponding reactivities between 1% and 80% conversion are plotted in Figure III.43.

Table III.8 | Inorganic composition of the mixture of beech wood and amorphous silica, sunflower seed shells and amorphous silica and of rice husks alone (in dry basis).

Biomass sample	Rice husks	Sunflower seed shells	Sunflower seed shells + 17wt% SiO ₂	Beech	Beech + 17wt% SiO ₂
Ash at 550 °C (wt%)	14.6	3.3	19.8*	0.6	17.8*
Si	63955	194	80302	115	81128
K	5822	9729	8058	910	752
Ca	1797	4489	3718	2516	2079
Mg	659	1838	1522	475	393
P	981	896	742	75	62
Na	413	9	7	3.6	3
Al	228	150	124	12	10
Fe	192	1099	910	34	28
SiO ₂	97.2	1.3	86.9	4.1	97.9
K ₂ O	5.0	35.5	4.9	18.3	0.5
CaO	1.8	19.0	2.6	58.7	1.6
MgO	0.8	9.2	1.3	13.1	0.4
P ₂ O ₅	1.6	6.2	0.9	2.9	0.1
Na ₂ O	0.4	0.0	0.0	0.1	0.0
Al ₂ O ₃	0.3	0.9	0.1	0.4	0.0
Fe ₂ O ₃	0.2	4.8	0.7	0.8	0.0
Main inorganic elements	Si – K – Ca	K – Ca – Mg	Si – K – Ca	Ca – K – Mg	Si – Ca – K
Gasification average reactivity between 1 and 80% conversion (%.min ⁻¹)	1.4	30.3	2.2	4.9	2.1

*Theoretical, calculated as: %SiO₂ + (100 - %SiO₂) × Ash of pure biomass

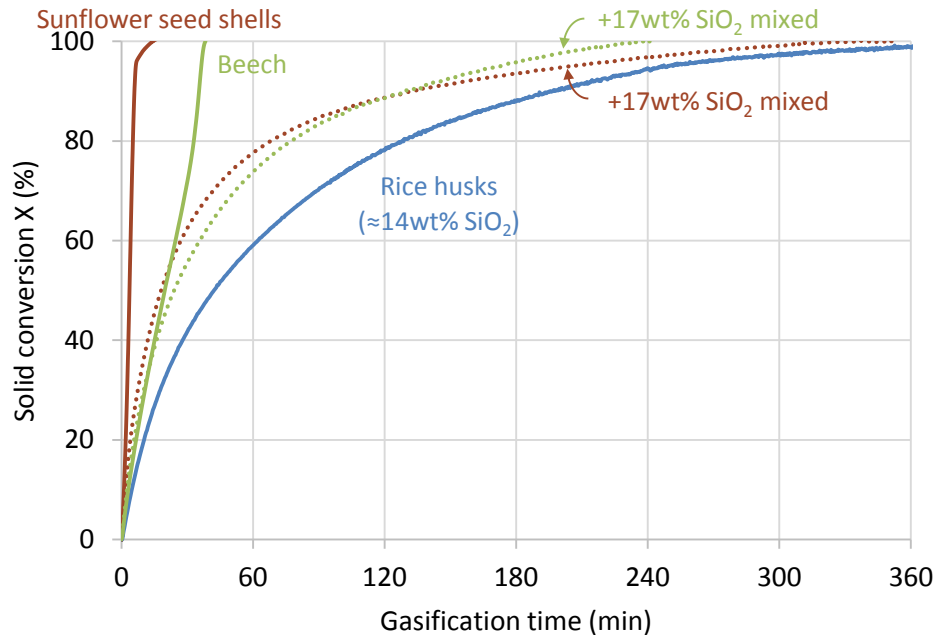


Figure III.42 | Gasification solid conversion as a function of time of beech wood and sunflower seed shells both alone and with 17wt% mixed amorphous silica, and of rice husks alone.

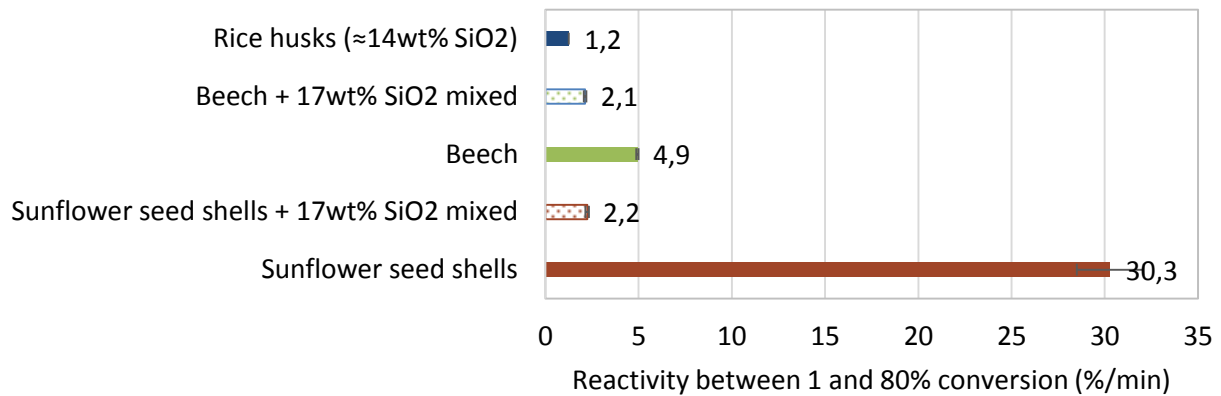


Figure III.43 | Gasification average reactivity between 1% and 80% conversion of beech wood and sunflower seed shells both alone and with 17wt% mixed amorphous silica, and of rice husks alone.

When silica was mixed with beech wood, its gasification slowed down as expected. Its reactivity was identical to the reactivity of sunflower seed shells mixed with 17wt% silica. Moreover, the shape of the kinetic profile became similar to the rice husk profile.

However, these mixtures have a higher reactivity than rice husks (2.1 and 2.2%.min⁻¹ for mixtures of 17wt% silica with sunflower seed shells or beech wood, respectively, compared to 1.2%.min⁻¹ for rice husks, Figure III.43) but they also have a higher Si content (80302 and 81128 mg.kg⁻¹, respectively, for the mixtures, compared to 63955 mg.kg⁻¹ for rice husks, Table III.8). This higher reactivity cannot be explained with the K content. Indeed, the K content of the sunflower seed shells-silica mixture (8058 mg.kg⁻¹, Table III.8) is slightly higher than rice husks (5822 mg.kg⁻¹, Table III.8), which might have induced a stronger catalysis and explained its higher reactivity. However, this reasoning does not work in the case of beech wood-silica mixture, whose K content is very significantly lower (752 mg.kg⁻¹, Table III.8). **This result supports the idea that the K and Si concentrations alone are not enough to explain the behavior in gasification, even though they explain the main trends.** The influence of other elements such as Ca (which can preferentially form silicates compared to K (Arnold et al., 2017)) or Al and P (which can form stable compounds with K or Ca in the same way as Si (Arnold and Hill, 2019; Porbatzki et al., 2011)) might be of importance in the gasification mechanisms.

1.1.1. Conclusions on the influence of SiO₂ addition

The aim of this section was to investigate how SiO₂ reacts with K-compounds and how it influences the steam gasification reactivity. In particular, quantitative results were obtained in relation to the concentration of SiO₂ in mixtures with biomass.

No significant effect of SiO₂ on the K-rich sunflower seed shell gasification was observed when they were not in contact. On the opposite and as expected from the results of K₂CO₃ influence (see 3.1), a strong decrease in gasification rate was observed in the case of mixtures (whatever the SiO₂ crystalline form, quartz or amorphous). This was attributed to the fact that, in the case without contact, the volatile K-species were inherent to the sunflower seed shell char and farther from the SiO₂. Therefore they might have catalyzed the gasification before having reached the SiO₂, whereas in mixtures their catalytic effect might have been directly inhibited by their reaction with SiO₂.

The effect of SiO₂ on steam gasification kinetics was quantified. Increasing the SiO₂ content of the biomass decreased its steam gasification reactivity in a non-linear way until a saturation effect.

4. Conclusions

This chapter demonstrates the competition between SiO_2 and the carbonaceous matrix to react with K_2CO_3 mixed or through the gas phase as $\text{KOH}(\text{g})$. On the one hand, K_2CO_3 catalyzes the high temperature pyrolysis and the steam gasification of the carbonaceous matrix of biomass. On the other hand, its decomposition product reacts with the SiO_2 inherent to biomass. In both cases, effects were observed including when K_2CO_3 was not in direct contact with the biomass which demonstrates that the mechanisms of action involve the gas phase.

During the pyrolysis at high temperature, an additional mass loss occurred in presence of K_2CO_3 . This observation is in accordance with the carbon chemical activation literature. It was demonstrated in the present work that it is related to an additional volatilization of the carbon matrix in relation with the formation of $\text{KOH}(\text{g})$. The latter is formed from the reaction of K_2CO_3 with $\text{H}_2\text{O}(\text{g})$ released from the devolatilization of the carbon matrix.

Regarding the gasification step itself, K_2CO_3 increases the reaction rate both with and without contact with the biomass. It was demonstrated in the present study that the interaction of K_2CO_3 with the biomass during the pyrolysis step is decisive for the ulterior gasification.

However, there is a competition with the reaction between SiO_2 and $\text{KOH}(\text{g})$ that limits the catalytic effect on Si-rich biomass species. Nevertheless, it has been shown through the quantitative analysis of the results that the K and Si concentrations alone are not enough to explain the behavior in gasification, even though they explain the main trends. The influence of other elements such as Ca (which can preferentially form silicates compared to K) or Al and P (which can form stable compounds with K or Ca in the same way as Si) might be important to consider for a better understanding of the mechanisms involved in gasification.

Conclusions and perspectives

1. Conclusions

Two factors can strongly influence its steam gasification kinetics: the char morphology and its inorganic content. The inorganic content seems to be the most influential parameter but no clear proof has been proposed in literature.

In particular, two inorganic elements have been described to have a high occurrence in biomass as well as a strong influence on gasification kinetics: potassium (K) and silicon (Si). K is known to have a catalytic effect while Si tends to inhibit this catalysis and therefore slow the gasification down. However, even though these effects are today well-known, the mechanisms behind them are still poorly known.

The objective of this work was then to contribute to the understanding of the phenomena involving K and Si during biomass steam gasification. Particular attention was paid to their influence on the reaction kinetics.

To reach this purpose, three experimental studies were conducted. The first study aimed to determine the factor having the strongest influence on steam gasification kinetics between the char morphology and its inorganic content. It consisted in the characterization of the chars derived from two biomass species, one K-rich and one Si-rich, at several gasification conversion values, both regarding their morphology and their kinetic behavior. The second and third studies were thermogravimetric analyses of these biomass samples with added model inorganic compounds. The second study aimed to investigate the mechanisms of action of K on steam gasification kinetics by adding K_2CO_3 to the Si-rich biomass. The experiments were designed more specifically to assess the gas phase influence. The third study aimed to investigate the effect of Si on steam gasification kinetics. SiO_2 was added to the K-rich biomass and steam gasification was conducted varying several operating conditions, the SiO_2 mode of addition, its crystalline form and its concentration.

The results from these experimental studies, supported by the data from literature, allowed to reach the following conclusions:

- The inorganic composition is the main parameter that explains the differences between the gasification kinetic behaviors of the biomass species. On the opposite, the physical properties of the carbon matrix do not have a major influence. However, the inorganic composition seems to affect some physical properties of the chars, such as their microporosity and the amount of functions at their surface.
- A catalytic effect of the K-species produced from K_2CO_3 , probably $KOH(g)$, was observed during the pyrolysis reaction. $KOH(g)$ can be produced from the reaction of K_2CO_3 with $H_2O(g)$ released during the biomass pyrolysis.
- **The K influence on the steam gasification kinetics has a mechanism involving the gas phase.** Indeed, biomass steam gasification was catalyzed by the addition of K_2CO_3 including when it was not in direct contact. The catalytic effect was attributed to the formation of $KOH(g)$ formed from the reaction of K_2CO_3 with $H_2O(g)$, either added during the steam gasification or produced during the biomass pyrolysis, as explained above.

- The reactions involving K during biomass pyrolysis, i.e. during char formation, have a major influence on the subsequent char gasification. This behavior was demonstrated by producing a char in presence of K_2CO_3 without direct contact and by gasifying the resulting char alone. The resulting char showed a higher reactivity than the char produced from raw biomass alone.
- There is a competition between two reactions involving the formed K-species, probably $KOH(g)$: i) the catalysis of the steam gasification on the one hand, and ii) the heterogeneous reaction between $KOH(g)$ and SiO_2 to form non-catalytic species on the other hand. Indeed, the catalytic activity of K was strongly decreased in presence of Si. The K-species preferentially reacted on SiO_2 to form K-silicates and/or liquid phases. Additions of K_2CO_3 had a stronger catalytic effect on the Si-poor biomass than on the Si-rich biomass.
- It was demonstrated in a direct way that the inherent K in biomass reacted with added SiO_2 and, reversely, that added K_2CO_3 formed $KOH(g)$ that reacted with the inherent Si in biomass.
- **SiO_2 addition slows the steam gasification down until a saturation effect from around $30000\text{ mg}\cdot\text{kg}^{-1}$ Si in the biomass.** Even before the saturation the relation between the average reactivity and SiO_2 addition is not linear. The inhibiting effect of SiO_2 was demonstrated to be independent of its crystalline form, i.e. quartz or amorphous.
- K and Si concentrations in biomass can explain the main trends of steam gasification kinetics. However, they are not enough to describe them accurately and other elements, such as Ca, P or Al, must be taken into account to get a more complete understanding.

2. Perspectives

2.1. Towards a full understanding of the K-catalysis mechanisms

As stated in the above conclusions, the present work enabled to better understand the K-catalysis mechanisms. However, the investigations must be continued in order to fully understand these mechanisms. To this end, the three following experimental perspectives should be implemented:

- The experimental setup used in the present work, i.e. the thermobalance with a crucible divided in two compartments, can cause issues for data treatment. Indeed, both the char side and the inorganic side are weighed together with several phenomena occurring on each side. Therefore it is difficult to decorrelate the phenomena by using these global mass measurements. **Experimental investigations should be conducted in a similar setup but with the biomass and the inorganic compound in two separate crucibles next to each other and independently weighed.**
- The catalytic activity of K_2CO_3 was attributed to the release of $KOH(g)$. This conclusion was based on indirect observations, i.e. observations of resulting condensed phases, supported by literature review and thermodynamic calculations. However, the gas phase was not directly analyzed in this work due to the difficulty of such analysis. **It would be interesting to confirm the formation of $KOH(g)$, for example with an online mass spectrometer placed after the thermogravimetric analyzer or any other gasification system.**
- It was demonstrated that the phenomena involving K-species during biomass pyrolysis had a major influence on the subsequent gasification. However, the mechanisms associated are still not clearly understood. **Therefore, more investigations could be conducted regarding the K-species behavior during the pyrolysis step and how it influences the gasification step. In particular, the physicochemical properties of the chars could be assessed more deeply.** In the present work, their analysis was conducted in depth for two biomass species but it would also be interesting to conduct the same analysis on chars produced with K_2CO_3 added with and without contact. It may allow to determine the active species and how they interact with the carbon matrix.

2.2. Towards a phenomenological modeling of the inorganics influence on biomass gasification kinetics

A long term major perspective to the present work is to design a gasification kinetic model that takes into account the inorganic elements influence and that is based on phenomenological parameters. Indeed, as stated in Chapter I, several models are available in literature (Arnold et al., 2017; Ding et al., 2017; Dupont et al., 2011; Hognon et al., 2014; Kramb et al., 2016; López-González et al., 2014; Romero Millán et al., 2019; Struis et al., 2002; Umeki et al., 2012; Zhang et al., 2008). However, these models are semi-empirical, coming from correlations between the gasification rate or reactivity and the inorganic elements concentrations. The kinetic parameters have no physical meaning or they are not unified, i.e. there are several parameters depending on the conditions and not one equation for all biomass species. The perspective would be to have one single model for all biomass species with unified parameters correlated with physical values.

From our results, it appeared that K was a major inorganic element influencing the gasification kinetics and it was demonstrated that its mechanism of action was through the gas phase. It was also shown that the catalytic effect of K was inhibited by SiO₂ which reacted with KOH(g) to form non-catalytic condensed phases. Additionally, it was demonstrated that, even though they can explain the main trends, K and Si are not sufficient to describe the inorganics influence on steam gasification kinetics and that the influence of other elements must be considered. In particular, it has been demonstrated in literature that Ca, which is a main inorganic element in biomass, also interacts with SiO₂. It reacts preferentially with SiO₂ compared to K (Arnold et al., 2017). The latter then remains available to catalyze the gasification. Moreover, Al and P can form stable compounds with K or Ca in the same way as Si (Arnold and Hill, 2019; Porbatzki et al., 2011). They are not often the major inorganic elements in biomass but they can reach significant concentrations in some species, such as sugar cane bagasse (14.60 wt% Al₂O₃ in ashes), bamboo, palm kernels or plum pits (20.33, 31.06 and 20.40 wt% P₂O₅ in ashes respectively) (Vassilev et al., 2010). These Ca, Al and P influences therefore seem to all be related to the capacity of K to be released and stay into the gas phase around the carbon matrix. It would then be this capacity that would determine its catalytic effect. As a result, **the physical value suggested to be introduced in a future kinetic model is the quantity of volatilized K.**

This quantity of volatilized K could be obtained from calculations at thermodynamic equilibrium from the initial biomass composition. With an accurate database, these calculations would take into account the aforementioned reactions. However, the database still is poorly known in some crucial parts of the considered system, for example K-Ca equilibria.

To reach this long term perspective, shorter term perspectives can be suggested:

- Similarly to this work with additions of K₂CO₃ and SiO₂, the effect on biomass gasification kinetics of the addition of Ca-, P- and Al-species may be investigated.
- The reaction of K and Si inherent to the biomass species could be studied in more details to determine the composition of the resulting K-silicates and K-Si-containing liquids. In particular, quantification of the crystalline phases as well as of the composition of the amorphous phases could be conducted. Indeed, in the present work, only the measurement of the global inorganic composition could be conducted along with a qualitative investigation of these phases in order to determine their occurrence. Such study would help to determine the fraction of volatilized K, i.e. the remaining fraction of K after its reaction with SiO₂.
- The influence of the reaction temperature and atmosphere (H₂O or CO₂) on the catalytic effect and on the reaction between K-species and SiO₂ should also be investigated.

2.3. Towards practical applications to the gasification process

At a process level, the understanding of the K-catalysis mechanisms, from the present work as well as from potential future investigations, will allow to control the phenomena in order to optimize the gasification process. Three first perspectives can already be described:

- As the K-catalysis occurs through the gas phase, catalytic gasification could be conducted by adding a K-source in the gas inlet, instead of adding it to the biomass. However, K-compounds condensate at high temperature, therefore a close control of the temperature should be carried out in order to avoid slagging and corrosion issues.

- **Since SiO₂ strongly inhibits the K-catalysis, removing the SiO₂ fraction of the biomass would increase its gasification rate.** Therefore, Si-rich species may be studied in order to identify if SiO₂ is located in a specific part of the plant that could be put aside. It could also be investigated if SiO₂ has a specific behavior during grinding that would allow to remove it through sieving.
- In the present work, a model K-compound (K₂CO₃) was added to biomass. This model compound was chosen because it can be found naturally in biomass. Therefore, **similar effects might be observed with the addition of a K-rich biomass or ashes as a catalyst. A similar investigation to the present one but with biomass mixtures with and without contact should be conducted.**

References

- Ahmed, I.I., and Gupta, A.K. (2011). Kinetics of woodchips char gasification with steam and carbon dioxide. *Appl. Energy* 88, 1613–1619.
- Alalwan, H.A., Alminshid, A.H., and Aljaafari, H.A.S. (2019). Promising evolution of biofuel generations. Subject review. *Renew. Energy Focus* 28, 127–139.
- Allen, M.R., Dube, O.P., Solecki, W., Aragón-Durand, F., Cramer, W., Humphreys, S., Kainuma, M., Kala, J., Mahowald, N., Mulugetta, Y., et al. (2018). Framing and Context. In *Global Warming of 1.5°C. An IPCC Special Report on the Impacts of Global Warming of 1.5°C above Pre-Industrial Levels and Related Global Greenhouse Gas Emission Pathways, in the Context of Strengthening the Global Response to the Threat of Climate Change, Sustainable Development, and Efforts to Eradicate Poverty*, V. Masson-Delmotte, P. Zhai, H.-O. Pörtner, D. Roberts, J. Skea, P.R. Shukla, A. Pirani, W. Moufouma-Okia, C. Péan, R. Pidcock, et al., eds. p.
- Anca-Couce, A. (2016). Reaction mechanisms and multi-scale modelling of lignocellulosic biomass pyrolysis. *Prog. Energy Combust. Sci.* 53, 41–79.
- Anicic, B., Lin, W., Dam-Johansen, K., and Wu, H. (2018). Agglomeration mechanism in biomass fluidized bed combustion – Reaction between potassium carbonate and silica sand. *Fuel Process. Technol.* 173, 182–190.
- Appavou, F., Brown, A., Epp, B., Gibb, D., Kondev, B., McCrone, A., Murdock, H.E., Musolino, E., Ranalder, L., Sawin, J.L., et al. (2019). *REN21 Renewables Global Status Report*.
- Arnold, R.A., and Hill, J.M. (2019). Catalysts for gasification: a review. *Sustain. Energy Fuels* 3, 656–672.
- Arnold, R.A., Habibi, R., Kopyscinski, J., and Hill, J.M. (2017). Interaction of Potassium and Calcium in the Catalytic Gasification of Biosolids and Switchgrass. *Energy Fuels* 31, 6240–6247.
- Arriagada, R., García, R., Molina-Sabio, M., and Rodriguez-Reinoso, F. (1997). Effect of steam activation on the porosity and chemical nature of activated carbons from *Eucalyptus globulus* and peach stones. *Microporous Mater.* 8, 123–130.
- Arvelakis, S., Jensen, P.A., and Dam-Johansen, K. (2004). Simultaneous Thermal Analysis (STA) on Ash from High-Alkali Biomass. *Energy Fuels* 18, 1066–1076.
- Bach-Oller, A., Fursujo, E., and Umeki, K. (2019). Effect of potassium impregnation on the emission of tar and soot from biomass gasification. *Energy Procedia* 158, 619–624.
- Bajpai, P. (2016). Structure of Lignocellulosic Biomass. In *Pretreatment of Lignocellulosic Biomass for Biofuel Production*, (Springer, Singapore), pp. 7–12.
- Baker, E.G., and Mudge, L.K. (1984). Mechanisms of catalytic biomass gasification. *J. Anal. Appl. Pyrolysis* 6, 285–297.
- Bale, C.W., Chartrand, P., Degterov, S.A., Eriksson, G., Hack, K., Ben Mahfoud, R., Melançon, J., Pelton, A.D., and Petersen, S. (2002). FactSage thermochemical software and databases. *Calphad* 26, 189–228.

- Barrio, M., Gøbel, B., Rimes, H., Henriksen, U., Hustad, J.E., and Sørensen, L.H. (2001). Steam Gasification of Wood Char and the Effect of Hydrogen Inhibition on the Chemical Kinetics. In *Progress in Thermochemical Biomass Conversion*, A.V. Bridgwater, ed. (John Wiley & Sons, Ltd), pp. 32–46.
- Bartels, M., Lin, W., Nijenhuis, J., Kapteijn, F., and van Ommen, J.R. (2008). Agglomeration in fluidized beds at high temperatures: Mechanisms, detection and prevention. *Prog. Energy Combust. Sci.* *34*, 633–666.
- Basu, P. (2010a). Chapter 5 - Gasification Theory and Modeling of Gasifiers. In *Biomass Gasification and Pyrolysis*, (Boston: Academic Press), pp. 117–165.
- Basu, P. (2010b). Chapter 6 - Design of Biomass Gasifiers. In *Biomass Gasification and Pyrolysis*, (Boston: Academic Press), pp. 167–228.
- Bennici, S., Jeguirim, M., Limousy, L., Haddad, K., Vaulot, C., Michelin, L., Josien, L., and Zorpas, A.A. (2019). Influence of CO₂ Concentration and Inorganic Species on the Gasification of Lignocellulosic Biomass Derived Chars. *Waste Biomass Valorization*.
- Biswas, R.K., Khan, P., Mukherjee, S., Mukhopadhyay, A.K., Ghosh, J., and Muraleedharan, K. (2018). Study of short range structure of amorphous Silica from PDF using Ag radiation in laboratory XRD system, RAMAN and NEXAFS. *J. Non-Cryst. Solids* *488*, 1–9.
- Björkman, E., and Strömberg, B. (1997). Release of Chlorine from Biomass at Pyrolysis and Gasification Conditions. *Energy Fuels* *11*, 1026–1032.
- Bläsing, M., Zini, M., and Müller, M. (2013). Influence of Feedstock on the Release of Potassium, Sodium, Chlorine, Sulfur, and Phosphorus Species during Gasification of Wood and Biomass Shells. *Energy Fuels* *27*, 1439–1445.
- Bouraoui, Z., Dupont, C., Jeguirim, M., Limousy, L., and Gadiou, R. (2016). CO₂ gasification of woody biomass chars: The influence of K and Si on char reactivity. *Comptes Rendus Chim.* *19*, 457–465.
- Bridgwater, A.V. (2015). Pyrolysis of Biomass. In *Biomass Power for the World: Transformations to Effective Use*, W.P.M. Van Swaaij, S.R.A. Kersten, and W. Palz, eds. (Singapore: Pan Stanford Publishing), pp. 473–513.
- Chabalala, V.P., Wagner, N., and Potgieter-Vermaak, S. (2011). Investigation into the evolution of char structure using Raman spectroscopy in conjunction with coal petrography; Part 1. *Fuel Process. Technol.* *92*, 750–756.
- de Coninck, H., Revi, A., Babiker, M., Bertoldi, P., Buckeridge, M., Cartwright, A., Dong, W., Ford, J., Fuss, S., Hourcade, J.-C., et al. (2018). Strengthening and Implementing the Global Response. In *Global Warming of 1.5°C. An IPCC Special Report on the Impacts of Global Warming of 1.5°C above Pre-Industrial Levels and Related Global Greenhouse Gas Emission Pathways, in the Context of Strengthening the Global Response to the Threat of Climate Change, Sustainable Development, and Efforts to Eradicate Poverty*, V. Masson-Delmotte, P. Zhai, H.-O. Pörtner, D. Roberts, J. Skeea, P.R. Shukla, A. Pirani, W. Moufouma-Okia, C. Péan, R. Pidcock, et al., eds. p.
- Dahmen, N., and Sauer, J. (2015). Synfuels via Biomass Gasification. In *Biomass Power for the World: Transformations to Effective Use*, W.P.M. Van Swaaij, S.R.A. Kersten, and W. Palz, eds. (Singapore: Pan Stanford Publishing), pp. 323–341.

- Dahou, T., Defoort, F., Thiéry, S., Grateau, M., Campargue, M., Bennici, S., Jeguirim, M., and Dupont, C. (2018). The Influence of Char Preparation and Biomass Type on Char Steam Gasification Kinetics. *Energies* *11*, 2126.
- Deglise, X., and Donnot, A. (2017). Bois énergie - Propriétés et voies de valorisation. Tech. Ing. Énerg. Renouvelables.
- DeGroot, W.F., and Shafizadeh, F. (1984). Kinetics of gasification of Douglas Fir and Cottonwood chars by carbon dioxide. *Fuel* *63*, 210–216.
- DeGroot, W.F., Kannan, M.P., Richards, G.N., and Theander, O. (1990). Gasification of agricultural residues (biomass): influence of inorganic constituents. *J. Agric. Food Chem.* *38*, 320–323.
- Delannay, F., Tysoe, W.T., Heinemann, H., and Somorjai, G.A. (1984). The role of KOH in the steam gasification of graphite: Identification of the reaction steps. *Carbon* *22*, 401–407.
- Di Blasi, C. (2008). Modeling chemical and physical processes of wood and biomass pyrolysis. *Prog. Energy Combust. Sci.* *34*, 47–90.
- Di Blasi, C. (2009). Combustion and gasification rates of lignocellulosic chars. *Prog. Energy Combust. Sci.* *35*, 121–140.
- Di Blasi, C., Galgano, A., and Branca, C. (2009). Effects of Potassium Hydroxide Impregnation on Wood Pyrolysis. *Energy Fuels* *23*, 1045–1054.
- Ding, L., Dai, Z., Wei, J., Zhou, Z., and Yu, G. (2017). Catalytic effects of alkali carbonates on coal char gasification. *J. Energy Inst.* *90*, 588–601.
- Dirbeba, M.J., Brink, A., DeMartini, N., Lindberg, D., and Hupa, M. (2016). Sugarcane vinasse CO₂ gasification and release of ash-forming matters in CO₂ and N₂ atmospheres. *Bioresour. Technol.* *218*, 606–614.
- Dupont, C., Boissonnet, G., Seiler, J.-M., Gauthier, P., and Schweich, D. (2007). Study about the kinetic processes of biomass steam gasification. *Fuel* *86*, 32–40.
- Dupont, C., Nocquet, T., Da Costa, J.A., and Verne-Tournon, C. (2011). Kinetic modelling of steam gasification of various woody biomass chars: Influence of inorganic elements. *Bioresour. Technol.* *102*, 9743–9748.
- Dupont, C., Jacob, S., Marrakchy, K.O., Hognon, C., Grateau, M., Labalette, F., and Da Silva Perez, D. (2016). How inorganic elements of biomass influence char steam gasification kinetics. *Energy* *109*, 430–435.
- Elliott, D.C., Hallen, R.T., and Sealock, L.J. (1984). Alkali catalysis in biomass gasification. *J. Anal. Appl. Pyrolysis* *6*, 299–316.
- ENS Lyon (2019). Handbook of Minerals Raman Spectra.
- European Commission (2018). Press release - Europe leads the global clean energy transition: Commission welcomes ambitious agreement on further renewable energy development in the EU.

- European Parliament (2009). Directive 2009/28/EC of the European Parliament and of the Council of 23 April 2009 on the promotion of the use of energy from renewable sources and amending and subsequently repealing Directives 2001/77/EC and 2003/30/EC.
- European Standards (2009). Solid biofuels - Determination of ash content (EN 14775).
- Eurostat (2019). Renewable energy statistics.
- Feng, D., Zhao, Y., Zhang, Y., Sun, S., and Gao, J. (2018a). Steam Gasification of Sawdust Biochar Influenced by Chemical Speciation of Alkali and Alkaline Earth Metallic Species. *Energies* *11*, 205.
- Feng, D., Zhao, Y., Zhang, Y., Xu, H., Zhang, L., and Sun, S. (2018b). Catalytic mechanism of ion-exchanging alkali and alkaline earth metallic species on biochar reactivity during CO₂/H₂O gasification. *Fuel* *212*, 523–532.
- Fermoso, J., Arias, B., Pevida, C., Plaza, M.G., Rubiera, F., and Pis, J.J. (2008). Kinetic models comparison for steam gasification of different nature fuel chars. *J. Therm. Anal. Calorim.* *91*, 779–786.
- Figueiredo, J.L., Pereira, M.F.R., Freitas, M.M.A., and Órfão, J.J.M. (1999). Modification of the surface chemistry of activated carbons. *Carbon* *37*, 1379–1389.
- Ganesh, A., Dutt Grover, P., and Iyer, P.V.R. (1992). Combustion and gasification characteristics of rice husk. *Fuel* *71*, 889–894.
- Gauthier, G., Melkior, T., Grateau, M., Thiery, S., and Salvador, S. (2013). Pyrolysis of centimetre-scale wood particles: New experimental developments and results. *J. Anal. Appl. Pyrolysis* *104*, 521–530.
- González-Vázquez, M.P., García, R., Gil, M.V., Pevida, C., and Rubiera, F. (2018). Unconventional biomass fuels for steam gasification: Kinetic analysis and effect of ash composition on reactivity. *Energy* *155*, 426–437.
- Guerrero, M., Ruiz, M.P., Millera, Á., Alzueta, M.U., and Bilbao, R. (2008). Oxidation Kinetics of Eucalyptus Chars Produced at Low and High Heating Rates. *Energy Fuels* *22*, 2084–2090.
- Guizani, C., Jeguirim, M., Gadiou, R., Escudero Sanz, F.J., and Salvador, S. (2016). Biomass char gasification by H₂O, CO₂ and their mixture: Evolution of chemical, textural and structural properties of the chars. *Energy* *112*, 133–145.
- Guizani, C., Jeguirim, M., Valin, S., Limousy, L., and Salvador, S. (2017). Biomass Chars: The Effects of Pyrolysis Conditions on Their Morphology, Structure, Chemical Properties and Reactivity. *Energies* *10*, 796.
- Gupta, A., Thengane, S.K., and Mahajani, S. (2018). CO₂ gasification of char from lignocellulosic garden waste: Experimental and kinetic study. *Bioresour. Technol.* *263*, 180–191.
- Hack, K., Jantzen, T., Müller, M., Yazhenskikh, E., and Wu, G. (2012). A novel thermodynamic database for slag systems and refractory materials. In *Proceedings of the 5th International Congress on the Science and Technology of Steelmaking (Dresden, Germany)*.
- Hognon, C., Dupont, C., Grateau, M., and Delrue, F. (2014). Comparison of steam gasification reactivity of algal and lignocellulosic biomass: Influence of inorganic elements. *Bioresour. Technol.* *164*, 347–353.

- Huang, Y., Yin, X., Wu, C., Wang, C., Xie, J., Zhou, Z., Ma, L., and Li, H. (2009). Effects of metal catalysts on CO₂ gasification reactivity of biomass char. *Biotechnol. Adv.* *27*, 568–572.
- Hüttinger, K.J., and Mingos, R. (1986a). Influence of the catalyst precursor anion in catalysis of water vapour gasification of carbon by potassium: 1. Activation of the catalyst precursors. *Fuel* *65*, 1112–1121.
- Hüttinger, K.J., and Mingos, R. (1986b). The influence of the catalyst precursor anion in catalysis of water vapour gasification of carbon by potassium: 2. Catalytic activity as influenced by activation and deactivation reactions. *Fuel* *65*, 1122–1128.
- International Energy Agency (2019a). Climate change.
- International Energy Agency (2019b). Bioenergy.
- International Organization for Standardization (2010). Solid mineral fuels - Determination of ash (ISO 1171:2010).
- International Organization for Standardization (2015). Solid biofuels - Determination of major elements - Al, Ca, Fe, Mg, P, K, Si, Na and Ti (ISO 16967:2015).
- Jiang, L., Hu, S., Xu, K., Wang, Y., Syed-Hassan, S.S.A., Su, S., Liu, C., and Xiang, J. (2017). Formation, fates and roles of catalytic precursors generated from the K₂CO₃-carbon interactions in the K₂CO₃-catalyzed CO₂ gasification of coal char. *J. Anal. Appl. Pyrolysis* *124*, 384–392.
- Kannan, M.P., and Richards, G.N. (1990). Gasification of biomass chars in carbon dioxide: dependence of gasification rate on the indigenous metal content. *Fuel* *69*, 747–753.
- Kersten, S.R.A., Palz, W.D., Spitzer, J.D., Prins, W., Drift, A. van der, Maniatis, K.D., Kwant, K.D., Helm, P.D., and Grassi, A.D. (2002). Interpretation of biomass gasification by 'Quasi'-Equilibrium models. (Sustainable Process Technology), pp. 772–776.
- Kilpinen, P., Hupa, M., and Leppälähti, J. (1991). Nitrogen Chemistry at Gasification - A Thermodynamic Analysis (Åbo Akademi University).
- Kirtania, K., Axelsson, J., Matsakas, L., Christakopoulos, P., Umeki, K., and Furusjö, E. (2017). Kinetic study of catalytic gasification of wood char impregnated with different alkali salts. *Energy* *118*, 1055–1065.
- Knudsen, J.N., Jensen, P.A., and Dam-Johansen, K. (2004). Transformation and Release to the Gas Phase of Cl, K, and S during Combustion of Annual Biomass. *Energy Fuels* *18*, 1385–1399.
- Koukios, E.G. (1993). Progress in Thermochemical, Solid-State Refining of Biofuels — From Research to Commercialization. In *Advances in Thermochemical Biomass Conversion*, A.V. Bridgwater, ed. (Dordrecht: Springer Netherlands), pp. 1678–1692.
- Kramb, J., DeMartini, N., Perander, M., Moilanen, A., and Konttinen, J. (2016). Modeling of the catalytic effects of potassium and calcium on spruce wood gasification in CO₂. *Fuel Process. Technol.* *148*, 50–59.
- Kramb, J., Gómez-Barea, A., DeMartini, N., Romar, H., Doddapaneni, T.R.K.C., and Konttinen, J. (2017). The effects of calcium and potassium on CO₂ gasification of birch wood in a fluidized bed. *Fuel* *196*, 398–407.

- Krishnarao, R.V., Subrahmanyam, J., and Jagadish Kumar, T. (2001). Studies on the formation of black particles in rice husk silica ash. *J. Eur. Ceram. Soc.* *21*, 99–104.
- Lahijani, P., Zainal, Z.A., Mohamed, A.R., and Mohammadi, M. (2013). CO₂ gasification reactivity of biomass char: Catalytic influence of alkali, alkaline earth and transition metal salts. *Bioresour. Technol.* *144*, 288–295.
- Lane, D.J., van Eyk, P.J., Ashman, P.J., Kwong, C.W., de Nys, R., Roberts, D.A., Cole, A.J., and Lewis, D.M. (2015). Release of Cl, S, P, K, and Na during Thermal Conversion of Algal Biomass. *Energy Fuels* *29*, 2542–2554.
- de Lasa, H., Salaices, E., Mazumder, J., and Lucky, R. (2011). Catalytic Steam Gasification of Biomass: Catalysts, Thermodynamics and Kinetics. *Chem. Rev.* *111*, 5404–5433.
- Lide, D.R. (1996). *CRC Handbook of Chemistry and Physics* (Boca Raton: CRC Press).
- Lindberg, D., Backman, R., Chartrand, P., and Hupa, M. (2013). Towards a comprehensive thermodynamic database for ash-forming elements in biomass and waste combustion — Current situation and future developments. *Fuel Process. Technol.* *105*, 129–141.
- Link, S., Arvelakis, S., Hupa, M., Yrjas, P., Külaots, I., and Paist, A. (2010). Reactivity of the Biomass Chars Originating from Reed, Douglas Fir, and Pine. *Energy Fuels* *24*, 6533–6539.
- Liu, X., Zheng, Y., Liu, Z., Ding, H., Huang, X., and Zheng, C. (2015). Study on the evolution of the char structure during hydrogasification process using Raman spectroscopy. *Fuel* *157*, 97–106.
- López-González, D., Fernandez-Lopez, M., Valverde, J.L., and Sanchez-Silva, L. (2014). Gasification of lignocellulosic biomass char obtained from pyrolysis: Kinetic and evolved gas analyses. *Energy* *71*, 456–467.
- Luque, R., Herrero-Davila, L., Campelo, J.M., Clark, J.H., Hidalgo, J.M., Luna, D., Marinas, J.M., and Romero, A.A. (2008). Biofuels: a technological perspective. *Energy Environ. Sci.* *1*, 542–564.
- Lv, P., Bai, Y., Yang, X., Gao, M., Bao, W., and Li, F. (2018). Impacts of char structure evolution and inherent alkali and alkaline earth metallic species catalysis on reactivity during the coal char gasification with CO₂/H₂O. *Int. J. Energy Res.* *42*, 3633–3642.
- Lv, X., Xiao, J., Shen, L., and Zhou, Y. (2016). Experimental study on the optimization of parameters during biomass pyrolysis and char gasification for hydrogen-rich gas. *Int. J. Hydrog. Energy* *41*, 21913–21925.
- Marquez-Montesinos, F., Cordero, T., Rodríguez-Mirasol, J., and Rodríguez, J.J. (2002). CO₂ and steam gasification of a grapefruit skin char. *Fuel* *81*, 423–429.
- Marsh, H., and Rodríguez-Reinoso, F. (2006a). CHAPTER 5 - Activation Processes (Thermal or Physical). In *Activated Carbon*, H. Marsh, and F. Rodríguez-Reinoso, eds. (Oxford: Elsevier Science Ltd), pp. 243–321.
- Marsh, H., and Rodríguez-Reinoso, F. (2006b). CHAPTER 6 - Activation Processes (Chemical). In *Activated Carbon*, H. Marsh, and F. Rodríguez-Reinoso, eds. (Oxford: Elsevier Science Ltd), pp. 322–365.

- McKee, D.W. (1983). Mechanisms of the alkali metal catalysed gasification of carbon. *Fuel* 62, 170–175.
- McKendry, P. (2002a). Energy production from biomass (part 1): overview of biomass. *Bioresour. Technol.* 83, 37–46.
- McKendry, P. (2002b). Energy production from biomass (part 2): conversion technologies. *Bioresour. Technol.* 83, 47–54.
- McKendry, P. (2002c). Energy production from biomass (part 3): gasification technologies. *Bioresour. Technol.* 83, 55–63.
- Meijer, R., Kapteijn, F., and Moulijn, J.A. (1994). Kinetics of the alkali-carbonate catalysed gasification of carbon: 3. H₂O gasification. *Fuel* 73, 723–730.
- Min'ko, N.I., and Binaliev, I.M. (2013). Role of sodium sulfate in glass technology. *Glass Ceram.* 69, 361–365.
- Moulijn, J.A., Cerfontain, M.B., and Kapteijn, F. (1984). Mechanism of the potassium catalysed gasification of carbon in CO₂. *Fuel* 63, 1043–1047.
- Mudge, L.K., Sealock, L.J., and Weber, S.L. (1979). Catalyzed steam gasification of biomass. *J. Anal. Appl. Pyrolysis* 1, 165–175.
- Nzihou, A., Stanmore, B., and Sharrock, P. (2013). A review of catalysts for the gasification of biomass char, with some reference to coal. *Energy* 58, 305–317.
- Park, B.-D., Wi, S.G., Lee, K.H., Singh, A.P., Yoon, T.-H., and Kim, Y.S. (2003). Characterization of anatomical features and silica distribution in rice husk using microscopic and micro-analytical techniques. *Biomass Bioenergy* 25, 319–327.
- Patel, M., Zhang, X., and Kumar, A. (2016). Techno-economic and life cycle assessment on lignocellulosic biomass thermochemical conversion technologies: A review. *Renew. Sustain. Energy Rev.* 53, 1486–1499.
- Perander, M., DeMartini, N., Brink, A., Kramb, J., Karlström, O., Hemming, J., Moilanen, A., Konttinen, J., and Hupa, M. (2015). Catalytic effect of Ca and K on CO₂ gasification of spruce wood char. *Fuel* 150, 464–472.
- Petit, M., Froment, K., Patisson, F., Seiler, J.-M., and Defoort, F. (2009). VP2.2.23 Relation between oxygen partial pressure in the syngas and inorganic releases during biomass gasification. In 17th European Biomass Conference & Exhibition, (Hamburg), pp. 960–965.
- Porbatzki, D., Stemmler, M., and Müller, M. (2011). Release of inorganic trace elements during gasification of wood, straw, and miscanthus. *Biomass Bioenergy* 35, S79–S86.
- Rodríguez-Reinoso, F., Molina-Sabio, M., and González, M.T. (1995). The use of steam and CO₂ as activating agents in the preparation of activated carbons. *Carbon* 33, 15–23.
- Romero Millán, L.M., Sierra Vargas, F.E., and Nzihou, A. (2019). Steam gasification behavior of tropical agrowaste: A new modeling approach based on the inorganic composition. *Fuel* 235, 45–53.
- Rubin, E.M. (2008). Genomics of cellulosic biofuels. *Nature* 454, 841–845.

- Ryu, S.-E., Kim, T.-N., and Kang, T.-K. (1997). Pulverization of rice husks and the changes of husk densities. *J. Mater. Sci.* *32*, 6639–6643.
- Saavedra Rios, C. del M., Simone, V., Simonin, L., Martinet, S., and Dupont, C. (2018). Biochars from various biomass types as precursors for hard carbon anodes in sodium-ion batteries. *Biomass Bioenergy* *117*, 32–37.
- Sadezky, A., Muckenhuber, H., Grothe, H., Niessner, R., and Pöschl, U. (2005). Raman microspectroscopy of soot and related carbonaceous materials: Spectral analysis and structural information. *Carbon* *43*, 1731–1742.
- Sansaniwal, S.K., Rosen, M.A., and Tyagi, S.K. (2017). Global challenges in the sustainable development of biomass gasification: An overview. *Renew. Sustain. Energy Rev.* *80*, 23–43.
- Scarlat, N., Martinov, M., and Dallemand, J.-F. (2010). Assessment of the availability of agricultural crop residues in the European Union: Potential and limitations for bioenergy use. *Waste Manag.* *30*, 1889–1897.
- Septien, S., Escudero Sanz, F.J., Salvador, S., and Valin, S. (2018). The effect of pyrolysis heating rate on the steam gasification reactivity of char from woodchips. *Energy* *142*, 68–78.
- Sergeev, D., Yazhenskikh, E., Kobertz, D., and Müller, M. (2019). Vaporization behavior of Na₂CO₃ and K₂CO₃. *Calphad* *65*, 42–49.
- Shafeeyan, M.S., Daud, W.M.A.W., Houshmand, A., and Shamiri, A. (2010). A review on surface modification of activated carbon for carbon dioxide adsorption. *J. Anal. Appl. Pyrolysis* *89*, 143–151.
- Sheng, C. (2007). Char structure characterised by Raman spectroscopy and its correlations with combustion reactivity. *Fuel* *86*, 2316–2324.
- Sikarwar, V.S., Zhao, M., Clough, P., Yao, J., Zhong, X., Memon, M.Z., Shah, N., Anthony, E.J., and Fennell, P.S. (2016). An overview of advances in biomass gasification. *Energy Environ. Sci.* *9*, 2939–2977.
- Sikarwar, V.S., Zhao, M., Fennell, P.S., Shah, N., and Anthony, E.J. (2017). Progress in biofuel production from gasification. *Prog. Energy Combust. Sci.* *61*, 189–248.
- Strandberg, A., Holmgren, P., Wagner, D.R., Molinder, R., Wiinikka, H., Umeki, K., and Broström, M. (2017). Effects of Pyrolysis Conditions and Ash Formation on Gasification Rates of Biomass Char. *Energy Fuels* *31*, 6507–6514.
- Struis, R.P.W.J., von Scala, C., Stucki, S., and Prins, R. (2002). Gasification reactivity of charcoal with CO₂. Part I: Conversion and structural phenomena. *Chem. Eng. Sci.* *57*, 3581–3592.
- Sueyasu, T., Oike, T., Mori, A., Kudo, S., Norinaga, K., and Hayashi, J. (2012). Simultaneous Steam Reforming of Tar and Steam Gasification of Char from the Pyrolysis of Potassium-Loaded Woody Biomass. *Energy Fuels* *26*, 199–208.
- Tascón, J.M. (2012). *Novel Carbon Adsorbents* (Elsevier).
- Thommes, M., Kaneko, K., Neimark, A.V., Olivier, J.P., Rodriguez-Reinoso, F., Rouquerol, J., and Sing, K.S.W. (2015). Physisorption of gases, with special reference to the evaluation of surface area and pore size distribution (IUPAC Technical Report). *Pure Appl. Chem.* *87*, 1051–1069.

- Tromp, P.J.J., and Cordfunke, E.H.P. (1984). A thermochemical study of the reactive intermediate in the alkali-catalyzed carbon gasification. I. X-ray diffraction results on the alkali-carbon interaction. *Thermochim. Acta* 77, 49–58.
- Umeki, K., Moilanen, A., Gómez-Barea, A., and Konttinen, J. (2012). A model of biomass char gasification describing the change in catalytic activity of ash. *Chem. Eng. J.* 207–208, 616–624.
- United Nations Framework Convention on Climate Change (2015). Paris Agreement.
- United Nations Framework Convention on Climate Change (2019). Paris Agreement - Status of Ratification.
- Van Swaaij, W.P.M. (1981). Gasification — the process and the technology. *Resour. Conserv.* 7, 337–349.
- Vassilev, S.V., Baxter, D., Andersen, L.K., and Vassileva, C.G. (2010). An overview of the chemical composition of biomass. *Fuel* 89, 913–933.
- Vassilev, S.V., Baxter, D., Andersen, L.K., Vassileva, C.G., and Morgan, T.J. (2012). An overview of the organic and inorganic phase composition of biomass. *Fuel* 94, 1–33.
- Vassilev, S.V., Baxter, D., Andersen, L.K., and Vassileva, C.G. (2013). An overview of the composition and application of biomass ash. Part 1. Phase-mineral and chemical composition and classification. *Fuel* 105, 40–76.
- Wang, Q., Zhang, R., Luo, Z., Fang, M., and Cen, K. (2016). Effects of Pyrolysis Atmosphere and Temperature on Coal Char Characteristics and Gasification Reactivity. *Energy Technol.* 4, 543–550.
- Wang, S., Wang, C., and Ji, X. (2017). Towards understanding the salt-intercalation exfoliation of graphite into graphene. *RSC Adv.* 7, 52252–52260.
- Wen, W.-Y. (1980). Mechanisms of Alkali Metal Catalysis in the Gasification of Coal, Char, or Graphite. *Catal. Rev.* 22, 1–28.
- de Wild, P. (2011). Biomass pyrolysis for chemicals. University of Groningen.
- Wood, B.J., and Sancier, K.M. (1984). The Mechanism of the Catalytic Gasification of Coal Char: A Critical Review. *Catal. Rev.* 26, 233–279.
- Xiao, R., Chen, X., Wang, F., and Yu, G. (2011). The physicochemical properties of different biomass ashes at different ashing temperature. *Renew. Energy* 36, 244–249.
- Yip, K., Tian, F., Hayashi, J., and Wu, H. (2009). Effect of Alkali and Alkaline Earth Metallic Species on Biochar Reactivity and Syngas Compositions during Steam Gasification. *Energy Fuels* 24, 173–181.
- Zahara, Z.F., Kudo, S., Daniyanto, Ashik, U.P.M., Norinaga, K., Budiman, A., and Hayashi, J. (2018). CO₂ Gasification of Sugar Cane Bagasse: Quantitative Understanding of Kinetics and Catalytic Roles of Inherent Metallic Species. *Energy Fuels* 32, 4255–4268.
- Zaror, C.A., Hutchings, I.S., Pyle, D.L., Stiles, H.N., and Kandiyoti, R. (1985). Secondary char formation in the catalytic pyrolysis of biomass. *Fuel* 64, 990–994.

- Zhang, Y., Ashizawa, M., Kajitani, S., and Miura, K. (2008). Proposal of a semi-empirical kinetic model to reconcile with gasification reactivity profiles of biomass chars. *Fuel* *87*, 475–481.
- Zhao, D., Dai, Y., Chen, K., Sun, Y., Yang, F., and Chen, K. (2013). Effect of potassium inorganic and organic salts on the pyrolysis kinetics of cigarette paper. *J. Anal. Appl. Pyrolysis* *102*, 114–123.
- Zhao, H., Xu, W., Song, Q., Zhuo, J., and Yao, Q. (2018). Effect of Steam and SiO₂ on the Release and Transformation of K₂CO₃ and KCl during Biomass Thermal Conversion. *Energy Fuels*.
- Zhao, Y., Feng, D., Zhang, Y., Huang, Y., and Sun, S. (2016). Effect of pyrolysis temperature on char structure and chemical speciation of alkali and alkaline earth metallic species in biochar. *Fuel Process. Technol.* *141*, 54–60.

Annex A. Determination of the TGA chemical regime conditions

To ensure that the TGA measurements represent the intrinsic kinetics, the experiments must be performed in chemical regime. This means that the gasification kinetics must be controlled by the chemical reaction. The heat and mass transfers must be faster and therefore not limiting, i.e. considered as instantaneous compared to the chemical reaction.

Experiments with several initial masses are conducted in order to determine the mass required for the chemical regime.

For this study, the samples are chars from sunflower seed shells produced in the slow pyrolysis furnace MATISSE (see 1.2.1 in Chapter II). Results of the gasification solid conversion as a function of time are plotted in Figure Annex A.1.

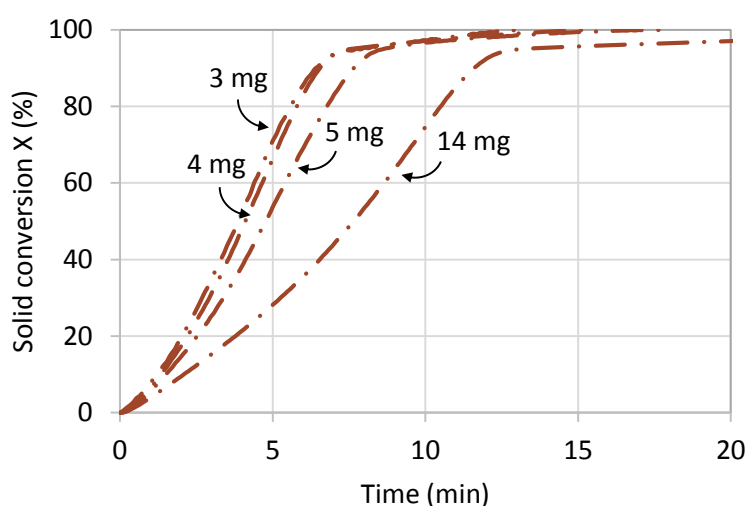


Figure Annex A.1 | Gasification conversion as a function of time for several initial mass of sunflower seed shells chars.

The gasification kinetics are similar for 3 and 4 mg of initial char. On the opposite, for an initial mass of 5 mg and above, gasification takes a longer time, i.e. the apparent reactivity decreases. These observations indicate that there are transfer limitations from 5 mg of initial char.

It is better to use the highest mass as possible to reduce the uncertainties, i.e. to reduce the signal-to-noise ratio. Consequently, the mass of char to use in the TGA must be of approximately 4 mg. Considering the mass loss of around 75% occurring during pyrolysis in the TGA (see 2.1 in Chapter II), it corresponds to a mass of raw biomass of approximately 15 mg.

Annex B. Article published in Energies: “The influence of char preparation and biomass type on char steam gasification kinetics”

The following article was published under the reference:

Dahou, T., Defoort, F., Thiéry, S., Gâteau, M., Campargue, M., Bennici, S., Jeguirim, M., and Dupont, C. (2018). The Influence of Char Preparation and Biomass Type on Char Steam Gasification Kinetics. *Energies* *11*, 2126.

Article

The Influence of Char Preparation and Biomass Type on Char Steam Gasification Kinetics

Tilia Dahou ^{1,2,3,*} , Françoise Defoort ¹, Sébastien Thiéry ¹, Maguelone Grateau ¹, Matthieu Campargue ⁴, Simona Bennici ², Mejdi Jeguirim ²  and Capucine Dupont ⁵

¹ Université Grenoble Alpes, CEA, LITEN, DTBH, 17 avenue des Martyrs, 38054 Grenoble CEDEX 09, France; francoise.defoort@cea.fr (F.D.); sebastien.thiery@cea.fr (S.T.); maguelone.grateau@cea.fr (M.G.)

² Institut de Sciences des Matériaux de Mulhouse, UMR 7661 CNRS, 15 rue Jean-Starcky, 68057 Mulhouse CEDEX, France; simona.bennici@uha.fr (S.B.); mejdi.jeguirim@uha.fr (M.J.)

³ Agence de l'Environnement et de la Maîtrise de l'Energie (ADEME), 20 avenue du Grésillé, BP 90406, 49004 Angers CEDEX 01, France

⁴ RAGT Energie, Zone Innoprod, Chemin de la Teulière, 81012 Albi CEDEX 9, France; mcampargue@ragt.fr

⁵ IHE Delft Institute for Water Education, Westvest 7, 2611 AX Delft, The Netherlands; c.dupont@un-ihe.org

* Correspondence: tilia.dahou@cea.fr; Tel.: +33-4-38-78-54-69

Received: 23 July 2018; Accepted: 14 August 2018; Published: 15 August 2018



Abstract: A study was conducted to investigate the parameter that has influence on steam gasification kinetics between the biomass type and char preparation. Thermogravimetric analysis (TGA) was carried out on steam gasification of seven biomass samples as well as chars from three of these samples. Chars were prepared using three different sets of low heating rate (LHR) pyrolysis conditions including temperature and biomass bed geometry. It was shown by a characteristic time analysis that these pyrolysis conditions were not associated with a chemical regime in a large amount of devices. However, it has been shown experimentally that conditions used to prepare the char had a much lower influence on steam gasification kinetics than the biomass type.

Keywords: biomass; steam gasification; kinetics; pyrolysis conditions; thermogravimetric analysis; characteristic time analysis

1. Introduction

Today, there is a consensus about the increasing need of biomass use for energy applications. Given the limited availability of wood, it seems essential to identify and to convert other biomass resources such as agricultural co-products. Among the various techniques for biomass conversion to energy, the gasification process is a promising one [1] such as in the case of hydrogen production [2–4] or liquid fuel synthesis [5–7]. This process includes two main steps that can overlap: biomass pyrolysis leading to char formation and gasification of the char producing syngas, i.e., a gas mixture of mainly CO and H₂. It has been shown that, with steam as a gasifying agent, the char gasification reaction has the slowest reaction under typical operating conditions [8]. Therefore, the design of industrial gasifiers requires the understanding and control of the steam gasification kinetics.

Since char is the starting material for gasification, it is important to identify the main parameter affecting char gasification kinetics.

In literature, two charring parameters are identified as having a potential influence on the steam gasification kinetics including pyrolysis operating conditions and biomass type [9]. The influence of pyrolysis conditions is largely related to the heating rate. Differences are especially noted between slow pyrolysis—low heating rate (LHR), <50 °C·min⁻¹—and fast pyrolysis—high heating rate (HHR), 500 °C·min⁻¹ [10]. The steam gasification rate increases when the heating rate increases, which is

linked to char morphology differences. During LHR pyrolysis, the char keeps its natural porosity while, in HHR pyrolysis, larger cavities are formed [9]. This larger surface area in the case of HHR pyrolysis along with the higher content in oxygen and hydrogen results in more available active sites [11]. The influence of the biomass type is basically related to the inorganic elements content of the biomass [12], which can attain high values for some resources such as agricultural residues [13]. In particular, alkali and alkaline earth metals (AAEMs) have a catalytic effect on gasification [14–17]. In contrast, elements such as silicon or phosphorus have an inhibiting effect [18,19].

To explain the origin of the influence of these two parameters, the first step is to determine the regime of the transformation, i.e., the phenomenon—chemical reaction or transfer—limiting its kinetics. Char preparation in conditions outside the chemical regime could result in variations in the properties of the chars. Differences between the chars obtained could lead to differences between their gasification behaviors. The regime of the transformation can be assessed through an analysis of the characteristic times of the phenomena involved. In literature, such an analysis has already been conducted by several authors. For instance, this can include pyrolysis [20–24], pyrogasification [8], and torrefaction [25] at the particle scale. However, most of these studies were performed for fast pyrolysis (HHR) and not slow pyrolysis (LHR). Moreover, time scale analysis is usually applied to a particle (for micrometric to centimetric scale particles), but more rarely to a bed of fine particles. One example can be found for torrefaction for which Gonzalez Martinez et al. [25] performed such an analysis at particle as well as at bed scale.

The present work combines the analysis of these characteristic times both at a particle scale and at a bed scale and an experimental study through thermogravimetric analysis (TGA). It focuses on slow pyrolysis (LHR) conditions (10 to 24 °C·min⁻¹) and parameters as the amount of biomass treated, i.e., geometry (height and surface) of the crucible and the working temperature (450 °C or 800 °C in one or two steps). Gasification was carried out on seven biomass samples as well as on chars prepared from three of these samples in four different sets of conditions. It aims to assess the relative influence of the two parameters previously discussed including char preparation conditions and biomass type on steam gasification kinetics.

2. Materials and Methods

2.1. Biomass Samples

Seven biomass samples covering a variety of compositions were selected for this study. The selection mainly includes agricultural residues. Samples were ground below 200 µm in a rotor mill. The ash content and inorganic element composition of the samples was measured, according to solid fuel standards NF EN 14775 [26] and NF EN ISO 16967 [27], respectively. Values obtained for each biomass sample can be found in Table 1. From these values, the three main inorganic elements in mass were identified.

The main inorganic elements contained in all biomasses are Ca and K. The third main element is Si, Mg, or P. Rice husk and wheat straw can be classified as silica-rich. Sunflower seed shells and alfalfa have a high potassium content. The others are rich in calcium.

Table 1. Ash and inorganic element content of the biomass samples (on dry basis).

Biomass Sample	Rice Husk	Wheat Straw [28]	Apple Orchard Residue [28]	Apricot Orchard Residue [28]	Vineyard Residue [28]	Sunflower Seed Shells	Alfalfa
Ash at 550 °C (wt %)	14.1	6.8	3.8	3.7	2.6	3.3	7.8
Si (mg·kg ⁻¹)	60,750	20,757	820	990	1012	258	510
K (mg·kg ⁻¹)	5363	13,063	3771	7254	5045	12,926	25,695
Ca (mg·kg ⁻¹)	1718	5627	9472	10,927	7808	6392	9694
Mg (mg·kg ⁻¹)	538	693	872	1374	1604	2812	1123
P (mg·kg ⁻¹)	630	1373	1325	1161	1011	1323	2997
Na (mg·kg ⁻¹)	270	164	25	41	37	20	289
Al (mg·kg ⁻¹)	166	429	71	104	151	257	83
Fe (mg·kg ⁻¹)	163	299	58	88	113	233	109
Mn (mg·kg ⁻¹)	183	50	11	20	42	12	<11
Main Inorganic Elements	Si	Si	Ca	Ca	Ca	K	K
	K	K	K	K	K	Ca	Ca
	Ca	Ca	P	Mg	Mg	Mg	P

2.2. Char Preparation

LHR pyrolysis in 1 L·min⁻¹ N₂ was carried out in three different sets of conditions in order to prepare large amounts of char from the different biomass feedstocks. Two devices were used to carry out the pyrolysis. They are illustrated in Figure 1.



Figure 1. (a) Device M used for pyrolysis; (b) Device P used for pyrolysis.

Device M consists of a sample holder swept by nitrogen and placed in an oven. It can be used for large quantities of sample (30 g to 50 g depending on biomass) but only operates at moderate temperatures (450 °C). Device P consists of a mesh basket sample holder placed in a tube swept by nitrogen and heated by induction. It can reach higher temperatures (800 °C), but a lower amount of sample (approximately 5 g) can be converted at once.

Each set of conditions for char preparation from the biomass samples is described in Table 2. The first set of conditions (char M) is at a low temperature (450 °C) while the two other sets of conditions (char M-P and char P-P) have two temperature steps (450 °C and 800 °C) in the same or different devices.

In addition, char was produced from in-situ pyrolysis of the biomass before gasification in the thermo-balance (see following section), which pyrolysis conditions (char TGA) are listed in Table 2.

Table 2. Pyrolysis conditions for char preparation from the biomass samples.

	Char TGA	Char M	Char M-P	Char P-P
Device for treatment at 450 °C	TGA	Device M	Device M	Device P
Sample holder dimension at 450 °C height × diameter (mm × mm)	2.5 × 7	40 × 70	40 × 70	48 × 32
Heating rate to 450 °C (°C·min ⁻¹)	24	10	10	24
Holding time at 450 °C (min)	60	60	60	60
Cooling between treatment at 450 °C and 800 °C	No	–	Yes	No
Device for treatment at 800 °C	TGA	–	Device P	Device P
Heating rate to 800 °C (°C·min ⁻¹)	24	–	24	24
Holding time at 800 °C (min)	30	–	30	30

TGA: thermogravimetric analysis.

2.3. Steam Gasification Reactivity

Steam gasification reactivities of the four types of char (Table 2) were obtained through thermogravimetric analysis (TGA). Experiments were carried out at an atmospheric pressure using a Setsys thermobalance (SETARAM, Caluire, France) coupled with a Wetsys steam generator. For chars M, M-P, and P-P, which is a mass of 3 mg to 4 mg—i.e., the mass experimentally determined to be independent from heat and mass transfer influence—was placed in a cylindrical crucible of 2.5 mm height and 7 mm diameter. Samples were heated at 24 °C·min⁻¹ until 800 °C under 0.05 L·min⁻¹ N₂ except for char TGA, which starting material was biomass and for which an intermediate step at 450 °C was performed, which is shown in Table 2. In this last case, a mass of 14 mg of biomass was placed in the crucible. Samples were swept by N₂ for 45 min after the final temperature was reached to ensure pyrolysis completion and mass stability. Gas was then switched to a mixture of 20 vol % H₂O in N₂.

Steam gasification reactivities of the biomass samples were also measured. It corresponds to the preparation of char TGA described in the previous section, which is directly followed by steam gasification. The experimental procedure was similar to the one used for chars.

A solid conversion was then defined from mass loss measured as a function of time during TGA by using the following expression.

$$X = \frac{m_i - m(t)}{m_i - m_f}, \quad (1)$$

where m_i , $m(t)$, and m_f are the masses of char before gasification (at the time of steam injection) at the time t and at the end of gasification (remaining ash), respectively.

The gasification rate could then be defined as the variation of conversion versus the equation below.

$$r = X \frac{dX}{dt}. \quad (2)$$

An average reactivity between two values of conversion X_1 and X_2 was also defined below.

$$r_{X_1-X_2} = \frac{\int_{t_{X_1}}^{t_{X_2}} \frac{r(t)dt}{1-X(t)}}{t_{X_2} - t_{X_1}}. \quad (3)$$

2.4. Characteristic Time Calculation

The characteristic time of a phenomenon is the theoretical time needed for a process to occur when it is only controlled by this phenomenon [29]. It depends on the operating conditions. Phenomena to consider can be chemical reactions, heat transfers, mass transport, or other phenomena. From comparing characteristic times, the limiting phenomenon can be identified and the regime of the process can be defined.

In this study, characteristic times were calculated for char preparation through pyrolysis and for steam gasification of the char to represent the chosen experimental procedure as closely as possible in which the two reactions occur one after the other. Analysis of the characteristic times of the pyrolysis step is important since, if other phenomena than the chemical reaction occur, it could result in the production of different chars in the different conditions. Since char is the starting material to gasification, it could mean that these chars would behave differently during gasification. Analysis of the characteristic times of the gasification step is meant to validate the results from steam gasification TGA since reactivities are meaningful only in a chemical regime, i.e., when the chemical reaction is the leading phenomenon.

Phenomena involved in each process are illustrated in Figure 2.

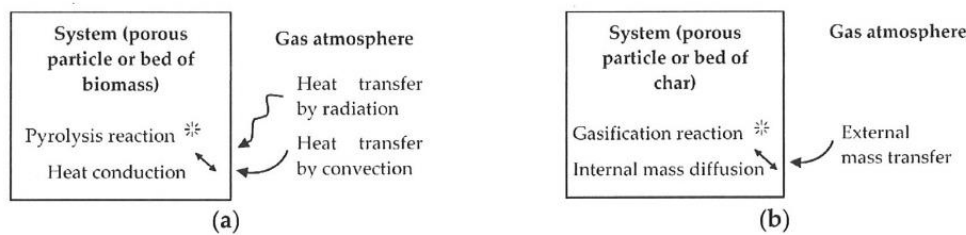


Figure 2. (a) Phenomena involved in pyrolysis; (b) Phenomena involved in gasification.

In the case of pyrolysis, the process is not led under isothermal conditions. Therefore, the characteristic times of the phenomena were compared to the heating time.

Characteristic times of each phenomenon as well as heating time are defined in Tables 3 and 4 for pyrolysis and gasification, respectively.

Table 3. Characteristic time definition for the pyrolysis of biomass.

Phenomenon	Definition of Characteristic Time
Pyrolysis chemical reaction	$t_{pyro} = \frac{1}{k_{pyro}}$
External heat transfer by convection	$t_{conv} = \frac{\rho_{solid} c_p \text{ solid } L_c}{h_i}$
External heat transfer by radiation	$t_{rad} = \frac{\rho_{solid} c_p \text{ solid } L_c}{\omega_{solid} \sigma (T_{gas} + T_{solid})(T_{gas}^2 + T_{solid}^2)}$
Internal heat transfer by conduction	$t_{cond} = \frac{\rho_{solid} c_p \text{ solid } L_c^2}{\lambda_{solid}}$
Heating	$t_{heating} = \frac{T_{gas} - T_{solid}}{r_{heating}}$

Table 4. Characteristic time definition for the gasification of biomass.

Phenomenon	Definition of Characteristic Time
Gasification chemical reaction	$t_{gasif} = \frac{1}{k_{gasif}}$
External mass transfer	$t_{mass \ ext} = \frac{\rho_{solid} R T_{gas} L_c}{h_m P_{H_2O} M_{H_2O}}$
Internal mass diffusion	$t_{diff \ int} = \frac{L_c^2}{D_{eff}}$

Pyrolysis and gasification chemical reactions of kinetic parameters were taken from literature. Pyrolysis kinetic parameters were taken from Di Blasi’s review [30]: results were calculated both for the fastest [31] and the slowest [32] laws. For gasification, a law taking into account biomass composition was chosen [18]. Among a fast-reacting biomass, alfalfa, and a slow reacting one, barley straw were chosen for comparison. All kinetic constants and their parameters values are gathered in Table 5.

Table 5. Kinetic constants for pyrolysis and gasification reactions.

Reaction	Kinetic Constant Expression	Biomass	k_0 (s ⁻¹)	E_a (kJ·mol ⁻¹)	$\frac{m_K}{m_{Si}}$	a	b
Pyrolysis	$k_{pyro} \exp\left(-\frac{E_a}{RT_{gas}}\right)$	Rice husk	5.8×10^{14}	200	-	-	-
		Sunflower shells	1.0×10^3	78.15	-	-	-
Gasification	$k_{gasif} \exp\left(-\frac{E_a}{RT_{gas}}\right) P_{H_2O}^{0.6} \left(a \frac{m_K}{m_{Si}} + b\right)$	Barley straw	8.8×10^4	167	0.1	0.18	0.59
		Alfalfa	8.8×10^4	167	50	0.18	0.59

Characteristic lengths used in characteristic time calculations are defined in Table 6.

Table 6. Characteristic lengths used for characteristic time calculations with d_p the particle diameter, D_c the bed diameter, and H_c the bed height.

System Considered	Characteristic Length L_c Definition	Device	Characteristic Length L_c Value (m)
Particle scale	$\frac{d_p}{6}$	All devices	3.3×10^{-5}
		TGA	6.3×10^{-4}
Bed scale	$\frac{D_c H_c}{2D_c + 4H_c}$	Device M	1.6×10^{-3}
		Device P	5.3×10^{-3}

Properties of the solids—biomass and char—were estimated from literature data or from our own measurements. They are gathered in Table 7.

Table 7. Physical properties of biomass and char particles and beds.

Property	Biomass Particle	Biomass Bed	Char Particle	Char Bed
Porosity ϵ_{solid} (-)	-	0.5 (estimated)	0.7 [33]	0.5 (estimated)
Tortuosity τ_{solid} (-)	-	-	3 [34]	1.57 [35]
Density ρ_{solid} (kg·m ⁻³)	860	430 (measured)	400 (estimated)	200
Specific heat c_p (J·kg ⁻¹ ·K ⁻¹)	1266 [36]	1266	-	-
Thermal conductivity λ_{solid} (W·m ⁻¹ ·K ⁻¹)	0.18 [37]	0.09	-	-
Emissivity ω_{solid} (-)	0.9 [37]	0.9	-	-

Lastly, transfer coefficients were obtained from correlations from literature. They use gas properties from literature [37] and are defined in Table 8.

Table 8. Definition of transfer coefficients.

Transfer Coefficient	Coefficient Definition	Correlation
Heat transfer coefficient h_t (W·m ⁻² ·K ⁻¹)	$\frac{\lambda_{gas} Nu}{L_c}$	$Nu = 2 + \left(0.4Re^{\frac{1}{2}} + 0.06Re^{\frac{2}{3}}\right) Pr^{0.4}$ [38]
Effective diffusion coefficient D_{eff} (m ² ·s ⁻¹)	$\frac{\epsilon_{solid}}{\tau_{solid}} D_{H_2O-N_2}$	$D_{H_2O-N_2} = \frac{0.0017^{1.75} \left(\frac{1}{M_{H_2O}} + \frac{1}{M_{N_2}}\right)^{\frac{1}{2}}}{P_{gas} \left(\sum v_{H_2O}^{\frac{1}{3}} + \sum v_{N_2}^{\frac{1}{3}}\right)^2}$ [39]
Mass transfer coefficient h_m (m·s ⁻¹)	$\frac{D_{H_2O-N_2} Sh}{L_c}$	$Sh = 2 + \left(0.4Re^{\frac{1}{2}} + 0.06Re^{\frac{2}{3}}\right) Sc^{0.4}$ [38]

Gas properties have a satisfactory accuracy while biomass and char properties as well as heat and mass transfer coefficients and kinetic parameters are estimated or calculated from empirical equations. Therefore, this low accuracy on the values used for calculations must be taken into account when analyzing the results obtained for characteristic times.

3. Results and Discussion

The experimental method used to demonstrate the influence of char preparation and biomass type involves various experimental devices at different scales. Therefore, it is necessary to look at the time scales of the phenomena involved in the process to determine its regime, i.e., chemical regime or regime led by heat or mass transfer. The analysis was conducted separately on pyrolysis and on gasification since these two steps were experimentally separated.

3.1. Characteristic Time Analysis

3.1.1. Analysis of Characteristic Times of the Pyrolysis Step

Characteristic times of the pyrolysis step are represented in Figure 3 for particle scale and for bed scale in the conditions of TGA, device M, and device P for a particle size below 200 μm . Results are shown as a function of temperature between 200 $^{\circ}\text{C}$ and 450 $^{\circ}\text{C}$, i.e., in the range of temperature corresponding to biomass degradation, according to the literature [40].

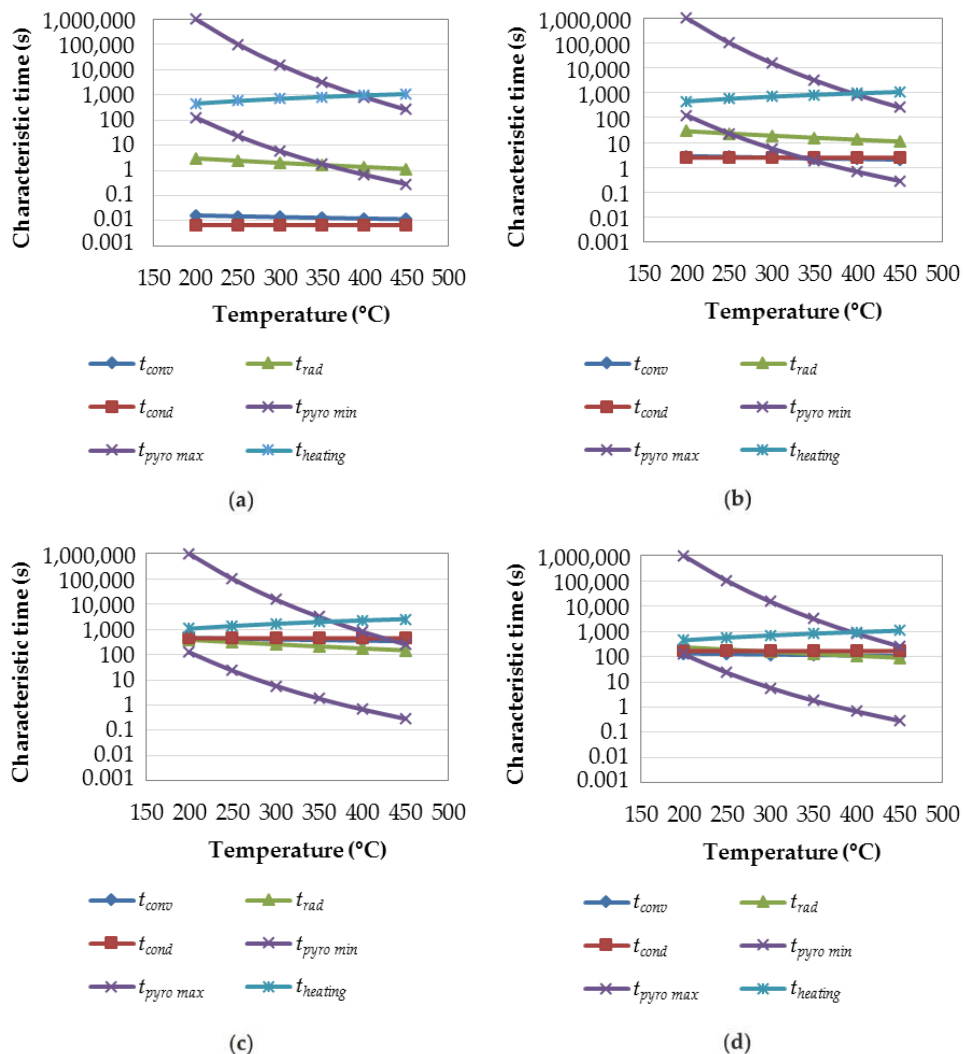


Figure 3. Characteristic times of the pyrolysis step as a function of temperature for: (a) particle scale in TGA conditions; (b) bed scale in TGA conditions; (c) bed scale in device M conditions; and (d) bed scale in device P condition. TGA: thermogravimetric analysis.

Calculations at particle scale were carried out for each of the three device conditions but results showed very negligible differences that were not noticeable through graphical representation. Therefore, only results obtained from TGA conditions are presented in this paper.

In all four cases, heating time and pyrolysis reaction times are the same except for heating time in device M conditions, but its variation is negligible. Only the three heat transfer characteristic times vary since they depend on the geometry of the system. Clearly, these characteristic times increase when the scale of the system—particle and beds of different sizes—increases.

When comparing heat transfers to the pyrolysis chemical reaction, it can be seen that their characteristic times are of the same order magnitude at least in part of the temperature range. This indicates that these phenomena occur simultaneously and none can be neglected.

Moreover, since pyrolysis was experimentally carried out in a dynamic mode, these times need to be compared with the heating time. For the phenomena to have enough time to occur, heating time should be higher than the phenomena characteristic times. In this study, heating times chosen for preparing the chars are of the same order of magnitude as the characteristic times of the phenomena involved.

In conclusion, characteristic time analysis shows that the pyrolysis step does not occur in a chemical regime. All phenomena occur simultaneously—none of them is negligible—and heating is too fast for the phenomena to occur.

Not being in a chemical regime during pyrolysis could result in chars that have different properties. Having different starting materials for gasification could, therefore, induce different kinetic behaviors. This is why it is important to check experimentally that chars produced under various conditions give the same gasification kinetics.

3.1.2. Analysis of Characteristic Times of the Gasification Step

Characteristic times of the gasification step are represented in Figure 4 for particle scale and bed scale under TGA conditions. Results are shown as a function of temperature between 500 °C and 1000 °C with the experimental study carried out at 800 °C in our study.

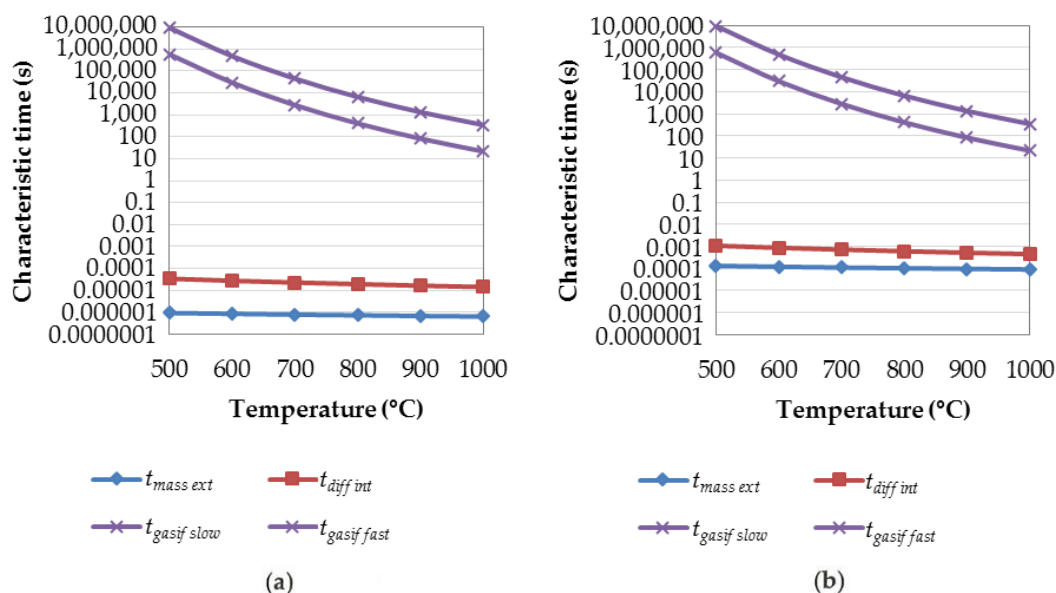


Figure 4. Characteristic times of the gasification step as a function of temperature for TGA conditions at: (a) particle scale and (b) bed scale.

At both scales, gasification chemical reactions with characteristic times remain the same. Mass transfer times slightly increase when the scale increases. However, at both scales and for both gasification kinetic laws, the gasification chemical reaction times are significantly higher—five to eight orders of magnitude—than mass transfer times. Therefore, according to time scales analysis, the gasification chemical reaction is the limiting phenomenon and mass transfers are negligible in comparison. The process occurs in the chemical regime.

This result is important since it means that kinetics obtained through TGA in these conditions should be intrinsic. According to this analysis, they exclusively represent the gasification chemical reaction without any bias from mass transfers.

However, Di Blasi’s review [9] states that, even in TGA, typical operating condition mass transfers can have a non-negligible effect on char gasification. To verify this result experimentally for the conditions of the work presented in this study, gasification was carried out on different masses of the same char sample ranging from the full crucible (14 mg) to 3 mg. Only gasification of 4 mg or below showed the same kinetics. Higher masses of samples reacted more slowly, which indicated mass transfer limitations. These observations were close to previous results obtained on the same apparatus under similar conditions [12]. It shows the limits of characteristic time analysis, which relies on parameters known with limited accuracy.

3.2. Influence of Biomass Type

The influence of the biomass type on gasification kinetics was investigated through TGA of the biomass samples, i.e., preparation of char TGA and gasification of this char. Results from the mass loss as a function of time in these experiments are presented in Figure 5. Replicates are not shown in this paper but were carried out to ensure repeatability of the process, which was validated—variability can be seen in Figure 6 through error bars.

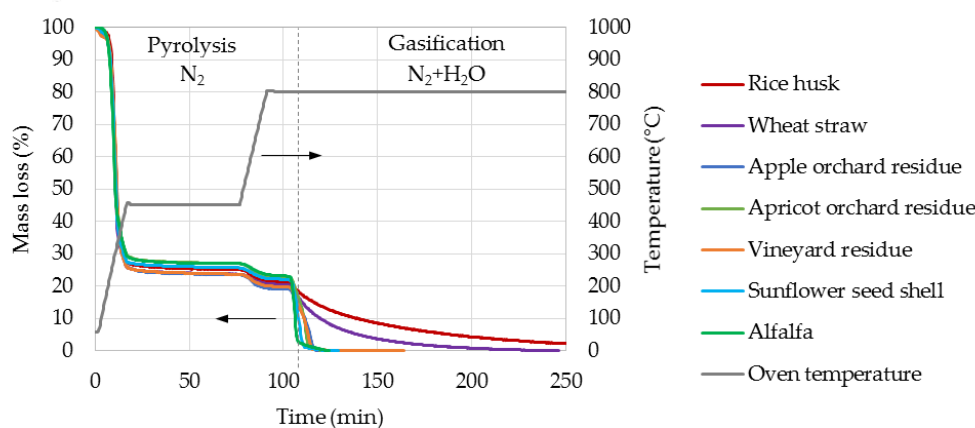


Figure 5. TGA of biomass samples presented as a mass loss and as a function of time. Pyrolysis: $0.05 \text{ L}\cdot\text{min}^{-1} \text{ N}_2$, $24 \text{ }^\circ\text{C}/\text{minutes}$, 1 h hold at $450 \text{ }^\circ\text{C}$, 15-min hold at $800 \text{ }^\circ\text{C}$. Gasification: $0.05 \text{ L}\cdot\text{min}^{-1}$ mixture 80 vol % N_2 /20 vol % H_2O , $800 \text{ }^\circ\text{C}$.

It can be noted that mass loss profiles obtained during the pyrolysis of biomass samples are very similar.

The highest mass loss is observed for temperatures below $450 \text{ }^\circ\text{C}$ with approximately 75% of the mass volatilized. Subsequently, around 5% of the mass is lost between $450 \text{ }^\circ\text{C}$ and $800 \text{ }^\circ\text{C}$. These yields align with results from literature [41]. They can be compared with char yields obtained after pyrolysis in other devices used for char preparation, which are gathered in Figure 6.

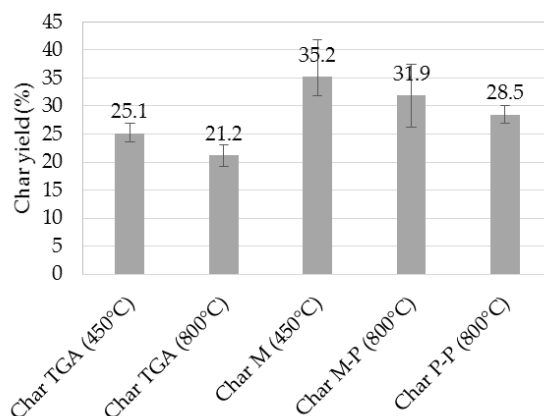


Figure 6. Char yield obtained in each char preparation condition (see Table 2).

There is a visible difference between values obtained at the thermo-balance scale and values obtained on devices M and P. This observation might be due to heat transfer limitations that are higher in the devices M and P, which are seen with characteristic times and can result in a lower solid conversion, i.e., a higher char yield. However, large scale values are close to what is expected for slow pyrolysis at pilot or industrial scale—35% char, 30% condensable products, and 35% non-condensable products [40,42].

The focus is made on the gasification step in Figure 7 and presented as a solid conversion and as a function of time.

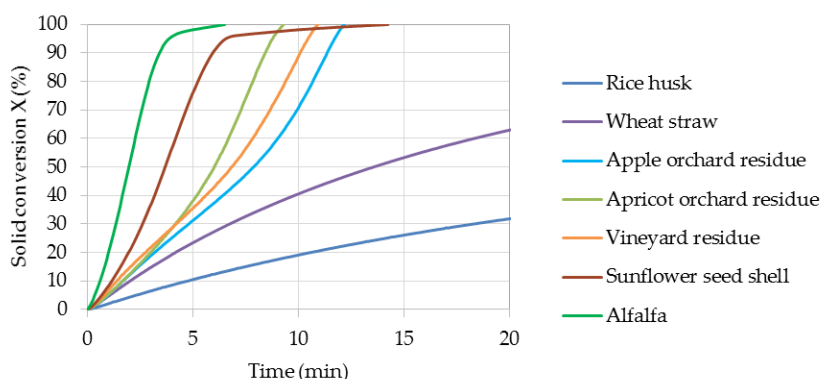


Figure 7. Solid conversion of biomass samples as a function of time during the gasification step (char TGA, $0.05 \text{ L}\cdot\text{min}^{-1}$ mixture 80 vol % N_2 /20 vol % H_2O , 800°C). Including data from Dupont et al. [28].

Three families of behavior can be identified, which is identified in literature [18]:

- Family 1 and its conversion rate is the highest and is constant and then increases such as in apple orchard residue, apricot orchard residue, and vineyard residue.
- Family 2 and its conversion rate is the slowest and is continuously decreasing such as in a rice husk and wheat straw.
- Family 3 and its conversion rate is intermediate and is constant and then decreases such as in sunflower seed shells and in alfalfa.

In addition, average reactivities of these biomass samples can be compared. Values of average reactivities between 1% and 80% conversion rates are gathered in Figure 8.

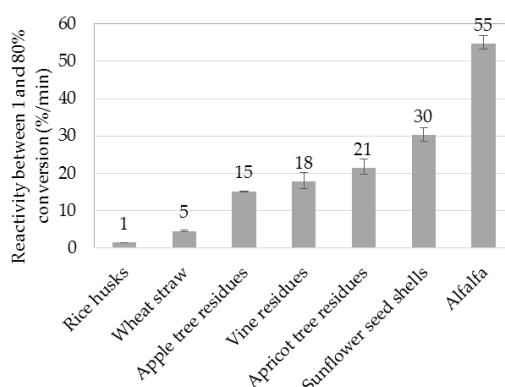


Figure 8. Gasification average reactivity between 1% and 80% conversion of biomass samples (char TGA, $0.05 \text{ L}\cdot\text{min}^{-1}$ mixture 80 vol % N_2 /20 vol % H_2O , $800 \text{ }^\circ\text{C}$).

Substantial variation between biomasses is noted due to a factor of almost 50 between average reactivities of rice husk—slowest sample to be gasified at $1.2\% \cdot \text{min}^{-1}$ —and alfalfa—fastest sample to be gasified at $54.7\% \cdot \text{min}^{-1}$.

These results could be related to inorganic composition of biomass samples. Silica-rich samples tended to have lower reaction rates than silica-poor samples. Among the latter, the reaction rate tends to increase with increasing content of potassium, which is in accordance with literature [18,43]. Other physicochemical characterizations such as a surface area measurement or H and O quantification have not been performed in the present study and may bring a better understanding of the results.

3.3. Influence of Char Preparation

To investigate the influence of char preparation, steam gasification kinetics of chars prepared in different conditions were compared. To carry out this comparison, samples with extreme behaviors were selected from the study of biomass samples. Sunflower seed shells and alfalfa were chosen for their high reactivity, high potassium content, and low silicon content. The rice husk was chosen for its low reactivity, low potassium content, and high silicon content.

TGA of the gasification step was conducted on this chars selection. Results expressed in the form of solid conversion as a function of time are presented in Figure 9. Reactivities between 1% and 80% were derived from these results and are given in Figure 10.

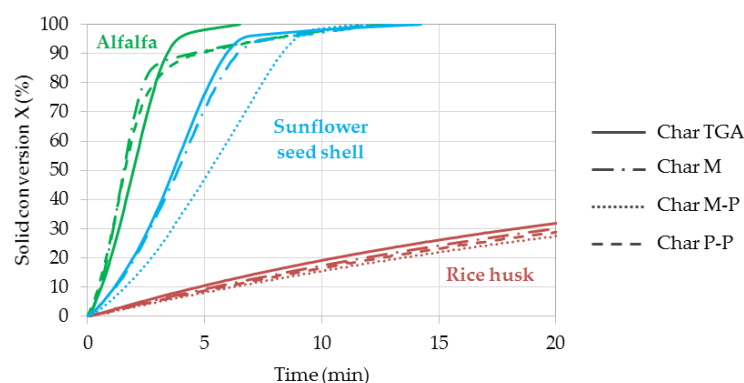


Figure 9. Solid conversion of chars as a function of time during gasification ($0.05 \text{ L}\cdot\text{min}^{-1}$ mixture 80 vol % N_2 /20 vol % H_2O , $800 \text{ }^\circ\text{C}$).

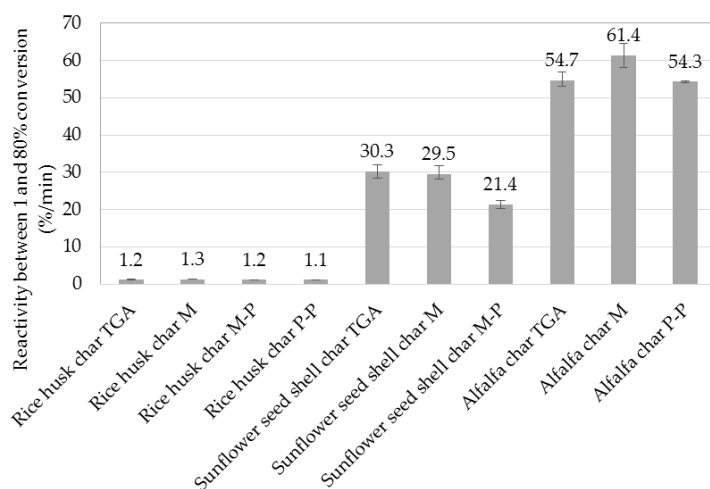


Figure 10. Gasification average reactivity between 1% and 80% conversion of biomass and char samples (see Table 2).

For each biomass, chars prepared in different conditions—in particular LHR pyrolysis conditions and not in a chemical regime—have the same reactivity during gasification. One exception for char M-P comes from the sunflower seed shells. No explanation was found regarding this result but it may be found by characterizing the chars. However, variations are negligible compared to differences that are observed between fast-reacting and slow-reacting biomass types. There is a factor of 1.2 in average between reactivities of the various char samples from each biomass, which is very low when compared to the factor of almost 50 calculated between reactivities of rice husk and alfalfa.

4. Conclusions

Thermogravimetric analysis (TGA) of biomass samples and of chars prepared from these biomasses in different LHR pyrolysis conditions outside the chemical regime showed that the biomass type has a significantly higher influence on steam gasification kinetics than char preparation conditions. In the range of the seven studied biomass samples, a factor of almost 50 was measured between average reactivities of the two samples with extreme behavior (rice husk with $1.2\% \cdot \text{min}^{-1}$ and alfalfa with $54.7\% \cdot \text{min}^{-1}$). In comparison, chars prepared in conditions outside the chemical regime from various amounts of biomass depending on the crucible geometry (height and surface) and several working temperatures ($450\text{ }^{\circ}\text{C}$ or $800\text{ }^{\circ}\text{C}$ in one or two steps) showed a much lower difference with an average factor of 1.2 for a given biomass type.

The influence of biomass type could be assumed to be related to inorganic content of the biomass as opposed to its molecular constituents—lignin, hemicellulose, cellulose. This assumption is supported by literature data. However, further investigations are in progress and consist of physicochemical characterization of chars from different biomass samples. It will confirm if inorganic composition is the main influential parameter or if it should rather be explained by structural or textural properties of the char.

Author Contributions: Conceptualization, F.D., M.C., S.B., M.J. and C.D. Investigation, T.D., S.T. and M.G. Formal Analysis, T.D. Resources, M.C. Writing-Original Draft Preparation, T.D. Writing-Review & Editing, F.D., M.J. and C.D. Supervision, F.D., M.J. and C.D.

Funding: This research was funded by the Agence de l’Environnement et de la Maîtrise de l’Energie.

Conflicts of Interest: The authors declare no conflict of interest.

Nomenclature

$c_{p\ solid}$	$(J \cdot kg^{-1} \cdot K^{-1})$	Specific heat of the solid phase (bed or particle)
d_p	(m)	Particle diameter
D_c	(m)	Diameter of the cylindrical bed
D_{eff}	$(m^2 \cdot s^{-1})$	Effective diffusion coefficient
$D_{H_2O-N_2}$	$(m^2 \cdot s^{-1})$	Diffusion coefficient of the mixture N_2 - H_2O
h_m	$(m \cdot s^{-1})$	External mass transfer coefficient
h_t	$(W \cdot m^{-2} \cdot K^{-1})$	Heat transfer coefficient
H_c	(m)	Height of the cylindrical bed
k_{gasif}	(s^{-1})	Kinetic constant of the gasification reaction
k_{pyro}	(s^{-1})	Kinetic constant of the pyrolysis reaction
M_{H_2O}	$(kg \cdot mol^{-1})$	Molecular weight of water
M_{N_2}	$(kg \cdot mol^{-1})$	Molecular weight of nitrogen
Nu	(–)	Nusselt number
P_{H_2O}	(Pa)	Partial pressure of steam
P_{gas}	(Pa)	Pressure of the gas
Pr	(–)	Prandtl number
r	(s^{-1})	Gasification rate
$r_{heating}$	$(K \cdot s^{-1})$	Heating rate
R	$(J \cdot mol^{-1} \cdot K^{-1})$	Universal gas constant
Re	(–)	Reynolds number
Sc	(–)	Schmidt number
Sh	(–)	Sherwood number
t_{cond}	(s)	Internal heat conduction time
t_{conv}	(s)	External heat convection time
$t_{diff\ int}$	(s)	Characteristic time of internal mass diffusion
t_{gasif}	(s)	Characteristic time of the gasification chemical reaction
$t_{heating}$	(s)	Heating time
$t_{mass\ ext}$	(s)	Characteristic time of external mass transfer
t_{pyro}	(s)	Characteristic time of the pyrolysis chemical reaction
t_{rad}	(s)	External radiation time
T_{gas}	(K)	Gas temperature
T_{solid}	(K)	Solid (bed or particle) temperature
X	(–)	Solid conversion
ϵ_{solid}	(–)	Porosity of the solid phase (bed or particle)
λ_{gas}	$(W \cdot m^{-1} \cdot K^{-1})$	Thermal conductivity of the gas phase
λ_{solid}	$(W \cdot m^{-1} \cdot K^{-1})$	Thermal conductivity of the solid phase (bed or particle)
ρ_{solid}	$(kg \cdot m^{-3})$	Density of the solid phase (bed or particle)
σ	$(W \cdot m^{-2} \cdot K^{-4})$	Boltzmann constant
$(\Sigma v)_{H_2O}$	$(m^3 \cdot mol^{-1})$	Diffusion volume of H_2O
$(\Sigma v)_{N_2}$	$(m^3 \cdot mol^{-1})$	Diffusion volume of N_2
τ_{solid}	(–)	Tortuosity of the solid phase (bed or particle)
ω_{solid}	(–)	Emissivity of the biomass

References

1. Kumar, A.; Jones, D.D.; Hanna, M.A. Thermochemical Biomass Gasification: A Review of the Current Status of the Technology. *Energies* **2009**, *2*, 556–581. [CrossRef]
2. Bartocci, P.; Zampilli, M.; Bidini, G.; Fantozzi, F. Hydrogen-rich gas production through steam gasification of charcoal pellet. *Appl. Therm. Eng.* **2018**, *132*, 817–823. [CrossRef]
3. Luo, S.; Xiao, B.; Guo, X.; Hu, Z.; Liu, S.; He, M. Hydrogen-rich gas from catalytic steam gasification of biomass in a fixed bed reactor: Influence of particle size on gasification performance. *Int. J. Hydrog. Energy* **2009**, *34*, 1260–1264. [CrossRef]

4. Yan, F.; Luo, S.; Hu, Z.; Xiao, B.; Cheng, G. Hydrogen-rich gas production by steam gasification of char from biomass fast pyrolysis in a fixed-bed reactor: Influence of temperature and steam on hydrogen yield and syngas composition. *Bioresour. Technol.* **2010**, *101*, 5633–5637. [[CrossRef](#)] [[PubMed](#)]
5. Rafati, M.; Wang, L.; Dayton, D.C.; Schimmel, K.; Kabadi, V.; Shahbazi, A. Techno-economic analysis of production of Fischer-Tropsch liquids via biomass gasification: The effects of Fischer-Tropsch catalysts and natural gas co-feeding. *Energy Convers. Manag.* **2017**, *133*, 153–166. [[CrossRef](#)]
6. Snehes, A.S.; Mukunda, H.S.; Mahapatra, S.; Dasappa, S. Fischer-Tropsch route for the conversion of biomass to liquid fuels—Technical and economic analysis. *Energy* **2017**, *130*, 182–191. [[CrossRef](#)]
7. Chiodini, A.; Bua, L.; Carnelli, L.; Zwart, R.; Vreugdenhil, B.; Vocciante, M. Enhancements in Biomass-to-Liquid processes: Gasification aiming at high hydrogen/carbon monoxide ratios for direct Fischer-Tropsch synthesis applications. *Biomass Bioenergy* **2017**, *106*, 104–114. [[CrossRef](#)]
8. Dupont, C.; Boissonnet, G.; Seiler, J.-M.; Gauthier, P.; Schweich, D. Study about the kinetic processes of biomass steam gasification. *Fuel* **2007**, *86*, 32–40. [[CrossRef](#)]
9. Di Blasi, C. Combustion and gasification rates of lignocellulosic chars. *Prog. Energy Combust. Sci.* **2009**, *35*, 121–140. [[CrossRef](#)]
10. Ballerini, D.; Alazard-Toux, N. *Les Biocarburants*; Editions Technip: Paris, France, 2006; ISBN 978-2-7108-0969-2.
11. Guerrero, M.; Ruiz, M.P.; Millera, Á.; Alzueta, M.U.; Bilbao, R. Oxidation Kinetics of Eucalyptus Chars Produced at Low and High Heating Rates. *Energy Fuels* **2008**, *22*, 2084–2090. [[CrossRef](#)]
12. Dupont, C.; Nocquet, T.; Da Costa, J.A.; Verne-Tourmon, C. Kinetic modelling of steam gasification of various woody biomass chars: Influence of inorganic elements. *Bioresour. Technol.* **2011**, *102*, 9743–9748. [[CrossRef](#)] [[PubMed](#)]
13. Vassilev, S.V.; Baxter, D.; Andersen, L.K.; Vassileva, C.G. An overview of the chemical composition of biomass. *Fuel* **2010**, *89*, 913–933. [[CrossRef](#)]
14. Feng, D.; Zhao, Y.; Zhang, Y.; Xu, H.; Zhang, L.; Sun, S. Catalytic mechanism of ion-exchanging alkali and alkaline earth metallic species on biochar reactivity during CO₂/H₂O gasification. *Fuel* **2018**, *212*, 523–532. [[CrossRef](#)]
15. Jiang, L.; Hu, S.; Wang, Y.; Su, S.; Sun, L.; Xu, B.; He, L.; Xiang, J. Catalytic effects of inherent alkali and alkaline earth metallic species on steam gasification of biomass. *Int. J. Hydrog. Energy* **2015**, *40*, 15460–15469. [[CrossRef](#)]
16. Kajita, M.; Kimura, T.; Norinaga, K.; Li, C.Z.; Hayashi, J.I. Catalytic and noncatalytic mechanisms in steam gasification of char from the pyrolysis of biomass. *Energy Fuels* **2009**, *24*, 108–116. [[CrossRef](#)]
17. Lahijani, P.; Zainal, Z.A.; Mohamed, A.R.; Mohammadi, M. CO₂ gasification reactivity of biomass char: Catalytic influence of alkali, alkaline earth and transition metal salts. *Bioresour. Technol.* **2013**, *144*, 288–295. [[CrossRef](#)] [[PubMed](#)]
18. Dupont, C.; Jacob, S.; Marrakchy, K.O.; Hognon, C.; Grateau, M.; Labalette, F.; Da Silva Perez, D. How inorganic elements of biomass influence char steam gasification kinetics. *Energy* **2016**, *109*, 430–435. [[CrossRef](#)]
19. Kannan, M.P.; Richards, G.N. Gasification of biomass chars in carbon dioxide: dependence of gasification rate on the indigenous metal content. *Fuel* **1990**, *69*, 747–753. [[CrossRef](#)]
20. Cuervo, N.; Dufaud, O.; Torrado, D.; Bardin-Monnier, N.; Perrin, L.; Laurent, A. Experimental study and modeling of the pyrolysis of organic dusts: application to dust explosions. *Chem. Eng. Trans.* **2013**, 931–936. [[CrossRef](#)]
21. Dufour, A.; Quartassi, B.; Bounaceur, R.; Zoulalian, A. Modelling intra-particle phenomena of biomass pyrolysis. *Chem. Eng. Res. Des.* **2011**, *89*, 2136–2146. [[CrossRef](#)]
22. Gómez-Barea, A.; Leckner, B. Modeling of biomass gasification in fluidized bed. *Prog. Energy Combust. Sci.* **2010**, *36*, 444–509. [[CrossRef](#)]
23. Palumbo, A.W.; Weimer, A.W. Heat transfer-limited flash pyrolysis of woody biomass: Overall reaction rate and time analysis using an integral model with experimental support. *J. Anal. Appl. Pyrolysis* **2015**, *113*, 474–482. [[CrossRef](#)]
24. Septien, S.; Valin, S.; Dupont, C.; Peyrot, M.; Salvador, S. Effect of particle size and temperature on woody biomass fast pyrolysis at high temperature (1000–1400 °C). *Fuel* **2012**, *97*, 202–210. [[CrossRef](#)]

25. Martinez, M.G.; Dupont, C.; Thiery, S.; Meyer, X.M.; Gourdon, C. Characteristic time analysis of biomass torrefaction phenomena—Application to thermogravimetric analysis device. *Chem. Eng. Trans.* **2016**, *50*, 61–66. [CrossRef]
26. European Standards. Solid Biofuels—Determination of Ash Content (EN 14775). Available online: https://www.google.com.tw/url?sa=t&rct=j&q=&esrc=s&source=web&cd=1&ved=2ahUKewjPrM-E1t_cAhVWfd4KHUe6BNIQFjAAegQIABAC&url=https%3A%2F%2Fwww.researchgate.net%2Fprofile%2FAlain_Celzard%2Fpost%2Fwhich_ASTM_standard_should_I_refer_to_in_order_to_determine_the_moisture_and_volatiles_content_in_biomass%2Fattachment%2F59d62117c49f478072e9848e%2FAS%253A271759398375424%25401441803897376%2Fdownload%2FSolid%2Bbiofuels%2B-%2BDetermination%2Bof%2Bash%2Bcontent.pdf&usg=AOvVaw0FjluSmH5RWZsNzKmNjEL_ (accessed on 11 June 2018).
27. International Organization for Standardization. Solid Biofuels—Determination of Major Elements—Al, Ca, Fe, Mg, P, K, Si, Na and Ti (ISO 16967: 2015). Available online: <https://www.iso.org/standard/58065.html> (accessed on 11 June 2018).
28. Dupont, C.; Karakashov, B.; Dahou, T.; Martinez, M.G.; Saavedra, C.; Da Silva Perez, D.; Karakasova, L. Quality of agricultural waste from orchards and vineyards as feedstock for thermal processes with focus on torrefaction and gasification. *Biomass Bioenergy* **2018**. submitted.
29. Villermaux, J.; Antoine, B. Pyrolyse éclair de solides divisés dans un réacteur continu: 1. Un nouveau modèle de volatilisation thermique de particules solides. *Rev. Générale Therm.* **1980**, *227*, 851–860.
30. Di Blasi, C. Modeling chemical and physical processes of wood and biomass pyrolysis. *Prog. Energy Combust. Sci.* **2008**, *34*, 47–90. [CrossRef]
31. Nunn, T.R.; Howard, J.B.; Longwell, J.P.; Peters, W.A. Product compositions and kinetics in the rapid pyrolysis of sweet gum hardwood. *Ind. Eng. Chem. Process Des. Dev.* **1985**, *24*, 3. [CrossRef]
32. Samolada, M.C.; Vasalos, I.A. A kinetic approach to the flash pyrolysis of biomass in a fluidized bed reactor. *Fuel* **1991**, *70*, 883–889. [CrossRef]
33. Brewer, C.E.; Chuang, V.J.; Masiello, C.A.; Gonnermann, H.; Gao, X.; Dugan, B.; Driver, L.E.; Panzacchi, P.; Zygourakis, K.; Davies, C.A. New approaches to measuring biochar density and porosity. *Biomass Bioenergy* **2014**, *66*, 176–185. [CrossRef]
34. Johnsson, J.E.; Jensen, A. Effective diffusion coefficients in coal chars. *Proc. Combust. Inst.* **2000**, *28*, 2353–2359. [CrossRef]
35. Dalloz-Dubrujeaud, B.; Faure, R.; Tadriss, L.; Giraud, G. Perte de pression et vitesse minimum de fluidisation dans un lit de particules 2D. *Comptes Rendus l’Académie Sci.-Ser. IIB-Mech. Phys. Astron.* **2000**, *328*, 231–236. [CrossRef]
36. Dupont, C.; Chiriach, R.; Gauthier, G.; Toche, F. Heat capacity measurements of various biomass types and pyrolysis residues. *Fuel* **2014**, *115*, 644–651. [CrossRef]
37. Perry, R.H.; Green, D.W. *Perry’s Chemical Engineers’ Handbook*; McGraw-Hill: London, UK, 1998; ISBN 978-0-07-115982-1.
38. Whitaker, S. Forced convection heat transfer correlations for flow in pipes, past flat plates, single cylinders, single spheres, and for flow in packed beds and tube bundles. *AIChE J.* **1972**, *18*, 361–371. [CrossRef]
39. Fuller, E.N.; Schettler, P.D.; Giddings, J.C. New method for prediction of binary gas-phase diffusion coefficients. *Ind. Eng. Chem.* **1966**, *58*, 18–27. [CrossRef]
40. Kan, T.; Strezov, V.; Evans, T.J. Lignocellulosic biomass pyrolysis: A review of product properties and effects of pyrolysis parameters. *Renew. Sustain. Energy Rev.* **2016**, *57*, 1126–1140. [CrossRef]
41. Anca-Couce, A. Reaction mechanisms and multi-scale modelling of lignocellulosic biomass pyrolysis. *Prog. Energy Combust. Sci.* **2016**, *53*, 41–79. [CrossRef]
42. Deglise, X.; Donnot, A. Bois énergie—Propriétés et voies de valorisation. *Tech. Ing. Énerg. Renouvelables* **2017**. Available online: <https://www.techniques-ingenieur.fr/base-documentaire/energies-th4/energies-renouvelables-42594210/bois-energie-be8535/> (accessed on 11 June 2018).
43. Zhang, Y.; Ashizawa, M.; Kajitani, S.; Miura, K. Proposal of a semi-empirical kinetic model to reconcile with gasification reactivity profiles of biomass chars. *Fuel* **2008**, *87*, 475–481. [CrossRef]



© 2018 by the authors. Licensee MDPI, Basel, Switzerland. This article is an open access article distributed under the terms and conditions of the Creative Commons Attribution (CC BY) license (<http://creativecommons.org/licenses/by/4.0/>).

Annex C. Characteristic time analysis of the gasification step

This annex presents the results of the characteristic time analysis of the gasification step both at particle scale and at bed scale for the cases of TGA and of the induction furnace PYRATES. The method and the data used for the calculations are given in a published article (Dahou et al., 2018). The “device P” in the article corresponds to the induction furnace PYRATES.

1. Characteristic times analysis of the gasification step

Characteristic times of the gasification step are represented as a function of temperature for the particle scale in Figure Annex C.6 for a particle diameter of $d_p = 0.2 \text{ mm}$, for the bed scale in Figure Annex C.4 and Figure Annex C.2 for TGA and PYRATES respectively for a bed height of and $H_c = 2 \text{ mm}$ and $H_c = 48 \text{ mm}$ respectively. Results are also displayed as a function of the particle diameter and the bed height for a temperature of $T_{gas} = 800 \text{ }^\circ\text{C}$ in Figure Annex C.5 and Figure Annex C.3.

At particle scale, the experimental device only has an influence on characteristic time of external mass transfer and this influence is negligible compared to differences between the characteristic times of the different phenomena.

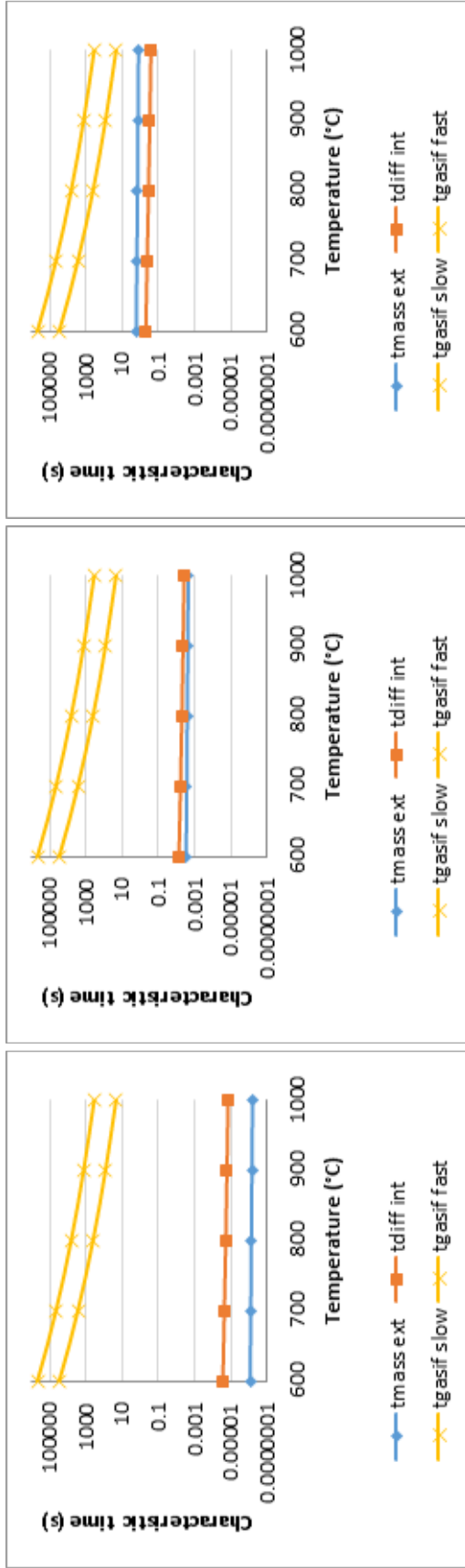


Figure Annex C.6 | Characteristic times for the gasification step at particle-scale

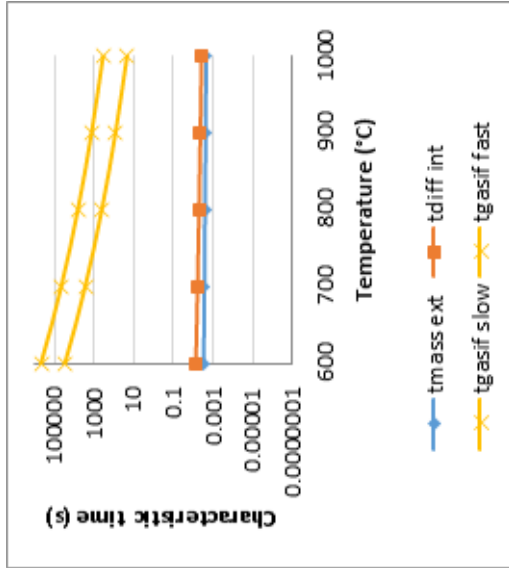


Figure Annex C.4 | Characteristic times for the gasification step at bed scale

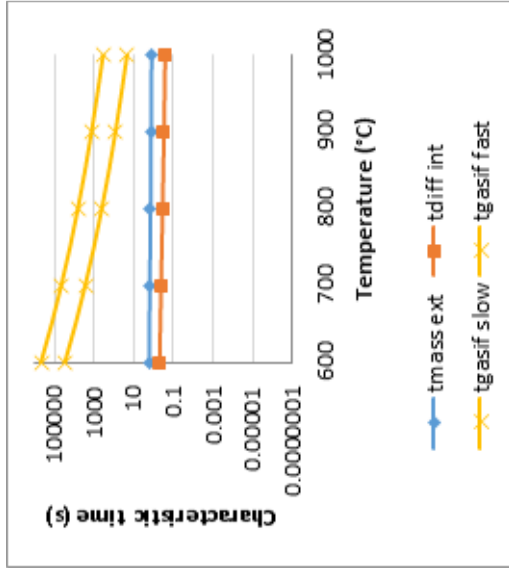


Figure Annex C.2 | Characteristic times for the gasification step at bed scale

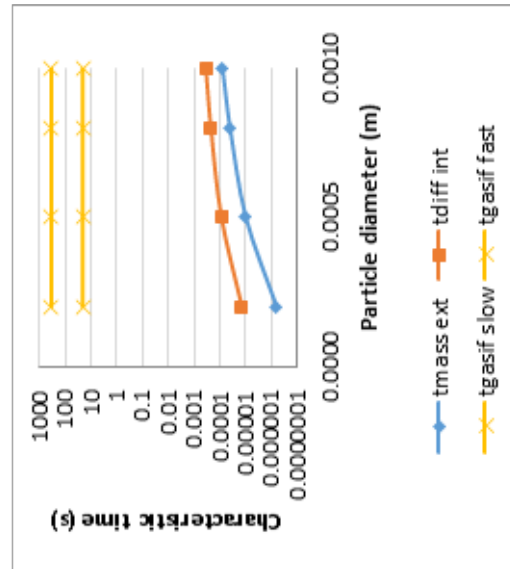


Figure Annex C.5 | Characteristic times for the gasification step at particle-scale for T_{gas} = 800 °C.

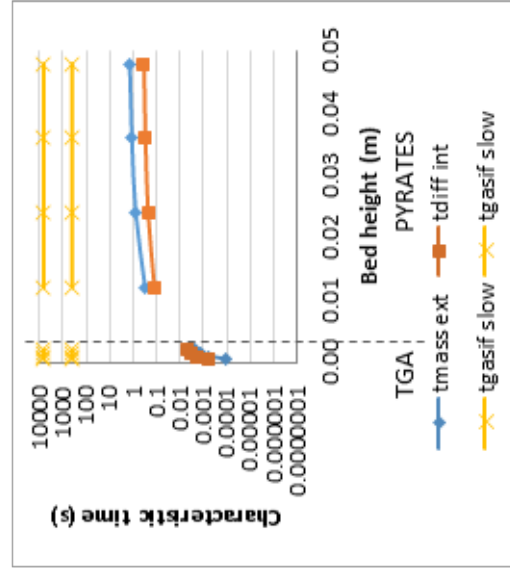


Figure Annex C.3 | Characteristic times for the gasification step at bed scale for T_{gas} = 800 °C.

Conclusions are the same at bed scale whatever the set up (TGA or PYRATES) and at particle scale. Characteristic times of mass transfers are of the same order of magnitude but they are significantly lower than the characteristic time of gasification chemical reaction—except for high temperatures in PYRATES. The gasification reaction is therefore the limiting phenomenon during the gasification step and the transformation occurs in chemical regime at 800 °C. This means that the transformation occurs homogeneously inside the bed of particles and inside each particle under the conditions of the calculations.

2. Sensitivity analysis of the characteristic times of the gasification step

Several numerical data used in this analysis have some uncertainties like the bed porosity and tortuosity. Some other numerical data like the gasification kinetics law have different values depending the biomass, the temperature range and the slow or fast pyrolysis thermal process.

Bed porosity and tortuosity have an effect into the characteristic times of internal mass diffusion and external mass transfer at particle and bed scale. These parameters could not be measured and have been estimated (Table 7 in (Dahou et al., 2018)) based on literature review. The sensitivity of these two parameters have been investigated ($\pm 50\%$) for $T_{gas} = 800\text{ °C}$, $d_p = 200\text{ }\mu\text{m}$ and $H_c = 48\text{ mm}$ at particle and bed scale respectively. Results from these analyses are presented in Figure Annex C.7 and Figure Annex C.8 where a bar uncertainty represent the minimum and the maximum values obtained.

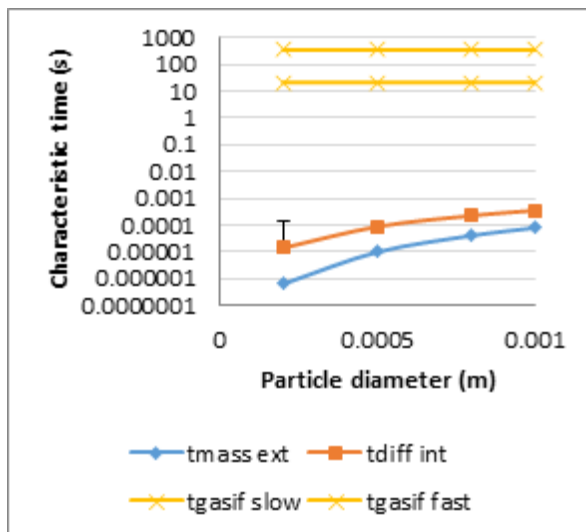


Figure Annex C.7 | Characteristic times for the gasification step at particle-scale for $T_{gas} = 800\text{ °C}$ with the uncertainty related to bed porosity and tortuosity values.

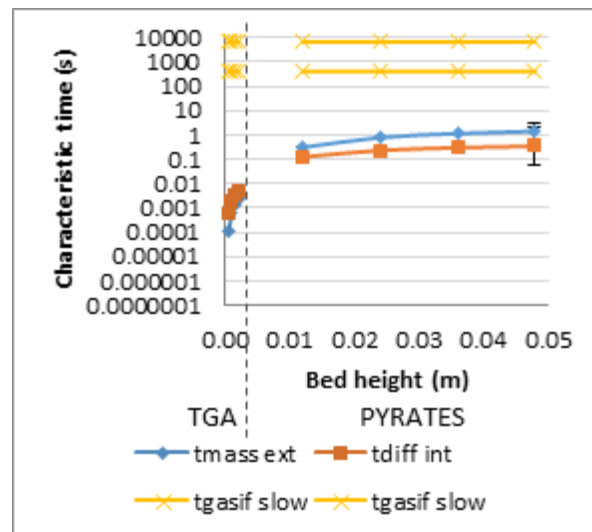


Figure Annex C.8 | Characteristic times for the gasification step at bed scale for $T_{gas} = 800\text{ °C}$ with the uncertainty related to bed porosity and tortuosity values.

Results show that for both characteristic times (internal mass diffusion and external mass transfer) changes of one to two orders of magnitude in relation to bed porosity and tortuosity, in the analyzed ranges, but remains several orders of magnitude lower than gasification characteristic time for both particle and bed scale.

Annex D. Pore size distribution of rice husk and sunflower seed shell chars expressed in incremental volume

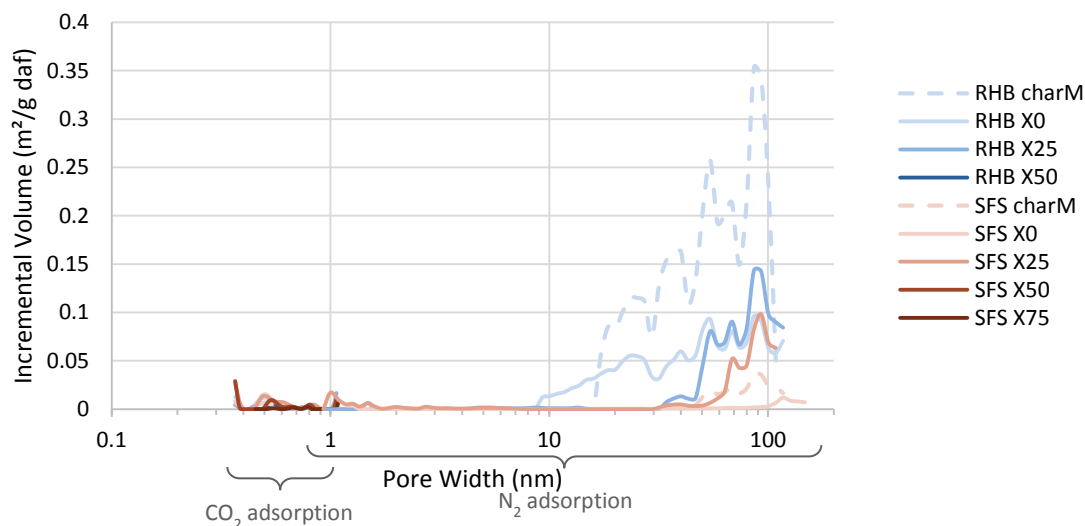


Figure Annex D.9 | Pore size distribution using DFT model from N₂ and CO₂ adsorption isotherms of rice husk and sunflower seed shell chars at several pyrolysis and gasification conversions expressed in terms of incremental volume.

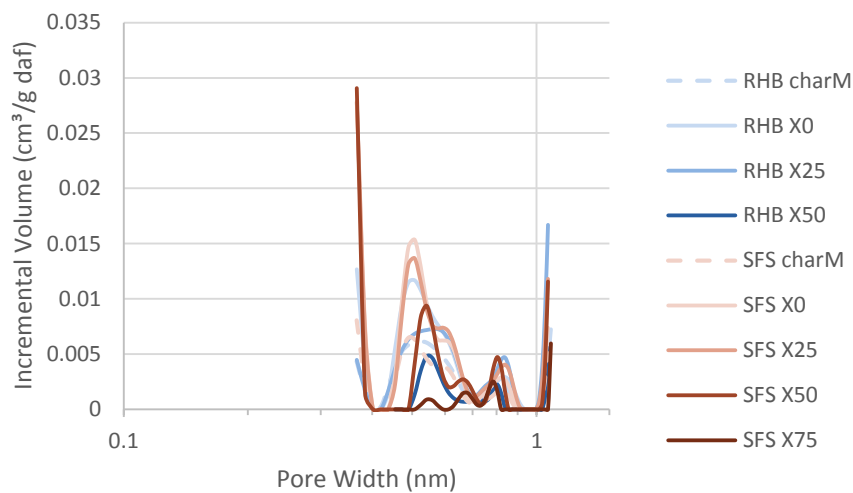


Figure Annex D.10 | Ultramicropore size distribution using DFT model from CO₂ adsorption isotherms of rice husk and sunflower seed shell chars at several pyrolysis and gasification conversions expressed in terms of incremental volume.

Annex E. Example of detailed results from calculations at thermodynamic equilibrium

1. Simulation of the rice husks X0 sample from charM data

FactSage 7.2

```
(gram) 0.08565 C + 0.00495 H + 0.0345 O + 0.0012 N +  
(gram) 0.00028 S + 0.00015 Cl + 0.0195 Si + 0.00225 K +  
(gram) 0.0006 Ca + 0.00015 Mg + 0.0003 P + 0.00015 Na +  
(gram) 0.00015 Al + 0.00015 Fe + 25 N2 =
```

```
0.89562 mol gas_ideal  
(25.026 gram, 0.89562 mol, 78.868 litre, 3.1731E-04 gram.cm-3)  
(800 C, 1 atm, a=1.0000)  
( 0.99649 N2  
+ 2.7355E-03 H2  
+ 7.6536E-04 CO  
+ 4.7053E-06 H2S  
+ 4.6455E-06 KCl  
+ 7.9626E-07 HCN  
+ 3.4734E-07 CH4  
+ 2.7652E-07 H2O  
+ 8.4961E-08 CO2  
+ 5.3721E-08 NH3  
+ 5.2516E-08 KCN  
+ 4.8099E-08 HCl  
+ 4.1673E-08 COS  
+ 4.0111E-08 K  
+ 1.5215E-08 (KCl)2  
+ 6.8012E-03 gram Slag  
(6.8012E-03 gram, 3.8050E-05 mol)  
(800 C, 1 atm, a=1.0000)  
+ 0.23801 wt.% K4Si2O6  
+ 15.589 wt.% K2Si2O5  
+ 4.9899 wt.% K2Si4O9  
+ 32.377 wt.% Si2O4  
+ 14.966 wt.% KSi2AlO6  
+ 0.57139 wt.% CaSiO3  
+ 15.579 wt.% K2Si5MgO12  
+ 3.4510 wt.% FeS
```

Annex E. Example of detailed results from calculations at thermodynamic equilibrium

+ 1.3574 wt.% Na4P2O7
 + 1.7058 wt.% KAlS2
 + 2.8864 wt.% K3PO4
 + 0.34445 wt.% K4P2O7
 + 5.6751 wt.% Na4MgP2O8)

System component	Amount/mol	Amount/gram	Mole fraction	Mass fraction
Fe	2.6860E-06	1.5000E-04	8.6989E-03	2.2055E-02
Ca	3.6251E-07	1.4529E-05	1.1740E-03	2.1362E-03
K	2.5680E-05	1.0041E-03	8.3168E-02	0.14763
S	4.4684E-06	1.4328E-04	1.4471E-02	2.1067E-02
P	4.3555E-06	1.3491E-04	1.4106E-02	1.9836E-02
Si	7.2580E-05	2.0385E-03	0.23506	0.29972
Al	5.5594E-06	1.5000E-04	1.8005E-02	2.2055E-02
Mg	3.7494E-06	9.1129E-05	1.2143E-02	1.3399E-02
Na	6.5246E-06	1.5000E-04	2.1131E-02	2.2055E-02
O	1.8281E-04	2.9248E-03	0.59205	0.43005

+ 1.0898E-03 gram K3P_MT
 (1.0898E-03 gram, 2.6651E-06 mol)
 (800 C, 1 atm, a=1.0000)
 (8.6442 wt.% (K2O)2 (P2O5) (K2O)
 + 0.74318 wt.% (K2O)2 (P2O5) (CaO)
 + 2.7530E-04 wt.% (K2O)2 (P2O5) (K2CaO2)
 + 49.987 wt.% (K2O)2 (P2O5) (MgO)
 + 40.625 wt.% (K2O)2 (P2O5) (K2MgO2))

System component	Amount/mol	Amount/gram	Mole fraction	Mass fraction
Ca	2.0966E-08	8.4027E-07	4.8695E-04	7.7104E-04
K	1.3009E-05	5.0863E-04	0.30215	0.46672
P	5.3301E-06	1.6509E-04	0.12380	0.15149
Mg	2.4222E-06	5.8871E-05	5.6258E-02	5.4021E-02
O	2.2273E-05	3.5635E-04	0.51731	0.32699

+ 7.7403E-02 gram C_Graphite
 (7.7403E-02 gram, 6.4445E-03 mol)
 (800 C, 1 atm, S1, a=1.0000)
 + 3.3412E-02 gram SiO2_quartz_beta(s3)
 (3.3412E-02 gram, 5.5609E-04 mol)
 (800 C, 1 atm, S2, a=1.0000)

+ 5.4492E-03 gram Ca2K2Si9O21_solid
 (5.4492E-03 gram, 7.2937E-06 mol)
 (800 C, 1 atm, S1, a=1.0000)

H	G	V	S	Cp
(J)	(J)	(litre)	(J/K)	(J/K)
2.07315E+04	-2.01020E+05	7.88685E+01	2.06636E+02	2.98299E+01

	H	G	S	Cp
	(J)	(J)	(J/K)	(J/K)
gas_ideal	2.12950E+04	-2.00173E+05	2.06372E+02	2.96252E+01
K3P_MT	-1.37068E+01	-1.61841E+01	2.30841E-03	2.15587E-03
Slag	-8.57252E+01	-1.02908E+02	1.60116E-02	1.53409E-02
C_Graphite	8.63116E+01	-9.34791E+01	1.67535E-01	1.42369E-01
SiO2_quartz_beta(s3)	-4.78380E+02	-5.50555E+02	6.72549E-02	3.87429E-02
Ca2K2Si9O21_solid	-7.20195E+01	-8.33393E+01	1.05482E-02	6.08256E-03

Total mass/gram = 25.150

Total mass/gram excluding gas_ideal = 0.12415

Databases: FTSalt 7.2, GTOX, FactPS 7.2

2. Simulation of the sunflower seed shells X0 sample from charM data

FactSage 7.2

(gram) 0.1149 C + 0.0057 H + 0.0186 O + 0.0018 N +
 (gram) 0.00018 S + 0.00015 Cl + 0.00015 Si + 0.00405 K +
 (gram) 0.00195 Ca + 0.0009 Mg + 0.00045 P + 0.00015 Na +
 (gram) 0.00015 Al + 0.00075 Fe + 25 N2 =

0.89638 mol gas_ideal
 (25.039 gram, 0.89638 mol, 78.935 litre, 3.1721E-04 gram.cm-3)
 (800 C, 1 atm, a=1.0000)
 (0.99565 N2
 + 3.1525E-03 H2
 + 1.1207E-03 CO
 + 3.9431E-05 KCN
 + 3.0129E-05 K
 + 4.6890E-06 KCl

Annex E. Example of detailed results from calculations at thermodynamic equilibrium

+ 8.5444E-07 HCN
 + 4.6663E-07 H2O
 + 4.6131E-07 CH4
 + 1.8218E-07 CO2
 + 6.6434E-08 NH3
 + 4.3220E-08 (KCN)2
 + 1.5501E-08 (KCl)2
 + 1.2442E-08 KOH

+ 2.8597E-03 gram K3P_MT

(2.8597E-03 gram, 6.1520E-06 mol)

(800 C, 1 atm, a=1.0000)
 (2.6151E-03 wt.% (K2O)2 (P2O5) (K2O)
 + 6.7414E-05 wt.% (K2O)2 (P2O5) (CaO)
 + 2.0252E-02 wt.% (K2O)2 (P2O5) (K2CaO2)
 + 1.4889E-04 wt.% (K2O)2 (P2O5) (MgO)
 + 99.977 wt.% (K2O)2 (P2O5) (K2MgO2))

System component	Amount/mol	Amount/gram	Mole fraction	Mass fraction
Ca	1.2100E-09	4.8495E-08	1.0927E-05	1.6958E-05
K	3.6912E-05	1.4432E-03	0.33333	0.50467
P	1.2304E-05	3.8110E-04	0.11111	0.13327
Mg	6.1507E-06	1.4949E-04	5.5543E-02	5.2275E-02
O	5.5368E-05	8.8586E-04	0.50000	0.30977

+ 1.6010E-03 gram MeO#2

(1.6010E-03 gram, 2.8553E-05 mol)

(800 C, 1 atm, a=1.0000)
 (4.4029E-04 wt.% Al+3:O-2
 + 99.970 wt.% Ca+2:O-2
 + 5.3339E-04 wt.% Fe+2:O-2
 + 1.3266E-05 wt.% Fe+3:O-2
 + 2.8574E-02 wt.% Mg+2:O-2
 + 8.3431E-05 wt.% Va:O-2
 + 1.4147E-25 wt.% Na+1:O-2)

System component	Amount/mol	Amount/gram	Mole fraction	Mass fraction
Fe	1.2182E-10	6.8030E-09	2.1332E-06	4.2492E-06
Ca	2.8541E-05	1.1439E-03	0.49980	0.71448
Al	1.6401E-10	4.4251E-09	2.8719E-06	2.7640E-06
Mg	1.1350E-08	2.7587E-07	1.9876E-04	1.7231E-04

Annex E. Example of detailed results from calculations at thermodynamic equilibrium

Na	7.3090E-32	1.6803E-30	1.2799E-27	1.0495E-27
O	2.8553E-05	4.5683E-04	0.50000	0.28534

+ 1.2100E-03 gram MeO#1

(1.2100E-03 gram, 2.9985E-05 mol)

(800 C, 1 atm, a=1.0000)

(2.9013E-03 wt.% Al+3:O-2

+ 2.4188E-03 wt.% Ca+2:O-2

+ 0.26722 wt.% Fe+2:O-2

+ 5.7341E-05 wt.% Fe+3:O-2

+ 99.727 wt.% Mg+2:O-2

+ 5.4642E-04 wt.% Va:O-2

+ 1.9867E-25 wt.% Na+1:O-2)

System component	Amount/mol	Amount/gram	Mole fraction	Mass fraction
Fe	4.5012E-08	2.5137E-06	7.5058E-04	2.0775E-03
Ca	5.2189E-10	2.0916E-08	8.7025E-06	1.7287E-05
Al	8.1675E-10	2.2037E-08	1.3619E-05	1.8213E-05
Mg	2.9938E-05	7.2765E-04	0.49922	0.60139
Na	7.7568E-32	1.7833E-30	1.2934E-27	1.4738E-27
O	2.9985E-05	4.7974E-04	0.50000	0.39650

+ 8.0925E-04 gram OLIVINE

(8.0925E-04 gram, 4.6995E-06 mol)

(800 C, 1 atm, a=1.0000)

(99.776 wt.% Ca+2:Ca+2:Si+4:O-2

+ 1.4035E-07 wt.% Ca+2:Fe+2:Si+4:O-2

+ 1.9185E-14 wt.% Ca+2:Mg+2:Si+4:O-2

+ 1.9343E-04 wt.% Fe+2:Ca+2:Si+4:O-2

+ 2.7017E-13 wt.% Fe+2:Fe+2:Si+4:O-2

+ 3.7507E-20 wt.% Fe+2:Mg+2:Si+4:O-2

+ 0.22350 wt.% Mg+2:Ca+2:Si+4:O-2

+ 3.1703E-10 wt.% Mg+2:Fe+2:Si+4:O-2

+ 4.2537E-17 wt.% Mg+2:Mg+2:Si+4:O-2)

System component	Amount/mol	Amount/gram	Mole fraction	Mass fraction
Fe	8.3321E-12	4.6530E-10	2.5328E-07	5.7498E-07
Ca	9.3874E-06	3.7623E-04	0.28536	0.46491
Si	4.6995E-06	1.3199E-04	0.14286	0.16310
Mg	1.1559E-08	2.8095E-07	3.5139E-04	3.4718E-04
O	1.8798E-05	3.0076E-04	0.57143	0.37165

+ 4.1805E-04 gram N3P_HT
 (4.1805E-04 gram, 1.1122E-06 mol)
 (800 C, 1 atm, a=1.0000)
 (2.7556E-02 wt.% Na6P2O8
 + 76.747 wt.% CaP2Na6O9
 + 1.7178E-03 wt.% K2P2Na4O8
 + 5.4333 wt.% Na4MgP2O8
 + 17.790 wt.% Na6MgP2O9)

System component	Amount/mol	Amount/gram	Mole fraction	Mass fraction
Ca	8.3563E-07	3.3490E-05	4.2212E-02	8.0110E-02
K	3.9884E-11	1.5594E-09	2.0148E-06	3.7302E-06
P	2.2243E-06	6.8896E-05	0.11236	0.16480
Mg	2.7618E-07	6.7125E-06	1.3951E-02	1.6056E-02
Na	6.5246E-06	1.5000E-04	0.32960	0.35880
O	9.9350E-06	1.5895E-04	0.50187	0.38022

+ 4.0495E-04 gram Oldhamite
 (4.0495E-04 gram, 5.6132E-06 mol)
 (800 C, 1 atm, a=1.0000)
 (3.6951E-05 wt.% FeS
 + 2.0445E-04 wt.% MgS
 +100.000 wt.% CaS)

System component	Amount/mol	Amount/gram	Mole fraction	Mass fraction
Fe	1.7021E-12	9.5056E-11	1.5162E-07	2.3473E-07
Ca	5.6132E-06	2.2497E-04	0.50000	0.55553
S	5.6132E-06	1.7999E-04	0.50000	0.44446
Mg	1.4687E-11	3.5697E-10	1.3083E-06	8.8151E-07

+ 0.10239 gram C_Graphite
 (0.10239 gram, 8.5251E-03 mol)
 (800 C, 1 atm, S1, a=1.0000)

+ 7.4748E-04 gram Fe_bcc_a2(s)
 (7.4748E-04 gram, 1.3385E-05 mol)
 (800 C, 1 atm, S1, a=1.0000)

+ 5.8752E-04 gram Al26Ca20Mg3Si3068_Pleochroite
 (5.8752E-04 gram, 2.1378E-07 mol)

Annex E. Example of detailed results from calculations at thermodynamic equilibrium

(800 C, 1 atm, S1, a=1.0000)

H	G	V	S	Cp
(J)	(J)	(litre)	(J/K)	(J/K)

2.13013E+04	-2.00635E+05	7.89351E+01	2.06808E+02	2.98508E+01
-------------	--------------	-------------	-------------	-------------

	H	G	S	Cp
	(J)	(J)	(J/K)	(J/K)
gas_ideal	2.12832E+04	-2.00397E+05	2.06570E+02	2.96490E+01
MeO#1	-1.69249E+01	-1.96930E+01	2.57937E-03	1.67078E-03
MeO#2	-1.70078E+01	-2.01203E+01	2.90037E-03	1.54221E-03
K3P_MT	-3.43011E+01	-4.07214E+01	5.98270E-03	3.55307E-03
Oldhamite	-2.44156E+00	-3.17440E+00	6.82886E-04	3.09706E-04
OLIVINE	-1.03162E+01	-1.19321E+01	1.50576E-03	8.79970E-04
N3P_HT	-7.31054E+00	-8.27680E+00	9.00388E-04	4.20316E-03
C_Graphite	1.14177E+02	-1.23659E+02	2.21625E-01	1.88333E-01
Al26Ca20Mg3Si3O68_Pleochroite	-8.10501E+00	-9.29757E+00	1.11127E-03	6.57596E-04
Fe_bcc_a2(s)	3.83454E-01	-6.33321E-01	9.47468E-04	6.42261E-04

Total mass/gram = 25.150

Total mass/gram excluding gas_ideal = 0.11103

Databases: FTsalt 7.2, GTX, FactPS 7.2

Annex F. P-XRD analysis of the model inorganic compounds

1. Amorphous silica

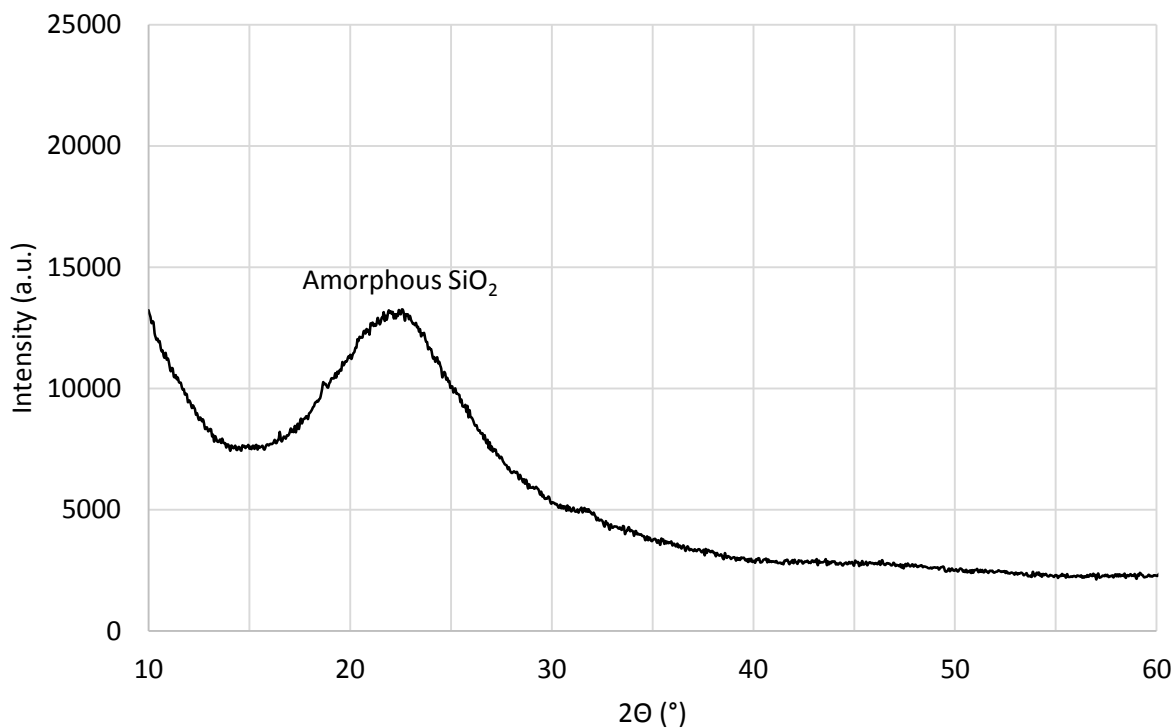


Figure Annex F.11 | P-XRD diffractogram of the pure amorphous silica.

2. Quartz

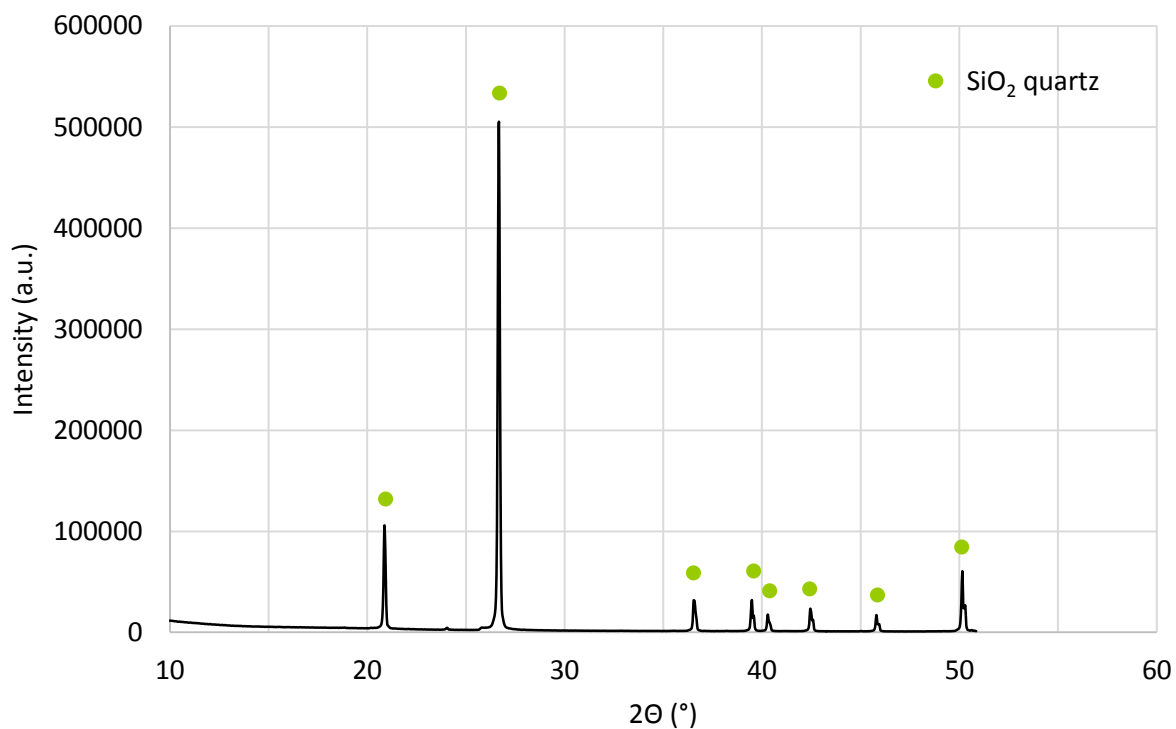
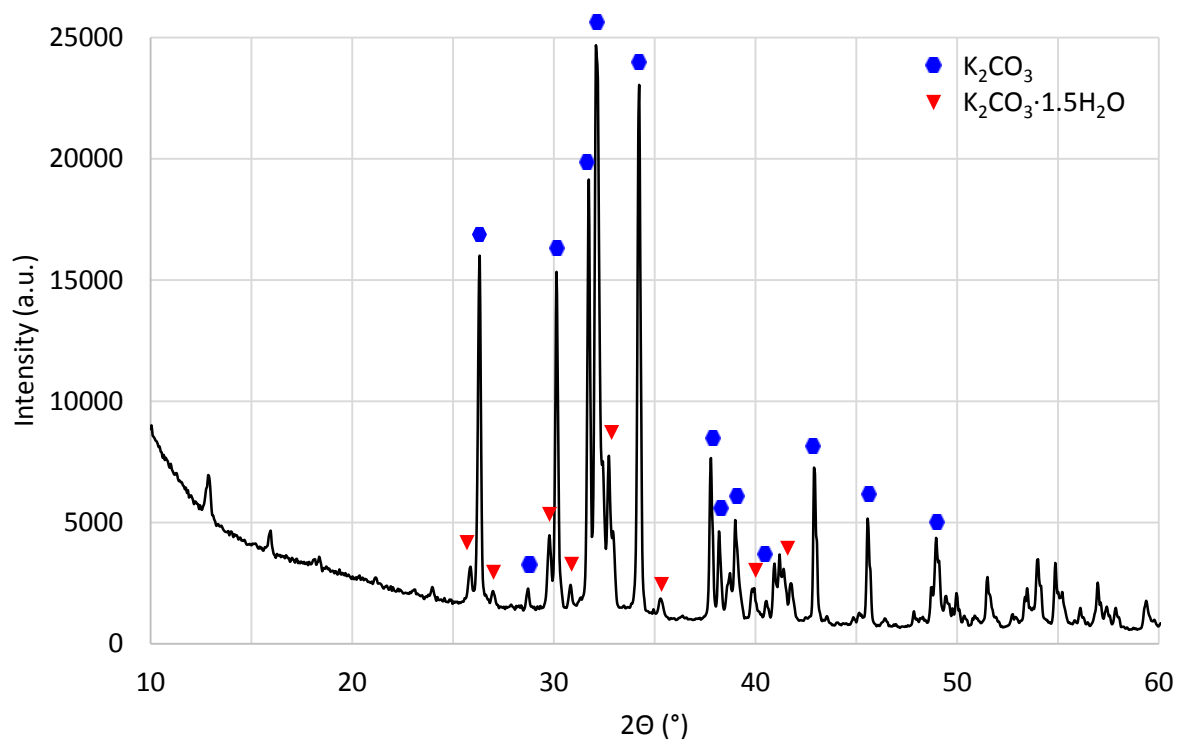


Figure Annex F.12 | P-XRD diffractogram of the pure quartz.

3. Potassium carbonate

Figure Annex F.13 | P-XRD diffractogram of the pure K_2CO_3 .

Annex G. Characterization of the residue on the K_2CO_3 from the pyrolysis at 800 °C of rice husks and K_2CO_3 added without contact

1. Ionic chromatography

The analysis was not quantitative due to a lack of calibration on some ions.

Table Annex G.1 | Detected elements through ionic chromatography in the residue.

Ion	Na^+	Ca^{2+}	K^+	Cl^-	NO_3^-	SO_4^{2-}	CO_3^{2-}
Detected?	No	No	Yes	No	No	No	Yes

2. SEM-EDX analysis

The sample was coated with graphite before analysis.

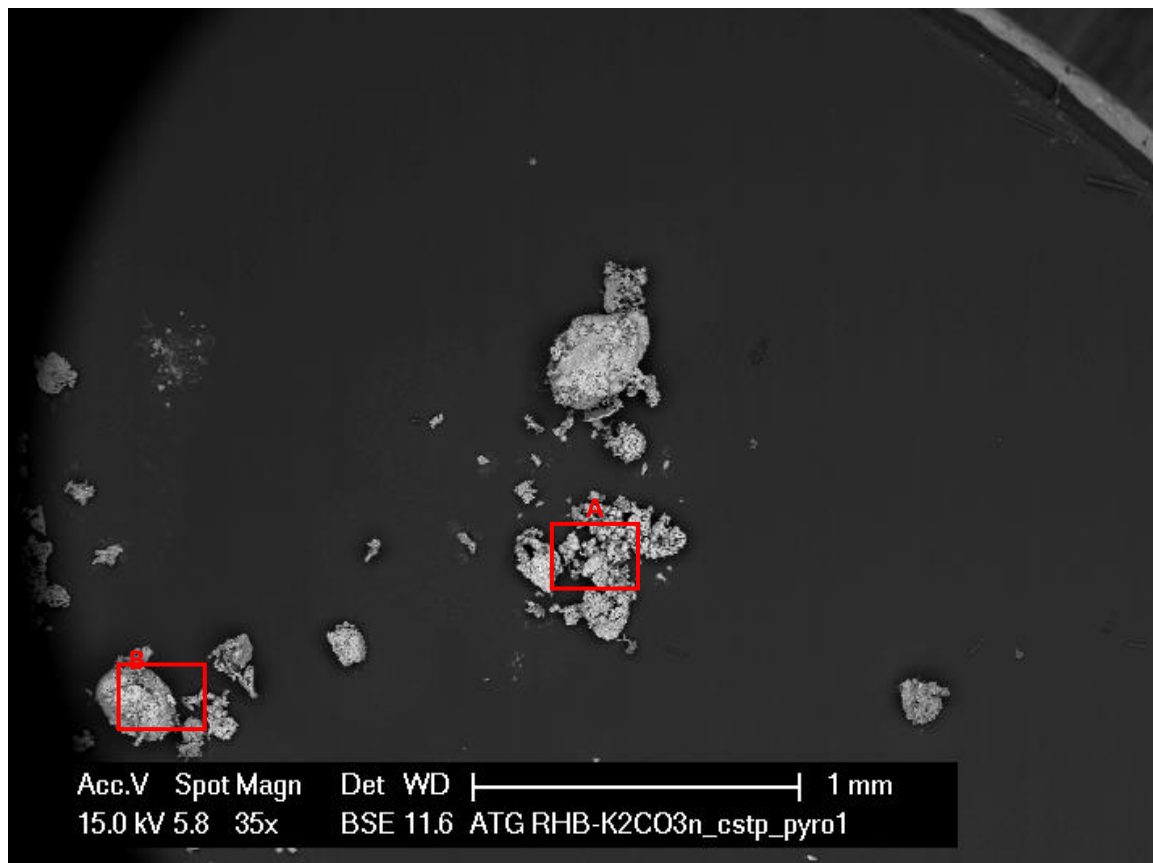


Figure Annex G.14 | SEM observation of the residue.

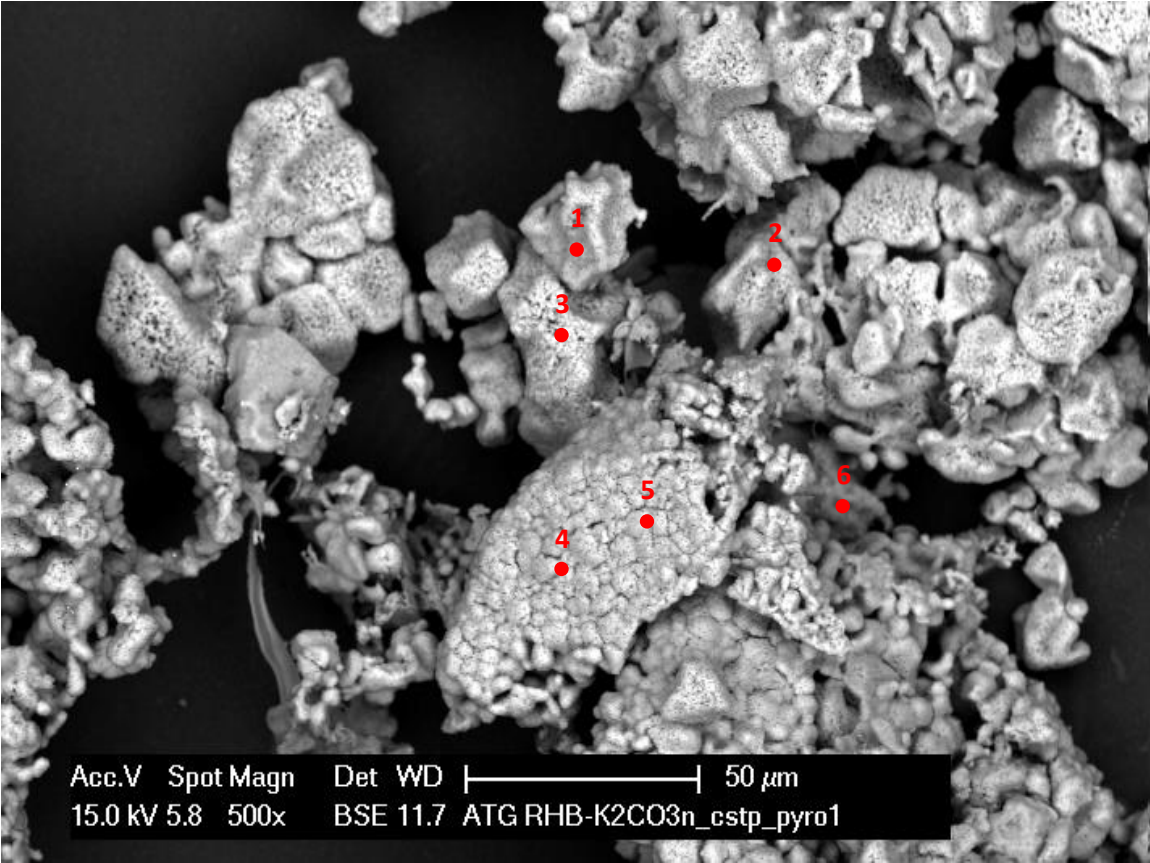


Figure Annex G.15 | SEM observation of the residue. Zoom on zone A.



Figure Annex G.16 | SEM observation of the residue. Zoom on zone B.

Table Annex G.2 | EDX analysis of the residue.

Point	C (wt%)	O (wt%)	K (wt%)	Total (wt%)
1	19.50	45.17	35.34	100
2	1.29	0	98.71	100
3	15.72	39.02	45.26	100
4	17.89	40.40	41.71	100
5	0	51.32	48.68	100
6	3.18	10.49	86.33	100
7	17.13	34.10	48.77	100
8	1.73	0	98.27	100
9	17.12	12.95	69.94	100
10	18.67	14.51	66.82	100

Abstract: Contribution to the understanding of the role of inorganic elements in biomass steam gasification.

In the current energy context, there is a need to develop the use of renewable energy sources, such as biomass. A promising way to produce energy from biomass is through gasification. However, some biomass species can be problematic during the gasification process due to their high inorganic content that can strongly influence the reaction kinetics. To date, the inorganic effects are known but the underlying mechanisms are still poorly understood. In this context, the objective of the present work was to contribute to the understanding of the inorganic elements role during the biomass steam gasification. In particular, the phenomena involving K and Si during the biomass steam gasification, especially through the gas phase, and with particular attention on their influence on the reaction kinetics were investigated. Investigations were conducted at an experimental level, with thermogravimetric analyses and physicochemical characterizations of the chars and ashes. They were supported by calculations at thermodynamic equilibrium as well as by literature review. The results have proven that the biomass inorganic composition is the main parameter explaining the differences between the gasification kinetic behaviors of the biomass species. From this conclusion, the specific effects of K and Si—two major inorganic elements in biomass—were further investigated in details. A competition was highlighted between two reactions involving K, most likely in the form of KOH(g): i) the catalysis of the steam gasification—whose mechanism starts from the pyrolysis step—on the one hand, and ii) the heterogeneous reaction between KOH(g) and SiO₂ to form non-catalytic species on the other hand. Additionally, it was showed that increasing the biomass SiO₂ content, whatever its crystalline form, slows its gasification down in a non-linear way and until a saturation effect.

Keywords: biomass; steam gasification; reaction kinetics; catalysis; potassium; silica.

Résumé : Contribution à la compréhension du rôle des éléments inorganiques sur la cinétique de gazéification sous vapeur d'eau de la biomasse.

Dans le contexte énergétique actuel, l'utilisation de sources d'énergie renouvelables, telle que la biomasse, doit être développée. La gazéification est l'une des voies prometteuses de production d'énergie à partir de la biomasse. Cependant, certaines biomasses peuvent être problématiques lors de la gazéification à cause de leur taux élevé en éléments inorganiques qui peut fortement influencer la cinétique de la réaction. A ce jour, ces effets sont connus mais les mécanismes en jeu restent mal compris. Dans ce contexte, l'objectif de ce travail était de contribuer à la compréhension du rôle des éléments inorganiques au cours de la gazéification sous vapeur d'eau de la biomasse. En particulier, les recherches se sont concentrées sur les phénomènes impliquant K et Si au cours de la gazéification sous vapeur d'eau de la biomasse, notamment dans la phase gaz, et avec une attention particulière vis-à-vis de leur influence sur la cinétique de la réaction. Les résultats ont démontrés que la composition en éléments inorganiques de la biomasse est le paramètre principal permettant d'expliquer les différences entre les cinétiques de gazéification des différentes espèces de biomasse. A partir de cette conclusion, l'effet particulier de K et Si (deux des éléments inorganiques majeurs de la biomasse) a été étudié en détails. Une compétition a été mise en évidence entre deux réactions impliquant K, très probablement présent sous forme de KOH(g) : i) la catalyse de la gazéification, dont le mécanisme commence dès la pyrolyse, d'une part, et ii) la réaction hétérogène entre KOH(g) et SiO₂ pour former des espèces non-catalytiques d'autre part. De plus, il a été montré qu'augmenter la concentration en SiO₂, quelle que soit sa forme cristalline, de la biomasse ralentit sa gazéification de façon non-linéaire et jusqu'à une saturation.

Mots-clés : biomasse ; gazéification sous vapeur d'eau ; cinétique de réaction ; catalyse ; potassium ; silice.